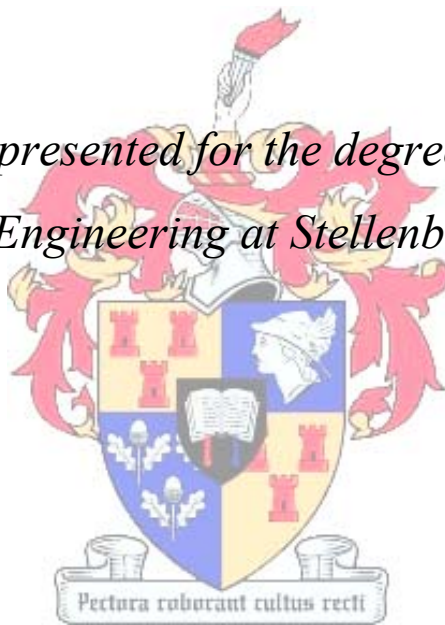


Cabling and Interfaces for Karoo Array Telescopes: Modelling and Metrology

by

Paul Stephanus van der Merwe

*Dissertation presented for the degree of Doctor of
Philosophy in Engineering at Stellenbosch University*



Promoter: Prof. Howard Charles Reader
Faculty of Engineering
Department of Electrical and Electronic Engineering

March 2011

Declaration

By submitting this dissertation electronically, I declare that the entirety of the work contained therein is my own, original work, and that I have not previously in its entirety or in part submitted it for obtaining any qualification

March 2011

Acknowledgements

I would first and foremost like to give thanks to Jesus Christ our Lord for all the blessings which I undeservingly receive from Him.

I would also like to acknowledge the following people without whom this dissertation would not have been possible:

My mother, father, and two sisters who believed in me every step of the way. Thank you.

Carmi, for her love, support, and lots of patience and understanding. Thank you for everything.

Prof. Howard Reader, for his support, guidance and enthusiasm. Our relationship started at an undergraduate level and he would always encourage us to “explore the territory”. He gave me the opportunity to do my masters degree and, when the time came, showed his faith in my abilities by recommending that I pursue a doctoral degree. Thank you Professor.

The South African SKA offices and the National Research Foundation for their very generous support over the past four years. Thank you.

Braam Otto whom I met when I started as a postgraduate student. Thank you, for your support, all the reading you had to do of my chapters, and the long hours spent in the lab. More importantly thank you for your friendship.

Wessel Croukamp firstly, for all the alterations which had to be made to the scale model of the KAT-7 telescope in a very short space of time. Secondly, for his willingness to help in order to find a solution. Thank you.

Martin Siebers for his assistance and technical expertise in making measurements in the antenna laboratory. Thank you.

ACKNOWLEDGEMENTS

Philip Kibet for his assistance with the measurements in the Antenna Laboratory, but also his friendship. Thank you Phil.

Gideon Wiid for his help and assistance in making the measurements at the either very hot or very cold Karoo KAT-7 site. Thank you.

To the rest of the students in the lab (Room E212). It has been a challenging four years, but your support and friendships made it a memorable journey. Thank you.

Contents

| | |
|---|---------------|
| Declaration..... | i |
| Acknowledgements..... | ii |
| Contents..... | iv |
| List of Figures..... | viii |
| List of Tables..... | xviii |
| Nomenclature..... | xix |
| Opsomming..... | - 1 - |
| Abstract..... | - 3 - |
| Chapter 1 Introduction..... | - 5 - |
| 1.1. Square Kilometre Array in South Africa..... | - 5 - |
| 1.2. Why is Radio Frequency Interference Mitigation Relevant? | - 6 - |
| 1.3. Dissertation Topics..... | - 7 - |
| 1.4. Contributions..... | - 9 - |
| 1.5. Layout of the Dissertation | - 11 - |
| Chapter 2 Literature Survey and Background Material | - 13 - |
| 2.1. Introduction: Cable Trays..... | - 13 - |
| 2.2. Transfer Impedance of Conductive Systems..... | - 13 - |
| 2.3. Reducing Transfer Impedance of Conductive Systems | - 15 - |
| 2.3.1. Earthed Parallel Conductor (EPC) | - 16 - |
| 2.3.2. Quasi-static Analysis of Simplified Geometry..... | - 17 - |
| 2.3.3. Theoretical Analysis of Cable Tray Transfer Impedance | - 19 - |
| 2.4. Cable Tray Connections | - 21 - |
| 2.4.1. Mid-span Connections..... | - 21 - |
| 2.4.2. End-connections | - 23 - |
| 2.5. Cable Tray Protection for Increased Frequencies | - 23 - |
| 2.6. Cable Tray Measurements..... | - 25 - |
| 2.7. Two-port Analysis of Cable Tray Model | - 27 - |
| 2.8. Physical and Computational Scale Modelling | - 28 - |
| 2.8.1. Physical Modelling..... | - 29 - |
| 2.8.2. Computational Modelling | - 30 - |
| 2.9. Direct Current Injection and Plane Wave Illumination..... | - 32 - |

CONTENTS

| | |
|--|---------------|
| 2.9.1. Coaxial Return Conductor..... | - 33 - |
| 2.9.2. Ground Plane Return Conductor | - 34 - |
| 2.9.3. Comparison: DCI Test Setups..... | - 34 - |
| 2.9.4. Comparison: DCI with Plane Wave Illumination | - 35 - |
| 2.10. Shielding Effectiveness of Enclosures | - 35 - |
| 2.10.1. Electric and Magnetic Shielding Effectiveness..... | - 36 - |
| 2.10.2. Electromagnetic Shielding Effectiveness..... | - 37 - |
| 2.11. Conclusion..... | - 38 - |
| Chapter 3 Computation and Metrological Issues..... | - 40 - |
| 3.1. Introduction | - 40 - |
| 3.2. Defining a Computational Model..... | - 41 - |
| 3.2.1. The Computational Environment | - 41 - |
| 3.2.2. Simplification of Objects Defined in CST MWS..... | - 43 - |
| 3.2.3. Computational Port Definitions | - 48 - |
| 3.3. Developing the Computational Analysis..... | - 49 - |
| 3.3.1. Connecting to the Model | - 49 - |
| 3.3.2. Cable Tray Model: Next Iteration | - 54 - |
| 3.3.3. Computational Boundary Definitions | - 57 - |
| 3.4. Conclusion..... | - 60 - |
| Chapter 4 Modelling and Measurement of Cable Tray Connections | - 62 - |
| 4.1. Introduction | - 62 - |
| 4.2. Defining the Investigation..... | - 64 - |
| 4.2.1. End-Connections | - 64 - |
| 4.2.2. Mid-span Connections..... | - 65 - |
| 4.2.3. Computational and Physical Model Dimensions | - 66 - |
| 4.2.4. Field Distributions around Computational Models..... | - 67 - |
| 4.3. Simulation, Measurement and Coupling Parameters | - 70 - |
| 4.3.1. Model 1 | - 70 - |
| 4.3.2. Model 2 | - 74 - |
| 4.3.3. Coupling Parameters | - 75 - |
| 4.4. Computed Results: Mid-tray Connections | - 76 - |
| 4.4.1. Model 1 | - 76 - |
| 4.4.2. Model 2 | - 78 - |
| 4.5. Computed Results: Enclosure Connections | - 81 - |

CONTENTS

| | |
|--|----------------|
| 4.5.1. Model 1 | - 81 - |
| 4.5.2. Model 2 | - 84 - |
| 4.6. B-Field Discussion | - 85 - |
| 4.7. CM Current Discussion | - 87 - |
| 4.8. Conclusion | - 89 - |
| Chapter 5 High Frequency Cable Tray Analysis | - 90 - |
| 5.1. Introduction | - 90 - |
| 5.2. Gain Calculations | - 92 - |
| 5.3. Induced Voltage Calculation | - 96 - |
| 5.4. Antenna Calibration | - 97 - |
| 5.5. Computational Equivalent Calculations | - 99 - |
| 5.5.1. Far Field Gain | - 99 - |
| 5.5.2. Plane Wave Illumination | - 100 - |
| 5.6. Measurements of Cable Tray Model | - 103 - |
| 5.6.1. Using the OATS | - 104 - |
| 5.6.2. Using an Anechoic Chamber | - 108 - |
| 5.7. Conclusion | - 118 - |
| Chapter 6 RF Current Audit for KAT-7 Telescope | - 120 - |
| 6.1. Introduction | - 120 - |
| Part 1 – Physical and Computational Model Development | - 122 - |
| 6.2. KAT-7 RF Audit Measurement Description | - 122 - |
| 6.3. Model Definitions | - 124 - |
| 6.3.1. Physical Scale Model | - 124 - |
| 6.3.2. Computational Scale Model | - 126 - |
| 6.4. Verification of Measurement and Computation | - 127 - |
| 6.4.1. S-parameter Measurements: Scale Models | - 128 - |
| 6.4.2. Current Measurements: Scale Models | - 132 - |
| 6.4.3. Current Measurements: KAT-7 Telescope | - 136 - |
| 6.4.4. Discussion | - 138 - |
| Part 2 – Measurement Setup Evaluation | - 139 - |
| 6.5. Current Distribution on KAT-7 Telescope | - 139 - |
| 6.5.1. Influence of Direct Injection | - 139 - |
| 6.5.2. Induced Current Distribution | - 142 - |
| 6.5.3. Discussion | - 144 - |

| | |
|--|----------------|
| Part 3 – Evaluation of Shielding Measures | - 145 - |
| 6.6. Comparison: Hardened vs. Non-hardened Telescope | - 145 - |
| 6.6.1. Hardened vs. Non-hardened for Direct Injection | - 146 - |
| 6.6.2. Hardened vs. Non-hardened for Induced CM Current | - 148 - |
| 6.6.3. Discussion | - 149 - |
| Part 4 – Evaluate Pedestal Shielding | - 150 - |
| 6.7. Level of Interface Shielding | - 150 - |
| 6.7.1. Defining a Computational Model | - 150 - |
| 6.7.2. Definition of Shielding Effectiveness | - 151 - |
| 6.7.3. Adaptation of Shielding Effectiveness | - 153 - |
| 6.7.4. Effects of Standing Waves | - 153 - |
| 6.7.5. Comparative Shielding Effectiveness Results: Radiative vs. Conductive | - 155 - |
| 6.7.6. Discussion | - 157 - |
| 6.8. Conclusion | - 157 - |
| Chapter 7 Conclusion, Recommendations and Future Work | - 160 - |
| Bibliography | - 165 - |
| Appendix A. Modelling of Cable Tray Connection | - 169 - |
| A.1. Model 1 Mid-span Connections | - 169 - |
| Appendix B. Antenna and Cable Tray High Frequency Analysis | - 170 - |
| B.1 Antenna Gain Calculations | - 170 - |
| B.2. Antenna Gain Functions | - 171 - |
| B.3. Comparison of Cable Tray Gain Functions | - 172 - |
| B.4. Comparison of Induced Voltages | - 173 - |
| Appendix C. KAT-7 RF Current Audit Results | - 175 - |
| C.1. Comparison of Scale Model S-parameter: Measured and Computed | - 175 - |
| C.2. Comparison of Current Distributions: Measured and Computed | - 178 - |
| C.2. Current Distribution: Direct Injection | - 181 - |
| C.3. Current Comparisons: Hardened vs. Non-hardened Direct Injection | - 181 - |

List of Figures

| | | |
|--------------|---|--------|
| Figure 1.1: | Aerial view of the KAT-7 site showing all seven dishes installed [2]. | - 5 - |
| Figure 1.2: | One of the KAT-7 composite-reflector, single pixel feed telescopes. | - 7 - |
| Figure 2.1: | Two conductors connecting a signal source U_s with source impedance Z_s , to load impedance Z_l . The DM circuit is made up by the source, conductors, and load. The CM current path is made up of an earth return conductor at the load and a parasitic capacitance at the source (after [8]). | - 14 - |
| Figure 2.2: | The magnetic field due to CM current on the wall of the coaxial system penetrates to the inside when the outer conductor is meshed as shown in [8]. | - 16 - |
| Figure 2.3: | Different EPCs used alongside a normal coaxial cable. The values shown below each EPC is typical values of mutual inductance in nH/m at frequencies where the wavelength is similar to the length of the coaxial cable that is being protected [8]. | - 16 - |
| Figure 2.4: | The geometry of incident fields, cables, and cable tray considered for coupling study presented in [10]. | - 18 - |
| Figure 2.5: | Schematic of the coupling mechanism between DM and CM voltage as used in [12]. This illustrates how the middle conductor in the distributed system is replaced with a non-magnetic cable tray. | - 19 - |
| Figure 2.6: | (a) Some of the cable tray mid-span connections referred to in the literature and included in this investigation (after [13]). The implementation of side connections consisting of two wide plates is shown in (b). | - 22 - |
| Figure 2.7: | The position of the conductors inside the cable tray being illuminated by an incident plane wave is shown. The various orientations of the cable tray with respect to the incident wave are also indicated [Kapora et al. 19]. | - 24 - |
| Figure 2.8: | Current is injected onto the cable tray with the victim conductor inside the tray visible. The receiver inside an EMC cabinet is also shown [11]. | - 26 - |
| Figure 2.9: | Computational representation of cable tray model used in [12] which indicates the direct injection of CM current onto the cable tray. | - 26 - |
| Figure 2.10: | Incident and reflected parameters for two-port network (after [22]). | - 27 - |

LIST OF FIGURES

| | |
|---|--------|
| Figure 2.11: Schematic of various mesh arrangement which highlight the need for different mesh densities when analysing real-world EMC problems [27]... | - 31 - |
| Figure 2.12: Approximation of curved boundary using (a) the Cartesian mesh and (b) triangular meshing [28]. | - 31 - |
| Figure 2.13: Schematic of the measurement setup used for HIRF testing. In this case the broadband coaxial return conductor setup is shown [33]. | - 33 - |
| Figure 2.14: Schematic of a measurement setup implementing a broadband ground plane return conductor [33]. | - 34 - |
| Figure 3.1: Discretisation of the computational domain as illustrated in [21] is shown. The dual meshing required for the calculation of E and H-fields are also shown. | - 42 - |
| Figure 3.2: As illustrated in [21], the incorrect alignment of mesh cell edges is shown in (a), with the correct alignment shown in (b). The mesh line ratio limit is directly responsible for this enhanced meshing. | - 42 - |
| Figure 3.3: (a) The increased meshing used to discretise the round edge of the object is shown in [21]. (b) An actual panel mount SMA connector. (c) The somewhat simplified CST version. Small savings on each component ultimately adds to make a big difference. | - 43 - |
| Figure 3.4: (a) One of the KAT-7 radio telescopes that was built as part of the MeerKAT pathfinder. (b) The CAD model from which the actual dish was created. (c) The CST MWS equivalent model after the CAD model was imported and simplified. | - 44 - |
| Figure 3.5: Closer comparison between (a) the KAT-7 telescope and (b) the CST MWS computational model in terms of the backing structure and elevation drive. | - 45 - |
| Figure 3.6: The mesh density required to resolve a small gap accurately, needs to be at least a factor of two smaller than the gap length. | - 46 - |
| Figure 3.7: Copper connection provided between the mesh inlay in the dish reflector and the backing structure. The backing structure along with the rest of the telescope is properly earthed. | - 47 - |
| Figure 3.8: Sectional view of the computational representation of the dish and backing structure as one component. | - 47 - |
| Figure 3.9: Discrete port representation in (a) normal view and (b) mesh view. Notice the difference in the port connection in the mesh view. | - 49 - |

LIST OF FIGURES

- Figure 3.10: (a) Equivalent cable tray model created in CST MWS. Notice the absence of cables that would normally connect to the model. A finite ground plane is also included. (b) Photograph of a cable tray measurement inside a screened room in a setup replicating the experiment done by Ebertsohn in [12]. - 50 -
- Figure 3.11: S_{11} measurement of cable tray model shown in Figure 3.10 (b). Notice the strong resonance at approximately 17 MHz. - 51 -
- Figure 3.12: Schematic of a three wire experiment which is analogous to the cable tray measurement setup discussed thus far. By connecting the measuring cables on either side of the DUT a ground loop is created along which unwanted CM current is flowing (After [43]). - 52 -
- Figure 3.13: Surface current plot at 17 MHz of L-plate through which the feed element injects current onto the cable tray. (a) Shows the front face and (b) the back face of the plate. This is the cable tray model used by Ebertsohn in [12] to investigate cable tray Z_t - 53 -
- Figure 3.14: Schematic of a three wire experiment which is analogous to the cable tray measurement setup for the new cable tray model. By connecting the measuring cables on one side of the DUT, the size of the ground loop is significantly reduced, minimising the unwanted induced CM current. - 55 -
- Figure 3.15: New cable tray model created to study the effects various connections had on the cable tray's overall shielding ability. - 56 -
- Figure 3.16: Surface current plot at 17 MHz of the widened L-plate of the new cable tray model with (a) the front face and (b) the back face. Notice the reduced level of current on the back face. - 57 -
- Figure 3.17: Boundary definitions available in CST MWS [21]. - 58 -
- Figure 3.18: Initial comparison between measurements of the new cable tray model made inside the screened room and CST MWS results using *open boundary* definitions. Note that this definition does not predict the resonance and simply allows energy to pass through the boundary with minimal reflection. - 59 -
- Figure 4.1: Cable tray models with an L-plate connection on the feeding side and an enclosure on the other. External excitation is achieved with: (a) an exposed centre conductor underneath the cable tray, Model 1 and (b) an

LIST OF FIGURES

| | | |
|--------------|---|------|
| | end-feed, Model 2. In both cases a victim loop is included inside the cable tray and enclosure. | 63 - |
| Figure 4.2: | Different types of end-connections for the termination of cable trays as specified in [13], and used in this investigation, are shown..... | 65 - |
| Figure 4.3: | Centre connections advised for use with cable trays as specified in [15].... | 65 - |
| Figure 4.4: | Computational representation of the following mid-span connections referred to in literature and included in this investigation: (a) full U-bracket, (b) bottom connection, (c) L-brackets, and (d) side straps..... | 66 - |
| Figure 4.5: | Investigation of magnetic field distribution around the cable tray for Model 1 without a victim conductor inside the cable tray. Shown in (a) is a vector plot of the magnitude of the magnetic field at 10 MHz and in (b) an indication of the current flow on the model. | 68 - |
| Figure 4.6: | Investigation of the electric field distribution at 10 MHz around the cable tray for Model 1 without a victim conductor inside the tray..... | 68 - |
| Figure 4.7: | Investigation of magnetic field distribution around the cable tray for Model 2 without a victim conductor inside the cable tray. Shown in (a) is a vector plot of the magnitude of the magnetic field at 10 MHz and in (b) an indication of the current flow on the model. | 69 - |
| Figure 4.8: | Investigation of the electric field distribution at 10 MHz around the cable tray for Model 2 without a victim conductor inside the tray..... | 70 - |
| Figure 4.9: | The screened room used for the cable tray measurements is shown in (a). Model 1 set up inside the screened room is shown in (b). | 71 - |
| Figure 4.10: | Schematic representing the screened room used to identify the orientation in which the dimensions of the room were applied to (15). The modal pattern was calculated accordingly. | 72 - |
| Figure 4.11: | Modal distribution inside screened room at 81 MHz. The indicated volume has the same dimensions as the actual room. | 73 - |
| Figure 4.12: | Computed and measured results compared for Model 1 cable tray measured in screened room. The room resonance was replicated in measurement up to -100 dB. | 73 - |
| Figure 4.13: | The finite computational domain showing the cable tray on top of a ground plane, which is earthed via copper straps, can be seen. Note the <i>conducting</i> boundary definitions used making up the sides and roof, with a zero potential floor. | 74 - |

LIST OF FIGURES

| | |
|---|--------|
| Figure 4.14: Comparison of measured and computed S_{21} values for Model 2 comparing previous measurement made as part of [12], a subsequent measurement made using the same calibrated VNA, and CST MWS simulation using open boundaries. | - 75 - |
| Figure 4.15: Model 1 computation of cable tray, enclosure, L-plate and mid-span connection showing peak surface current distribution at 10 MHz on the outside of the tray. | - 77 - |
| Figure 4.16: The simulated S_{21} coupling for the four mid-span connections investigated using Model 1 is shown in (a). The associated Z_t calculated using the various S-parameters are shown in (b). | - 77 - |
| Figure 4.17: Surface current for Model 2 at 10 MHz on the outside of the cable tray and enclosure, investigating side strap connections. | - 78 - |
| Figure 4.18: The change in S_{21} coupling associated with the four different mid-span connections simulated using Model 2 is shown in (a). The accompanying Z_t , also for Model 2, is shown in (b). | - 79 - |
| Figure 4.19: Comparison of calculated mutual inductance for the four mid-span connections using Model 2 shown in (a) with an enlarged area shown in (b). | - 80 - |
| Figure 4.20: Impression of magnetic field circulating around (a) side strap connection and (b) L-bracket [47]. | - 81 - |
| Figure 4.21: Two of the three cable tray-to-enclosure connections shown with (a) being the side only L-plates and (b) a full U-connection which consists of the continuous bottom and side L-plate connection. | - 82 - |
| Figure 4.22: Model 1 surface current distribution on the inside of the enclosure at 10 MHz with only two L-bracket side connections made to the enclosure. | - 82 - |
| Figure 4.23: The change in S_{21} coupling associated with the three different end-connections analysed using Model 1 is shown in (a). The accompanying Z_t also for Model 1 is shown in (b). | - 83 - |
| Figure 4.24: Model 1 surface current distribution at 10 MHz with bottom and side connections made to the enclosure. | - 83 - |
| Figure 4.25: Computed peak surface currents induced at 10 MHz inside the cable tray and enclosure for Model 2. | - 84 - |

LIST OF FIGURES

| | |
|--|---------|
| Figure 4.26: The change in S_{21} coupling associated with the three different end-connections analysed using Model 2 is shown in (a). An enlarged view of the same parameters is shown in (b). | - 84 - |
| Figure 4.27: Comparison of the three end-termination connections investigated using Model 2. The Z_t is shown in (a) with the mutual inductance shown in (b).. | - 85 - |
| Figure 4.28: Cable tray connections as advised by [15]. | - 87 - |
| Figure 5.1: Cable tray Model 1 viewed end-on, indicating the different angles of incidence to identify the change in cable tray shielding. | - 91 - |
| Figure 5.2: Two-port measurement setup. | - 92 - |
| Figure 5.3: Measurement setup for cable tray illumination measurements. | - 93 - |
| Figure 5.4: Basic transmit-and-receive system. | - 94 - |
| Figure 5.5: Cable tray far field gain calculated at 4005 MHz. | - 99 - |
| Figure 5.6: Computational environment showing the cable tray model and plane wave excitation. | - 100 - |
| Figure 5.7: Close-up view of voltage monitor included at SMA port to measure the induced voltage with frequency. | - 101 - |
| Figure 5.8: Spherical coordinate system. | - 102 - |
| Figure 5.9: This photo taken from above the cable tray model shows a detailed view of the enclosure at end of the tray (a) without a cover and (b) with a cover. The termination of the victim conductor inside the enclosure can also be seen. | - 103 - |
| Figure 5.10: The OATS at ISSA (near Grabouw in the Western Cape) used for initial high frequency cable tray measurements. | - 104 - |
| Figure 5.11: (a) Shows the OATS measurement being made for a single angle of incidence. Shown schematically in (b) is the attempt to minimise the multi-path interference by positioning the cable tray on the ground. The VNA indicated in the schematic was replaced by a separate SG and SA.. | - 106 - |
| Figure 5.12: Comparison of (a) gain function and (b) induced voltage both calculated from measured results and computed using CST MWS for a 45° angle of incidence for the OATS measurement environment. | - 107 - |
| Figure 5.13: Cable tray measurement setup inside anechoic chamber at the Stellenbosch University. | - 109 - |
| Figure 5.14: Schematic showing the setup for the cable tray measurements inside anechoic chamber. | - 109 - |

LIST OF FIGURES

| | |
|--|---------|
| Figure 5.15: Two-port system..... | - 110 - |
| Figure 5.16: Comparison of calculated and computed cable tray gain functions for horizontal polarisation of the E-field for three different angles of incidence; (a) 0°, (b) 45°, and (c) 90°. Note that these results are for an open enclosure at the end of the cable tray. | - 111 - |
| Figure 5.17: Comparison of the gain functions calculated from measurements of the cable tray for horizontal polarisation of the E-field with the receiving antenna positioned at three different angles of incidence. | - 112 - |
| Figure 5.18: Comparison of the gain functions calculated from measurements of the cable tray, with the antenna positioned to receive vertically polarised E-field, is considered for two angles of incidence. | - 113 - |
| Figure 5.19: Comparison of the change in calculated gain functions of the cable tray using measured results, for a 45° angle of incidence, are shown. Results for the horizontal polarisation of the antenna, with and without an enclosure cover are shown in (a), and for vertical polarisation with and without an enclosure cover shown in (b). | - 114 - |
| Figure 5.20: Comparison of calculated and computed induced voltages on the victim conductor inside the cable tray for a horizontally polarised antenna, are shown in (a) for a 45° angle of incidence. The comparison between the calculated voltages for all three angles is shown in (b)..... | - 115 - |
| Figure 5.21: End-view schematic of the cable tray and victim conductor. | - 116 - |
| Figure 5.22: Comparison of induced voltage on the victim conductor inside the cable tray calculated from measurements for a vertically polarised antenna, is shown for two different angles of incidence. | - 117 - |
| Figure 5.23: Comparison of the change in induced voltage calculated using measured results for a 45° angle of incidence is shown. The results for horizontal polarisation with and without enclosure cover are shown in (a), and for vertical polarisation with and without cover shown in (b)..... | - 117 - |
| Figure 6.1: One of the KAT-7 dishes built in the Northern Cape as part of the South African demonstrator project. A CM current probe was used during the audit to measure the current around the telescope is shown in the insert. . | - 122 - |
| Figure 6.2: View of the galvanic connection between the upper and lower pedestal where the copper shoe and LDC connection to the rotation plate are (a) aligned and (b) misaligned. Note that the four copper shoes on each | |

LIST OF FIGURES

| | | |
|--------------|---|---------|
| | telescope (only one shown in both (a) and (b)) are fixed to the lower pedestal..... | - 123 - |
| Figure 6.3: | Computational representation of (a) scenario one and (b) scenario two. The feed conductors used in the direct injection analysis together with the excitation and termination ports are all shown..... | - 124 - |
| Figure 6.4: | Physical scale model of the KAT-7 radio telescope in a stow position being measured inside an anechoic chamber. | - 125 - |
| Figure 6.5: | Cross-sectional view of the upper half of the scale model implemented in CST MWS. In the mesh view, the change in mesh density as applied by the subgridding algorithm is clearly visible. Note the staircase meshing visible in the insert. | - 127 - |
| Figure 6.6: | Computational model of the KAT-7 radio telescope scenario one aligned, with the measurement setup indicated. | - 129 - |
| Figure 6.7: | No modelled SMA connectors were used for the termination of the four earthing connections. Discrete ports were sufficient. | - 129 - |
| Figure 6.8: | Comparison of measured and computed S_{11} for both models in scenario one aligned state..... | - 130 - |
| Figure 6.9: | Comparison of measured and computed S-parameters for both models in scenario one aligned state. All four earthing connections are shown with (a) north-facing, (b) east-facing, (c) south-facing and (d) west-facing..... | - 131 - |
| Figure 6.10: | Comparison of S_{21} measured and computed using the physical and computational scale models. The north-facing earthing connection for scenario two aligned is shown..... | - 131 - |
| Figure 6.11: | Comparison of measured current using the VNA and SA as receiver. The currents were measured on the north-facing earthing connection for (a) scenario one aligned and (b) scenario one misaligned..... | - 133 - |
| Figure 6.12: | Computational representation of the earthing connections. The closed contours around which the magnetic fields are integrated are also shown. | - 134 - |
| Figure 6.13: | Comparison between measured results using a VNA and SA as receiver, and computed results using CST MWS. | - 135 - |
| Figure 6.14: | Setup illustrated for making current measurements on KAT-7 telescope using FSH 8 SA in VNA mode. | - 136 - |
| Figure 6.15: | Comparison of currents flowing on the north-facing earth connection. These include measured results for the physical model using the VNA | |

LIST OF FIGURES

| | |
|---|---------|
| and SA, computed results for the computational model, and measurements on the KAT-7 telescope. Results are shown for (a) scenario one aligned, (b) scenario one misaligned, (c) scenario two aligned and (d) scenario two misaligned..... | - 137 - |
| Figure 6.16: Comparison of injected currents measured on the four earthing connections for the KAT-7 telescope. Scenario one aligned is shown in (a) and misaligned shown in (b)..... | - 139 - |
| Figure 6.17: Comparison of injected currents measured on the four earthing connections for the physical scale model for scenario three..... | - 140 - |
| Figure 6.18: Comparison of injected currents measured on the four earthing connections for the physical scale model for scenario four. | - 141 - |
| Figure 6.19: Illumination measurement done on one of the KAT-7 telescopes for (a) scenario two aligned and (b) scenario one aligned. | - 142 - |
| Figure 6.20: Comparison of induced currents on the four earthing connections of the KAT-7 telescope with scenario one aligned shown in (a) and scenario two aligned shown in (b)..... | - 143 - |
| Figure 6.21: The hardening policies used in one of the KAT-7 telescopes include (a) a multi-sectioned metallic interface plate and (b) gasketting added to interface for braided cables. | - 146 - |
| Figure 6.22: Current measured on the west-facing connection for scenario one aligned and misaligned compared for (a) a non-hardened telescope and (b) a hardened telescope. | - 147 - |
| Figure 6.23: Current compared for a hardened and non-hardened telescope for scenario one aligned..... | - 148 - |
| Figure 6.24: Current compared for a hardened and non-hardened telescope for scenario two aligned..... | - 149 - |
| Figure 6.25: Pedestal in sectioned view with conductor and interface plates added. The plane wave used to excite the system is also shown. | - 150 - |
| Figure 6.26: The connection between the cable and interface replicated in CST MWS.- | - 151 - |
| Figure 6.27: Current sampled along the length of the conductor at four discrete frequencies without the top interface present..... | - 154 - |
| Figure 6.28: Current sampled along the length of the conductor at four discrete frequencies with the top interface present..... | - 154 - |

LIST OF FIGURES

| | |
|--|---------|
| Figure 6.29: Calculated E-field on the inside of the pedestal with the shielding interface in place | - 156 - |
|--|---------|

List of Tables

| | | |
|------------|--|---------|
| Table 6:1: | Comparison of average injected currents measured on the four earthing connections..... | - 141 - |
| Table 6:2: | Comparison of average induced currents measured on the four earthing connections..... | - 144 - |
| Table 6:3: | Marker frequencies..... | - 156 - |
| Table 6:4: | Comparison of shielding values calculated for E-field and current measurements..... | - 156 - |

Nomenclature

Abbreviations

| | |
|----------|---|
| ASKAP | Australian Square Kilometre Array Pathfinder |
| CAD | Computer Aided Design |
| CEM | Computational Electromagnetics |
| CM | Common Mode |
| CST MWS | Computer Simulation Technology Microwave Studio TM |
| dB | Decibels |
| DC | Direct Current |
| DCI | Direct Current Injection |
| DM | Differential Mode |
| DUT | Device under Test |
| EPC | Earthed Parallel Conductor |
| EM | Electromagnetic |
| EMC | Electromagnetic Compatibility |
| EMI | Electromagnetic Interference |
| EMP | Electromagnetic Pulse |
| FD | Frequency Domain |
| FDTD | Finite Difference Time Domain |
| FEM | Finite Element Method |
| FIT | Finite Integration Technique |
| FSH 8 SA | Rohde and Schwarz TM FSH 8 Spectrum Analyser |
| GHz | Giga-Hertz |
| HF | High Frequency |
| HIRF | High-Intensity Radiated Field |
| ITU | International Telecommunications Union |
| KAT | Karoo Array Telescope (KAT-7, MeerKAT) |
| kHz | kilo-Hertz |
| LDC | Lightning down Conductor |
| LPDA | Log Periodic Dipole Antenna |
| MHz | Mega-Hertz |
| MoM | Method of Moments |

NOMENCLADTURE

| | |
|---------------|------------------------------|
| ms | milli-seconds |
| nH | nano-Henry |
| OATS | Open Area Test Site |
| PEC | Parallel Earth Conductor |
| RF | Radio Frequency |
| RFI | Radio Frequency Interference |
| RX | Receive |
| SA | Spectrum Analyser |
| SE | Shielding Effectiveness |
| SG | Signal Generator |
| SKA | Square Kilometre Array |
| SMA | Sub-Miniature Version A |
| TD | Time Domain |
| TEM | Transverse Electromagnetic |
| TLM | Transmission-Line Modelling |
| TM | Transverse Magnetic |
| TX | Transmit |
| μV | Micro-Volt |
| VHF | Very High Frequency |
| VNA | Vector Network Analyser |

Symbols

| | |
|--------------|--------------------------------|
| a | Square Root of Incident Power |
| b | Square Root of Reflected Power |
| A | Area |
| C | Contour |
| D | Directivity |
| ϵ_0 | Permittivity of Free Space |
| e | Efficiency |
| \vec{E} | Electric Field Vector |
| E | Magnitude of Electric Field |
| ζ | Positional Angle |
| G | Gain |

NOMENCLADTURE

| | |
|------------|--|
| η_0 | Free Space Wave Impedance |
| \vec{H} | Magnetic Field |
| h | Height |
| θ | Angle of Incidence |
| I_{CM} | Current (Common Mode) |
| I_{DM} | Current (Differential Mode) |
| I_{ext} | External Current |
| i | Current |
| J | Current Density |
| λ | Wavelength |
| l | Length |
| μ_0 | Permeability of Free Space |
| M | Mutual Inductance |
| P | Power |
| R | Distance |
| R | Resistance |
| r | Radius |
| \vec{S} | Poynting Vector for Electromagnetic Fields |
| S | Power Density |
| t | Time |
| ϕ | Angle of Rotation |
| U_{dist} | Disturbance Voltage |
| U_{DM} | Voltage (Differential Mode) |
| U_s | Source Voltage |
| V_{DM} | Voltage (Differential Mode) |
| w | Width |
| Y | Admittance |
| Ω | Ohm |
| ω | Angular Frequency (radians) |
| Z_l | Load Impedance |
| Z_o | Characteristic Impedance |
| Z_s | Source Impedance |
| Z_t | Transfer Impedance |

Opsomming

Die Karoo Array Teleskop (KAT) sal gebruik word deur Suid-Afrika in sy poging om die bod te kry om die internasionale Square Kilometre Array (SKA) te huisves. Aangesien die SKA ordes meer sensitief sal wees as bestaande radioteleskope, sal dit terselfdertyd ook meer sensitief wees vir radio frekwensie steurnisse. Die invloed van radio frekwensie steurnisse op die differentiëlemodus KAT geleidende netwerk is iets onvermydeliks. Binne hierdie konteks kan die geleidende netwerk, in sy mees basiese vorm, bestaan uit 'n bron, 'n las, en verbindingsgeleiers. Dit kan ook, in die geval van die KAT-7 sewe-teleskoop interferometer, bestaan uit elke teleskoop, sy funksionele bekabeling, en die korrelator wat die verbinding is tussen al die teleskope. Daar is egter, addisionele verbindings tussen die netwerk en die onmiddellike omgewing rondom dit. Hierdie verbindings kan opsetlik gemaak word deur byvoorbeeld, verbinding van die netwerk se aardkabel aan die res van die beaarding, of onopsetlik deur parasitiese kapasitansies en induktiewe verbindings. As gevolg hiervan word addisionele geleidende netwerke geskep waarin gemenemodus strome kan vloei. Indien daar wel strome in die gemenemodus netwerk vloei, word dit oorgedra aan die differentiëlemodus netwerk deur 'n oordragimpedansie (Z_t) wat teenwoordig is tussen die twee. Om dus die steurnisse in die differentiëlemodus netwerk te verminder of te elimineer, moet Z_t tot 'n minimum beperk word.

Die gebruik van 'n geaarde parallelle geleier in die vorm van 'n kabelkanaal, word beskou as een van die mees doeltreffendste metodes om Z_t te verminder. Die eienskappe van kabelkanale as geaarde parallelle geleiers by frekwensies waar die golflengtes langer is as die van die kabelkanaal, is volledig gedokumenteerd. Een van die belangrikste fokuspunte in hierdie verhandeling is rakende die kabelkanale se middel en eindpuntverbindings. Hulle word nie goed beskryf in die beskikbare literatuur nie, en weliswaar vir wyeband doeleindes wat vir KAT ontwikkelinge verwag word. Die invloed van die mees algemeenste kabelkanaal verbindings op gemete en berekende Z_t word bepaal. Computer Simulation Technology's Microwave Studio (CST MWS) word eerstens, gebruik om die akkuraatheid van die gemete resultate te bewys en tweedens, deur visualisering van E-veld en gemenemodus oppervlak strome. Aanbevelings vir die beste verbindings vir enige kabelkanaal opstelling word gegee. Die algemene afskerminsvermoeë van 'n idiaal-verbinde kabelkanaal word bepaal deur middel van metings en

simulasies. In beide gevalle word die geïnduseerde spanning op 'n slagoffer kabel, en die verveld aanwinds funksie bepaal vir verskillende invalshoeke op die model. Die resultate toon verder dat vir spesifieke gevalle wat beskou word, die meeste koppeling binne die kabinet aan die einde van die kabelkanaal plaasvind. Oor die algemeen verskaf goed verbinde kabelkanale wel 'n sekere vlak van beskerming aan kables binne die kabelkanaal, selfs by frekwensies waar die golflengte baie korter is as die breedte van die kabelkanaal.

Die tweede belangrike fokuspunt spruit voort uit 'n radio frekwensie stroomoudit, wat twee van die KAT-7 teleskope evalueer het. Afskermingsmatreëls soos die kabelhindernisse op die vloer en dak van die onderste teleskoop voetstuk, word bestudeer. Tesame met die metings op die werklike teleskoop wat geneem is, word 'n akkurate fisiese en simulatie skaalmodel geskep om die metings beter te analiseer. Direkte stroominspuittings metode en platvlakgolf beligting word gebruik om gemenemodus strome op die teleskoop se struktuur te induseer. Die gemenemodus stroomverspreiding vir beide tegnieke word vergelyk in 'n poging om kommentaar te lewer rakende die geldigheid van die meettegniek. Die gemenemodus strome wat aan die buitekant van die teleskoop voetstuk gemeet word, is hoër wanneer 'n direkte stroompad na grond op die voetstuk geskep word in vergelyking met 'n ongedefinieerde pad. Hierdie verskynsel dui daarop dat ten minste twee metodes bestaan om die ongevraagde gemenemodus strome te verhoed om aan die binnekant van die teleskoop voetstuk te vloei. Die een is die verbetering van die vloer en dak kabelhindernisse, en die ander is verbetering van die stroompad (stroompaaie) aan die buitekant van die voetstuk sodat 'n meer direkte pad na grond geskep word. Die gemiddelde gemenemodus strome weerskante van die kabelhindernis, kan gebruik word om te bepaal hoeveel afskerming die hindernis bied. Indien die berekende waardes by verskillende frekwensies vergelyk word met die tradisionele filter doeltreffendheid (Z_t), word 'n meer konserwatiewe beraming verkry.

Die navorsing in hierdie verhandeling het alreeds, maar sal ook die toekomstige uitleg van galvaniese stelsels vir KAT-7 asook die verwagte MeerKAT beïnvloed.

Abstract

The Karoo Array Telescope (KAT) will be used by South Africa in its bid to host the international Square Kilometre Array (SKA). As the SKA will have orders of magnitude greater sensitivity than existing radio telescopes, it will also be concomitantly more sensitive to radio frequency interference (RFI). The influence of RFI on a differential mode (DM) KAT conductive system is an unavoidable phenomenon. In this context, the conductive or galvanic system can, in its most basic form, consist of a source, a load, and connecting conductors. It can also, in the case of the KAT-7 seven-dish interferometer, consist of each telescope, its functional cabling, and the main correlator connecting the telescopes together. However, additional connections between the system and the environment exist. These might be an intentional connection made to the earthing layout, or unintentional connections due to parasitic capacitances and inductive connections. As a result of this, additional conductive systems are created which carry common mode (CM) currents. Interference present in such CM paths enters the DM system through the transfer impedance (Z_t) between them. To reduce or eliminate this interference in the DM system, Z_t has to be minimised.

The use of an earthed parallel conductor (EPC as commonly referred to) in the form of a cable tray is considered to be one of the principal methods to reduce Z_t . The properties of cable trays as EPCs at wavelengths which are greater than the tray length are well documented. One main focus in this dissertation is on cable tray mid-span and end connections. They are not well described in the literature over the wide range of frequencies that is expected for KAT developments. The influence of the most common connections on the measured and computed Z_t of the cable tray is determined. Computer Simulation Technology's Microwave Studio (CST MWS) is employed to validate the measured results and also to enable visualisation of the fields and currents. Recommendations for the best connection to use for any cable tray installation is given. The overall shielding ability of optimally-connected cable trays has been evaluated using a physical and computational model. In both cases the induced voltage on a victim conductor, and far-field gain functions for varying angles of incidence onto the model, are determined. The results also show that for certain scenarios, most of the coupling to the victim conductor, takes place inside the end enclosure and not the cable tray. In general, properly-connected cable trays do provide protection to their enclosed conductors, even at frequencies where the wavelength is much shorter than the width of the tray.

ABSTRACT

The second main focus arises from an on-site radio frequency (RF) current audit undertaken on two of the seven KAT-7 telescopes. Shielding measures, such as interface barriers at the floor and roof of the lower telescope pedestal, are studied. The investigation is facilitated by the development of an accurate physical and computational scale model of the dish. Direct current injection and plane wave illumination methods are used to excite the system. The measured CM current distributions are compared and comments made regarding the validity of the measurement procedure. The CM currents, measured around the outside of the lower pedestal show higher levels when a direct current path to ground is established, as opposed to when no clear path exists. This finding suggests at least two methods of preventing CM interference entering or leaving the pedestal: harden the floor and roof barriers, or manage current paths outside the telescope. Related to this, CM currents measured either side of the telescope interface barriers, are used to determine the level of shielding the interface provides. When compared to the common definition of shielding effectiveness, the current measurement provides more conservative shielding estimates.

The research in this dissertation has influenced, and will continue to influence, the layout of galvanic systems for the present KAT-7 structures and the anticipated developments to MeerKAT.

Chapter 1

Introduction

1.1. Square Kilometre Array in South Africa

The Karoo Array Telescope (KAT or MeerKAT) will be used in the South African bid to host the Square Kilometre Array (SKA). While MeerKAT is a pathfinder project, it will ultimately be, in its own right, one of the most powerful radio telescopes in the world. The SKA originated from the need of the global radio astronomy community to have a telescope that would be an order of magnitude more sensitive than existing systems, and would have a wide field-of-view, especially below a few Gigahertz (Van Ardenne et al. [1]). After identifying suitable sites to host the SKA, the International SKA Steering Committee chose southern Africa and Australia to be the finalists in 2006 [2]. Due to the sheer scale of the SKA, pathfinder projects such as MeerKAT and the Australian Square Kilometre Array Pathfinder (ASKAP) are underway to develop and prove the proposed technology.

After the completion of a successful prototype telescope built at the Hartebeesthoek Radio Astronomy Observatory the next stage, a prototype interferometer KAT-7 shown in Figure 1.1, is nearing completion. This is a precursor to MeerKAT and consists of seven 12 m telescopes which will be increased to a projected 80¹ telescopes constituting MeerKAT [2].



Figure 1.1: Aerial view of the KAT-7 site showing all seven dishes installed [2].

¹ From August 2010 a formal decision was made to change the layout of MeerKAT to 64 offset fed Gregorian telescopes.

1.2. Why is Radio Frequency Interference Mitigation Relevant?

As the SKA will have orders of magnitude greater sensitivity than existing radio telescopes, it will also be concomitantly more sensitive to radio frequency interference (RFI). Both conducted and radiated RFI will have an impact on such a complex system. Strong sources (wideband and narrowband) of radiated interference, both inside and outside the antenna receiver's operational bandwidth have to be minimised. These sources can cause saturation and inter-modulation distortions, corrupting the data across the entire spectrum being investigated (Lord [3]). Conducted interference generates disturbance voltages evident in the system, mainly through the mechanism of transfer impedance. The transfer impedance is dependent on the resistance and mutual inductance of the entire galvanic layout including the earthing. Environmental RFI can be reduced, but it cannot be completely removed. The objective from an electromagnetic compatibility (EMC) point of view is, firstly, to ensure that minimal additional RFI enters the environment. Secondly, it is necessary to reduce the susceptibility of the various systems by lowering their transfer impedance.

This proposed site for MeerKAT and the potential SKA itself was chosen, after extensive RFI site surveys, specifically for its radio quietness. The quietness of the site in terms of terrestrial RFI is important because the SKA will operate outside frequency bands set aside for radio astronomy by the International Telecommunications Union (ITU) (Jonas [4]). The low population density of the Northern Cape in general, but also in particular around the radio astronomy reserve, will help to maintain an associated low level of RFI. With the installation of the required infrastructure, there will be an increase in self-generated RFI. Accompanying measures to reduce this have been included at every step of the project development. The most substantial example is the installation of a power line which has been designed to minimise the occurrence of sparking noise.

Reducing the effect of conducted interference for such sensitive instruments requires RFI mitigation measures far surpassing those of commercial applications. This included creating a completely shielded environment within the lower pedestal (Figure 1.2). The purpose of the additional shielding measures was to reduce common mode (CM) current induced on the telescope structure flowing on the inside of the pedestal and vice versa. A lightning down conductor (LDC) has been installed on each telescope. In the event of a direct strike, the majority

of the lightning current is directed to ground as quickly and effectively as possible [5]. The dissertation investigates these and other measures to see how they can also be used to reduce transfer impedance and improve shielding.

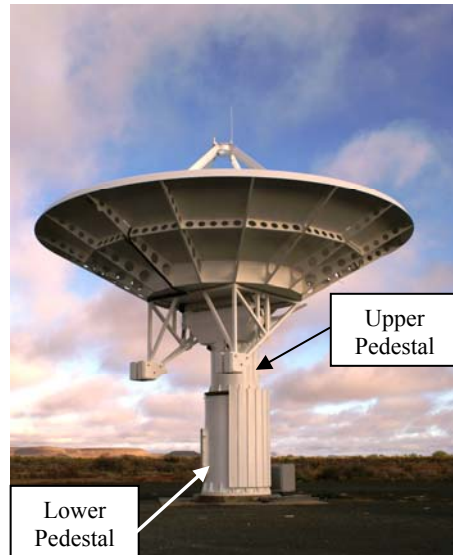


Figure 1.2: One of the KAT-7 composite-reflector, single pixel feed telescopes.

1.3. Dissertation Topics

In one case the system, mentioned in the previous section, might be a box of electronics and in another the entire pedestal or correlator room. Various concepts which will be used in the investigations are presented first. The objective of this overview is preparatory in nature, introducing concepts which will be discussed again in the relevant chapters. This includes transfer impedance and its mitigation through cable trays. As a related theme, cable tray connections which are found in the literature are considered. The use of physical and computational models as the primary method of investigation, the radiated and direct current injection (DCI) methods as means of excitation, and finally the concept of shielding effectiveness are all discussed.

With conductors being exposed to interference when they travel between two enclosures, open cable trays and the shielding they provide are investigated. Focus is placed particularly on cable tray mid-span and end-connections. The general shielding ability of cable trays at frequencies where the wavelength is significantly longer than the tray, has been well documented. Attention

here is on cable tray connections and the influences they have on the tray's overall transfer impedance.

The shielding ability of open cable trays at frequencies where the wavelength is shorter than the length of the tray is not as well reported. As this is important for the MeerKAT project, the topic is investigated by illuminating a physical cable tray model with a plane wave from an antenna with a known gain. The level of induced voltage on a victim conductor inside the tray is compared for different angles of incidence, as well as vertical and horizontal polarisations of the disturbance field. The influence of an enclosure, which provides a means of terminating the cable tray, is included in the analysis. With its inclusion, a more accurate representation of an actual cable tray installation is investigated. The objective, therefore, is to determine if most of the coupling to the victim conductor by the external field, will take place along the open cable tray. To determine this, an open and sealed enclosure representing a poorly and properly shielded cabinet respectively, are investigated.

To improve the EMC (both susceptibility and emission) of the electronics inside the lower pedestal of the KAT-7 telescope, additional hardening measures arising out of the research were recommended and installed. The most important of these measures are two interface barriers at the top and bottom of the lower pedestal section. Two telescopes were evaluated, one of which had the interface barriers installed (the hardened telescope). The other had no interface barriers installed. The distribution of CM current on the outside of the lower pedestal (Figure 1.2) for both telescopes is used in the examination of the following four objectives:

- Establish an accurate physical and computational scale model of the KAT-7 telescope shown in Figure 1.2. (Scale models can be used to study various effects regarding the actual telescope more efficiently).
- Evaluate the influence of DCI on the distribution of CM current on the outside of the pedestal. (Determine if the DCI method establishes a different distribution of CM current compared to when using the plane wave illumination method and comment on the applicability of the measurement setup).
- Determine the change in measured CM current on the outside of the pedestal for a hardened and non-hardened telescope. (With the added shielding interfaces, less CM current should flow on the inside of the pedestal. A resulting increase in current on the

outside should be measured. The objective is to determine how this changes for different orientations and positions of the dish.)

- Present a method to determine the level of shielding the top interface barrier inside the lower pedestal provides.

1.4. Contributions

Extensive use of computational analysis was made. The specific time domain discretisation technique is investigated. This helps to understand how to increase simulation efficiency through model simplification. Comparison of measured and computed data required replication of the influences of the measurement environment in the computational domain. Although similar investigations may have been done for other applications, a complete understanding of the problem and therefore every step involved in reconciling the presented results was needed.

Installation standards and literature on general EMC practises do not provide technical details as to why a particular cable tray mid-span and end connection is recommended or not. To study this effectively, two physical and computational models were created. A comprehensive analysis of mid-span and end-terminations are presented using both models. Definitive results stating why a specific type of connection should be used are given. The findings from this work have led to a recently accepted publication:

P S van der Merwe, H C Reader, D J Rossouw, "Cable Tray Connections for EMI Mitigation" - accepted by IEEE EMC Transactions, September, 2010.

Cable trays in practical installations will be exposed to both low and high frequency interference. Due to very little material detailing their shielding ability at higher frequencies being available, this dissertation aims to make a contribution. Both the induced voltage on a victim conductor inside the tray, and the cable tray far field gain function are determined for varying angles of incidence of a disturbance field. Measured results are compared with computation. By including an enclosure at the end of the cable tray in the analysis, the results show that for certain scenarios more coupling will occur elsewhere in the system. The open cable tray occasionally provides sufficient protection to surpass that of enclosures usually installed with it. This shows that cable trays should be simulated with as much of the surround environment included.

A comprehensive radio frequency (RF) current audit compared CM currents measured on the outside of the actual KAT-7 telescope to results calculated and computed using a physical and computational scale model. Initially the accuracy of the physical and computational scale models is established through laboratory measurements. The CM currents on the physical model are measured using a variety of measurement techniques all proving to be accurate. Next, measured CM current for a direct current injection (DCI) method and plane wave illumination are compared. It is indicated that the DCI method does indeed influence the distribution of CM current on the outside of the pedestal. Despite this the DCI method is still more appropriate for evaluating the effectiveness of the installed hardening measures.

Comparing CM current levels for the hardened and non-hardened telescopes shows an increase in the level of measured current on the outside of the pedestal. The results also show that the requirements of the shielding measures inside the pedestal could become less stringent by establishing a direct current path at multiple positions around the outside circumference of the pedestal.

Finally, a method to determine the level of shielding provided by the top interface barrier installed in the KAT-7 telescope pedestal is discussed. This investigation differs from the traditional shielding effectiveness problems. The proposed technique measures the reduction in CM current either side of the interface at multiple positions to obtain an average value for the current. By comparing these two averages, the level of shielding can be calculated. A comparison of results shows a more conservative estimation for the interface shielding predicted by measuring the current than what the classic definition of shielding effectiveness predicts.

The following is a list of publications and presentations originating from the research which is presented in this dissertation:

P L Kibet, P S van der Merwe, T Ikin, H C Reader, “CAT-7 System Evaluation for Square Kilometre Array, “CAT-7 System Evaluation for Square Kilometre Array”, submitted to SAIEE Transactions May 2010.

T.S. Ikin, P.N. Wilkinson, A.J. Faulkner, M. Jones, A. Baird, A.K. Brown, D. George, G. Harris, P.L. Kibet, M. Panahi, H.C. Reader, S. Schediwy, P.S. van der Merwe, K. Zarb-Adami, and Y. Zhang, “Progress on Analogue Front end for 2PAD”, Widefield Science and Technology for the SKA SKADS Conference 2009, S.A. Torchinsky, A. van Ardenne, T. van den Brink-Havinga, A. van Es, A.J. Faulkner (eds.), Chateau de Limelette, Belgium, 4-6 Nov. 2009, pp. 267-272.

P G Wiid, H C Reader, R H Geschke, P S van der Merwe, P L Kibet, “Developing RFI Studies on KAT-7: Lightning, Earthing and Cabling” 2009 SA IEEE AP/MTT Conference, all invited papers, abstracts published only, Technopark, Stellenbosch, Mar 2009.

P S van der Merwe and H C Reader, “Cable Trays and Associated Connections”, SAUPEC 2009, Proc. 18th Southern African Univ. Power Eng. Conf, Protea Hotel, Stellenbosch, Jan 2009, paper 20, CD ROM. **Won best presentation award.**

P S van der Merwe and H C Reader, “Modelling and Measurements of Cable Trays for RFI Mitigation”, South African SKA / MeerKAT Project, 2nd Annual Postgraduate Bursary Conference, SA Astronomical Observatory, Cape Town, Nov 2007, presentations available on SKA website: www.ska.ac.za . **Won a best MSc presentation award.**

P S van der Merwe and H C Reader, “Interface and cabling characterisation for SKA”, South African SKA / MeerKAT Project, 3rd Annual Postgraduate Bursary Conference, Stellenbosch, Dec 2008, presentations available on SKA website: www.ska.ac.za . **Won best engineering PhD presentation award.**

P S van der Merwe and H C Reader, “Notes on EMC Investigation for EMBRACE”, extensive report prepared for ASTRON after Paul van der Merwe’s SA SKA Office and Marie Curie sponsored 5-week visit in November, 2009.

H C Reader, R H Geschke, P G Wiid, P L Kibet, A J Otto and P S van der Merwe, “EMC and RFI Mitigation for Developing Large Systems: Experience from South Africa’s SKA Demonstrator, address given to EM Divisions of NIST (National Institute of Standards and Technology), Boulder, Colorado, December, 2009.)

1.5. Layout of the Dissertation

An overview of the major concepts of the dissertation is given in Chapter 2. The first section focuses on cable trays and their ability to lower system transfer impedance. Cable tray connections, and the shielding ability of cable trays at higher frequencies, are important in this discussion. Two-port representation of cable trays is explained. The remainder of the chapter considers using physical and computational, unscaled and scaled models as part of EMC investigations. The concept of DCI, originally used in the aviation industry, is introduced. Finally, the definitions of electric, magnetic and electromagnetic shielding effectiveness are given.

Because computational analysis is used extensively throughout this dissertation, Chapter 3 is devoted to introducing the basic functionality of CST MWS. It also discusses how the computational domain is discretised and the associated meshing issues which need consideration.

Measurements are an integral part of the investigations that are presented. An example illustrates the iterative process involved when attempting to correlate measured and computed results.

Chapter 4 focuses on investigating various mid-span and end-connections used in cable tray installations. The different connections are analysed using two cable tray models with different methods of excitation. The change in transfer impedance for each model and each connection is considered. Additionally, CST MWS generates visual representations of the relevant fields and currents. These are used in a current and field argument to explain which connections are best.

The shielding ability of cable trays at frequencies where the wavelength is comparable to the width of the tray is considered in Chapter 5. Induced voltages on a victim conductor inside the tray, as well as the cable tray far field gain function are determined for varying angles of incidence. Measured results are validated using computational analysis over a frequency range of 300 MHz to 6 GHz

Chapter 6 reflects all the results from an on-site RF current audit conducted on two of the KAT-7 radio telescope in terms of CM current distributions. It consists of four main parts:

Part 1 – The process of obtaining an accurate physical and computational 1/20th scale model is discussed. Agreement of results measured using these models with actual measured data from an RF current audit is shown.

Part 2 – A comparison of the change in measured distribution on the outside of the pedestal for directly injected and induced CM currents are presented. This comparison is used to comment on the validity of each of the method of excitation that was used.

Part 3 – An evaluation of the change in the distribution of CM current on the outside of the pedestal measured for a hardened and non-hardened telescope. Under best conditions, the additional shielding measures should force more CM current to flow on the outside of the pedestal.

Part 4 – A different method to calculate the level of shielding provided by the top pedestal interface barrier is presented

The dissertation concludes in Chapter 7 which also provides recommendations for future work.

Chapter 2

Literature Survey and Background Material

The Square Kilometre Array (SKA) presents a new project. Many other smaller-scale projects exist which are precursors to the SKA. Electromagnetic (EM) modelling of radio telescope systems have most likely been undertaken, but the information is not readily available. This chapter focuses principally on the literature and background to cable trays. Reference is also made to reviewed material regarding additional concepts and methods used in the dissertation. In the case of shielding effectiveness (SE), the review which is presented here is by no means comprehensive. It merely introduces the subject.

2.1. Introduction: Cable Trays

As discussed by both Decker in [6] and Kalupa in [7], until recently metallic cable trays fulfilled only a structural purpose of supporting cables. In [6] and [7] distinction is made between a cable tray, which is a meshed or ladder structure, and conduit which is a solid structure usually sealed-off with a cover. For the remainder of this dissertation reference will be made only to cable trays which are solid structures without a cover.

With rapid development in both electric and electronic systems, cable connected schemes became increasingly vulnerable to, or became the source of, electromagnetic interference (EMI). Shielding the exposed cabling was an obvious thing to do, so the role of cable trays began to evolve. This major section of the chapter provides an overview which investigates the reason for their evolution. This evolution has taken them from a mechanism providing structural support for cables, to a method of reducing the transfer impedance of conductive systems.

2.2. Transfer Impedance of Conductive Systems

To determine how interference through transfer impedance causes disturbances in a conductive system, a simple model shown in Figure 2.1 is considered. As described by Van Deursen [8], in any installation a signal source (with source impedance Z_s) is connected to a load (with load

impedance Z_l larger than Z_s), and requires two leads or conductors. One conductor takes the signal to the load, and one brings it back. This setup which involves the source, load, and two conductors forms the differential mode (DM) circuit distributed over a distance l . There is an additional circuit which is connected to the outside world. This circuit consists of one or both conductors, the device represented by the DM circuit, and the nearby earth. It exists in common mode (CM) to the DM circuit.

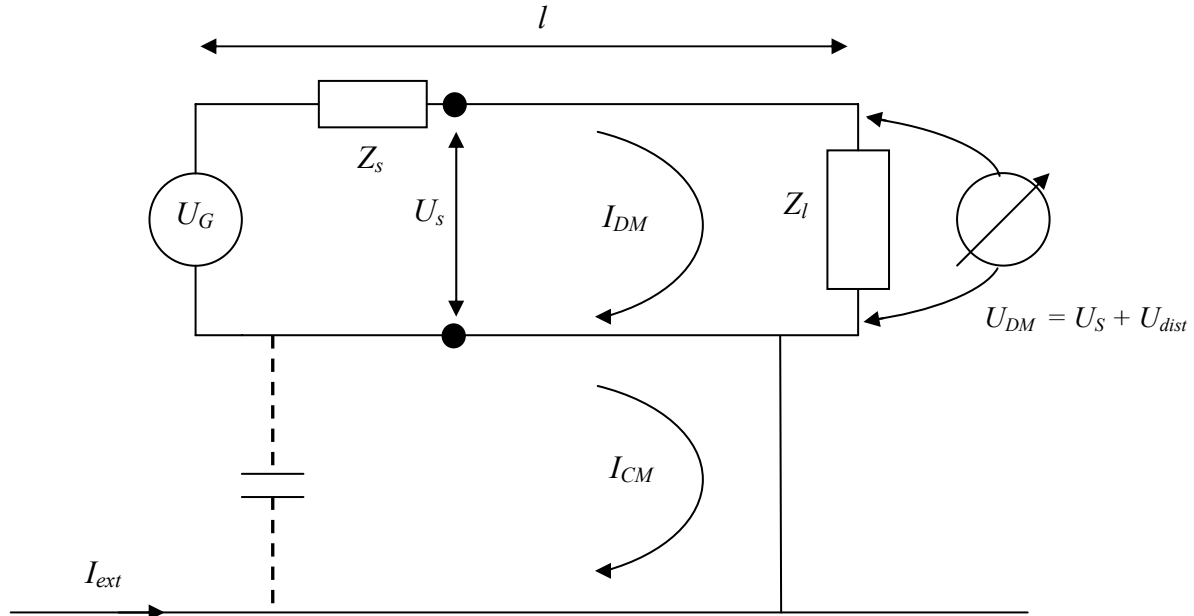


Figure 2.1: Two conductors connecting a signal source U_s with source impedance Z_s , to load impedance Z_l . The DM circuit is made up by the source, conductors, and load. The CM current path is made up of an earth return conductor at the load and a parasitic capacitance at the source (after [8]).

As indicated in [8] and mentioned by Van Helvoort [9], the CM circuit will always exist even without conductive continuity. It will be created through local galvanic and/or capacitive connections (parasitic or placed purposely) between the conductors, the load, and the earth as illustrated in Figure 2.1. When considering the measured voltage over the load impedance Z_l , it should be noted that U_{DM} , as defined in [8], will consist of a voltage induced by the DM current I_{DM} as well as a disturbance voltage U_{dist} . In U_{DM} , U_s is the wanted voltage generated by the DM circuit. U_{dist} is the disturbance voltage created due to the coupling with the CM circuit through the transfer impedance Z_l . The excitation of the CM circuit takes place through the CM current I_{CM} . Possible sources for I_{CM} which creates U_{dist} as stated in [8], firstly, include a resistive voltage drop due to the finite conductivity of the earthing system caused by I_{ext} . The second is the magnetic flux or B-field coupling through the earth loop also created by current I_{ext} . Currents due to direct lightning strikes or power faults are regular sources of I_{ext} .

Z_t should not be confused with the fixed Z_l indicated in Figure 2.1, as it consists of contributions from conductors and leads distributed throughout the entire system. It also represents terminal connections of all the cables connecting to the various loads in the system. For a low frequency approximation, the transfer impedance of the system shown in Figure 2.1 is described in [8] as follows:

$$\frac{U_{dist}}{I_{CM}} = Z_t = R + j\omega M \quad (1)$$

In (1), R is indicative of the resistive part of the system showing that a voltage drop is associated with the finite resistance of the copper conductors connecting the source to the load. The mutual inductance between the two leads, $|j\omega M|$, is mostly influenced by the size of the area created by the conductors of the DM loop. It represents the B-field coupling between the DM and CM loops. In the case of a coaxial cable this area is quite small. In other installations where the system uses separate conductors in its DM circuit, the area can be significantly larger. For frequencies where the wavelength becomes comparable or even shorter than the lengths of the conductors used in the system, the coupling through Z_t has to be integrated over the entire length l . Transfer impedance at the source and load are often dominated by the connectors and whether they have an effective earth reference.

The important highlights at this point are the identification of two circuits (DM and CM) in the conductive system shown in Figure 2.1. These two circuits interact with each other through the transfer impedance Z_t . DM circuits such as the one shown in Figure 2.1 are not designed with the additional CM circuit in mind. In most instances their susceptibility to coupling initiated by I_{CM} in the CM circuit will be high, and would require measures to reduce their associated Z_t . I_{CM} created by various sources and represented as I_{ext} will always be present. Possible sources of I_{ext} include currents due to direct lightning strikes and power faults. Measures to reduce U_{dist} include reducing either or both I_{CM} and Z_t .

2.3. Reducing Transfer Impedance of Conductive Systems

The objective from an electromagnetic compatibility (EMC) perspective is to lower the amount of induced disturbance voltage by decreasing the system Z_t . Assume that the system shown in Figure 2.1 is implemented using a coaxial cable with a braided outer conductor. The CM current that is induced on the outer conductor penetrates to the inside due to the openings and slits in the

braid as shown in Figure 2.2. The penetration of the flux to the inside of the outer conductor causes a net magnetic field on the inside of the coaxial cable. This causes the disturbance voltage which has been discussed. The contribution, however, of $|j\omega M|$ to Z_t in coaxial cables is orders of magnitude smaller than R of the same cable. More importantly M in coaxial cables is also orders of magnitude smaller than in systems using two separate conductors to connect to the load. The reason is because the area exposed to field coupling between the two conductors is much smaller in coaxial cables than in separate conductors. The main objective therefore is to find means to reduce Z_t in coaxial-based systems, which is dominated by the layout and types of connections used in the return path. One method of achieving this is to make use of an earthed parallel conductor (EPC) as proposed in [8].

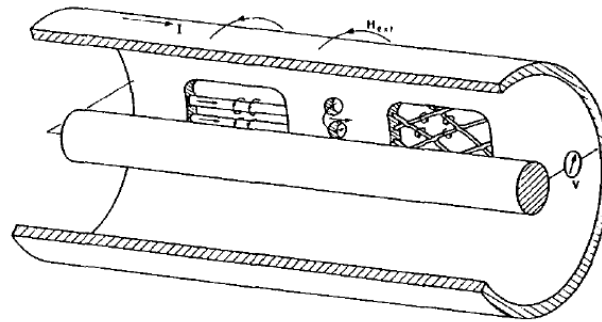


Figure 2.2: The magnetic field due to CM current on the wall of the coaxial system penetrates to the inside when the outer conductor is meshed as shown in [8].

2.3.1. Earthed Parallel Conductor (EPC)

The focus is to re-define what is used as an earthed return conductor in Figure 2.1 so that it has both a low resistive connection to ground, and shielding properties against B-fields. A physical barrier in the form of an EPC is required. EPCs come in a variety of shapes [8] shown in Figure 2.3, and depending on the type of application will have a strong influence on Z_t , especially at higher frequencies.

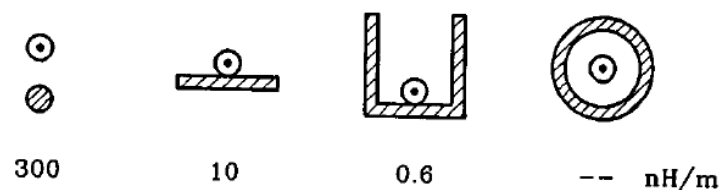


Figure 2.3: Different EPCs used alongside a normal coaxial cable. The values shown below each EPC is typical values of mutual inductance in nH/m at frequencies where the wavelength is similar to the length of the coaxial cable that is being protected [8].

The latter two shapes in particular provide a large cross-section over which an earth connection is made between the EPC and the structure against which it is terminated. The larger connection area decreases R in (1). The EPC also forms a physical barrier between the coaxial cable of the DM circuit and any external interference. The magnetic field associated with the CM current on the EPC firstly, interacts with a smaller loop area due to the close proximity of the EPC to the DM circuit cable. Secondly, in the case of the last two structures shown in Figure 2.3, the magnetic field finds it difficult to penetrate the structure. Both of these factors lead to a smaller contribution to Z_t by the mutual inductance coupling. Only the U-shaped EPC and its influence on the system Z_t is considered further and discussed in the following section.

2.3.2. Quasi-static Analysis of Simplified Geometry

The U-shaped EPC shown in Figure 2.3 is essentially a cable tray and will be referred to as such for the remainder of the dissertation. The figure indicates that for a coaxial system, the cable tray shares a common earth reference with the outer conductor of the coaxial cable. Pettus in [10] avoids this connection when analysing a conductor inside a metallic cable tray which was well earthed. Despite the cable outer not being connected to the cable tray, the tray helped to reduce the amount of CM current induced on the conductor by an external field. Pettus in [10] identifies that the level of shielding was dependent on the shape of the tray, and in particular its height/width ratio.

Analytical formulations describing the change in magnetic field at the top and bottom of the tray are provided in [10]. The magnetostatic analysis, which assumes that the tray is infinitely long, also assumes excitation signals where the wavelength is much longer than the width of the cable tray. Analysis of the propagation of time varying signals along the depth of the cable tray by making use of the conductor placed inside the tray is also presented. The analytical setup is shown in Figure 2.4. A plane wave excitation with magnetic field in the negative x -direction and electric field in the y -direction was considered first. Coupling only took place on the vertical sections of the conductor shown in Figure 2.4. This was mostly an academic exercise and so the excitation was changed to a magnetic field in the negative x -direction and electric field in the z -direction. The latter is referred to as an overhead excitation.

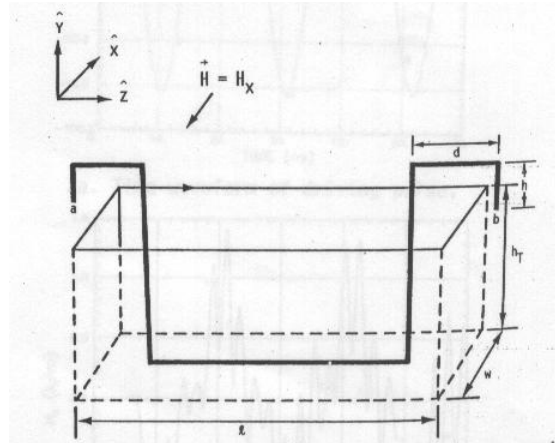


Figure 2.4: The geometry of incident fields, cables, and cable tray considered for coupling study presented in [10]

During the overhead excitation, four scenarios were considered. The magnetic field at the bottom of the tray, and the current induced on the conductor inside the tray, were calculated analytically and numerically. First, an empty tray was considered for which a reduction in the magnetic field from the top to the bottom of the tray was calculated. Next, to make the problem more realistic, the setup considered a conductor either entirely contained in the cable tray, or one which protruded from the tray at its ends as shown in Figure 2.4. Finally, an analysis was done when the conductor was earthed to the cable tray at one end.

Comparisons between analytical and numerical analysis show a reduction in the field at the bottom of the tray for all scenarios. The simulations show that when the conductor was allowed to leave the cable tray, it was exposed to stronger fields present at the top of the tray. This had a significant influence on the current calculated on the conductor. According to Pettus [10] this was a more practical setup because a fully immersed cable required complicated grounding and breaking of the cable at the end of the cable tray. Ultimately [10] concludes that uncovered trays are impractical and a better alternative, which is worth the effort, is a covered tray.

From the results in the literature the value of establishing a common earth connection between the coaxial outer conductor and the cable tray is seen. If the conductor and the tray are not connected, an undefined earth return path for the cable exists. Despite the cable tray being earthed, the induced current on the conductor is not diverted to the cable tray which provides a significantly lower impedance path to ground. Additionally, conductors cannot protrude from the side of a cable tray as shown in Figure 2.4. The cable tray provides no protection to the cable in that region. All the shielding provided by the central part of the tray would be made undone at the two ends.

2.3.3. Theoretical Analysis of Cable Tray Transfer Impedance

In section 2.2, transfer impedance and how it is established in a distributed system were discussed using a lumped circuit model. No evaluation of the cable tray's transfer impedance was provided in [10] of the previous section. There was no connection between the conductor inside the cable tray and the tray itself. The cable tray did not form a common conductor between the cable and the earth return. This approach was changed in subsequent investigations by Van Helvoort [9], Van Deursen et al. [11] and Ebertsohn [12]. Figure 2.5 below shows a sectioned-view of the cable tray with a victim conductor inside the tray, and an excitation conductor outside the tray as used in the literature.

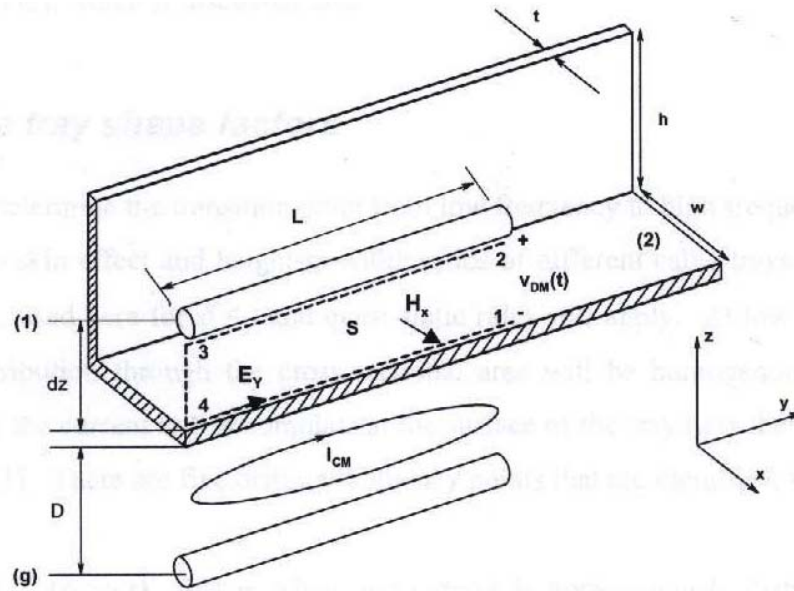


Figure 2.5: Schematic of the coupling mechanism between DM and CM voltage as used in [12]. This illustrates how the middle conductor in the distributed system is replaced with a non-magnetic cable tray.

I_{CM} circulates in a closed loop created between the outer conductor and the outside surface of the cable tray. It excites a magnetic field which circulates perpendicularly around the tray. The unwanted disturbance voltage V_{DM} , induced by the circulating magnetic field is measured between points 1 and 2. Similar as in section 2.2, the transfer impedance is again given by the ratio of the DM voltage and the CM current. It is described in [9], [11] and [12] for the scenario shown in Figure 2.5 and defined as a per unit length quantity as follows:

$$Z_t(x, z)/l = \frac{V_{DM}}{I_{CM}} = \frac{E_y}{I_{CM}} + \frac{j\omega\mu_0 \int_1^2 H_x(x, z) dz}{I_{CM}} \quad [\Omega/m] \quad (2)$$

The contributions to V_{DM} in (2), as described in the literature, consist firstly of the E_y component of the E-field present on the floor of the conduit between points 1 and 4. The victim conductor is terminated inside the cable tray and current is able to flow in a closed loop created by the conductor and tray combination. The finite conductivity of both the conductor and the tray is responsible for the potential difference between points 1 and 4. The second contribution is from the alternating H_x component around the tray intersecting a surface between 1, 2, 3 and 4.

The current induced by H_x is dependent on the size of the intersecting area created between the victim conductor and the inside surface of the cable tray. As a consequence Z_t , which is a per unit length quantity, is very dependent on the position of the conductor inside the tray. The investigations in [9] and [11] used the definition shown in (2) to evaluate the transfer impedance for not only cable trays, but different EPCs in general. The aim was to determine the crossover frequencies from where DC behaviour dominates Z_t , to where M starts to dominate. Method of Moments (MoM) and conformal transformations in a quasi-static two-dimensional approach were used to determine Z_t .

The focus in [12] was on evaluating the influence of a so-called shape factor. The shape factor described the change in transfer impedance due to a change in the height-to-width ratio of the cable tray as a function of frequency. The effect of moving the victim conductor to different positions inside the tray was also investigated. MoM analysis was used by Ebertsohn in [8] to confirm measured results and also show that transfer impedance is mainly a function of M at high frequencies. The results also indicated that transfer impedance is mainly a function of the height-to-width ratio and not of the material properties of the cable tray at similarly high frequencies. Cable trays with a height-to-width ratio $h/w > 1$ were shown to offer better shielding than shallower trays.

In all three investigations the analytical theory is only accurate for the central region of the cable tray, and end-effects of the tray are ignored. The results show that Z_t is dominated at low frequency by the DC resistance of the system. At higher frequencies, where quasi-static rules are still valid, Z_t becomes a function of M . The open U-shaped cable tray can be used to shield cables from environmental interference. This helps to lower the transfer impedance of a distributed system while still providing easy access to the cables inside the tray. The shielding is provided by the attenuating effect the U-shape has on an incident magnetic field. Equally, [11] shows that steel H and L-beams also provide some level of protection to conductors which are

fixed in the corners of these structures. If they are properly interconnected, they will provide a low impedance path to ground for the induced CM current.

2.4. Cable Tray Connections

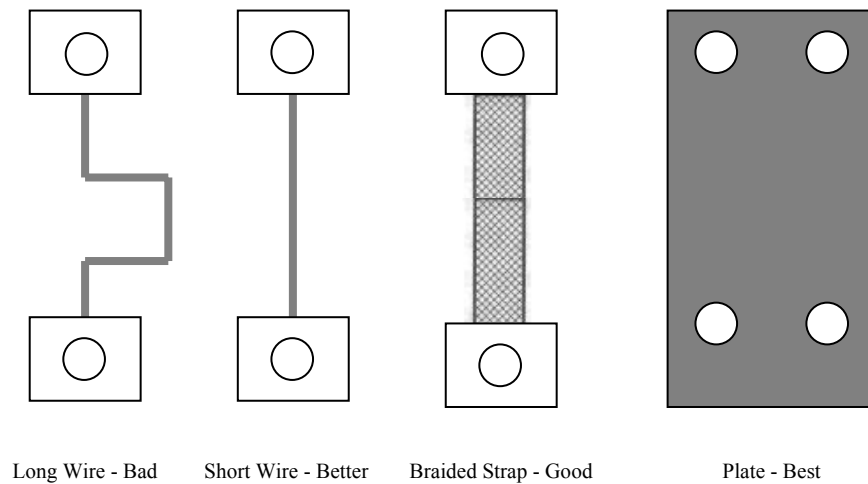
The analytical solution for cable tray transfer impedance discussed in section 2.3.3 does not account for terminations of the cable tray. It also assumed the shape of the tray remained uniform. This is very often not the case for actual implementations of cable trays. Cable tray sections of finite length not only have to be joined together, but they also have to be terminated in some fashion. The concept of transfer impedance associated with cable trays, as discussed up to this point, is again used to evaluate the performance of various connections.

2.4.1. Mid-span Connections

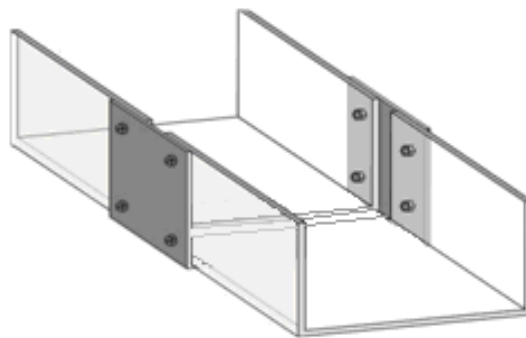
The use of various connections to join lengths of cable trays together are discussed in [9], described by Williams in [13], and recommended by standards on cable tray installation in [14]-[17]. In this dissertation all interconnections joining cable tray lengths together will be referred to as mid-span connections. In [9] it is noted that cable tray Z_t is treated as a distributed parameter, while the mid-span connections of the tray are treated as local parameters. The local Z_t was determined by measuring the overall Z_t without any mid-span connections. Then the connections were added and Z_t calculated again. The Z_t without the connection was subtracted from the new Z_t to obtain the influence of the connection. Combinations of wire connections, side plates, and a full U-shaped connection were considered by Van Helvoort in [9] between 10 Hz and 100 kHz. For the side plates considered in [9], different numbers of connecting bolts were considered. The results showed that the number of bolts only affected the lower and not the higher frequencies. As expected, the full U-shaped connection provided the lowest Z_t with the highest attributed to a single wire connection, made on only one side of the tray. The results show clearly how Z_t was dominated by the resistive component at frequencies between 10 Hz and 10 kHz, and then by the mutual inductance component from 10 kHz to 100 kHz. These results provide accurate information regarding which connection to use and why, but only for a very limited frequency range.

In [13] no transfer impedance results for cable tray connections are presented. The initial recommendations state that cable trays be joined by welding the seams or using U-shaped

connections. The associated connecting bolts should be spaced every 100 mm around the periphery of the tray. Seam-welding and full U-shaped connections require a lot of effort in a practical installation. The best compromise to a full U-connection according to [13] is a wide plate. A representation of this connection is shown in Figure 2.6 (a) with its implementation shown in Figure 2.6 (b). A short wide braided strap placed at multiple positions around the tray, is the only other recommended connection. Making use of shorter and wider connections compared to normal wires (shown in Figure 2.6 (a)) reduces the impedance of the connection and increases the frequencies at which the cable tray can be used. Cable tray mid-span connections, discussed by the literature, are recommended solely based on the impedance the particular connection has at frequencies higher than power frequencies (50/60 Hz).



(a)



(b)

Figure 2.6: (a) Some of the cable tray mid-span connections referred to in the literature and included in this investigation (after [13]). The implementation of side connections consisting of two wide plates is shown in (b).

The recommendations in [14]-[17] are similar to that given in [13]. It is only stated that a full U-connection is the best installation practice, with a wide bottom-only connection, a not-recommended alternative. Ensuring that the impedance of the mid-span connection is kept as low

as possible motivated the recommendations. Unlike [9], they do not provide detailed analysis of transfer impedance associated with each connection. In [16] the main objective of the connections is to ensure an adequate earth reference for power applications. Bonding jumpers which are advised, serve to provide an electrical connection only. For non-power applications it is stated that the cable tray should be properly bonded and earthed, with a recommended short braided connection similar to the one shown in Figure 2.6 (a).

2.4.2. End-connections

From the literature investigated, methods to terminate cable trays are only discussed by Williams in [13]. Recommendations for end-connections, similar as for mid-span connections, state that the connection should be frequency appropriate. This effectively means that a wide plate connection (Figure 2.6 (a)) should be used rather than a thin wire connection. A wider connection will provide a lower impedance path for both induced CM current, as well as fault currents when the tray is used as part of a safety earthing system.

Three examples of practical methods are described which terminate the cable tray at the side of an equipment cabinet. The first recommends that two or more straps between both sides of the tray will provide a better connection at higher frequencies than a single strap. Secondly, a bottom-only connection is considered as a suitable alternative. This connection is made using the bottom section of the cable tray which is bent down and terminated against the side of the enclosure with at least two connecting bolts. Thirdly, a U-bracket, which has been identified amongst the mid-span connections as providing the lowest transfer impedance, is mentioned as another alternative. The recommendations do not provide any technical details that specify which of the three connections will provide superior performance from an EMC point of view. They are only installation guidelines and rely on the reader's own judgement. It is here where the investigations of Chapter 4 aim to provide new information.

2.5. Cable Tray Protection for Increased Frequencies

The literature evaluated up to this point focused on determining the change in transfer impedance of cable trays. Transfer impedance, as explained in section 2.3.3, is an indication of the level of coupling between the CM current flowing on the outside of the tray, and the DM circuit on the inside. The DM circuit was represented by a victim conductor, which was terminated inside the

cable tray. This can be used to give a fairly accurate indication of how cable trays will perform in actual installations over a limited frequency range. In all the literature considered, frequencies are confined to wavelengths which are significantly longer than the length of the tray.

The investigation by Kapora [18] extended the frequency range to 5 GHz in certain instances and determined the protection a cable tray provides to enclosed conductors at these higher frequencies. A 1.5 m long cable tray with $h = 2w = 90$ mm was investigated. Four conductors were positioned inside the tray as shown in Figure 2.7. The induced voltage and current were evaluated on one of the four conductors at any-one time.

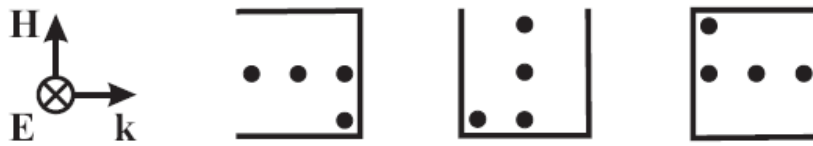


Figure 2.7: The position of the conductors inside the cable tray being illuminated by an incident plane wave is shown. The various orientations of the cable tray with respect to the incident wave are also indicated [Kapora et al. 19].

The investigation presented computed and measured results, with the computational analysis using both time and frequency domain (FD) simulations. The computational model was illuminated using a plane wave definition with a predominately horizontally polarised E-field. Results for a vertically polarised E-field are also discussed in [18]. The cable tray was analysed in three orientations with respect to the incident plane wave as shown in Figure 2.7.

In the computation, the voltage was evaluated on a particular conductor across a 50Ω termination impedance, with the remaining conductors terminated in 50Ω loads. The current flowing on the same conductor under test was monitored through a $1 \text{ m}\Omega$ lumped element situated in the centre of the cable tray. The results in [18] show the reduction in induced voltages and currents as the victim conductor is moved closer to the bottom corner of the tray. The shielding provided by the cable tray was determined by illuminating the four conductors again, but for the U-shaped cable tray removed from the model. An interesting consequence of having multiple conductors inside the tray is that each conductor has an influence on the voltage and currents that will be induced on adjacent conductors. The top conductor seems to ‘shield’ the rest of the conductors inside the tray. The comparison between results in [18] with and without the cable tray, showed a significant decrease in voltage and current level for all four conductors with the cable tray present.

Kapora in [18] conducted two sets of measurements, with one being done in a semi-anechoic chamber and the other in a fully anechoic chamber. The semi-anechoic chamber did not provide convincing results due to reflections from the conductive floor. The fully anechoic chamber performed better, with less interferences noticed. The model was illuminated using a log periodic dipole antenna (LPDA) for which the antenna factor was known. The voltage on each of the conductors was measured across the $50\ \Omega$ input impedance of the EMI receiver connected to the cable tray. The measured voltages had to be normalised to the $1\ \text{V/m}$ incident E-field of the computation to enable the comparison with computed results. The currents at the centre of the cable tray were measured using a CM current probe, which ultimately proved too invasive and did not provide accurate results.

A final investigation in [18] also considered adding a cover to the cable tray model. Results are compared for an open tray, one where the cover was fixed to the cable tray with bolts spaced 245 mm apart, and finally one where the cover was copper taped to the cable tray. The taped cover showed a significant reduction in the measured voltage. The bolted cover did show initial reduction of the interference, but only below 300 MHz. The cover generally in [18] also seemed to create some sort of resonant cavity at certain frequencies, ‘trapping’ the interference between the tray and the cover.

When the four conductors were placed inside the cable tray, significant reduction in levels of induced voltages and currents were measured and computed by Kapora in [18]. The bottom corners of the cable tray proved to provide the most protection from the surrounding B-fields. On the basis of the findings in [18], it is worth pursuing investigations into cable tray shielding for shorter wavelengths.

2.6. Cable Tray Measurements

Verifying the accuracy of analytically and numerically computed results is usually done with measurements similar to those conducted in [9], [11], [12] and [18]. In [9], [11] and [18] a separate source and receiver were used to excite and measure the response of the various models. In [9] and [11] current was directly injected onto the cable tray model. The induced voltage on the victim conductor inside the tray was measured with a separate lock-in receiver as shown in Figure 2.8. In order to obtain the level of CM current on the cable tray, a CM current probe was used to measure the current injected onto the tray.

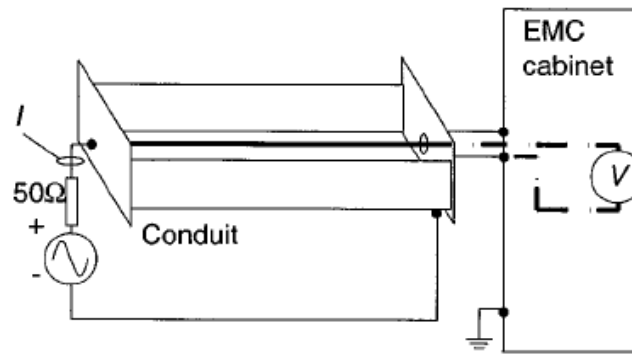


Figure 2.8: Current is injected onto the cable tray with the victim conductor inside the tray visible. The receiver inside an EMC cabinet is also shown [11].

In [12] a similar direct injection technique is used to inject CM current onto the cable tray. The model is shown in Figure 2.9.

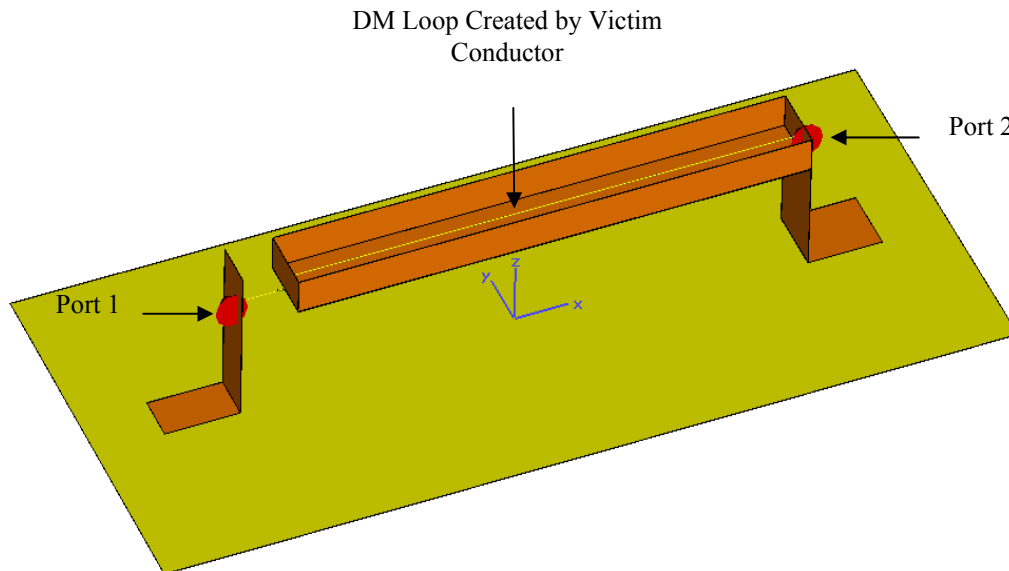


Figure 2.9: Computational representation of cable tray model used in [12] which indicates the direct injection of CM current onto the cable tray.

Van Helvoort in [9] discusses the fact that the setups shown in Figure 2.8 and Figure 2.9 are two port networks, and consequently can be described completely using scattering parameters. Scattering parameters, which are defined in the following section, can be measured by a vector network analyser (VNA) equipped with an S-parameter test set. The VNA injects current onto the cable tray at port one (Figure 2.9) and simultaneously measure the induced voltage on the victim conductor inside the tray at port two. Also described in the following section is how transfer impedance, used to describe the shielding ability of cable trays, can be calculated from S-parameters.

The model shown in Figure 2.9 is a computational representation used by Ebertsohn in [12] to study the change in transfer impedance for various height-to-width ratio cable trays. This model was originally developed in the MoM-based code FEKO [20]. In the model, injected current flows along the tray to the opposite end similar as in Figure 2.8, but return via a large metallic ground plane. This model is used again in Chapter 4 to study cable tray connections using Microwave Studio from Computer Simulation Technology (CST MWS) [21]. CST MWS, as will be explained in Chapter 3, implements the Finite Integration Technique (FIT). An additional model using the same B-field coupling principle is also introduced in Chapter 4.

2.7. Two-port Analysis of Cable Tray Model

The model in Figure 2.9 can be represented as a two-port network shown in Figure 2.10. S-parameters are chosen to describe the two-port network because the process of measuring these parameters is automated through the use of a VNA.

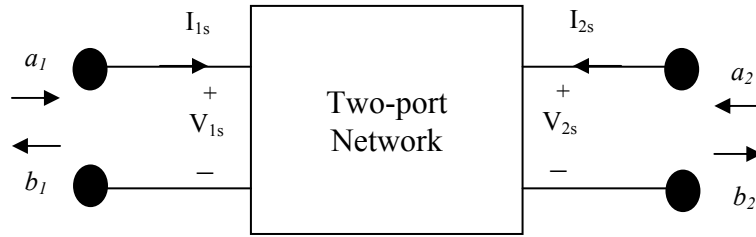


Figure 2.10: Incident and reflected parameters for two-port network (after [22]).

The incident, a , and reflected, b , parameters at each port for the above network, as described by Kaiser in [22], is given below:

$$a_1 = \frac{1}{2} \left(\frac{V_{1s}}{\sqrt{Z_0}} + \sqrt{Z_0} I_{1s} \right) \quad b_1 = \frac{1}{2} \left(\frac{V_{1s}}{\sqrt{Z_0}} - \sqrt{Z_0} I_{1s} \right) \quad (3)$$

$$a_2 = \frac{1}{2} \left(\frac{V_{2s}}{\sqrt{Z_0}} + \sqrt{Z_0} I_{2s} \right) \quad b_2 = \frac{1}{2} \left(\frac{V_{2s}}{\sqrt{Z_0}} - \sqrt{Z_0} I_{2s} \right) \quad (4)$$

In the above set of equations, Z_0 is the characteristic impedance of the circuit which connects to the above network at both ports. In this case that would be the approximate $50 \, \Omega$ characteristic impedance of the two-port VNA. By dividing the transmitted and reflected parameters by $\sqrt{Z_0}$, both a^2 and b^2 will have units of power. The corresponding S-parameters are defined in (5), (6),

(7) and (8). They can each be re-written, as discussed by Kurokawa in [23], as a power coefficient when the magnitude of the relevant parameter is squared, i.e. $|S|^2$. S-parameters are used throughout this dissertation in both their voltage and power ratio format.

$$b_1 = S_{11}a_1 + S_{12}a_2 \quad (5)$$

$$b_2 = S_{21}a_1 + S_{22}a_2 \quad (6)$$

$$S_{11} = \left. \frac{b_1}{a_1} \right|_{a_2=0} \quad S_{22} = \left. \frac{b_2}{a_2} \right|_{a_1=0} \quad (7)$$

$$S_{21} = \left. \frac{b_2}{a_1} \right|_{a_2=0} \quad S_{12} = \left. \frac{b_1}{a_2} \right|_{a_1=0} \quad (8)$$

The conventional S-parameters are obtained by setting the a_1 or a_2 equal to zero. Described in (7) is the reflection coefficient at port one, with port two terminated in Z_0 . Also shown in (7) is the reflection coefficient at port two, with port one terminated in Z_0 . In (8) the transmission coefficients from port one to port two, and from port two to port one are given.

With S-parameters defined, they can now be used to calculate the Z_t of the cable tray. The CM current induced at port one of the model is related to the DM voltage measured at port two. Transfer impedance is defined for the two port network in Figure 2.10 as follows [12]:

$$Z_t = \left. \frac{V_{DM}}{I_{CM}} \right|_{I_2=0} = \left. \frac{V_{2S}}{I_{1S}} \right|_{I_2=0} = Z_{21} / l \text{ [}\Omega/\text{m]} \quad (9)$$

The measured S-parameters from the VNA can then be converted to Z_{21} shown in (9) with ease, which enable comparison of measured and computed cable tray Z_t results.

2.8. Physical and Computational Scale Modelling

In the literature on cable tray shielding presented in the previous sections of this chapter, both measured and computed results were considered. The measured results were obtained from experiments conducted on unscaled physical models. The computed results were initially calculated using analytical techniques, but subsequently computed using a variety of well-known numerical implementations.

The motivation for using physical models (unscaled or scaled) to represent actual structures, has to do with measurement practicality, cost, ease of modification, and influence of the measurement environment. By measuring a model in a controlled environment, unwanted external influences in the results can be minimised. For investigations where the actual structure being analysed is large, measurements on the associated physical scale model are conducted with greater ease and accuracy. Modifications required for the investigation of various scenarios can be made much more efficiently on a physical model, saving time and costs.

The same motivations for using physical models are valid for using computational models (unscaled or scaled) to approximate actual structures or implementations. Additionally their results are used to verify the accuracy of measured data, and enable visualisations of generated E and H-fields. A distinction which exists, but is often not made, has to do with the type of computational analysis which is done. The interaction between a model and an applied field is described by an EM model only, as stated by Ruddle [24]. An EM model is used to comment on a device's susceptibility to radiated interference. In order to obtain an EMC solution, the model's susceptibility as well as conducted and radiated emissions of the electronic sub-systems inside the model, have to be determined.

As part of this dissertation, focus will only be on system susceptibility through the analysis of EM models. Furthermore, reference to computational analysis implies the use of only numerical techniques. The following two sections introduce, through the evaluation of available literature, the use of both physical and computational models for the purpose of susceptibility investigations.

2.8.1. Physical Modelling

Zhang et al. [25] consider the use of brass scale models of navy vessels in order to determine shipboard antenna design and placement, radar cross section, and transient electromagnetic events such as lightning and high power electromagnetic pulses (EMP). Inter-coupling between structures on the ship (communication antenna and mast) as well as coupling to cables within the cabin, are all investigated using time domain (TD) analysis. EMI to metre-wave-radar systems, while not providing actual measured results, is stated by [25] to be predicted successfully using scale model analysis.

Another example of the use of scale model analysis is described by Reader et al. [26]. In the investigation specific induced current paths on an experimental demonstrator Karoo Array Telescope (KAT) were investigated. The purpose of the investigation, as described in [26], was to determine where most of the induced current from indirect or direct lightning strikes, or radiated fields arising from operational equipment and cellular phones, would be localised on the telescope structure. The FD investigation was done between 2 GHz and 6 GHz and compared to measured results conducted in an available anechoic chamber. A direct lightning strike was simulated by injecting current onto both a physical and computational scale model, in a process similar to what will be described later in the chapter. The final outcome of the investigations described in [26] is included in the findings presented by Wiid [5].

2.8.2. Computational Modelling

Christopoulos in [27] introduces several generic numerical techniques which are well-known and used for general EM simulation. These include, Finite Difference Time Domain (FDTD), Finite Element Method (FEM), Methods of Moments (MoM) and Transmission-Line Modelling (TLM). Despite the variety of numerical codes available, computational analysis of EMC problems still present unique challenges to each as described in [27] and [28]. The first of these challenges is that efficient modelling is required over a wide frequency range due to the nature of EMC investigations. The second is that real-world complex systems, which cannot easily be simplified, are usually investigated.

When focussing on the modelling aspect, a particularly difficult modelling task encountered in many EM simulations, is the co-existence of electrically large and electrically small features [28]. An example, given in both [27] and [28], is a thin conductor placed inside a much larger cabinet as shown in Figure 2.11. While the cabinet size is equal to the wavelength, the thin conductor is not. Christopoulos [27] describes this as a multi-scale problem which presents severe difficulties to the automatic modeller which most numerical software packages incorporate. If a Cartesian mesh, shown in Figure 2.11, is considered, the default $\lambda/10$ mesh step is adequate for the dimensions of the cabinet. A resolution closer to $\lambda/50$ is required for the conductor inside the cabinet.

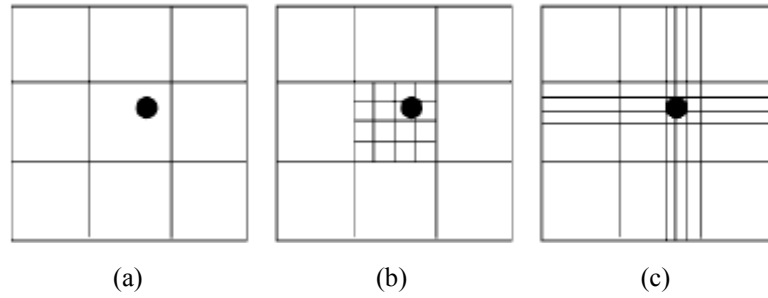


Figure 2.11: Schematic of various mesh arrangement which highlight the need for different mesh densities when analysing real-world EMC problems [27].

This example is used to highlight the need for a multi-grid mesh when Cartesian meshing is used. A number of implementations that realise this are discussed in [27]. However, it is also pointed out that there are certain disadvantages and difficulties associated with implementing multi-grid meshes shown in Figure 2.11. The fundamental difficulty is that the inherent simplicity of the Cartesian mesh is lost. Each finer mesh element has to be laboriously mapped into the surrounding mesh. This leads to more profound problems at the interfaces between the fine and coarse mesh regions. Information at these interfaces becomes available at different temporal and spatial rates [27]. Some form of averaging or filtering at the interface is therefore required. The specific implementation to achieve this multi-grid mesh is unique to each numerical method. The method used in CST MWS will be discussed in Chapter 6. Christopoulos [27] continues by describing some examples which have already been successfully implemented, but this is beyond the scope of this dissertation.

The added complexity of implementing multi-grid meshing can be overcome to some extent, if unstructured or triangular meshing is used. This type of meshing allows more freedom in the mesh allocation [28]. An example of this is shown in Figure 2.12 where the edge of a curved object is approximated by the Cartesian meshing in (a) and with the triangular meshing in (b).

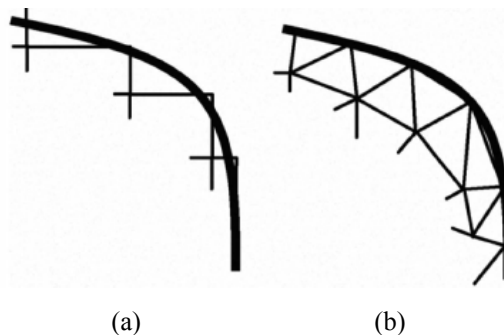


Figure 2.12: Approximation of curved boundary using (a) the Cartesian mesh and (b) triangular meshing [28].

With the Cartesian mesh, the number of neighbours to the computational cell remains constant throughout the mesh. This adds speed and efficiency, but restricts the resolution and therefore the accuracy of what can be achieved with this mesh. This is not the case with the triangular meshing. Here the number of neighbours to the computational cell is changed to suit the requirements placed on the modeller. The better resolution, however, comes at an increased computational cost. Triangular meshing is also mostly implemented in FD analysis, with TD implementations not having found any favour yet [27].

Some of the computational issues associated with EM investigations have been identified. Similar issues were encountered in the computational analysis which was done for this dissertation, and as a consequence they will be discussed further in the relevant chapters where they occur. The limited literature describing the use of physical scale models to study EMI and coupling mechanisms, was also reviewed. The next section compares different methods of excitation which will be used to establish CM currents on the KAT-7 telescope scale model analysed in Chapter 6.

2.9. Direct Current Injection and Plane Wave Illumination

The method of direct current injection (DCI) was derived from test procedures which evaluated indirect effects of lightning on aircraft. This has since been used for high level EMC testing on entire aircraft systems, as discussed by Bingwei and Xanxing [29], and in particular high-intensity radiated field (HIRF) certification evaluations (McQuilton et al. [30] and Rasek and Loos [31]). DCI is also starting to be used for general EMC compliance testing on systems not related to the aviation industry (Rautio and Uusimäki [32]). In [30]-[33] the DCI method is compared to a plane wave illumination method also referred to as free-field illumination. Plane wave illumination typically uses a wideband antenna, driven by a known power source, and positioned in the antenna far field to illuminate the particular device under test (DUT). The incident field couples to the DUT and induces CM current on the structure. Another method includes positioning the DUT in close proximity to the exposed centre conductor of a coaxial line, while the DUT is electrically floating [30].

The plane wave illumination method is traditionally more common, with the results used to confirm the accuracy of the DCI method. DCI is gaining favour over plane wave illumination for a number of reasons. The first, as explained in [30], is that much lower power levels are required

to establish the same surface current density with frequency as obtained by illumination methods. The second, described in [31], is that DCI is the only option available which allows complete system evaluation in the kilohertz range. This is confirmed by Rothenhäusler et al. [33] who state that the DCI method provides a more affordable means of system susceptibility analysis at low frequencies (low kHz up to 300 MHz). DCI does not require the use of large antennas or open area test sites (OATS). Two types of DCI measurement setups are generally used for HIRF testing. They are presented in the following two sections in order to explain the method of excitation.

2.9.1. Coaxial Return Conductor

An HIRF test rig implementing a coaxial return conductor (red) with the DUT (blue) acting as the centre conductor of the system [33] is indicated in Figure 2.13.

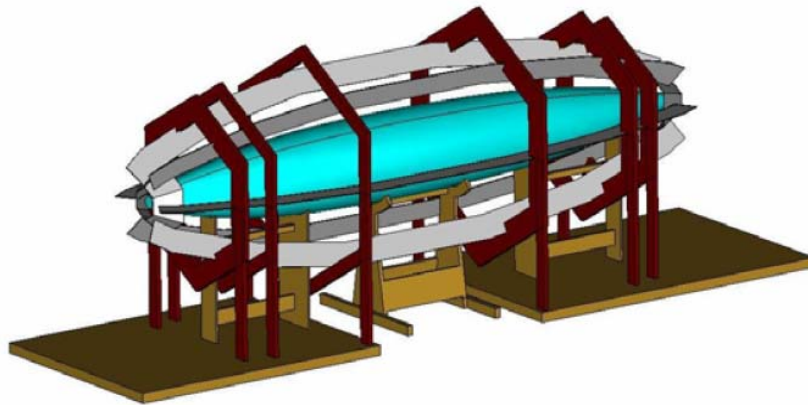


Figure 2.13: Schematic of the measurement setup used for HIRF testing. In this case the broadband coaxial return conductor setup is shown [33].

The purpose of the coaxial return conductor implementation, as explained in [29], is that the DUT is the centre conductor in the setup. The DUT is then completely enclosed by a conductor ring, effectively forming a transmission line. After the point of injection on the DUT has been chosen, the design of the return conductor should ensure constant characteristic impedance along the length of the DUT. A transverse electromagnetic (TEM) wave is then established in the space between the centre conductor (the DUT) and the outer conductor, by exciting the system at one end and terminating it at the other end. The termination ensures that as much energy as possible is transmitted through the system. In [29] it is stated that the coaxial return conductor setup, ensures minimum perturbation of the surface current on the DUT, compared with plane wave illumination.

2.9.2. Ground Plane Return Conductor

The ground plane return conductor test setup, shown in Figure 2.14, evaluates the same DUT as shown in Figure 2.13.

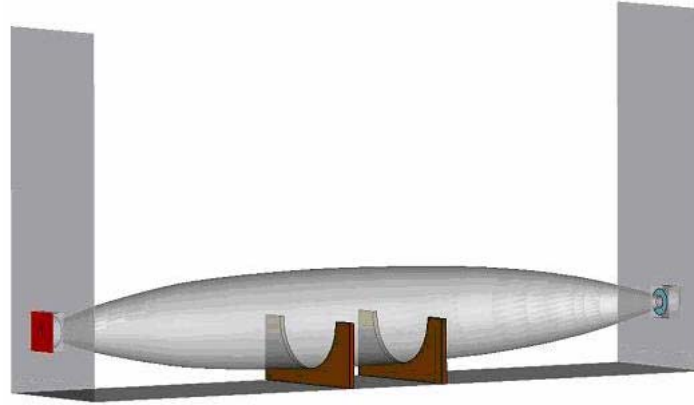


Figure 2.14: Schematic of a measurement setup implementing a broadband ground plane return conductor [33].

As stated in [29], this method defines a return path for the current injected onto the DUT through a ground plane or earth mat. The asymmetrical return path can be seen Figure 2.14. The injected current, after flowing over the DUT, is absorbed by a termination load which is equal to the input impedance of the DUT. This termination load ensures that as much of the energy is transmitted across the object as is possible. The cable tray model discussed in section 2.6 and shown in Figure 2.9, is an implementation of this form of DCI, with the ground plane providing the return conductor for the injected current.

2.9.3. Comparison: DCI Test Setups

The benefits of the coaxial return conductor method, as stated in [29] are, firstly, better correlation to the plane wave illumination method in terms of surface current distributions. Secondly, less excitation power is required due to more efficient transfer of energy onto the DUT. A limitation of this implementation, also discussed by [29], is the fact that the enclosing return conductor limits the use of the aircraft engines. From [33] it becomes clear that the design of the return conductor for the coaxial setup is not a trivial matter. This is mainly due to the fact that its characteristic impedance has to remain constant for the length of the DUT.

While the ground plane return conductor might be slightly simpler to implement than the coaxial return conductor, it causes problems with regard to broadband design [33]. The open architecture

of the ground plane return conductor, seen in Figure 2.14, means that significant amounts of energy is radiated into the immediate measurement environment. This could cause reflections from the environment to couple back to the DUT and influence the measured results [33]. A less uniform surface current distribution on the DUT is obtained due to the position of the large ground plane return conductor.

2.9.4. Comparison: DCI with Plane Wave Illumination

When implementing a coaxial return conductor, the findings in [30] suggest that similar surface current levels for both the plane wave illumination method and the DCI method were achieved. However, the DCI method required an order of magnitude less excitation power compared to the plane wave illumination method. The findings in both [30] and [31] are that the surface current distribution was similar in uniformity for the DCI and plane wave illumination methods. This is not surprising considering the symmetrical environment of the coaxial return conductor.

As stated in [31], when using a ground plane return conductor, a noticeable variation in the distribution around the entire circumference of the DUT was seen. The distribution was determined by the DCI setup and installation of the return conductor system. The distribution of surface current in [29]–[33] is important, and could therefore warrant the effort of designing a coaxial return conductor. For different applications such as the cable tray model and the pre-compliance testing described in [32], non-uniformity is not critical. For these scenarios the simpler DCI method using the ground plane return conductor is a suitable alternative.

2.10. Shielding Effectiveness of Enclosures

In this section the concept of electric, magnetic and electromagnetic shielding effectiveness is introduced. These two definitions, which are discussed in the presented literature, are merely used in comparative calculations in Chapter 6. There the level of shielding provided by an interface barrier installed inside the lower pedestal of a hardened KAT-7 telescope is evaluated. The results produced using these definitions are compared to levels of shielding which are calculated by evaluating the reduction in CM current on a conductor entering the lower pedestal.

2.10.1. Electric and Magnetic Shielding Effectiveness

According to Klinkenbusch [34], shielding is a fundamental step in improving the EMC of an active and/or passive device. The main factor which affects shielding effectiveness is frequency. It does so by influencing the physical principles which determine shielding [34]. These principles are fairly well understood for static and low frequency radiated E-fields. A metallic meshed enclosure with certain size apertures is considered. The electric charges at low frequency on the edges of the apertures will serve as end points for the lines of force for the divergence-type E-field [34]. Equally, the eddy currents induced in the enclosure material by the magnetic field component of the radiated interference are responsible for the magnetic shielding effect. For high frequency transient electromagnetic fields, the interaction between the fields and the meshed enclosure is much more complex. At shorter wavelengths, some of the electromagnetic radiation will start to penetrate into the enclosure.

The shielding mechanism for a particular enclosure with particular size apertures is continuously changing with frequency. This meant that a different means of determining the enclosure's shielding effectiveness was required. The definitions for both electric and magnetic shielding effectiveness for radiated interference as defined by [34]-[40] are given below.

$$SE_e|_q = 20 \log_{10} \frac{|\vec{E}^{unshield}|_q}{|\vec{E}^{shield}|_q} \text{ dB} \quad (10)$$

$$SE_m|_q = 20 \log_{10} \frac{|\vec{H}^{unshield}|_q}{|\vec{H}^{shield}|_q} \text{ dB} \quad (11)$$

The two definitions state that the radiated E and H-fields are measured at a particular point q inside the enclosure with and without the shield present. One problem, as stated by [34], is that the definitions in (10) and (11), for frequencies where the wavelength is less than the size of the enclosure, are dependent on the location of q . It is debatable where q should be placed in order to obtain a 'typical' value representative of the shielding effectiveness for the total interior region.

Khan et al. [35] presents a modal equivalent implementation of the popular MoM numerical code. The purpose of the code is to accommodate the modal behaviour of both the aperture and enclosure cavity. In [35] the shielding effectiveness was determined at the geometric centre of

the cavity and the results displayed with frequency. The resonant influences of the fields inside the cavity were identified. As a consequence it is stated in [35] that sampling at one particular position could lead to serious errors in the calculated shielding effectiveness. If the sampled position is located at the centre of a null in the field distribution for the frequency investigated, incorrect values will be obtained for the shielding effectiveness.

Nenghong et al. [36] state that despite the characteristic resonant behaviour of the enclosure, the shielding effectiveness can be calculated at the centre point of the enclosure, because this will also be the centre of the resonance enclosure. This, however, is only true for small enclosures. This means that the E-field strength at the geometric centre of the enclosure will always be high. As a result, a good indication of the best shielding a particular enclosure can provide will be obtained. Golestani-Rad and Rashed-Mohassel [37] and Robinson et al. [38] focuses on modelling the influence of the various apertures. This is necessary in order to determine how the radiation into the cavity influences the cavity resonance. In [37], an FDTD implementation was used to analyse the enclosure and aperture, and in [38] the slot impedance was calculated using the TLM method. Robinson et al. [38] also illustrate a method with which the E and H-fields inside the cavity were measured. By using a monopole and loop sensor in various positions inside the enclosure, the change in measured E and H-fields with and without the enclosure was obtained. Agreement between measured and computed results was found, but it was still necessary to sample both the E and H-fields at multiple positions inside the cavity.

2.10.2. Electromagnetic Shielding Effectiveness

Klinkenbusch in [34] derives electromagnetic shielding effectiveness, which represents the shield-induced reduction of radiated electromagnetic energy as shown below. The reason for the new definition is because the definitions given by (10) and (11) are intended for low frequency analysis [34].

$$SE_{em}|_q = 10 \log_{10} \frac{2}{\frac{|\vec{E}^{shield}|_q^2}{|\vec{E}^{unshield}|_q^2} + \frac{|\vec{H}^{shield}|_q^2}{|\vec{H}^{unshield}|_q^2}} \text{ dB} \quad (12)$$

For frequencies where the wavelength is approaching the size of the aperture, the definition in (12) has to be used. The electromagnetic shielding effectiveness is calculated as a combination of

electric and magnetic shielding effectiveness. It represents the shield-induced reduction in electromagnetic power which is delivered to an infinitesimal load located at position q [34]. The new definition, despite evaluating both the E and H-fields, still require sampling at multiple positions inside the enclosure. In his analysis using (12) Klinkenbusch [34], evaluates the fields in the centre of the enclosure.

From the discussions in the previous two sections, as well as the statement by Khan et al. [35], it becomes evident that determining the shielding effectiveness of a specific enclosure is a very challenging task. It is dependent on numerous parameters as expressed in [35]. For this reason, the purpose of the presented material is simply to introduce the concept of electric, magnetic and electromagnetic shielding effectiveness. This should therefore not be considered a complete evaluation of the subject matter. Both electric and electromagnetic shielding effectiveness, as defined by (10) and (12), are used in the investigation in Chapter 6.

2.11. Conclusion

This chapter introduced the major concepts relevant to the various studies presented in each of the following chapters in this dissertation. The concept of transfer impedance (Z_t) and how it is part of every DM conductive system distributed or otherwise, was highlighted. Z_t causes interference in a system, but it can be significantly reduced when using an EPC. EPC can be implemented in different forms but a more obvious one which was considered is cable trays. The influence cable trays have on system Z_t was discussed. This lead to the evaluation of the types of cable tray connections which have to be used to ensure that the low Z_t the tray establishes is retained when the tray is terminated or joined to each other.

The shielding ability of cable trays when illuminated with high frequency interference was considered next. This is an important consideration, because cable trays will not only be exposed to low frequency interference. Validating the parameters determined through computational analysis with results calculated using and physical model and measured data, confirms the accuracy of the computation. The representation of the cable tray physical model as a two-port network, which can be described completely using scattering parameters, was also explained.

Physical and computational unscaled and scaled models will be used extensively throughout this dissertation. The way in which they are used in other disciplines as well as computational issues

unique to EMC investigations were introduced. In the following chapters further discussions will be presented when similar computational issues are encountered. Two methods of DCI which are used extensively as means to excite our physical models were reviewed. More focus is placed on this, particularly by comparing it to using a plane wave illumination technique, in Chapter 6. Finally the concept of shielding effectiveness which is used to determine the shielding provided by an interface or enclosure was considered.

Chapter 3

Computation and Metrological Issues

3.1. Introduction

Introduced in this chapter is the functioning of Computer Simulation Technology's Microwave Studio (CST MWS) on a slightly more fundamental level. The technique that the software uses to discretise the computational volume into smaller subsections is discussed. The all important trade-off between simulation time and model complexity becomes a factor when a real-world scenario has to be accurately represented. With a more detailed understanding of CST MWS, methods used to simplify models and approximate actual implementations, while still achieving accurate results, are proposed. These methods are explained using examples from models investigated as part of this dissertation.

Validation of computed results with measured data is an important part of computational analysis. However, to obtain agreement between them introduces new challenges. The process to find agreement is more often than not an iterative one, which requires both the computation and measurement to be refined. Environmental influences and differences in the methods of excitation are only two examples of issues that need careful consideration when attempting to verify results. Possible errors when defining discrete ports in CST MWS are also considered.

In the final part of the chapter the process through which measured results and computational analysis were used to develop a new cable tray model is presented. The new model is a refinement of the model introduced in Chapter 2 which formed the basis of Ebersohn's study in [12]. It is used in Chapter 4 in an analysis of cable tray connections.

3.2. Defining a Computational Model

3.2.1. The Computational Environment

Focussing on a principal computational electromagnetic (CEM) code ensured increasingly detailed knowledge of refinements necessary for good agreement between measured and computed results. As mentioned in Chapter 2 section 2.6, CST MWS uses the Finite Integration Technique (FIT) which is based on the Finite Difference Time Domain (FDTD) method. Unlike most other numerical methods, FIT discretises the integral rather than the differential form of Maxwell's equations, which are given in [21] and shown below.

$$\oint_{\partial A} \vec{E} \cdot d\vec{s} = - \int_A \frac{\partial \vec{B}}{\partial t} \cdot d\vec{A} \quad \oint_{\partial A} \vec{H} \cdot d\vec{s} = \int_A \left(\frac{\partial \vec{D}}{\partial t} + \vec{J} \right) \cdot d\vec{A} \quad (13)$$

$$\oint_{\partial V} \vec{D} \cdot d\vec{A} = \int_V \rho dV \quad \oint_{\partial V} \vec{B} \cdot d\vec{A} = 0 \quad (14)$$

Methods of Moments (MoM) which is another popular numerical technique, replaces a radiating/scattering structure with surface currents. Volumetric currents can be calculated, but as explained by Davidson [41] it is computationally very expensive. The surface currents are then discretised into smaller sections creating a surface mesh. A matrix equation is set up which computes the influence of a particular mesh element on every other mesh element through the use of the Greens function. Particular boundary conditions are applied to each interaction which results in a set of linear equations as part of an iterative solution scheme. This, however, is not always the case with many direct MoM solvers existing. The solution to these linear equations provides an approximate current on each mesh element on the structure. MoM as mentioned in [41] operates traditionally in the frequency domain (FD), with time domain (TD) integral equation formulations showing problems with stability. It is the ideal technique for analysing perfectly or highly conducting surfaces, as only the surface and not the volume surrounding the surface, is meshed. The focus, however, in this chapter will not be on a MoM implementation.

Compared to MoM, FIT divides the calculation domain into three dimensional cubes commonly referred to as grid or mesh cells. Considering only an orthogonal hexahedral grid system, the E-field is calculated around the boundaries of each cell located in a primary mesh. This mesh, indicated in Figure 3.1, is viewable by the user. Similarly, the H-field is calculated around the boundaries of a dual mesh, also shown in Figure 3.1. This dual mesh is not visible to the user.

The spatial discretisation of Maxwell's equations is performed on these two orthogonal grid systems. The degrees of freedom are introduced as integral values.

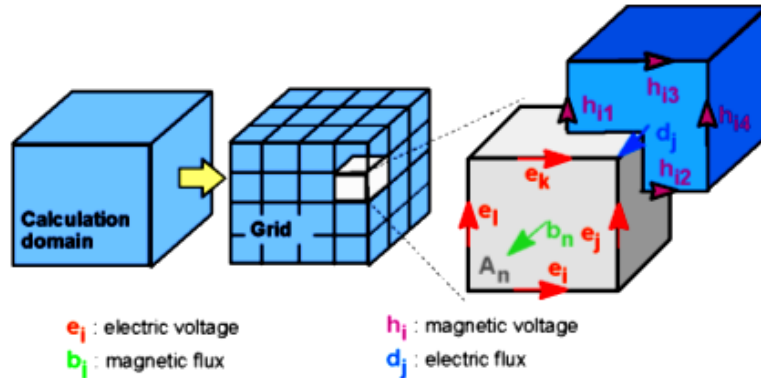


Figure 3.1: Discretisation of the computational domain as illustrated in [21] is shown. The dual meshing required for the calculation of E and H-fields are also shown.

With reference to Figure 3.1, the electric grid voltages \mathbf{e} and magnetic facet fluxes \mathbf{b} are located on the primary mesh. The dielectric fluxes \mathbf{d} as well as the magnetic grid voltages \mathbf{h} are defined on the dual grid. This calculation process is repeated for each cell facet, obtaining a three-dimensional solution. To ensure accurate representation of the computed grid voltages, it is important to align a cell facet or mesh edge with each physical edge or connection within the model. An example of this is shown in Figure 3.2 (a) and (b). The two-dimensional mesh view shows an inaccurate alignment in Figure 3.2 (a), with a more accurate alignment shown in Figure 3.2 (b). The mesh density that is shown is generated automatically by the meshing algorithm. It can be altered by the user when changing the mesh line ratio limit as shown in Figure 3.2. The mesh line ratio limit is an absolute ratio between the largest and smallest distance between mesh lines. Increasing this ratio enables the meshing algorithm to include smaller mesh steps compared to longer ones.

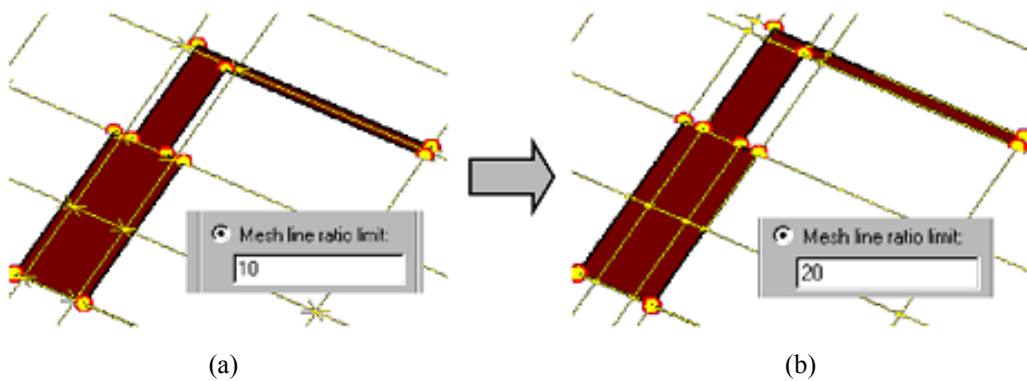


Figure 3.2: As illustrated in [21], the incorrect alignment of mesh cell edges is shown in (a), with the correct alignment shown in (b). The mesh line ratio limit is directly responsible for this enhanced meshing.

CST MWS uses a powerful solid-modelling front-end which is based on the ACIS modelling kernel [21]. This makes it possible for the user to add very small details and exceptional accuracy to the model. The solver will attempt to resolve all the added detail through the process described above. This, in turn, will lead to a very long simulation time because the size of the mesh step will be reduced. With a reduced mesh step size, the width of the time step used in the time-domain-based transient solver is also reduced. This means that it will take longer to simulate a period of electromagnetic fields. Finding a trade-off between model accuracy in terms of detail and simulation run time, directly influences the accuracy of the results. Certain details might not make a difference to the model's overall operation and can be ignored. The user has to interpret the problem and determine the level of simplification.

3.2.2. Simplification of Objects Defined in CST MWS

Having correct alignment between mesh and model edges as previously stated, is a pre-requisite for obtaining correct results. When using hexahedral meshing in CST MWS, straight edges can be discretised exactly but round edges can only be approximated as shown in Figure 3.3 (a). This approximation is again influenced by the mesh line ratio limit which was discussed previously. By increasing the ratio limit a round object can be meshed with increasing accuracy, but it will simultaneously increase the simulation time. Round objects cannot be excluded from a simulation but they can be simplified, which reduces their dependency on a very accurate mesh. A simple example of this is a Sub-Miniature version A (SMA) connector shown in Figure 3.3 (b) and (c).

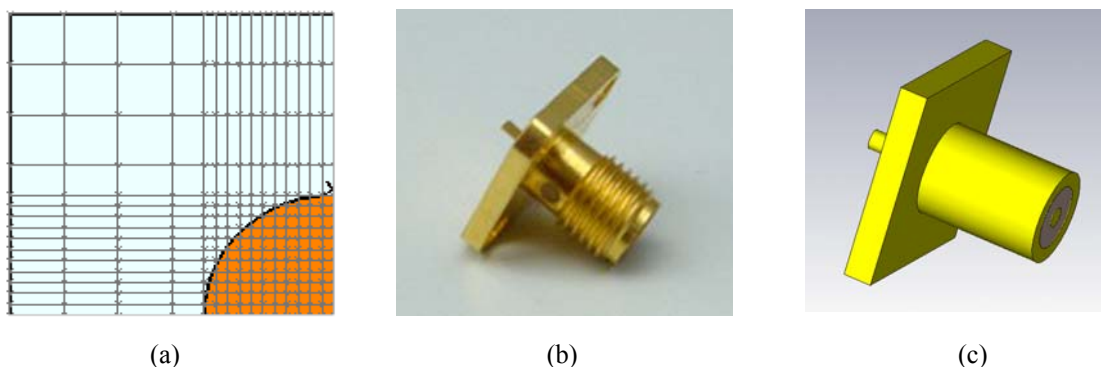


Figure 3.3: (a) The increased meshing used to discretise the round edge of the object is shown in [21]. (b) An actual panel mount SMA connector. (c) The somewhat simplified CST version. Small savings on each component ultimately adds to make a big difference.

Figure 3.3 shows a comparison between a physical connector (b), and its computational equivalent shown in (c). In this case some simplifications were made to the object by not

including the thread, the holes in the base, and the small recession for the Teflon. While this was done for only a small connector, the principle can be applied to any object within a model.

Simplification can also be applied to an entire system. It might be necessary to discard certain objects to obtain a more efficient model to simulate. An example of this is the investigation done on two of the seven Karoo Array Telescopes (KAT-7). Common mode (CM) current distributions on the telescope were studied for either directly injected or induced CM current. The model was incorporated into CST MWS to verify measured results conducted during an RF current audit. It required creating an efficient computational model of the complex telescope structure. More details of this measurement setup and results are discussed in Chapter 6.

The KAT-7 telescope, the computer aided design (CAD) equivalent and the simplified CST MWS computational model are all shown in Figure 3.4 (a), (b), and (c) respectively. The simplification of the telescope to incorporate it into an electromagnetic (EM) simulation environment was already done as part of the design of a lightning down conductor (LDC) system by Wiid [5]. Additional modifications and refinements were required before obtaining the CST MWS model shown in Figure 3.4 (c). Structural updates to the KAT-7 telescope added after the completion of [5] were also incorporated into the computational model.

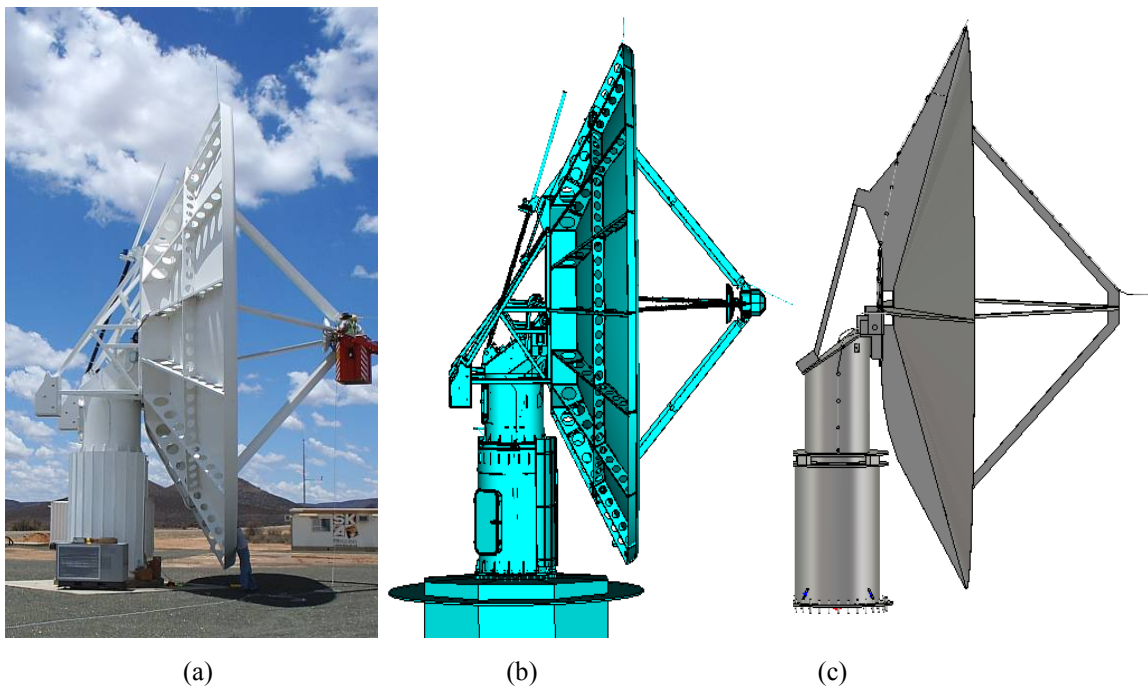


Figure 3.4: (a) One of the KAT-7 radio telescopes that was built as part of the MeerKAT pathfinder. (b) The CAD model from which the actual dish was created. (c) The CST MWS equivalent model after the CAD model was imported and simplified.

Comparing Figure 3.4 (b) and (c) it is clear that the major components of the KAT-7 telescope are still present in the simplified computational model. Starting at the bottom, the foundation bolts remain. The lower and upper pedestals are similar, but in (c) no additional features such as a sunshield were added. In (c) the connections between the two pedestals have been simplified, retaining only the four copper LDC shoes, and the rotation rings to which they connect. The backing structure including the frame that supports the counter weights was removed and replaced in (c) with four ‘ribs’ that support the dish and the feed legs. The dish in the computational model is a cone rather than a parabola as this was easier to create. No additional features are included. A sophisticated elevation motor drive system is used on the dish and shown in Figure 3.5 (a). For CM current investigations it was sufficient to represent the galvanic connection this elevation motor and drive shaft provide between the backing structure and the top pedestal as simple as possible. The equivalent representation in the computational model is shown in Figure 3.5 (b).

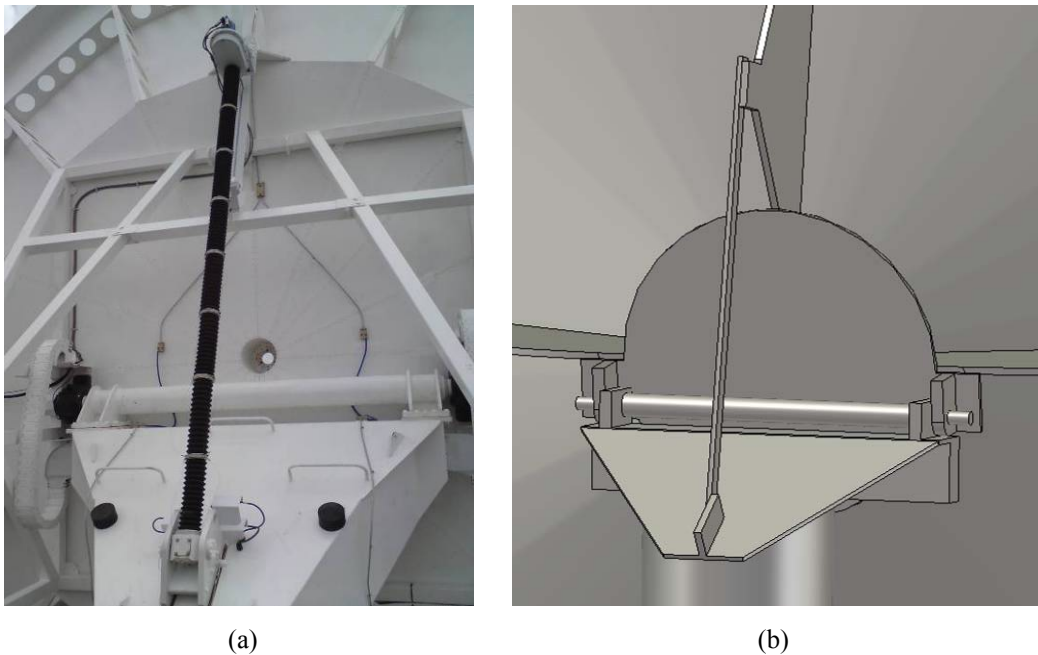


Figure 3.5: Closer comparison between (a) the KAT-7 telescope and (b) the CST MWS computational model in terms of the backing structure and elevation drive.

The hexahedral meshing, which was introduced in section 3.2.1, is very robust and can accommodate complex imported structures. Its efficiency is, however, inherently limited by the variation between the dimensions of the largest and smallest objects being discretised [28]. Methods to help improve this are available in CST MWS, and will be discussed in the following chapters when focussing on a specific aspect of the computational modelling. When modelling gaps or spaces between two objects, the mesh density needs to be at least a factor of two smaller

than the gap being modelled. An example of this is shown in Figure 3.6 which shows a gap between two metallic edges. As mentioned in section 3.2.1, the mesh edge needs to line up with the relative object edges forming the gap. If this gap size is very small compared to the rest of the model's dimensions, a high mesh line ratio limit is required to model it accurately. As previously discussed, this not only increases the total number of mesh cells, but also affects the simulation time negatively. In addition to these mesh refinements, simulations were also done for which the overall mesh density was increased for successive simulations. This process was repeated until negligibly small differences in the results were obtained. Occasionally this would lead to prohibitively large simulation runs. The consequence of the specific refinement must then be verified to confirm the advantages of the longer simulation time.

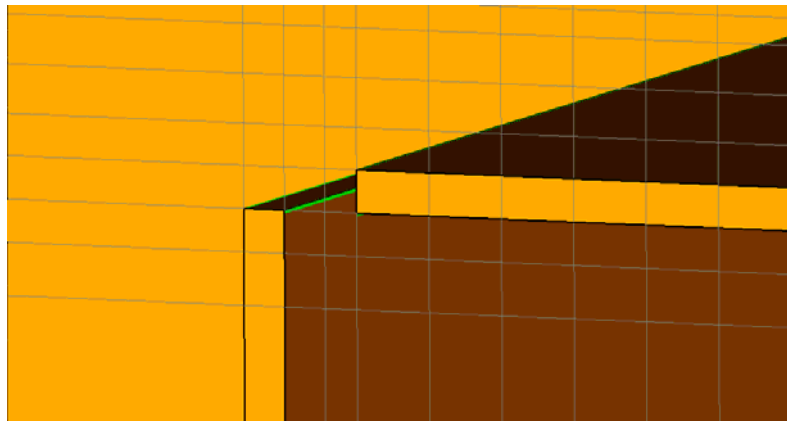


Figure 3.6: The mesh density required to resolve a small gap accurately, needs to be at least a factor of two smaller than the gap length.

In the case of the KAT-7 telescope the reflector consists of a composite material with a metallic mesh inlay. During the moulding process the backing structure is fixed onto the composite material to form a structurally strong unit. With the mesh surrounded by this composite material, there is no galvanic connection between it and the rest of the grounded telescope. From an electromagnetic compatibility (EMC) point of view that is not ideal. Having such a large structure not connected to any reference point, means it could accumulate static build-up and cause uncontrolled discharges. To prevent this, three copper connections as shown in Figure 3.7, were symmetrically placed around the dish. This provided the connection between the dish and a reference potential determined by the grounding of the telescope.

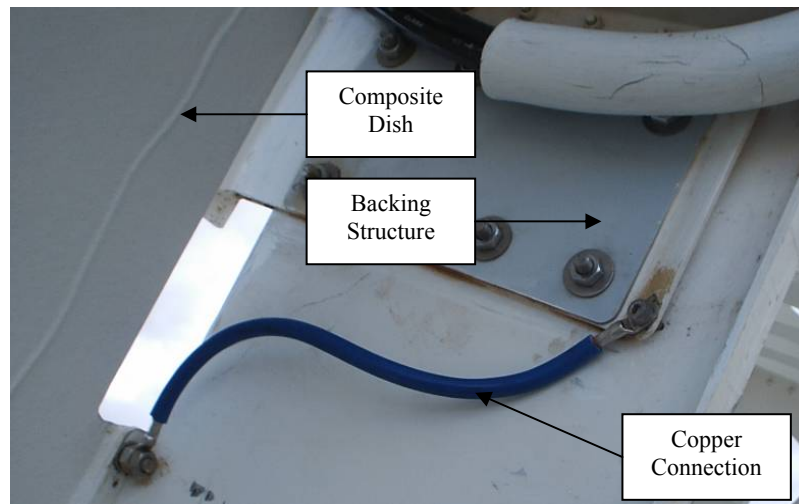


Figure 3.7: Copper connection provided between the mesh inlay in the dish reflector and the backing structure. The backing structure along with the rest of the telescope is properly earthed.

Replicating the above connection, or even putting in an offset between the dish and the backing structure, was not an option for the computational model. Not only was the gap too small but the angle associated with the cone shaped dish complicated the meshing. A fine mesh over the entire depth and surface area of the dish would then be required. Instead, a single object was created by joining the dish and the backing structure. This is seen in Figure 3.8 below.

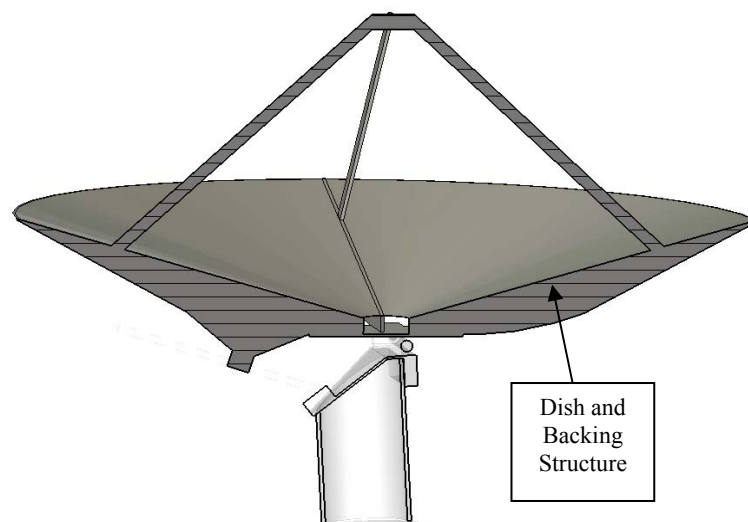


Figure 3.8: Sectional view of the computational representation of the dish and backing structure as one component.

Because of its size, it is our opinion that there is already a good capacitive connection between the actual dish and its backing structure. The negligible influence of this simplification is indeed proven by the computational and measurement result presented in Chapter 6.

Certain simplifications of a computational model could, however, influence the results negatively as discussed by Bachelier et al. [42]. Here the optimisation of the lighting protection system of the proposed VEGA and SOYUZ launching pads are discussed. In [42] the influence of the soil characteristics/layout when assumed homogeneous, gives different results to a non-homogeneous analysis. Caution should therefore be used when making simplifications and computed results should be compared with measured data to ultimately determine the accuracy of the model.

3.2.3. Computational Port Definitions

The various methods of excitation available in CST MWS are discrete port-, waveguide port-, or plane wave excitation. Each of these excitation methods has their own field in which their application is superior. For the investigations presented in this dissertation the most widely used form of excitation is the discrete port. For certain applications a plane wave excitation was specified. Three types of discrete ports can further be distinguished and include an S-parameter, constant voltage, and constant current port. Each one is self-explanatory with the S-parameter port required when calculating S-parameters. The constant voltage and current ports can be used when absolute voltages or currents have to be measured. They keep the relative parameter constant for the frequency band specified in the simulation. No S-parameter calculations can be made by CST MWS when making use of the plane wave excitation.

The discrete port definition is robust and can be used quite easily. Despite the ease of use it is necessary to verify the port's position using the mesh view after it has been defined. An example where the position of the port in the normal view does not correspond with the mesh view is shown in Figure 3.9. It shows inadequate discretisation of the port. The position of the port in the mesh view is what will actually be implemented in the solver. This is one possible reason for a simulation providing inaccurate results.

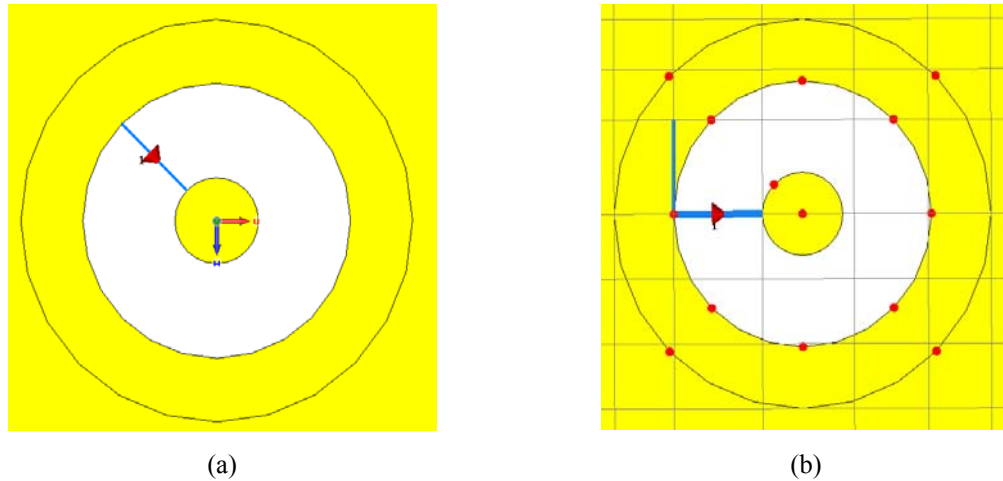


Figure 3.9: Discrete port representation in (a) normal view and (b) mesh view. Notice the difference in the port connection in the mesh view.

Discrete ports can only be defined along the mesh edges because it is here where FIT calculates the currents and voltage. In this case the port discretisation would have to be refined to enable the angled port connection. Refining the meshing will lead to a staircase implementation of the port. Another solution is to change the port location to coincide with the mesh orientation. For this example that would be the obvious solution because of the symmetry of the problem.

3.3. Developing the Computational Analysis

3.3.1. Connecting to the Model

In a measurement where cables are used, they occasionally form an undefined part of the setup. When using a vector network analyser (VNA) to make measurements, variations of the transfer impedance (Z_t), phase stability and temperature of the cables could all influence results even after calibration. The typical problems being investigated in computational analysis does not include any cables connecting to the device as part of the simulation. The absence of measuring cable becomes a moot point with no real attention given to it. Results could be significantly influenced by including or excluding them. As an example the cable tray model introduced in Chapter 2 section 2.6, and shown again in Figure 3.10 (a), is considered. The focus is on the effects the cable layout in the measurement setup has on the measured results. This model, which was used for measuring cable tray shielding and Z_t , is seen in Figure 3.10 (b).

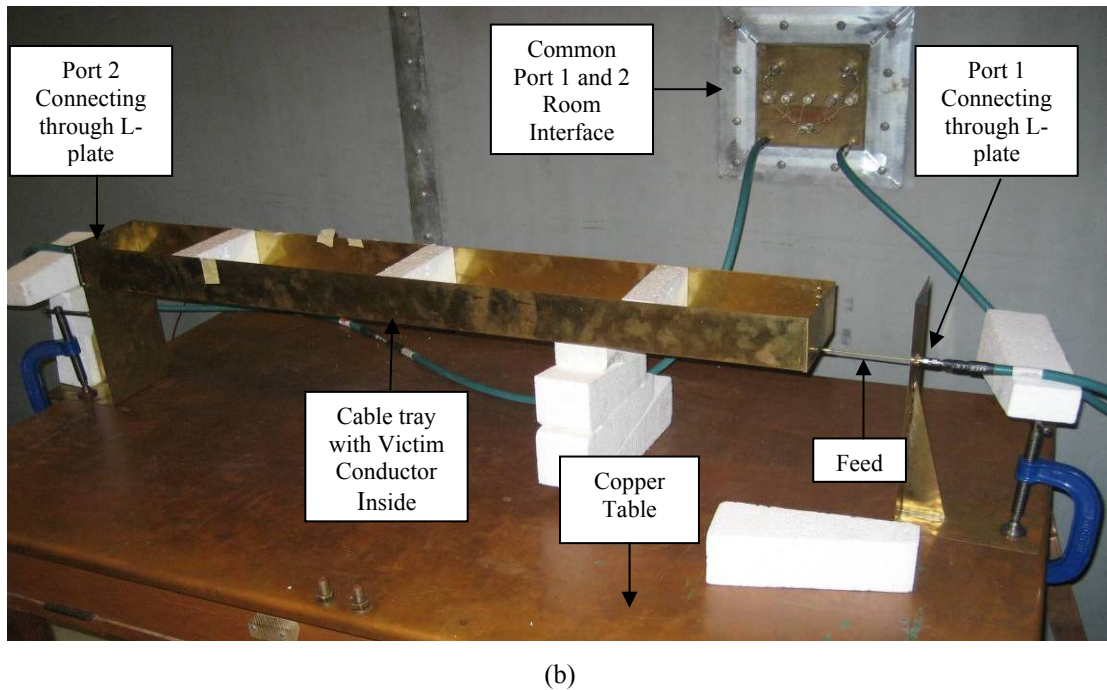
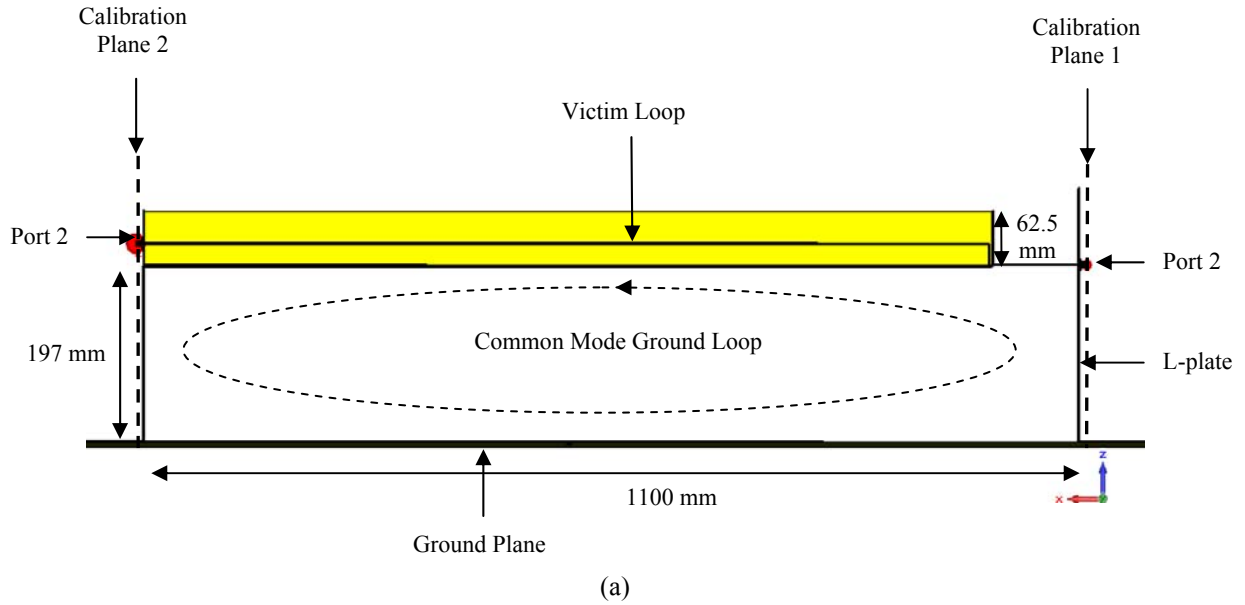


Figure 3.10: (a) Equivalent cable tray model created in CST MWS. Notice the absence of cables that would normally connect to the model. A finite ground plane is also included. (b) Photograph of a cable tray measurement inside a screened room in a setup replicating the experiment done by Ebertsohn in [12].

Measurements of the cable tray model shown in Figure 3.10 (b), which were made using a VNA, were conducted inside the screened room located at Stellenbosch University's Department of Electrical and Electronic Engineering. The reason for using a screened room is because of its isolating characteristics, with negligible levels of outside interference measurable inside the room. These measurements replicated those done by Ebertsohn in [12] and fulfilled an introductory role to firstly, stipulate the level of measurement and calibration accuracy required.

Secondly, it provided information on the requirements necessary to repeat the results presented in [12].

The cable tray length of 1 m meant that quite long cables were used inside the room to connect the measurement ports to either side of the model as shown in Figure 3.10. The magnetic field surrounding the cable tray due to the injected current on the tray, unintentionally involved the long cables in the experiment by inducing CM on them. The cabling layout, and the conductive environment in which the measurements were made, formed a ground loop which the magnetic field intersected. The presence of this ground loop was discovered when the cable tray's measured reflection coefficient, shown in Figure 3.11, was analysed. A resonance at approximately 17 MHz can clearly be seen. The reason for the resonance was initially unclear and only by noticing that its frequency changed as the cable was touched or moved provided some information. Also, as is confirmed by the analysis in Chapter 4 section 4.3, this was not a room resonance so standing waves were not being excited inside the room at this frequency.

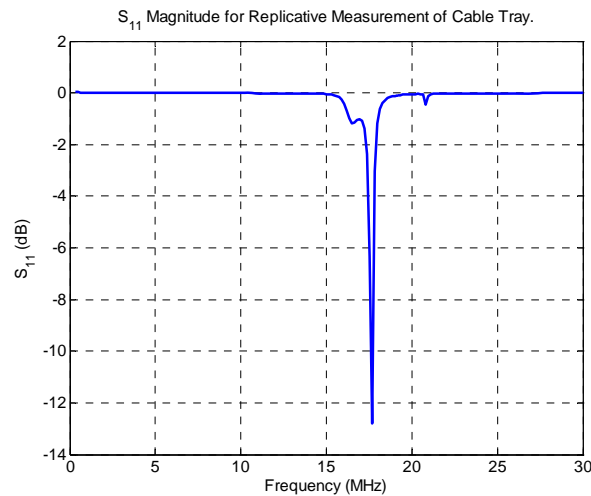


Figure 3.11: S_{11} measurement of cable tray model shown in Figure 3.10 (b). Notice the strong resonance at approximately 17 MHz.

CM currents were flowing on the outside of the cable connected to port one. The change in the resonant frequency when the cable was moved or lifted changed the capacitive coupling between the cable and the earthed copper table seen in Figure 3.10. Changing the capacitive coupling altered the CM current's return path and therefore the travel time of the reflected signal in S_{11} . It was also noticed that by placing a hand or any absorbing ferromagnetic material around the cable, the amplitude of the resonance reduced. The absorbing material reduced the magnetic field associated with the current on the cable. Similar effects were seen in S_{22} , suggesting that the CM

current was not confined to just the cable connected to port one. The exact source of the reflection could, however, not be identified in the measurement setup.

A schematic representation of the CM current path for the cable tray model and measuring cables in Figure 3.10 (b) is shown in Figure 3.12. For this setup port one of the VNA is connected to Loop 1 shown in the schematic. This is the excitation loop (refer to Figure 3.10 (a)) where current is injected onto the outer surface of the cable tray. The copper ground plane serves as the return conductor for the injected current and facilitates in establishing the magnetic field that surrounds the tray. Port two of the VNA is connected to the victim conductor inside the tray (represented by Loop 2). The victim conductor is in fact short-circuited to the inside of the cable tray close to port one as suggested by the schematic and shown in Figure 3.10 (a).. Current is induced in Loop 2 by the intersecting magnetic field created by Loop 1.

Unfortunately this magnetic field also intersects a third ground loop, and induces unwanted CM current flowing in the same direction as the wanted signal (Figure 3.12 after Reader et al [43]). Loop 3 is established by the outer conductors of both measuring cables, the common earth connection of the room interface, and the copper table on which the cable tray model was mounted. The CM current circulating in this loop influenced the measured results through the finite Z_t between the system and the earth reference.

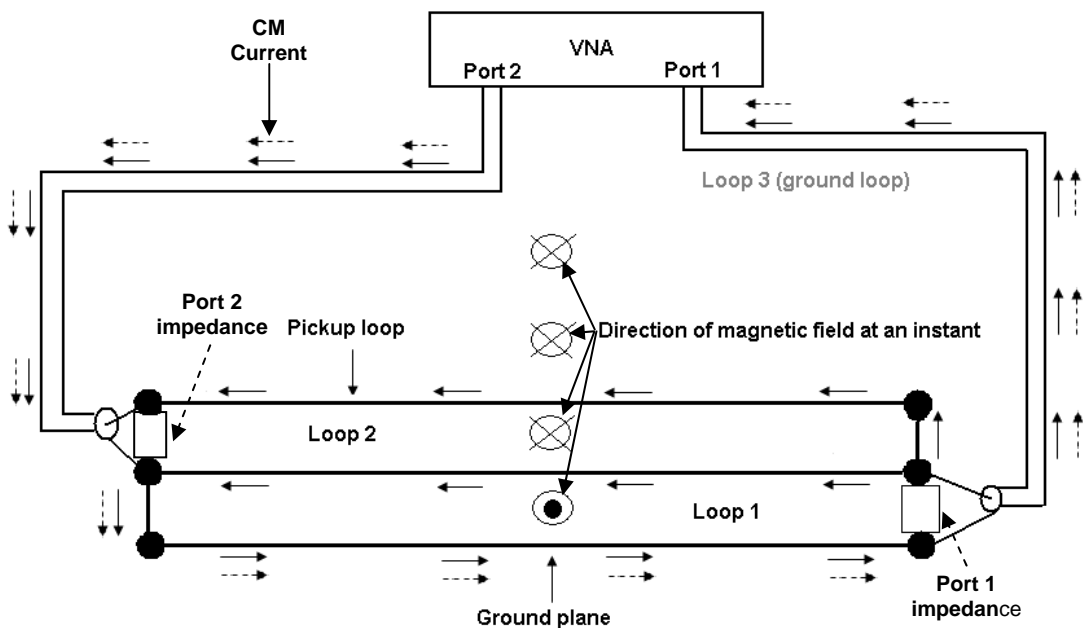


Figure 3.12: Schematic of a three wire experiment which is analogous to the cable tray measurement setup discussed thus far. By connecting the measuring cables on either side of the DUT a ground loop is created along which unwanted CM current is flowing (After [43]).

The mechanism through which CM current was being induced in Loop 3 was now known. However, the purpose of the L-plate at port one was to prevent current flowing in Loop 1 from adding to possible CM current flowing in Loop 3. It would do so by forming a physical barrier between the two loops. By visualising the surface current distribution on the L-plate using CST MWS, its effectiveness in forming such a barrier was analysed. This visualisation of surface currents is shown in Figure 3.13 (a) and (b) as magnitude plots calculated at 17 MHz.

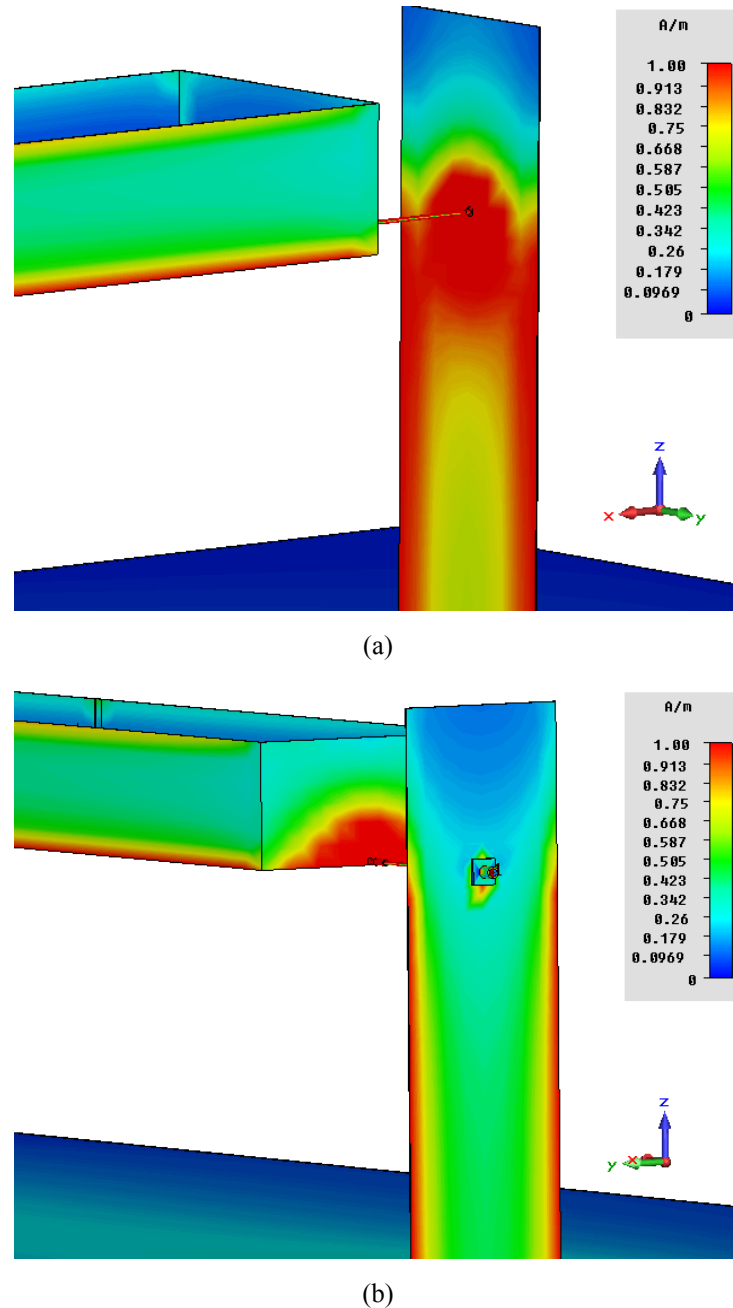


Figure 3.13: Surface current plot at 17 MHz of L-plate through which the feed element injects current onto the cable tray. (a) Shows the front face and (b) the back face of the plate. This is the cable tray model used by Ebertsohn in [12] to investigate cable tray Z_t .

Like charges have the tendency to repel each other which means that the current will distribute over the entire surface of the L-plate. Because of its relatively narrow width, this means that surface current present on the front face of the L-plate, seen in Figure 3.13 (a), will also flow on its back face, seen in Figure 3.13 (b). These results show that the L-plate was not as effective at preventing current flowing in Loop 1 (Figure 3.12) from getting onto the measuring cables as initially expected. This explained how current induced in Loop 3 by the surrounding magnetic field could successfully circulate around the measurement setup.

3.3.2. Cable Tray Model: Next Iteration

Characterising various types of cable tray connections is, as mentioned in Chapter 1, a contribution this dissertation aims to make. The type of mid-span and end-connections used in a cable tray installation has a direct influence on the tray's overall shielding ability against electromagnetic interference (EMI). After discovering that a ground loop was being created by the measuring cables in the measurement setup of the first model, it was decided to re-define the model before attempting to investigate the different connections.

The mechanism of magnetic field coupling present in the previous cable tray model, was always going to be similar for the new cable tray model. A victim conductor, positioned at a constant height inside the tray, would still be used to measure induced voltage caused by a magnetic field that surrounds the tray. With a different objective of what the model would be used for, a number of structural changes were made according to the following requirements:

Decrease the amount of unwanted CM current on the measuring cables.

Localise induced CM current on cable tray.

Evaluate end-connections specified in literature and commonly used on cable trays.

Evaluate mid-span connections specified in literature and commonly used on cable trays.

Increase measurement frequency range from 30 to 100 MHz.

A reduction in the amount of CM current on the measuring cables was required to minimise the unwanted influences in the results. This meant that the measurement setup inside the screened room had to be refined. A parallel earth conductor (PEC) closely positioned to the tray would serve as the method of exciting the model. PECs are sometimes installed on cable trays in practical installations to distribute functional earth connections to equipment. As a consequence

they occasionally carry fault currents which, when they do, produce significant levels of interference. The new model consisted of a fixed height-to-width ratio cable tray with an enclosure added to one end of the tray. Termination at the enclosure would allow investigating different end-connections. By removing a small section in the middle of the tray, centre connections could also be analysed.

Consider a similar schematic to Figure 3.12 shown in Figure 3.14 (except for the position of the measuring cables). The first priority was to create a model which reduces the amount of unwanted CM current induced by Loop 1 on the cables connecting to the device.

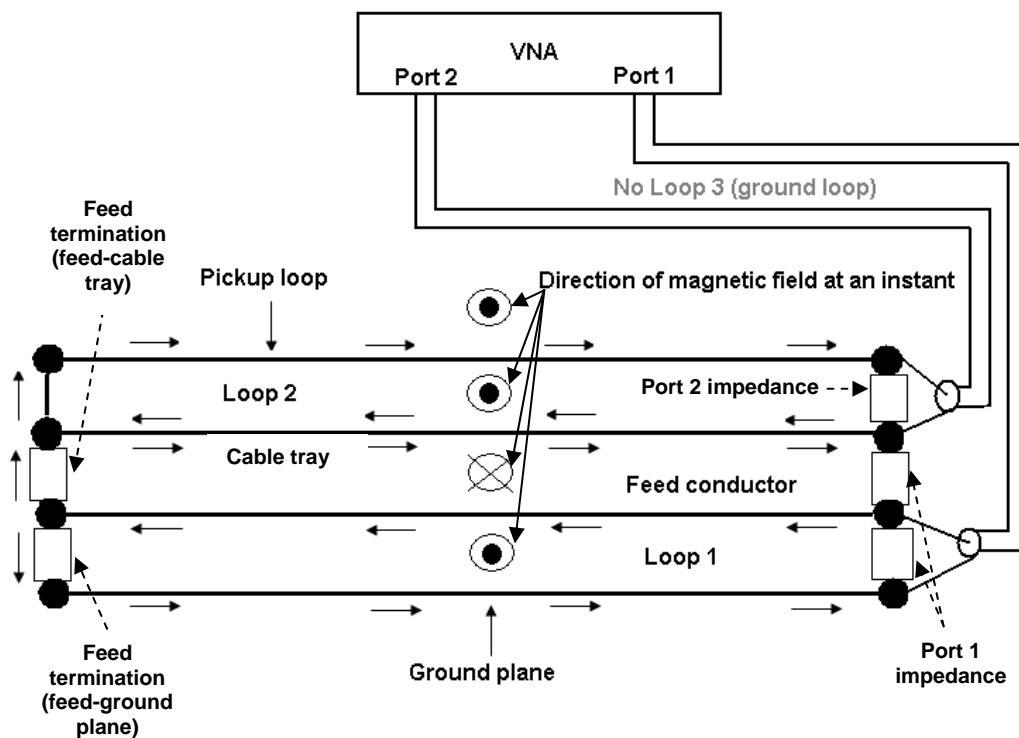


Figure 3.14: Schematic of a three wire experiment which is analogous to the cable tray measurement setup for the new cable tray model. By connecting the measuring cables on one side of the DUT, the size of the ground loop is significantly reduced, minimising the unwanted induced CM current.

From Figure 3.12, it is clear that the cable connected to Loop 2 should be moved to the same side of the DUT as the cable connected to Loop 1. This significantly reduces the area of Loop 3 intersected by the magnetic field generated by Loop 1. The result is a reduction in induced CM on the measuring cables. It was furthermore decided to widen the L-plate used at port one. This reduces the amount of current leaking around the edges of the L-plate and onto the cables. It provides a well defined calibration plane for both port one and two. The combination of these changes culminated in the new computational model seen in a sectioned view in Figure 3.15.

By shortening the cable tray to a length of 700 mm, an enclosure was added to the opposite end of the tray. The remaining dimensions of the new model are specified in more detail in Chapter 4. The shortened length helped to increase the upper frequency limit at which the model could be analysed, without becoming quarter-wavelength resonant. The victim conductor included in the tray is short-circuited inside the added enclosure. Their combination made it possible to investigate the change in shielding associated with different end-connections. Provision was also made to investigate mid-span connections.

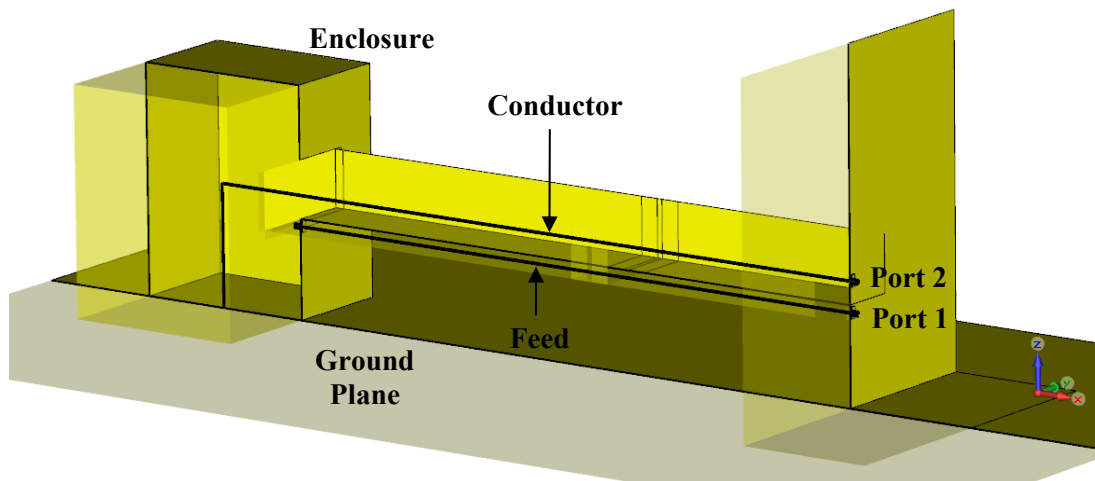


Figure 3.15: New cable tray model created to study the effects various connections had on the cable tray's overall shielding ability.

The PEC-like setup was replicated by extending the centre conductor from the SMA connector at port one the entire length of the tray. It terminates at the enclosure in a 50 Ω load impedance. Using this method of excitation meant that current was not directly injected onto the outer surface of the cable tray. Rather, the close proximity of the exposed centre conductor causes it to couple capacitively very strongly to the tray, and in the process induces current in the central part on the tray. The results from the investigation into different mid-span and end-connections are fully discussed in Chapter 4.

To validate the effectiveness of the wider L-plate, CST MWS was again used to investigate the surface current distribution on the new model at 17 MHz. The results are presented in Figure 3.16 with the front face shown in Figure 3.16 (a) and the back face in Figure 3.16 (b).

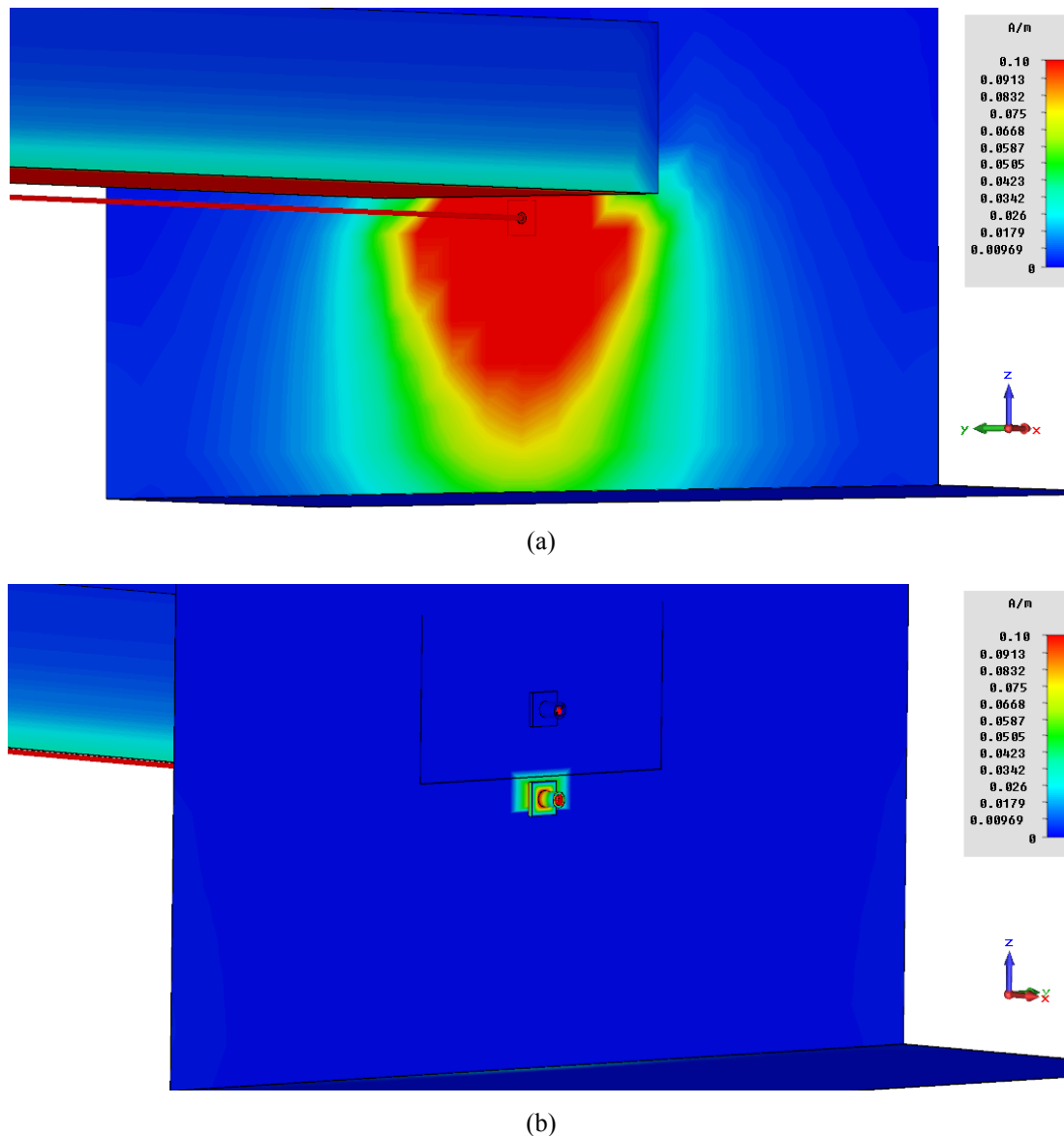


Figure 3.16: Surface current plot at 17 MHz of the widened L-plate of the new cable tray model with (a) the front face and (b) the back face. Notice the reduced level of current on the back face.

Significantly lower levels of surface current are present on the back face of the L-plate. The wider L-plate, which provides a larger inductive path, helped to reduce the involvement of the measuring cables when the model was analysed. The frequencies at which the new model was investigated were increased from 30 MHz to 100 MHz. As will be shown in Chapter 4, even with the shortened tray, the model still reaches quarter-wavelength resonance.

3.3.3. Computational Boundary Definitions

From the explanation given in section 3.2.1 it becomes clear that when using the time-domain based hexahedral meshing in CST MWS, a volumetric analysis is performed. A terminating definition for the associated volumetric discretisation is required to determine the size of the

computational domain. When using the transient solver, the energy pulse is injected into this volume using one of the previously mentioned port-excitation methods. The peak level of the chosen pulse is normalised to 1. After excitation, the energy is allowed to dissipate inside the volume. It is continuously measured and compared to the normalised level initially injected. Once the difference reaches a user-defined stop criterion, the simulation is terminated. The boundary conditions, which are set by the user and implement different types of terminating definitions, will inevitably influence the measured results. A simulation domain implementing all the available definitions is shown in Figure 3.17.

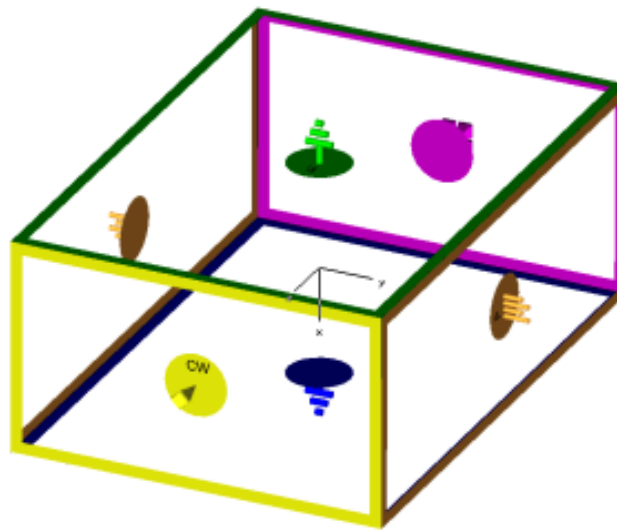




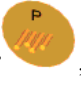




Figure 3.17: Boundary definitions available in CST MWS [21].

During our investigations the boundary definitions most frequently used in the simulation were

open , *open (add space)*  and *electric* ($E_t = 0$)  [21]. The two *open* definitions allow energy inside the volume to pass the boundary with negligible reflection. It effectively creates a free space environment around the model. Adding additional space with the *add space* definition, allows the user to do far field calculations. This was used for determining the gain of a cable tray at higher frequencies in Chapter 5. The *electric* boundary essentially creates a perfect electrical conductor. All tangential E -fields incident on this definition are terminated. In most cases it is used as a local earth reference.

Additional definitions that are available include, *magnetic* ($M_t = 0$) , *periodic* , and *unit cell* . The *conducting wall*  definition was also used as part of the cable tray

investigations. It essentially creates a lossy metallic wall that makes it possible for energy to be reflected back into the computational domain. Upon defining the new cable tray model introduced in section 3.3.2, this definition became especially useful during the validation process of this model's measured results. S-parameter measurements of the new model were again conducted in the screened room. Because the upper frequency limit was increased from 30 to 100 MHz, the involvement of the room and how it affected the measured results became apparent for the first time. Resonances, seen in Figure 3.18, were again noticed in the measured results.

The measuring cables were not responsible for the interference because the wider L-plate, discussed in section 3.3.2, did minimise the CM current on them. An explanation for the resonance was given when the room's door was opened. This caused the resonant frequency to change suggesting that the room itself was interacting with the model. It was forming a resonant cavity due to its reflective nature at approximately 80 MHz. A particular modal distribution was set up inside the room. Initial simulations of the new cable tray model in CST MWS using *open* definitions, did not indicate the same resonance. The *open* boundary provides minimal reflection of energy passing through it. Once the definition was changed from its original absorbing condition to the correctly dimensioned *conducting wall*, agreement between the results as seen in Figure 3.18 were obtained.

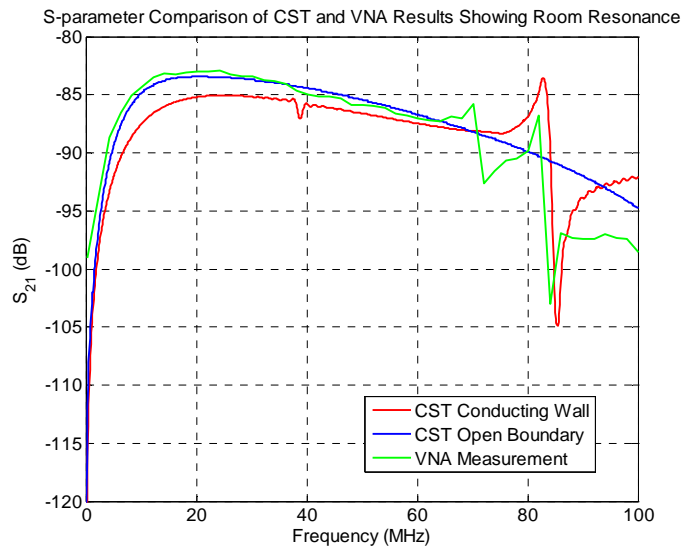


Figure 3.18: Initial comparison between measurements of the new cable tray model made inside the screened room and CST MWS results using *open boundary* definitions. Note that this definition does not predict the resonance and simply allows energy to pass through the boundary with minimal reflection.

Good agreement between measured and computed results is presented even at this low coupling level. Identifying the exact modal pattern inside the cavity using the modal equation for resonant cavities is discussed in more detail in Chapter 4. Here the interaction of the fields inside the volume is also shown. For now, highlighting the requirement for the correct representation of the interaction between the measurement environment and the DUT in the chosen boundary definition, is important. By not using the correct boundary definition, incorrect results will be obtained.

3.4. Conclusion

The focus of this chapter was on CST MWS and how it is used as a tool to verify measurement techniques. Its operation and hexahedral discretisation method was discussed in basic terms. The discretisation is represented in the form of three-dimensional cubes or mesh cells. A dual discretisation of the computational volume takes place to allow for electric and magnetic field calculations. The discretisation or meshing process of the computational model directly influences both the accuracy of the results obtained, and simulation time through the length of the mesh step. A denser mesh is required when more detail is included in the model but will increase the simulation time. The trade-off therefore lies in computational time versus accuracy of the results.

With this knowledge, methods were discussed that can be used to decrease the complexity of a model, which in turn reduces the mesh density. This might be achieved by simplifying certain objects within the model. It might also be achieved by removing inconsequential components that ultimately have no influence on the results investigated. Regardless of how simplified a model might be, the accuracy of the mesh still determines the accuracy of the results. It was also shown how the accuracy of the mesh alignment needs to be verified in the mesh view.

Verification of computed results is important and one method is to compare it to measured results. This comes with its own complexities. The most prominent is the fact that certain features in the measurement are not part of the computational analysis. Cabling issues and boundary definition effects were discussed by using a cable tray model defined in Chapter 2. Assuming the same measurement environment, the model can be adapted to remove influences caused by CM current on the measuring cables. This led to the development of a new cable tray model which will be used in the next chapter to investigate cable tray connections. Further

resonances were caused by the interaction between the computational model and the reflective environment of the screened room. In this case the influence on the results was replicated when the correct boundary definition was used. By becoming familiar with the way in which CST MWS operates, accurate computational models which are used in further investigations can now be created.

Chapter 4

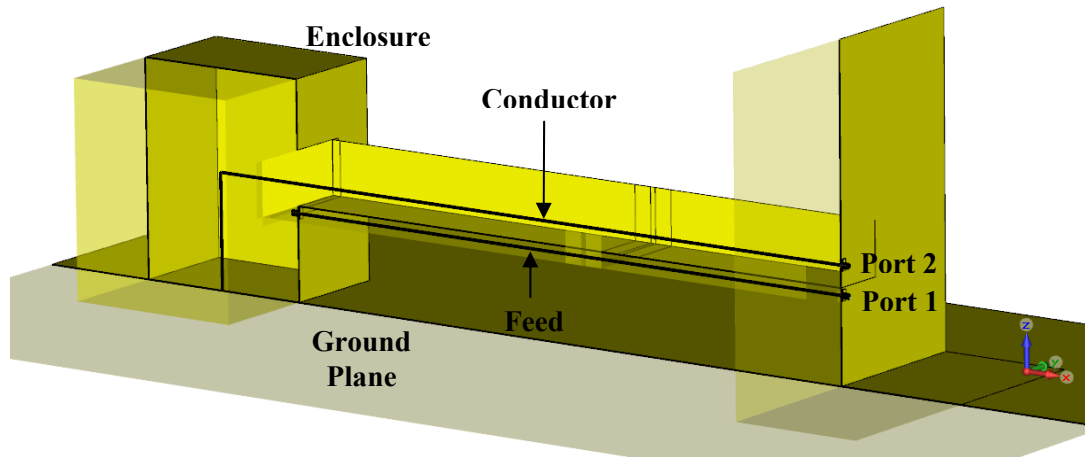
Modelling and Measurement of Cable Tray Connections

4.1. Introduction

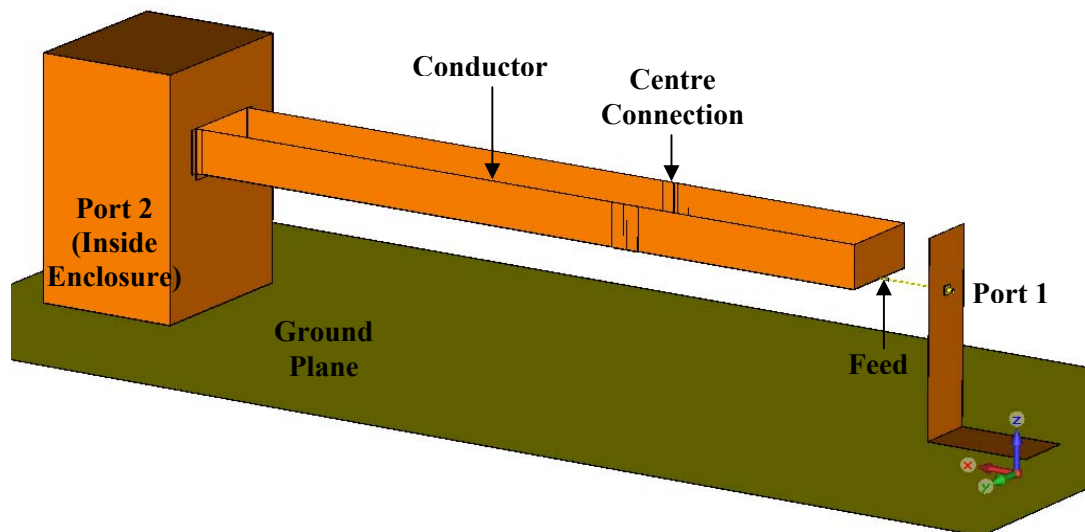
Several documents give explicit recommendations for the correct usage of cable trays for radio frequency interference (RFI) purposes [8]-[10] and [13]-[15]. However, the advice concerning cable tray end-terminations, mid-span connections and overall cabling layout is general, and specific connections are not explained. In this chapter the effect of different connection schemes on the overall shielding ability of cable trays is examined. Both S-parameters and transfer impedance (Z_t) are calculated for a particular setup. The focus is on visualising the change in surface currents and magnetic fields associated with each scheme. CST MWS [21] is, as introduced in Chapter 3 section 3.3, used to analyse the various connections on computational cable tray models replicating physical ones. Computed and measured results are compared to validate the accuracy of the analysis.

In addition to the new cable tray model introduced in Chapter 3 section 3.3.2, a slightly revised version of the model created by Ebertsohn in [12] was also used. The new model, shown in Figure 4.1 (a), will be referred to as Model 1. Excitation of the parallel earth conductor (PEC)-like feed at port one, simulates interference in the form of common mode (CM) current which is induced on, and flows along, the bottom surface of the tray. The second model, Model 2 Figure 4.1 (b), is equivalent to the model used in [12], except for the added enclosure and centre connection. As shown in Chapter 3 section 3.3.1, current is injected directly onto the outside bottom edge of the tray for this model. The difference between the two models is that current injected at port one in Model 2, distributes more evenly over the outer surface of the tray as it travels towards the enclosure. In contrast, a more localised CM current is induced on the tray for Model 1. In both cases a simulated victim conductor is included inside the cable tray, and

extends the entire length into the enclosure. The amount of magnetic field coupling to this loop is investigated.



(a)



(b)

Figure 4.1: Cable tray models with an L-plate connection on the feeding side and an enclosure on the other. External excitation is achieved with: (a) an exposed centre conductor underneath the cable tray, Model 1 and (b) an end-feed, Model 2. In both cases a victim loop is included inside the cable tray and enclosure.

The work in [12] analysed cable trays from 100 kHz to 30 MHz, but did not discuss connection schemes. In this investigation frequencies from 100 kHz up to 100 MHz are considered, at which point quarter-wavelength effects limit the experiment. Radiated coupling to the victim conductor above these frequencies is described in Chapter 5. For illustration purposes, most of the field plots are presented at a frequency of 10 MHz, however, results have been studied across the stated band. The chapter concludes by discussing, in general, the best connection schemes.

4.2. Defining the Investigation

Some knowledge on behalf of the reader concerning cable trays is assumed. Cable trays with increasing height-to-width ratios (e.g., 1:1 or more), provide better screening properties to enclosed cables than shallower trays as discussed by Van Helvoort [9], Pettus [10], Ebertsohn [12], and IEC installation standard [15]. For this investigation, only single compartment trays with a fixed height-to-width ratio of 1:2 are used. Cable trays incorporating a cover would provide the best solution to fully protect conductors from unwanted interference. They do, however, tend to be used in specialised applications, and the focus here is on more practical and widely used cable tray installations.

The type of connection helps to characterise the CM current path. It is fair to say that by placing a wider connection compared to a narrow connection, the associated path impedance decreases. In addition to the change in path impedance, different environments in which cable trays are used were also considered. Ultimately, the current path impedance is dependent not only on where most of the current is flowing, but also on what type of end-termination and mid-span connection is used.

4.2.1. End-Connections

The correct termination of cable trays is required to ensure an all-inclusive electromagnetic compatibility (EMC) policy. The type of connection impacts on the effectiveness of the tray to shield the conductors inside from interference in two ways. Firstly, providing a continuous path for CM current on the tray helps to reduce additional electromagnetic interference (EMI). Secondly, when used as part of a safety earthing system [16], cable trays with adequate connections provide a low impedance path to ground in case of fault conditions. This minimises damage to equipment and possible injury caused by flashover.

The end-connections considered are combinations of L-brackets as seen in Figure 4.2 and specified by Williams in [13]. These connections are also commonly referred to by standards and installation manuals. No reference is made in [13] as to how the shielding ability of the tray changes with each connection.

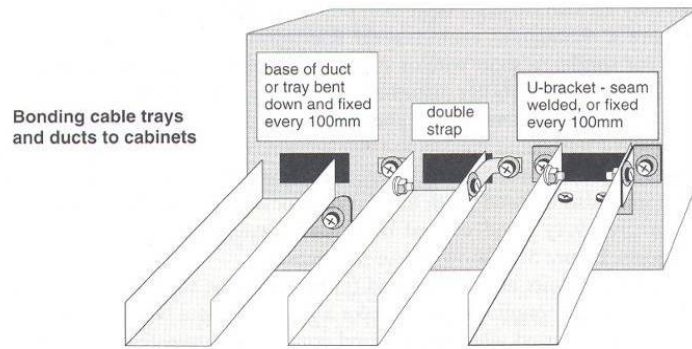


Figure 4.2: Different types of end-connections for the termination of cable trays as specified in [13], and used in this investigation, are shown.

4.2.2. Mid-span Connections

Standard cable trays are, more often than not, too short to form a continuously connected structure between two electromagnetic (EM) enclosures in a practical installation. This necessitates the use of mid-span connections. End- and mid-span connection schemes such as those found in [9] and [13]-[16] are discussed in general. Usually they are divided into the following categories: good, not recommended, and bad as indicated in Figure 4.3.

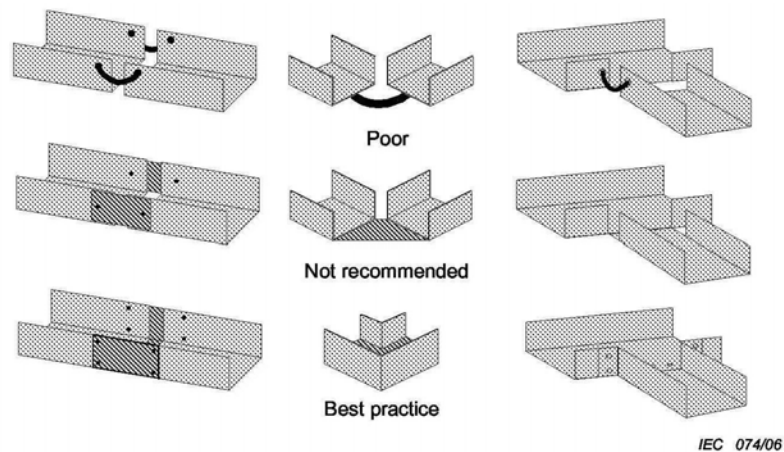


Figure 4.3: Centre connections advised for use with cable trays as specified in [15].

No definite explanation is given as to why a certain connection shape is better than another. In general, the literature advises the user that as much of the cable tray's original shape as possible needs to be retained where a connection or junction is to be placed. The connections that are studied in this investigation, and specified in literature, include: a full U-bracket Figure 4.4 (a), a single bottom connection Figure 4.4 (b), L-brackets Figure 4.4 (c), and finally side straps representing bondwires or pigtails Figure 4.4 (d).

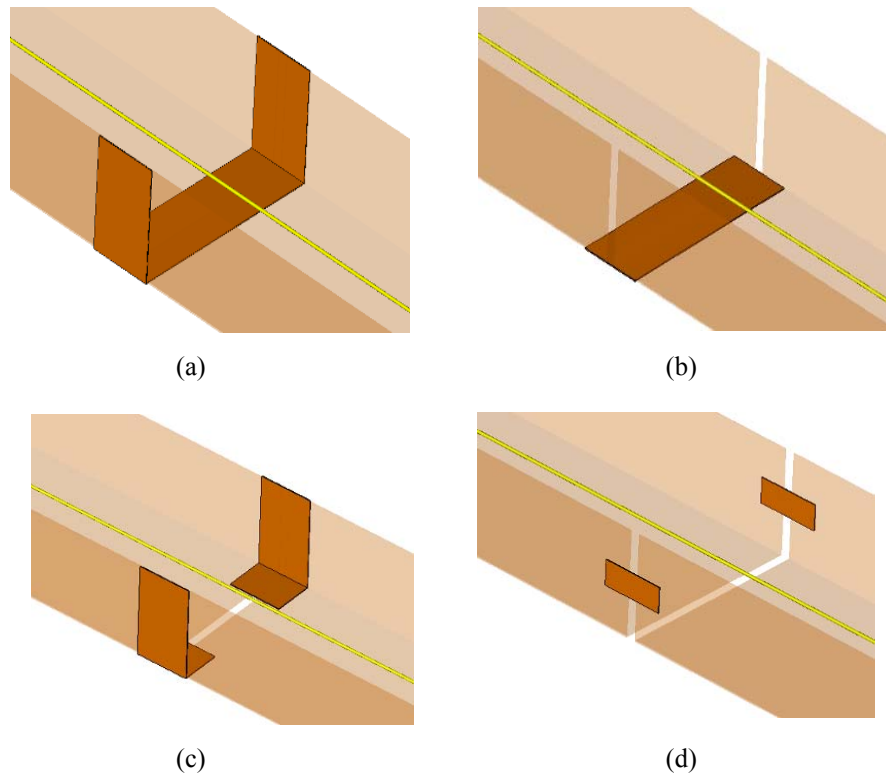


Figure 4.4: Computational representation of the following mid-span connections referred to in literature and included in this investigation: (a) full U-bracket, (b) bottom connection, (c) L-brackets, and (d) side straps.

To replicate the connection in CST MWS, the particular end- or mid-span connection was placed so that it makes contact with all the relevant surfaces. This is an ideal connection, however in the case of the end-connections, the cable tray was shortened by 1 mm. This attempts to simulate an imperfect connection between the cable tray and enclosure. It also provides the most prominent point of entry for the CM currents on the cable tray into the enclosure. This distance was kept the same for all the end-connections analysed in both models.

4.2.3. Computational and Physical Model Dimensions

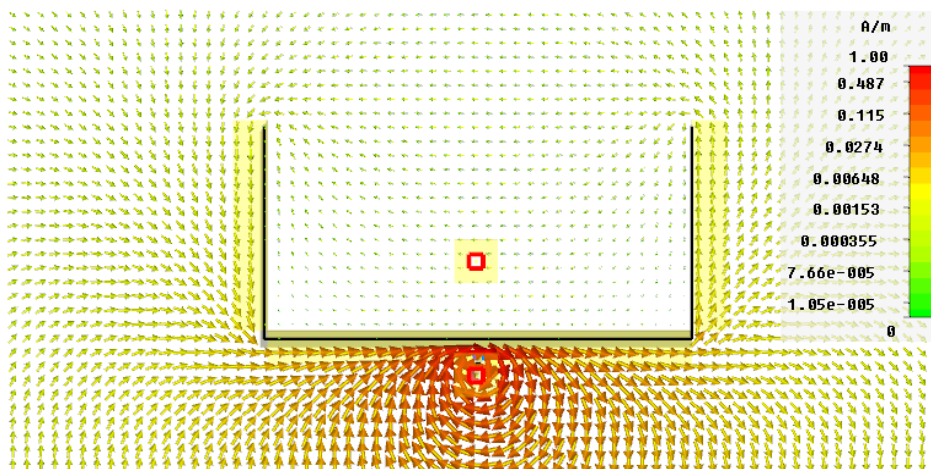
Both models created for this investigation have the same overall dimensions. The length of the cable tray was shortened to 700 mm and an enclosure added to enable investigating different end-connections. The length does cause travelling waves to manifest as will become evident from the results presented. It has a width of 125 mm and a side-wall height of 62.5 mm. These dimensions were originally established as part of [12]. The victim conductor inside the tray for both models is kept in the centre at a constant height of 25 mm above the bottom of the tray. The enclosure has a height of 350 mm, depth of 200 mm and a width of 250 mm. The depicted ground plane used with both models has a length of 1360 mm and a width of 750 mm.

4.2.4. Field Distributions around Computational Models

4.2.4.1. Model 1

Having a PEC connected in close proximity to a cable tray as described in [16], creates a source of concentrated current and magnetic field under fault current conditions. The induced CM currents on the cable tray under such conditions will be localised in a certain area of the tray. Using the correct cable tray connections for such an installation is not necessarily obvious. This prompted the idea of using a PEC as a method of excitation for Model 1. The process of defining Model 1 was discussed in Chapter 3 section 3.3.2. The refinements included the wider L-plate which limits the amount of CM current present on the measuring cables. A schematic representation of the current flow for this model was shown in the same section. Figure 4.5 (a) below, is a vector plot of the magnitude of the magnetic field at 10 MHz, created by exciting the feed conductor in CST MWS. Note the victim conductor inside the tray is not included. A simplified sketch of the current flow presented in Figure 3.15, is shown in Figure 4.5 (b).

Figure 4.5 (a) shows that the magnetic field intersecting a loop, created by the victim conductor inside the cable tray, is in an opposite direction to the field circulating around the feed. The reason for this is the return current flowing on the cable tray, indicated in Figure 4.5 (b). The termination of the feed at the enclosure creates two current return paths.



(a)

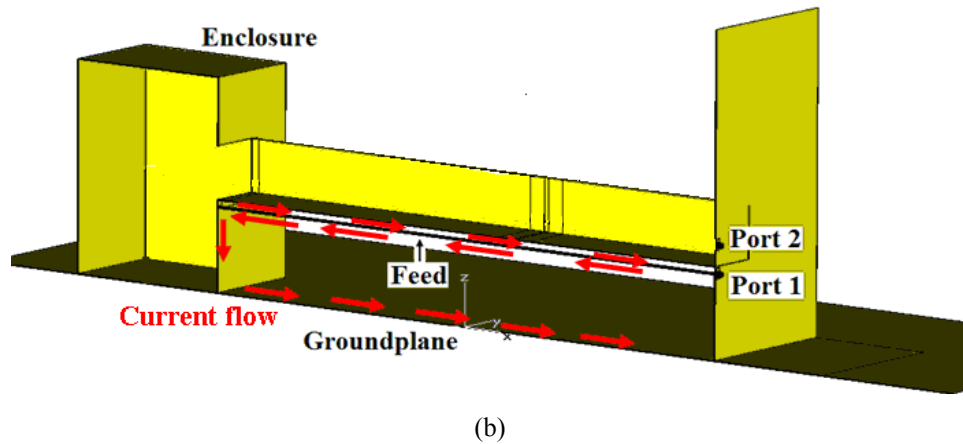


Figure 4.5: Investigation of magnetic field distribution around the cable tray for Model 1 without a victim conductor inside the cable tray. Shown in (a) is a vector plot of the magnitude of the magnetic field at 10 MHz and in (b) an indication of the current flow on the model.

The consequence of this is seen in Figure 4.6, which shows a similar vector plot of the electric field at the same frequency, also generated using CST MWS. The electric field is concentrated in the centre below the cable tray.

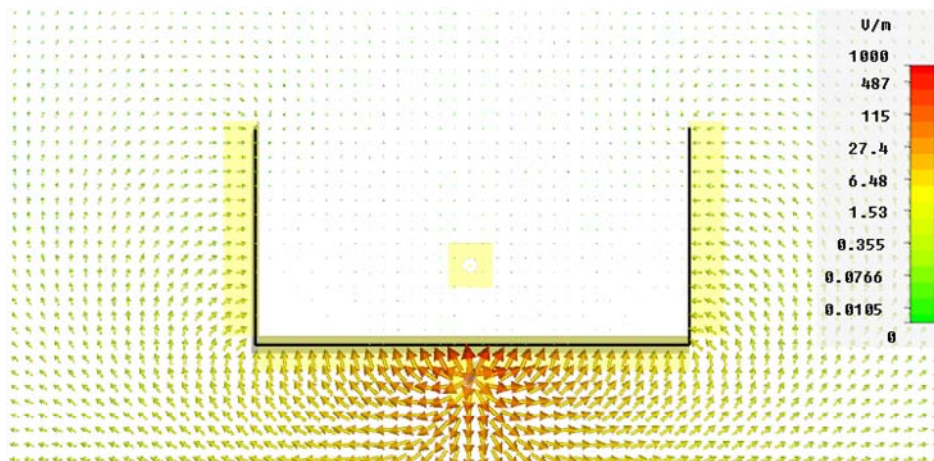
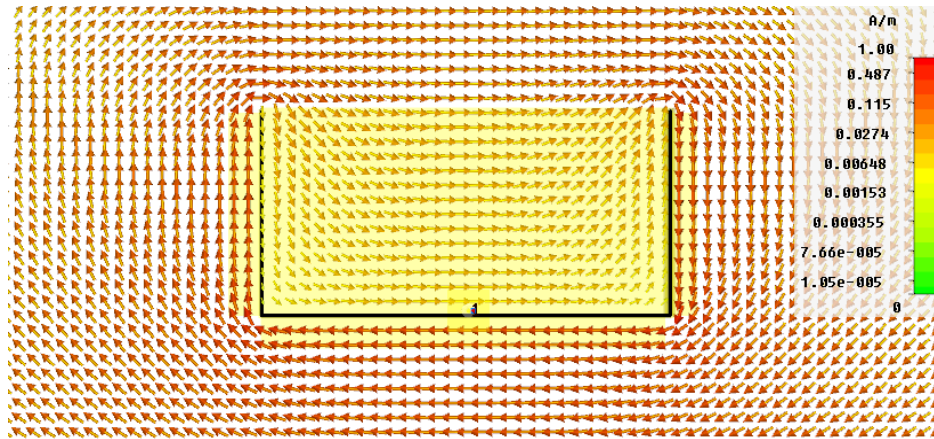


Figure 4.6: Investigation of the electric field distribution at 10 MHz around the cable tray for Model 1 without a victim conductor inside the tray.

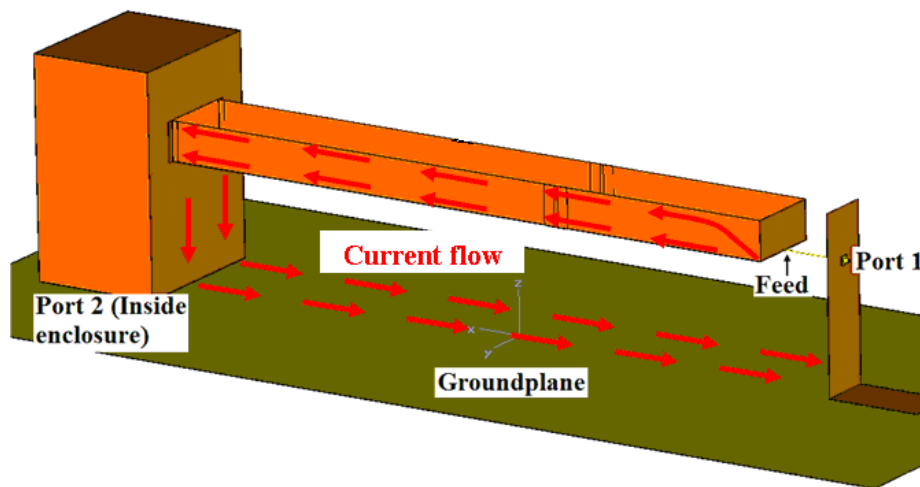
4.2.4.2. Model 2

It became apparent that the various mid-span and end-connections required analysis on a cable tray that has a more even distribution of CM current on it. This is relevant for cable trays installed in an environment where they are exposed to continuous high frequency (HF) interference. For lower voltage applications, the cable tray itself is occasionally used as the PEC. For such a scenario, under fault conditions, the CM current will distribute more evenly over the outer surface.

To achieve the more uniform distribution, the original model defined in [12] by Ebertsohn was used, but slightly shortened to accommodate the enclosure. The schematic indicating the current flow on this model was shown in Chapter 3 section 3.3.1. Here the cable tray is the common conductor between the excitation loop and the victim loop inside the tray. A CST MWS vector plot of the magnitude of the magnetic field at 10 MHz for this model is shown in Figure 4.7 (a). An indication of the current flow on the cable tray is given in Figure 4.7 (b).



(a)



(b)

Figure 4.7: Investigation of magnetic field distribution around the cable tray for Model 2 without a victim conductor inside the cable tray. Shown in (a) is a vector plot of the magnitude of the magnetic field at 10 MHz and in (b) an indication of the current flow on the model.

Compared to Figure 4.5 (a) a more uniform distribution of the magnetic field around the tray is seen for Model 2. The associated vector plot of the electric field at the same frequency is shown in Figure 4.8. The main difference between Model 1 and Model 2 is the method of excitation.

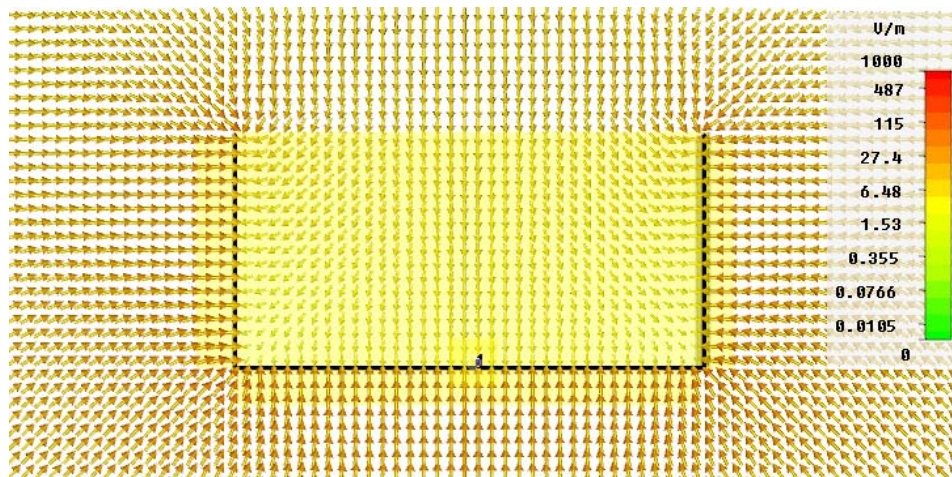


Figure 4.8: Investigation of the electric field distribution at 10 MHz around the cable tray for Model 2 without a victim conductor inside the tray.

When comparing Figure 4.6 and Figure 4.8 the difference in electric field distribution due to the different feeds becomes apparent. The same type of connection will therefore have a different effect on the cable tray shielding when used on each one of the models.

4.3. Simulation, Measurement and Coupling Parameters

Comparisons of S-parameter results were used to evaluate the accuracy of both computation and measurements. All the measurements for both models were conducted inside the same screened room located at Stellenbosch University as mentioned in Chapter 2 (Figure 4.9 (a)), using a calibrated Hewlett Packard 8753A vector network analyser (VNA). A full two-port as appose to a response calibration was performed despite only measuring S_{21} . This ensured maximum dynamic range for the measurement. This helped to achieve an additional improvement in the dynamic range. The screened room was required because of the sensitivity of the measurement. It prevented any unknown modulation interference which would be detectable at these low levels being measured.

4.3.1. Model 1

The evaluation process of Model 1 was briefly introduced as part of Chapter 3 Section 3.3.3. There, attention was given to the choice of boundary definitions used in CST MWS, and their influences on the generated results. Over the specified band of 100 kHz to 100 MHz, an S_{21} measurement of Model 1 (Figure 4.9 (b)) conducted in the screened room showed a resonance at approximately 81 MHz, which was not replicated in the computed results.

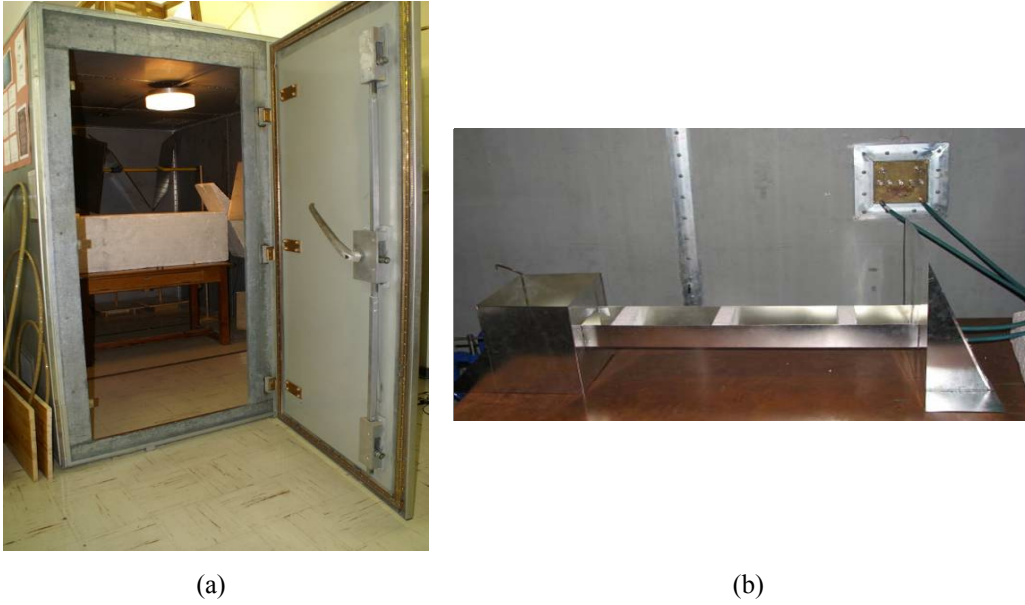


Figure 4.9: The screened room used for the cable tray measurements is shown in (a). Model 1 set up inside the screened room is shown in (b).

Due to the method with which the model was excited, energy was being radiated into the enclosed environment. This caused currents to flow on the conducting walls of the room, and essentially created a microwave cavity, which had a resonant mode at a particular frequency. To verify the cavity resonance and modal distribution, the following modal equation as specified by Chan and Reader, [44] was used.

$$\left(\omega\sqrt{\epsilon_0\mu_0}\right)^2 = \left(\frac{m\pi}{a}\right)^2 + \left(\frac{n\pi}{b}\right)^2 + \left(\frac{p\pi}{c}\right)^2 \quad (15)$$

In (15) $\epsilon_0 = 8.854 \times 10^{-12} \text{ F/m}$, $\mu_0 = 4\pi \times 10^{-7} \text{ H/m}$ and $\omega = 2\pi f$ with f the resonant frequency identified. The modal distribution is specified by m , n and p and this is related to the dimensions of the cavity given by a , b and c respectively. Figure 4.10 shows a schematic representation of the room dimensions with $w = 2.45 \text{ m}$, $l = 3.71 \text{ m}$ and $h = 2.45 \text{ m}$.

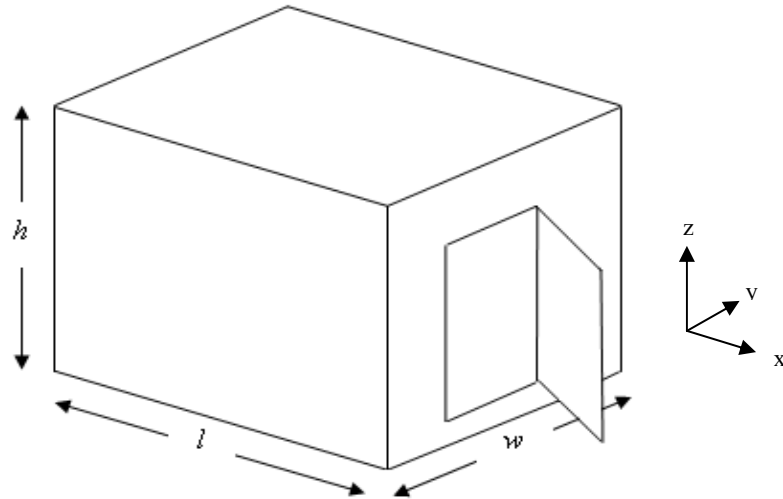


Figure 4.10: Schematic representing the screened room used to identify the orientation in which the dimensions of the room were applied to (15). The modal pattern was calculated accordingly.

The dimensions a , b and c in (15) are set according to (16) given below.

$$w = a, \quad h = b, \quad l = c \quad (16)$$

Substituting these dimensions into (15), a resonant frequency of 86 MHz is calculated for a modal distribution shown in (17).

$$m = 1, \quad n = 1, \quad p = 0 \quad (17)$$

This modal pattern that is identified, shows characteristics of a transverse magnetic (TM)₀₁₁ mode with the excitation in the x -direction. This result agrees well with what is predicted by Christopoulos and Argyri [45] for medium sized screened rooms. The difference between the calculated and measured resonant frequency predicted by (15), is because the screened room was not empty. The room is also used as a reverberation chamber, so metallic paddles are present inside; these were not rotated for any of the cable tray measurements. An indication of the modal pattern specified above and calculated in CST MWS is shown in Figure 4.11.

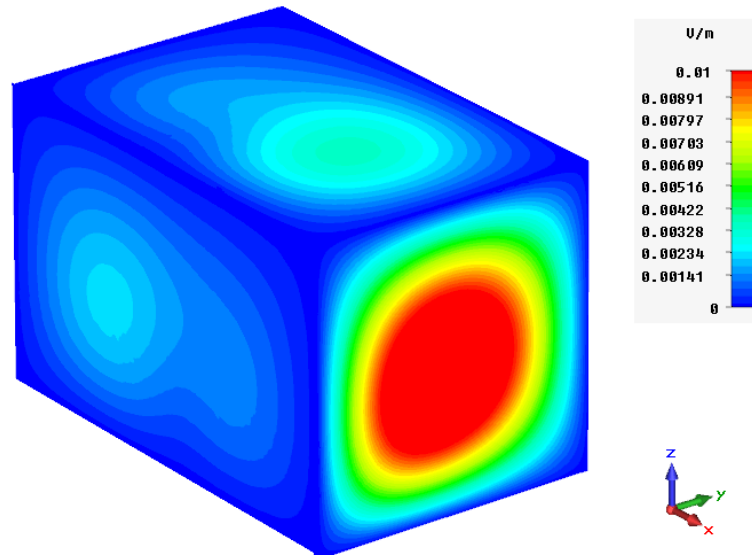


Figure 4.11: Modal distribution inside screened room at 81 MHz. The indicated volume has the same dimensions as the actual room.

The modal distribution can be identified in the zy -plane. Perturbations of the field caused by the cable tray model inside the volume are also seen on the remaining two surfaces. The resonance in the measured S_{21} , shown again in Figure 4.12, was replicated once the correct boundary definition was identified. The slight differences in the measured and computed results can be attributed to the presence of the paddles inside the enclosure.

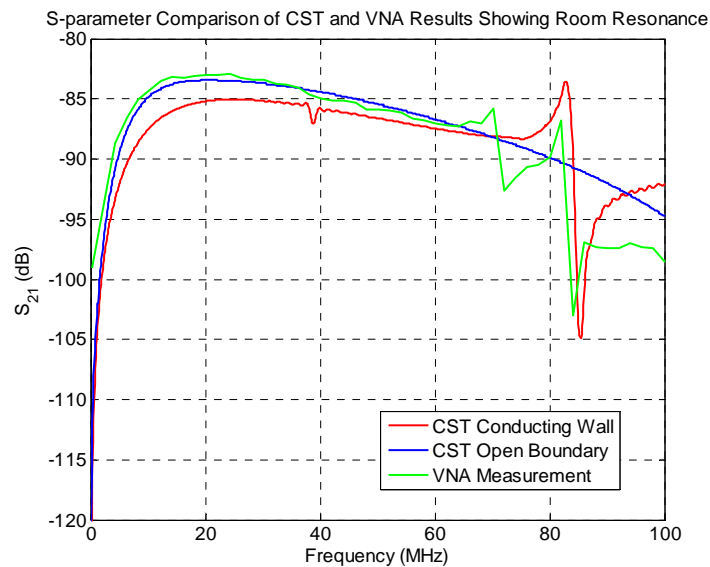


Figure 4.12: Computed and measured results compared for Model 1 cable tray measured in screened room. The room resonance was replicated in measurement up to -100 dB.

Figure 4.13 shows Model 1 in the computational domain where conducting boundaries, as discussed in Chapter 3 section 3.3.3, make up the walls and roof, and an *electric*($E_t = 0$)

boundary defines the floor. A simulation incorporating *conducting wall* definitions takes significantly longer compared to one using *open* boundary definitions, because re-reflection of energy takes place inside the computational volume. Once the accuracy of the computation was proven, the remaining simulations were all done using *open* boundaries. The comparative result showing no resonance is included in Figure 4.12. All the mid-span and end-connections were analysed using this more efficient model.

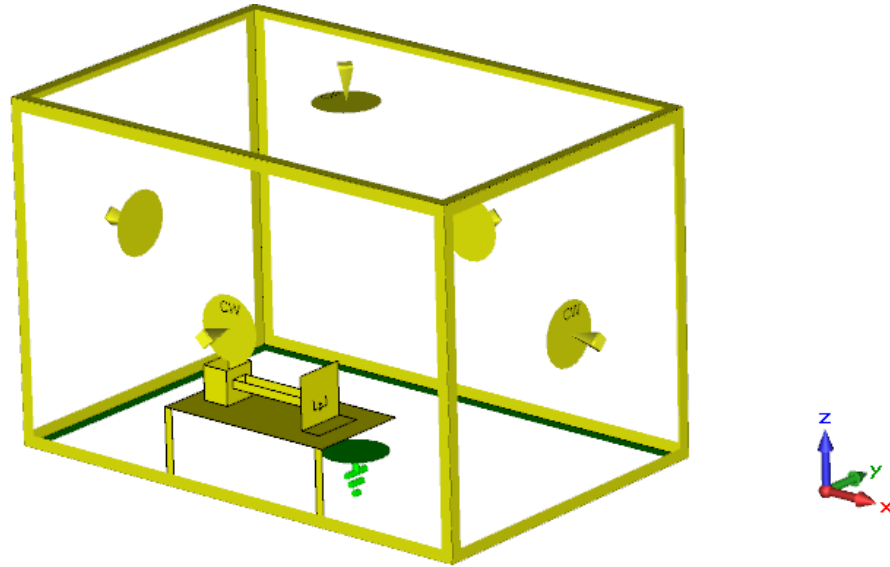


Figure 4.13: The finite computational domain showing the cable tray on top of a ground plane, which is earthed via copper straps, can be seen. Note the *conducting* boundary definitions used making up the sides and roof, with a zero potential floor.

4.3.2. Model 2

To allow comparison of results with measurements made by Ebertsohn in [12], a subsequent measurement made as part of this investigation, and a result from a CST MWS simulation of Model 2, are all shown in Figure 4.14. Notice that in Figure 4.14, the frequency range is limited to 30 MHz. This, as mentioned before, was the frequency range used for the investigations in [12]. Agreement of the results to within 5 dB can be seen. Note that a solid cable tray was used for both Model 1 and 2 in these two experiments.

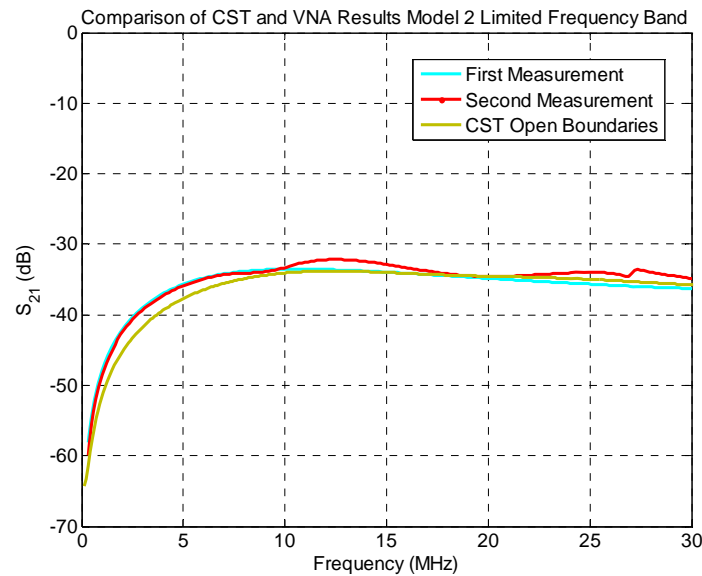


Figure 4.14: Comparison of measured and computed S_{21} values for Model 2 comparing previous measurement made as part of [12], a subsequent measurement made using the same calibrated VNA, and CST MWS simulation using open boundaries.

Achieving good agreement between computed and measured results for both models meant that subsequent changes to the models were done with confidence in the software. This is a more expedient way of analysing a large number of different configurations such as those proposed in this chapter.

4.3.3. Coupling Parameters

The computed S-parameter data that are shown should be considered as relative results, comparing the various connection schemes using a particular model. No direct comparison between results from different models should be made. A more widely-used term for evaluating the shielding ability of cable trays is Z_t . Z_t was introduced in Chapter 2 sections 2.2. It was shown how the contributions to Z_t changes depending on the system under investigation. A comprehensive study of Z_t , with the focus being cable trays, was done in [9] and by Van Deursen et al. [11]. For cable trays, the particular element of interest is the amount of mutual inductance which is calculated from Z_t . This is a direct indication of how effective a cable tray is at preventing magnetic field coupling to conductive loops inside the tray. Because of the frequencies at which the investigation is conducted, only magnetic and not electric field coupling takes place.

The Z-parameters are calculated from the measured S-parameters for each connection using (18) as given by [46].

$$Z = \frac{Z_0[I + S]}{[I - S]} \quad (18)$$

In (18) I denote the identity matrix and S the S-parameter matrix containing all four parameters. Consequently the four Z-parameters are calculated. Z_t given by (19), which is similar to (1) in Chapter 2 section 2.2, is of particular interest.

$$Z_t = Z_{21} = R + j\omega M_{21} \quad (19)$$

Z_t relates the induced differential mode voltage on the victim cable, and the effective CM current on the tray. R is the common resistance and M_{21} is indicative of the mutual inductance in the system. The mutual inductance will also be used to determine how the magnetic field is influenced by a particular connection. As part of the results both Z_t and S-parameters for the various models and connections are shown.

4.4. Computed Results: Mid-tray Connections

Using predominately CST MWS, the properties of mid-span connections are now investigated. In these experiments the end-connection to the enclosure is fully seamed, establishing the lowest possible impedance to ground for the cable tray termination. This ensures that the current path impedance is dominated by the specific mid-span connection that is considered. For each of the four mid-span connections complete galvanic contact is made between the connection and the cable tray. This is an idealisation of a bolted connection, because in reality small spaces will always be present unless soldered. The quarter-wavelength resonance of the cable tray can be identified from the Z_t results.

4.4.1. Model 1

The four mid-connections are first compared using Model 1. The high current concentration developed underneath the tray, as shown in Figure 4.15, would suggest that a continuous tray bottom is desirable to protect victim cables. This simulates a cable tray installation in which a separate safety earth is attached or placed in close proximity to the tray. Equally, the analysis can be done when the excitation conductor is placed on either side of the tray. Note that the ground

plane, while included in the simulation, is not shown in any of the field plots including Figure 4.15, for the sake of clarity.

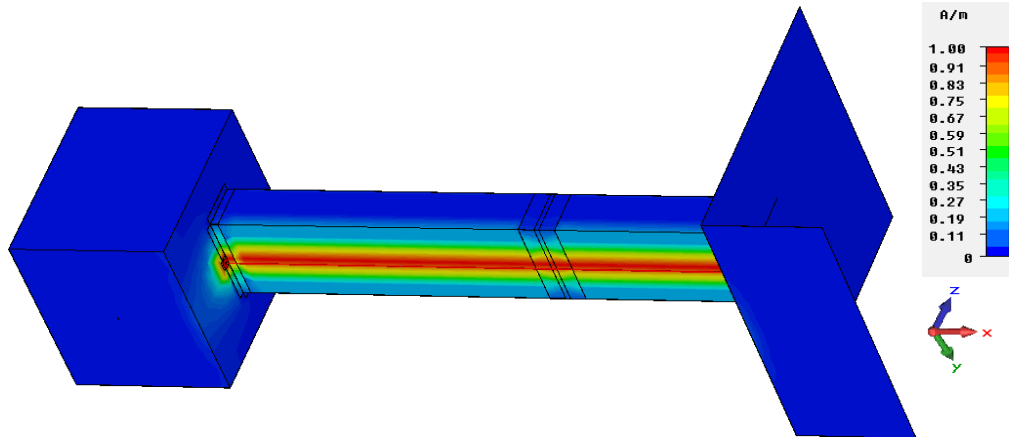


Figure 4.15: Model 1 computation of cable tray, enclosure, L-plate and mid-span connection showing peak surface current distribution at 10 MHz on the outside of the tray.

The full U-bracket connection is recommended in [9], [13]-[15], and in all cases the justification is to ensure that the conduit stay a continuous structure. The L-bracket and bottom connections are similar to the U-bracket, but without the middle-bottom section and side sections respectively, as shown in Figure 4.4. The effects of a side strap or bondwires, indicated in [13]-[15] as part of a safety earthing policy and in [9] as another method of connection, were also considered. Comparative results for the four mid-span connections for S_{21} can be seen in Figure 4.16 (a) with the calculated Z_t shown in Figure 4.16 (b). The calculated mutual inductance for this model is shown in Appendix A.

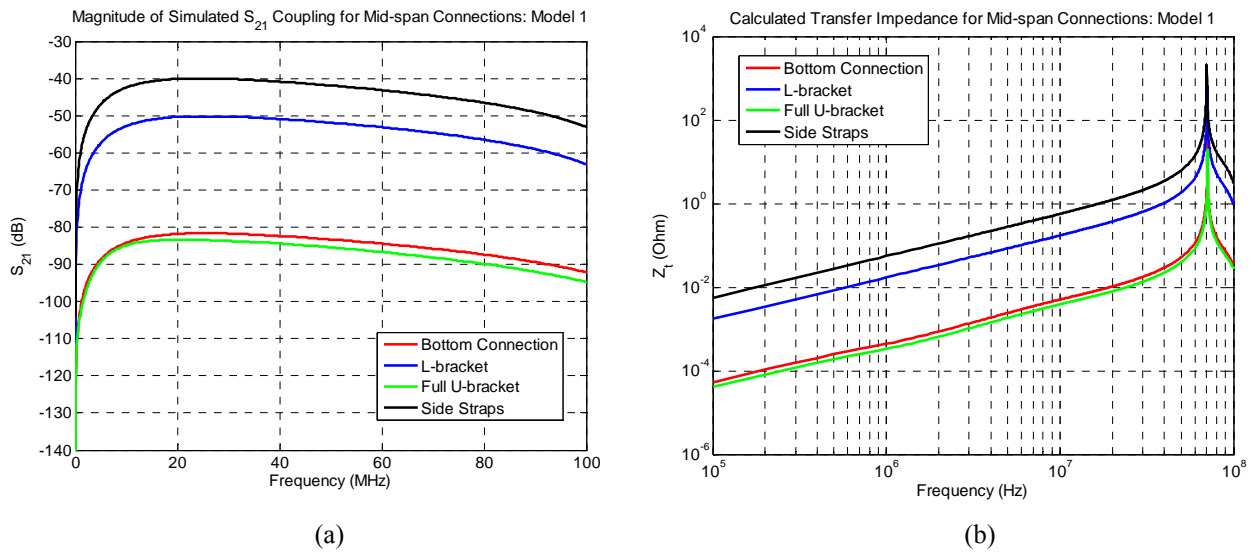


Figure 4.16: The simulated S_{21} coupling for the four mid-span connections investigated using Model 1 is shown in (a). The associated Z_t calculated using the various S-parameters are shown in (b).

The full U-bracket and single bottom connection perform the best in terms of S_{21} coupling. The L-bracket and side straps provide substantially less shielding, 30 dB and 40 dB respectively, compared to the U-bracket. These results confirm the initial expectation regarding a continuous tray bottom for this interference type, and underpin the value of understanding the CM current distribution. By removing the connection directly in the path of the induced surface current, causes it to find a low impedance alternative, and dramatically increase the amount of coupling to the inside of the tray.

The Z_t results show the U-bracket indicating the lowest Z_t and therefore allowing the least amount of magnetic field coupling to the victim conductor. Comparisons between results in Figure 4.16 (b) with calculated results for cable tray mid-span connections in [9] show good agreement in the overall levels. Despite the investigation in [9] being done over a range of 10 Hz to 100 kHz, the values at 100 kHz also vary between approximately 0.1 m Ω for a full U-bracket, to 6 m Ω for a double wire side connection.

4.4.2. Model 2

In a similar fashion, the mid-span connections are tested using Model 2. The more even distribution of surface current for this model can be seen in Figure 4.17. The current injection and distribution over the tray is comparable to situations where the tray itself is used as the safety earth. In case of a fault condition the current will travel along the tray trying to find a low impedance path to ground. However, it is interrupted by the side strap or bondwire connection in the middle of the tray, which is simulated here.

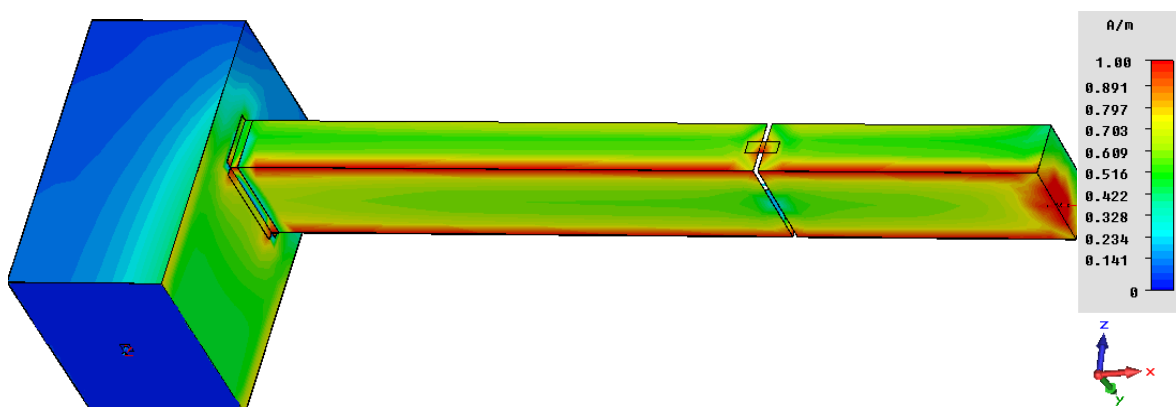


Figure 4.17: Surface current for Model 2 at 10 MHz on the outside of the cable tray and enclosure, investigating side strap connections.

A bondwire is typically part of an earthing policy. In order to cross the mid-span break, the side strap forces current to deviate more compared to a U- or L-bracket. This path change leads to both increased current leakage into the tray and interference to the victim cable. Comparative S_{21} coupling results for the different mid-span connections are shown in Figure 4.18 (a) with the calculated Z_t shown in Figure 4.18 (b).

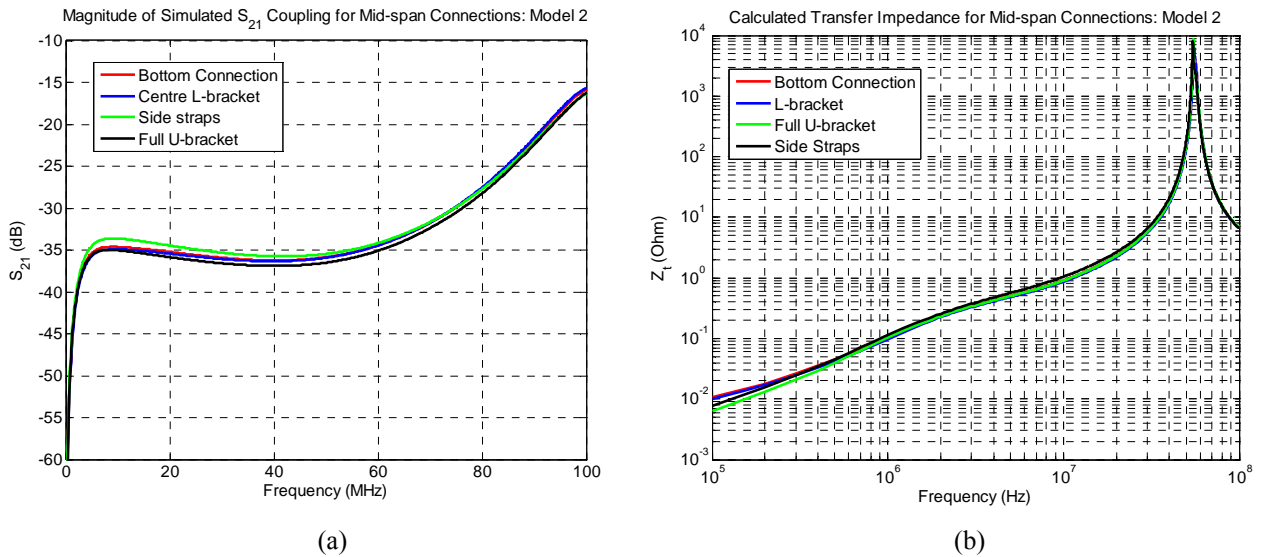


Figure 4.18: The change in S_{21} coupling associated with the four different mid-span connections simulated using Model 2 is shown in (a). The accompanying Z_t , also for Model 2, is shown in (b).

For this interference type there is a relatively small difference between any two schemes, with the side strap 3 dB worse than the best possible U-bracket connection at lower frequencies. These results, taken in isolation, could persuade practioners that any scheme would be universally acceptable. Small differences in the calculated Z_t are seen in Figure 4.18 (b). Shown in Figure 4.19 (a) and (b) is the change in the calculated mutual inductance associated with the four mid-span connections for Model 2.

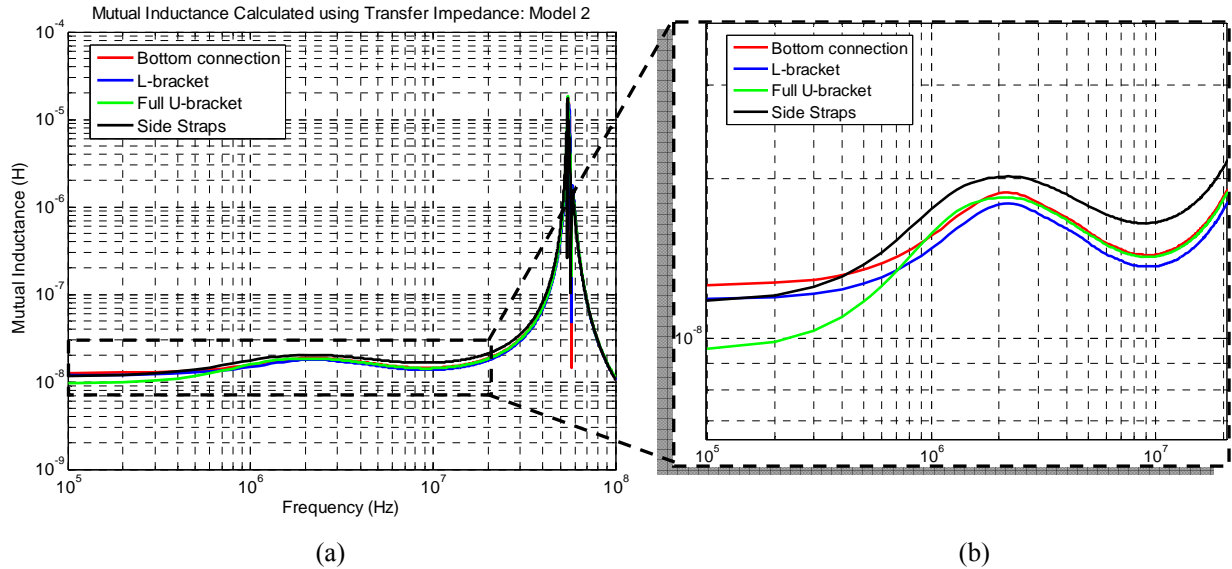


Figure 4.19: Comparison of calculated mutual inductance for the four mid-span connections using Model 2 shown in (a) with an enlarged area shown in (b).

Seen in Figure 4.19 (a) at approximately 55 MHz, is the quarter-wavelength resonance associated with the length of the cable tray and the short feed conductor injecting current onto the tray. Shown in Figure 4.19 (b) is an enlarged view of the same plot which highlights the differences in the mutual inductance of the various connections more clearly. In Figure 4.19 (b), the mutual inductance for the side strap connection increases noticeably with frequency. This is because the side straps (Figure 4.4 (d)), despite causing magnetic field to move in opposite directions in the centre of the tray, creates the least amount of bending and disruption of the field as shown in Figure 4.20 (a). Comparing this to the bottom connection (Figure 4.4 (b)), less coupling to the victim conductor takes place. With the bottom connection the field is stretched and compacted closer to the connection's surface, but there is no adjacent conductor producing opposing fields leading to field cancellation in the centre of the tray.

A natural increase with frequency in the mutual inductance associated with the full U-bracket is seen in Figure 4.19 (b). As the frequency increases the wavelength becomes shorter and the magnetic field is able to bend down onto the tray easier. The L-bracket shows the least amount of coupling because not only does it force the field to bend into the tray (Figure 4.20 (b)) similar to the U-bracket, but there is also field cancellation in the centre, similar to the side straps.

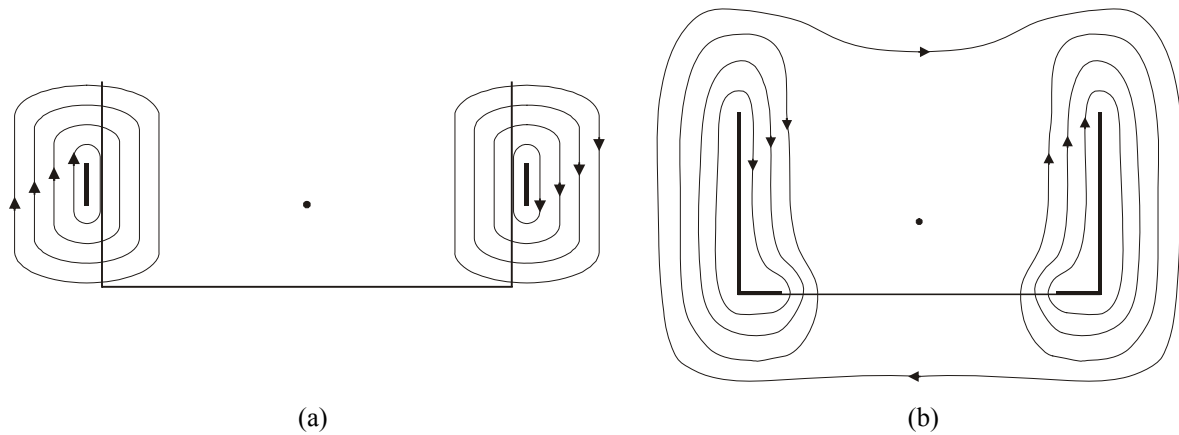


Figure 4.20: Impression of magnetic field circulating around (a) side strap connection and (b) L-bracket [47].

4.5. Computed Results: Enclosure Connections

The connections between the enclosure and ground plane, and also the ground plane and L-plate, are assumed to be ideal for both models. With this assumption, any change in the Z_t can only be attributed to different mid-span or end-connections. The various connections influence the circulation of CM current illustrated in Figure 4.5 (b) and Figure 4.7 (b). This not only changes the coupling mechanism to the victim conductor inside the tray, but increases the common resistance of the system R identified in (19). Both parameters combine to determine the overall shielding ability of the tray. To study the end-connections effectively, a tray continuous at its mid-point was used for both models.

4.5.1. Model 1

The actual implementation of two of the end-connections used in Model 1, is shown in Figure 4.21. The bolts used to fasten the connections are not replicated in the computational models. The full U-connection considered for the end-connection, is constructed from a single metal strip forming the equivalent bottom and side L-plate connection seen in Figure 4.21 (b). As previously mentioned, non-ideal construction techniques were approximated by creating a 1 mm gap between the cable tray and the enclosure in the computational model.

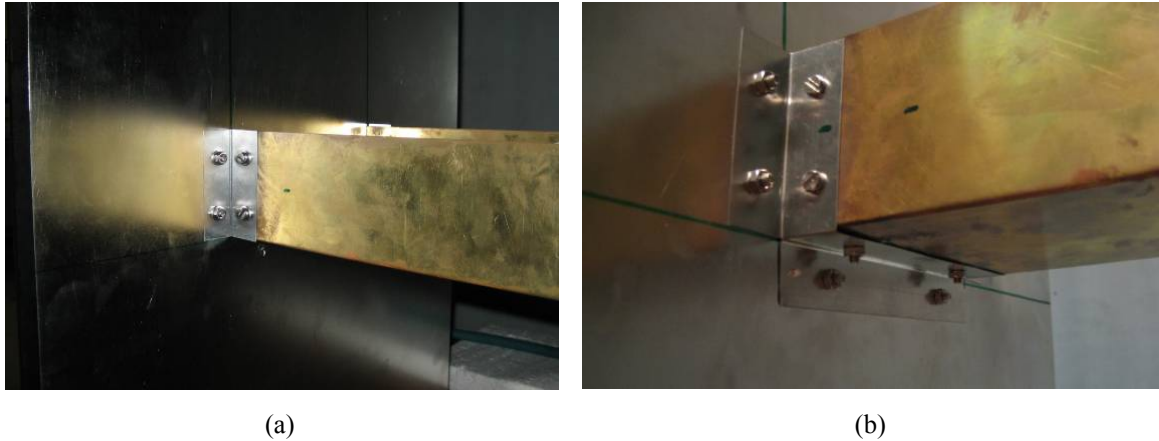


Figure 4.21: Two of the three cable tray-to-enclosure connections shown with (a) being the side only L-plates and (b) a full U-connection which consists of the continuous bottom and side L-plate connection.

In Figure 4.22 the level of surface current inside the cable tray, enclosure and on the victim cable is shown when the tray bottom is unconnected, and only side L-brackets (Figure 4.21 (a)) are used. The relatively high level of current on the inside of the enclosure is due to increased leakage caused by the poorly placed end-connection. Induced current is also just visible on the interior victim wire.

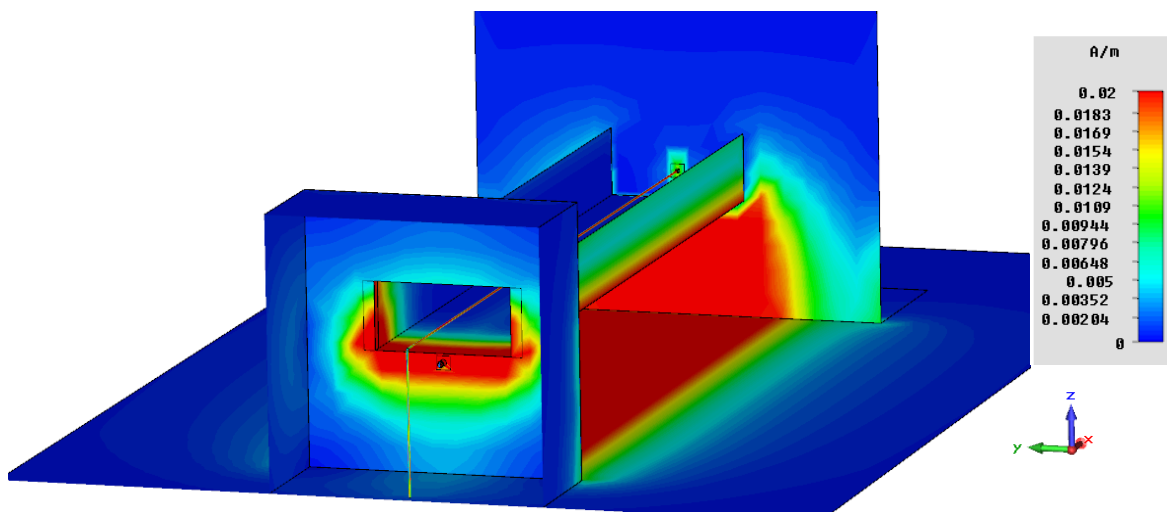


Figure 4.22: Model 1 surface current distribution on the inside of the enclosure at 10 MHz with only two L-bracket side connections made to the enclosure.

The S_{21} results shown in Figure 4.23 (a), show that when using only the bottom connection the level of coupling is comparable to a full U-connection. This is not completely surprising as most of the surface current in this model is concentrated underneath the cable tray, where the bottom connection is placed. The importance of a connection directly in the path of the highest concentration of surface current, is re-emphasised by the mid-band difference of more than

25 dB seen in Figure 4.23 (a). The comparison of calculated Z_t is shown in Figure 4.23 (b). The calculated mutual inductance is also shown in Appendix A.

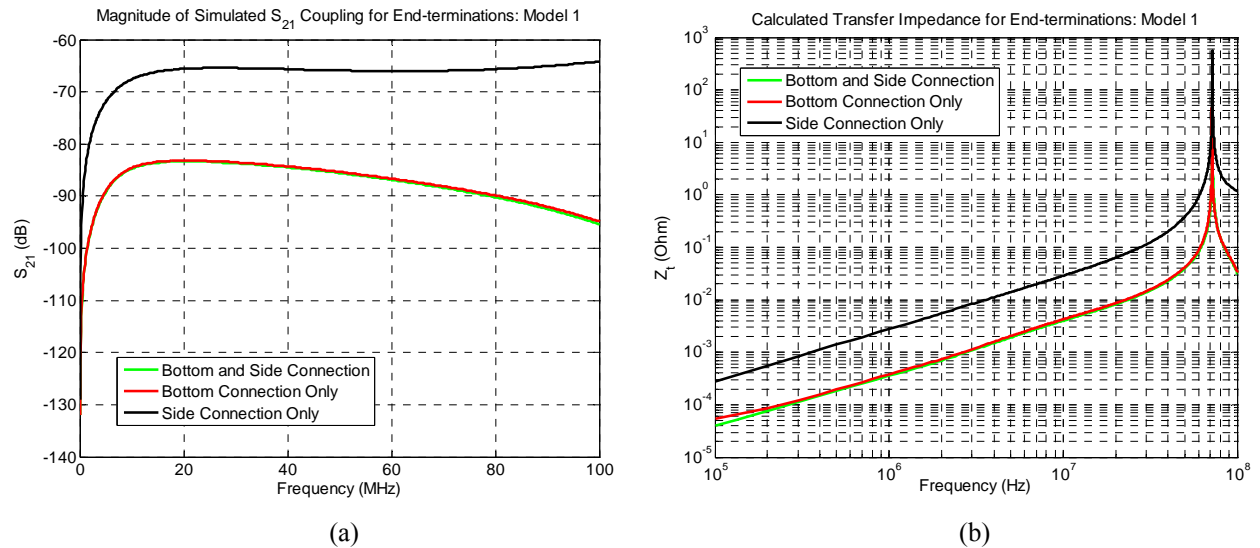


Figure 4.23: The change in S_{21} coupling associated with the three different end-connections analysed using Model 1 is shown in (a). The accompanying Z_t also for Model 1 is shown in (b).

The side straps show an appreciable increase in the Z_t as seen in Figure 4.23 (b). For this model, side straps cause a major diversion of the CM current flowing underneath the tray which consequently increases the disturbance voltage on the victim conductor. This is seen in a comparative surface current plot for a bottom and side connection shown in Figure 4.24

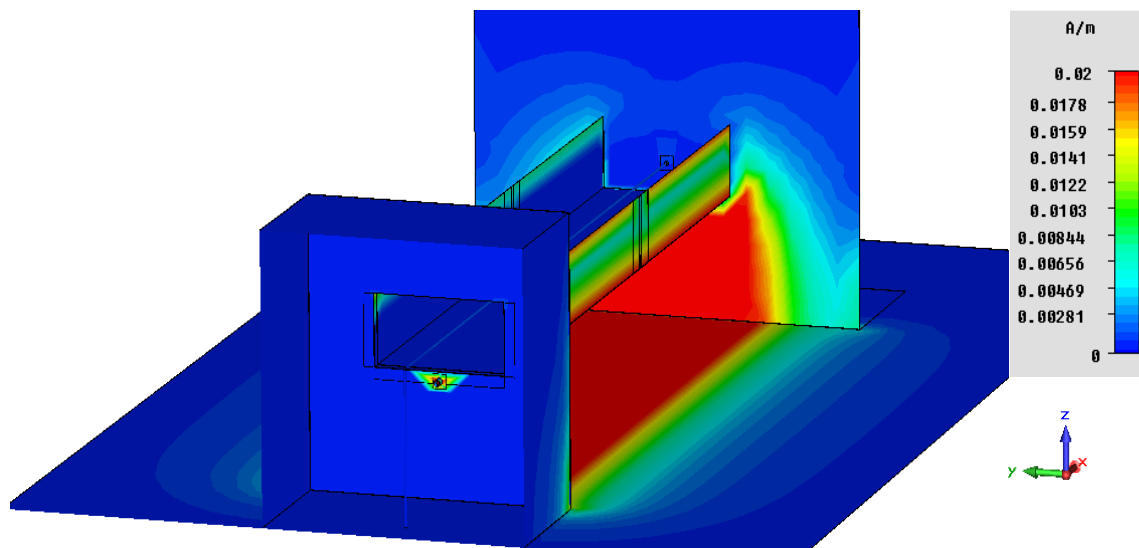


Figure 4.24: Model 1 surface current distribution at 10 MHz with bottom and side connections made to the enclosure.

4.5.2. Model 2

Figure 4.25 shows the computed peak currents at 10 MHz for a full U-connection using Model 2. This continuous connection was replicated in CST MWS by overlapping individually constructed side and bottom connections to ensure galvanic contact.

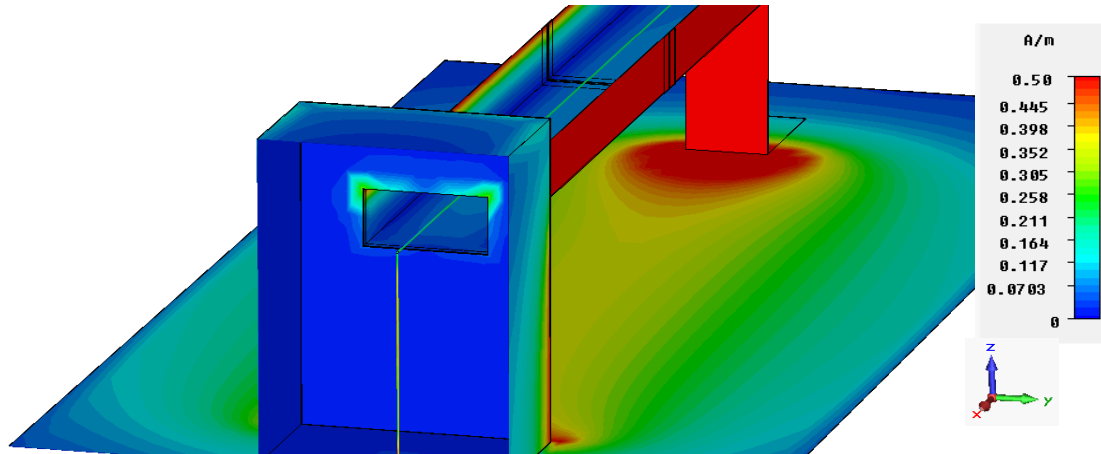


Figure 4.25: Computed peak surface currents induced at 10 MHz inside the cable tray and enclosure for Model 2.

For the other two connection schemes very similar results for Model 2 were obtained. The S_{21} coupling is shown in Figure 4.26 (a), where it is difficult to distinguish the individual traces, even in an enlarged view shown in Figure 4.26 (b). At very low frequencies the coupling is below -50 dB, and from 5 MHz to 70 MHz is below -30 dB. The same was seen for its mid-span connections. At higher frequencies, the tray length reaches quarter-wavelength proportions.

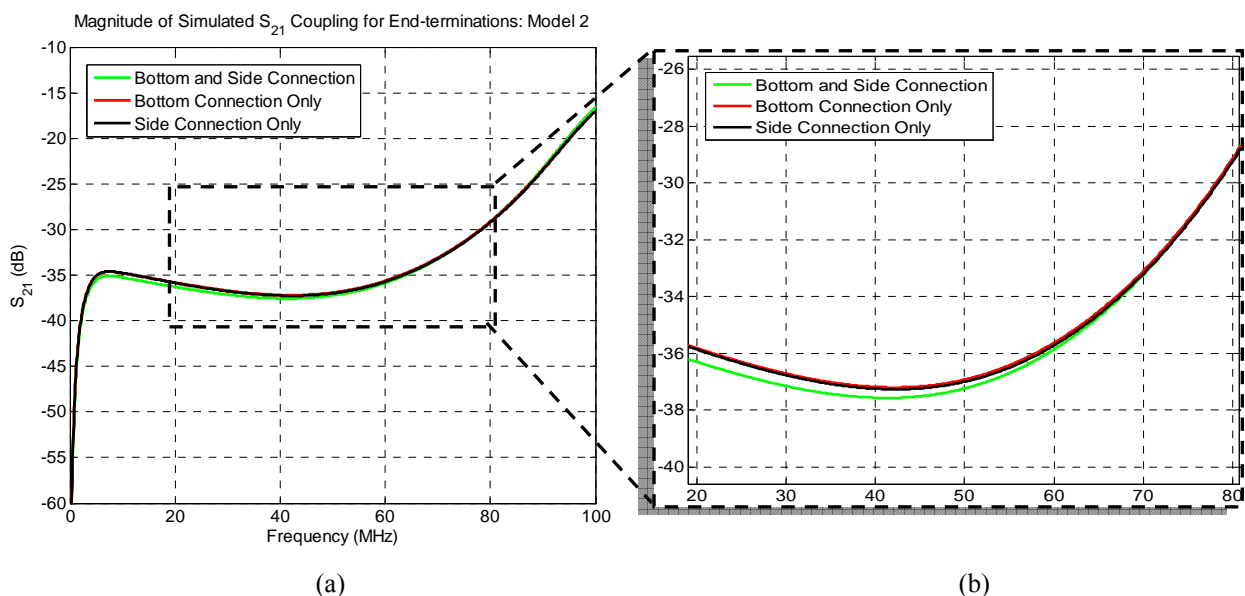


Figure 4.26: The change in S_{21} coupling associated with the three different end-connections analysed using Model 2 is shown in (a). An enlarged view of the same parameters is shown in (b).

The calculated transfer impedance (Z_t) and mutual inductance for each of the three end-termination connections for this model are compared in Figure 4.27 (a) and (b) respectively. It is difficult to distinguish between the individual traces on the plotted scale. The same small difference was noted for the mid-span connections. This can again be attributed to the even distribution of current on the tray, which ensures that none of the connections investigated caused a major increase in the mutual coupling to the victim conductor.

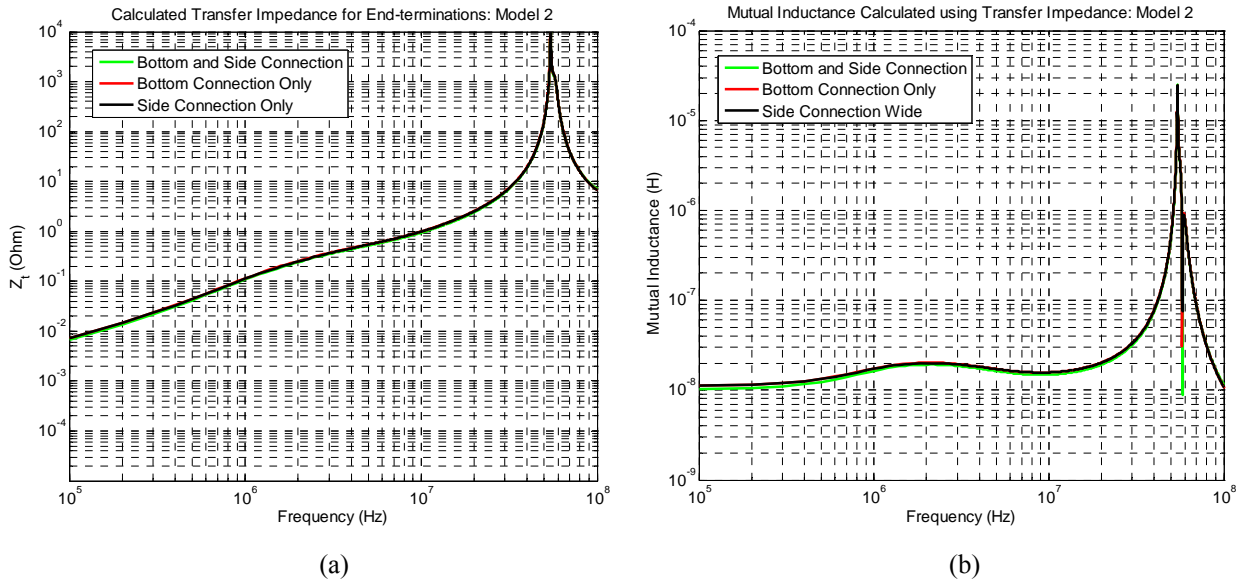


Figure 4.27: Comparison of the three end-termination connections investigated using Model 2. The Z_t is shown in (a) with the mutual inductance shown in (b).

The Z_t and therefore the mutual inductance of the bottom and side connection are fractionally lower than the other two connections. Similar as with the mid-span connections, the even distribution of CM current on the tray means no major diversion of the current when using either of the three.

4.6. B-Field Discussion

The significant differences in results for both the mid and end-connection schemes, tested on Model 1 (Figure 4.16 and Figure 4.23), compared to the modest differences for the same schemes on Model 2 (Figure 4.18 and Figure 4.27), require explanation. It is insightful here to study the magnetic fields in addition to the currents.

The magnetic field that is created by the CM currents flowing on the outside of a cable tray will cut the loop formed by the victim conductor and the inside of the cable tray. The type of

connection used will influence the shape of these fields. For a broad connection, the magnetic fields are stretched around its surface, and pulled closer in. For a narrow connection, the field extends out more circularly.

For Model 1 there is more than one current return path (Figure 4.5) as the current injected on the feeding conductor separates at the enclosure end into two paths. The resulting magnetic field cuts the victim loop in the tray. With any break in the cable tray, the victim conductor is directly exposed to the magnetic field generated by the feeding conductor underneath the tray. The bottom connection disrupts this direct coupling whereas the side connection does not. The change in both S_{21} and the Z_t is more pronounced for each connection because of the localised CM current.

With Model 2, any of the connections form a part of current loops both on the inside and outside of the cable tray. The reason for this is because the cable tray is the common conductor. Regardless of the field shape, similar amount of flux intersects the victim loop and cable tray return path for each of the various connections. This explains the small difference in the coupling between the different mid and end-connections.

In [15], Figures 44.R20 and 44.R22B shown as Figure 4.3 and Figure 4.28 could be mis-read to give conflicting advice. It would appear that in the first case a bottom connection only is not advisable, but that in the second it is acceptable. If the magnetic fields generated by the culprit conductor underneath the tray are considered, it would be clearer now that the inner victim loop should always be kept as close as possible to a broad connection if a full U-connection is not possible. The purpose of the bottom connection on the tray in Figure 4.28 is therefore to indicate its position relative to the conductor inside the tray and not to conflict the advice given in Figure 4.3.

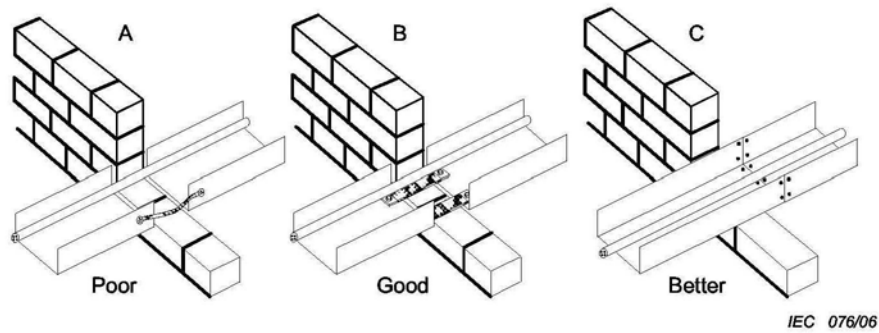


Figure 4.28: Cable tray connections as advised by [15].

4.7. CM Current Discussion

The underlying theme of this chapter has been to identify where induced CM currents flow, and what field distributions are generated around these paths. A sudden change of current direction due to a particular connection being used, leads to increased coupling. The coupling to the victim wire is related back to an induced voltage through the Z_t . A generic connection suitable for any application can now be identified.

Model 1, Figure 4.16 (a), considers induced currents that are concentrated underneath the tray. For a mid-tray connection in this case, as seen in Figure 4.16 (b) there is a substantial difference in S_{21} between the side strap and a full U-bracket. This is also reflected in the Z_t . The side straps cause a major diversion of the current path. The U-bracket, in comparison, forms an almost uninterrupted join between the two sections of cable tray. For the more uniformly induced current in Model 2, the coupling between the different schemes cannot be distinguished for the mid-connection. Here current is more easily diverted slightly to the sides, if there are only side connections, or to the bottom, if there is only a bottom connection. Similar results are shown in [9]. The best mid-span connection for any scenario would thus always be a U-bracket. Where the U-connection is not possible, a reasonable compromise would be a broad connection on the tray closest to a culprit conductor. As this is usually underneath the tray, the bottom connection would be the compromise recommendation.

For the end-connections, the most coupling to the victim cable, as shown in Figure 4.23 (a), is associated with the Model 1 side L-brackets with no bottom connection, seen in Figure 4.21 (a). The increase is greater than 25 dB, virtually across the entire frequency band. The absence of a bottom connection is thus undesirable for this case when a PEC is underneath the cable tray. The

best performance here is obtained from the bottom and side connection, or the bottom only connection, because there is no significant current path change.

For the Model 2 setup it can be seen from Figure 4.18 (a) and Figure 4.19 (a) and (b) that the coupling stays relatively constant regardless of the connection. The same argument for the mid-span current distribution is applicable to the end-connection. The even distribution of the induced current over the surface of the tray is the definitive factor. The best interface between the cable tray and enclosure would then also be a full U-bracket. This continues the shape of the cable tray across the interface and for safety earthing provides the lowest current impedance across the investigated band

In [14], there are several indications of slits in cable trays that are not recommended. With the current and magnetic field arguments that are presented, it is now easier to evaluate the recommendations given in [14]. Firstly, current diversion due to badly positioned connections or slits is always undesirable. This occurs if the slits are placed directly in the path of induced currents. Secondly, slits in the corners of a cable tray are not recommended as they are considered to increase the magnetic field coupling to the victim conductor. For these corner slits, some magnetic field also circulate around the floor of the tray, becoming more like a bottom centre connection, and not fully around its complete U-shape. However, from the results in Figure 4.16 (b) only a marginal increase in Z_t of the bottom connection over the full U-bracket is seen for Model 1. For the more uniformly-distributed current of Model 2, almost no difference between these two centre connections is seen in Figure 4.18 (b). From a current perspective, the exterior current only deviates slightly to flow around the corner slit. This does not imply that as a consequence slits in the corners of cable trays be allowed, but rather that the increase in Z_t when they are present, is modest

Our investigations considered one set of centre connections which can be related to a single pair of slits only. The results therefore, do not apply to a cable tray with multiple slits along its length. This would be akin to a meshed cable tray which requires a completely separate investigation.

4.8. Conclusion

EMI shielding provided by a cable tray extends further than the tray itself. To analyse a cable tray installation, two models were defined with different CM current distributions. The enclosure and mid-tray connection schemes were analysed experimentally and computationally with good correlation over a large dynamic range. The effect of the schemes on current distributions, B-fields and EMI shielding up to 100 MHz were presented. A full U-shaped connection of the tray to enclosures, or to the next tray, is always best.

Model 1 also considered a concentrated current distribution and how certain connections do not provide adequate diversion of the CM currents. The compromise choice, if the U-bracket is not possible, is a broad connection on the same side as the culprit conductor. If this positioning is unknown, the bottom connection should be chosen. Finally, any galvanic connection for both the mid and end-connection schemes is better than none. If a cable tray is not bonded, its EMI protection properties are completely lost.

Chapter 5

High Frequency Cable Tray Analysis

5.1. Introduction

This chapter continues the investigation into the usage of cable trays for electromagnetic interference (EMI) mitigation. The shielding ability of a cable tray with an added enclosure at frequencies where the wavelength of the disturbance field is similar, or even smaller than the width of the tray, is determined. This is a progression from the analysis of cable tray connections presented in Chapter 4. This work is also considered to be an addition to a similar study presented by Kaporas as part of [18], where the focus was on evaluating the penetration of high frequency interference, radiated by a known gain antenna, into a fixed height-to-width ratio cable tray. In [18] both induced voltage and current on different victim conductors positioned throughout the tray, were evaluated. This formed the basis of a discussion regarding the protection offered by open metal conduits at higher frequencies.

Cable tray installations are likely to be exposed to both low and high frequency interference. It is advantageous to evaluate their performance at higher frequencies, because their shielding ability at frequencies where the wavelength is much longer than the length of the tray is already well documented, [8]-[12] and Haigh and Hardwick [48]. The newly defined cable tray model of Chapter 4, Model 1 Figure 4.1 (a), was used again for this investigation. With the cable tray being terminated at an enclosure, the investigation includes the effects of having the enclosure open or closed.

The highest frequency under consideration was increased from 100 MHz, used in Chapter 4, to 6000 MHz. The lowest frequency was also increased from 100 kHz to 300 MHz. To investigate the performance at increased frequencies, a new method was needed to establish a fairly consistent electromagnetic field around the cable tray which will intersect the victim loop inside the tray. The most effective wideband method to induce common mode (CM) current on the cable tray and victim conductor was to make use of plane wave illumination from a known gain

antenna. The angle of incidence of the plane wave onto the model is varied from 0° to 90° in three discrete increments as shown in Figure 5.1.

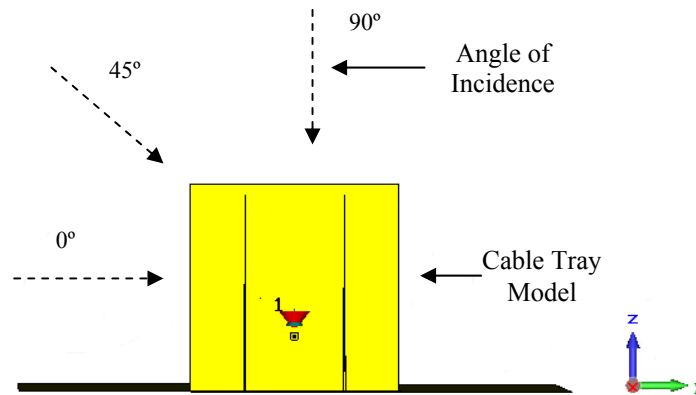


Figure 5.1: Cable tray Model 1 viewed end-on, indicating the different angles of incidence to identify the change in cable tray shielding.

The calculation of both the cable tray's gain function using the Friis transmission equation, as well as the voltage induced on the victim conductor, is presented. Both are calculated from S_{21} measurements for each angle of incidence as a function of frequency. With an increase in the incidence angle, a decrease of both the gain function and induced voltage are expected. The results for each angle are verified by using CST MWS as a method of computational analysis. In the computation a plane wave excitation, illuminating the model at the same angles of incidence as used in the measurements, induced similar voltages on the victim conductor. The process of comparing the calculated and computed voltages is described. The verification of the calculated gain functions using a dedicated far field monitor available in CST MWS is also discussed.

Initial measurements were made using a 2 GHz to 18 GHz horn antenna which was operated down to 1 GHz. Subsequent measurements using a Log Periodic Dipole Antenna (LPDA) functioning over the specified band was used. During the measurements a number of antennas were required to calculate the gain of the primary antenna. The process of determining each antenna's gain uniquely is shown. Minimising reflective interference from the environment around the device under test (DUT) required the use of either an open area test site (OATS) or anechoic chamber. Both were considered, however, the final results that are presented were conducted in the fully anechoic chamber. The layout of the measuring equipment inside the chamber required the law of reciprocity as described by Coren in [49] to be applied. This resulted in the victim conductor inside the cable tray being excited, with the antenna used as the

receiver to measure the response. The application of this law to the measurement setup is discussed.

5.2. Gain Calculations

Figure 5.2 shows a representation of a measurement setup where a DUT is connected to a vector network analyser (VNA). For this setup using a calibrated VNA, all four S-parameters of the DUT can be measured. Using the definition of S-parameters in terms of voltage, discussed in Chapter 2 section 2.7, the level increase of the applied voltage at port one as affected by the DUT is indicated in the forward transmission parameter S_{21} . This level or ratio is determined through the comparison of the received voltage at port two and the applied voltage at port one. Also mentioned in Chapter 2 section 2.7 is how the measured ratio can be defined in terms of power.

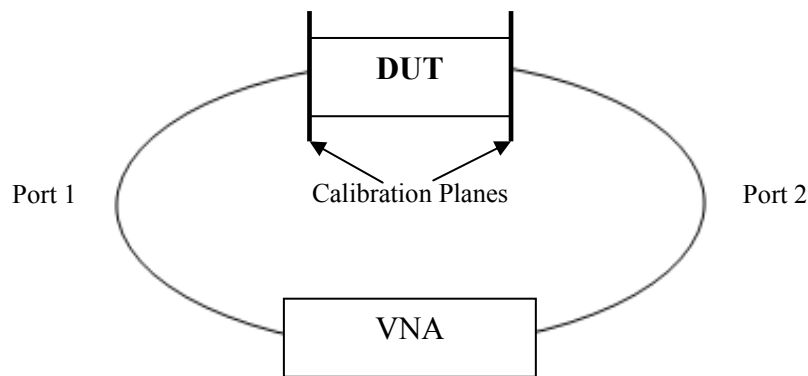


Figure 5.2: Two-port measurement setup.

For the investigations in Chapter 4, the DUT in Figure 5.2 was substituted by the cable tray models defined in that chapter. Port one of the VNA applied a voltage to the cable tray model which created current flowing on the cable tray. This current flow created a magnetic field circulating around the tray, which induced current on a victim conductor inside the tray. The current flowing on the victim conductor was measured as a potential difference across the input impedance of port two of the VNA. The ability of the cable tray to prevent the magnetic field from inducing current on the victim conductor was directly reflected in the measured S_{21} voltage ratio. As previously stated this S_{21} voltage ratio effectively indicated the gain of the cable tray for each connection discussed in Chapter 4 sections 4.4 and 4.5.

In this chapter a method of illumination using an antenna (schematic representation in Figure 5.3) establishes an electromagnetic field around the cable tray.

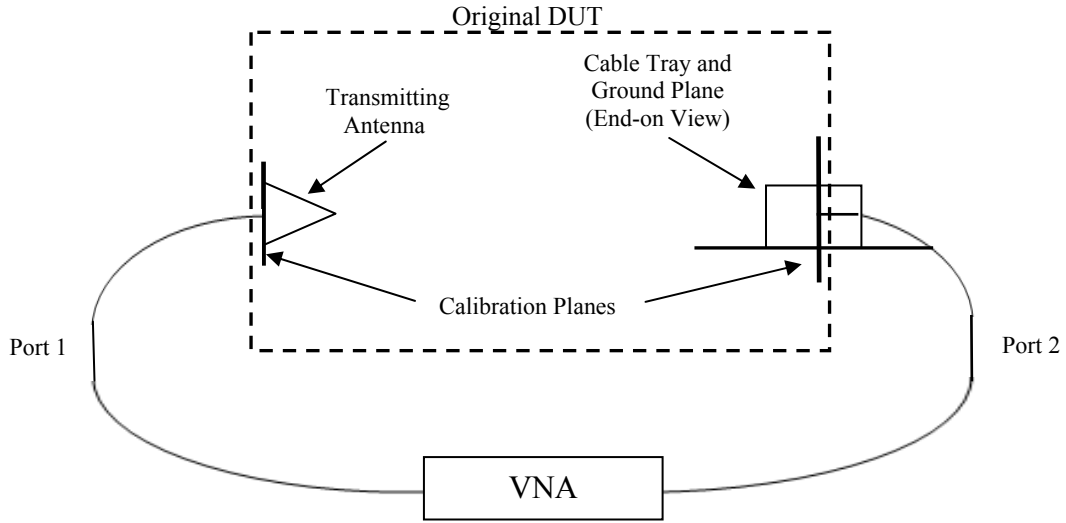


Figure 5.3: Measurement setup for cable tray illumination measurements.

The dotted area in the schematic encompasses everything which replaces the DUT in Figure 5.2. The radiated electromagnetic field from the antenna still induces current on the victim conductor inside the tray. This current is again measured by port two of the VNA as a potential difference across the port's input impedance. The S_{21} , however, can no longer be used directly as an indication of the cable tray's gain function. For the calibrated system, where the calibration planes are indicated, the gain of the transmitting antenna, free space loss, and reflection losses of both the antenna and cable tray have to be taken into account.

The gain of an antenna is defined by Pozar in [46] and given below:

$$G = e_{rad} D \quad (20)$$

In (20) D is called the directivity and e_{rad} called the radiation efficiency of the antenna. The radiation efficiency given by [46] is defined as follows:

$$e_{rad} = \frac{P_{rad}}{P_{in}} = \frac{P_{in} - P_{loss}}{P_{in}} = 1 - \frac{P_{loss}}{P_{in}} \quad (21)$$

In (21) P_{loss} is the power lost in the antenna and P_{in} the power delivered to the antenna. This highlights the gain definition in terms of power. As a consequence of this, to calculate the gain of the cable tray and enclosure in the setup shown in Figure 5.3, the measured S_{21} is best thought of in terms of power. The ratio then compares the power delivered to port two, and the available

power at port one of the VNA. This ratio is calculated for each angle of incidence shown in Figure 5.1.

Before the conversion of S_{21} from a voltage to a power ratio is discussed, it is valuable to identify how the gain of the cable tray is calculated, and how the transmission parameter enters the calculation. The Friis transmission equation given by [46], and shown in (22), is used to calculate the far field gain of the cable tray when using a known gain antenna to illuminate it.

$$\frac{P_{ava-in}}{P_{delv-out}} = \frac{G_{transmit} G_{receive} \lambda^2}{(4\pi R_{receive-transmit})^2} \quad (22)$$

This expression relates the available power from the receiving antenna (P_{ava-in}) and the power delivered by the source ($P_{delv-out}$), antenna gains ($G_{transmit}$, $G_{receive}$), range ($R_{receive-transmit}$) and frequency, and is used for all wireless systems such as the one shown in Figure 5.4. Pozar in [46] assumes that the losses of both antennas are accounted for by their relevant antenna gains rather than their directivity as indicated in (21). From (22) it is seen that either the individual power levels, or the power ratio $P_{ava-in}/P_{delv-out}$, are required to calculate the gain of either the receiving or transmitting device.

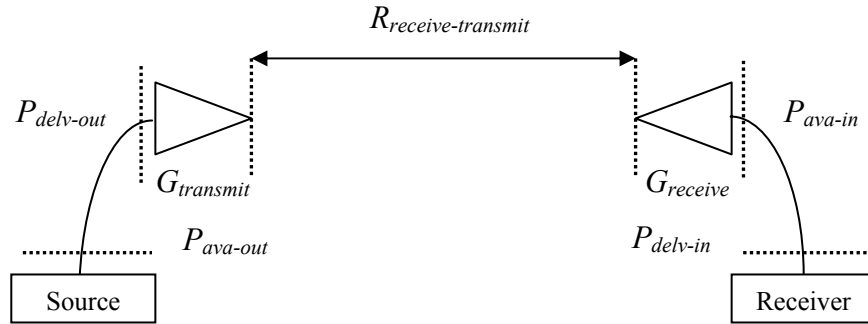


Figure 5.4: Basic transmit-and-receive system.

Regardless of whether the ratio or individual power levels are used, (22) has to be defined in terms of the power available from the source ($P_{ava-out}$), and the power delivered to the receiver ($P_{delv-in}$). This can be achieved by taking into account the impedance mismatches at both the transmitting and receiving sides in the following manner. Both (23) and (24) ignore the coupling between the two antennas.

$$P_{delv-out} = P_{ava-out} (1 - |S_{11}|^2) \quad (23)$$

$$P_{ava-in} = \frac{P_{delv-in}}{(1 - |S_{22}|^2)} \quad (24)$$

In (23) and (24) S_{11} and S_{22} refer to the input reflection coefficients of the transmitting and receiving devices respectively. (23) describes the power delivered to the transmitting antenna being less than the available power from the source on account of the S_{11} mismatch written as a power coefficient. Similarly, (24) shows that the power delivered to the receiver is less than the power available from the antenna, again due to the power equivalent S_{22} coefficient. Substituting (23) and (24) into (22) gives the following expression which incorporates the reflection coefficients of both the transmitting and receiving devices:

$$\frac{P_{delv-in}}{P_{ava-out} (1 - |S_{11}|^2)(1 - |S_{22}|^2)} = \frac{G_{transmit} G_{receive} \lambda^2}{(4\pi R_{receive-transmit})^2} \quad (25)$$

When using a separate source and receiver, the power delivered to the receiver as well as the power available from the source as indicated in (25), are known and measurable respectively. When using a VNA as shown in Figure 5.3, the exact power levels for the frequencies under consideration are no longer known. Instead, as mentioned before, the VNA measures a voltage ratio in the form of S_{21} . Therefore, if the source and receiver in Figure 5.4 are replaced with a VNA, the ratio $P_{delv-in}/P_{ava-out}$ can be re-written in terms of voltage as follows:

$$a_j = \frac{V_j^+}{\sqrt{Z_0}} \quad b_i = \frac{V_i^-}{\sqrt{Z_0}} \quad (26)$$

$$\frac{P_{delv-in}}{P_{ava-out}} = \left(\left| \frac{b_2}{a_1} \right| \right)_{Z_0=50\Omega}^2 = \left(\left| \frac{V_2^-}{V_1^+} \right| \right)^2 = |S_{21measured}|^2 \quad (27)$$

It is firstly done in terms of the square roots of the incident and reflected powers at the two ports given in general by (26). In (27) $P_{delv-in}$ and $P_{ava-out}$ are written in terms of the power measured by the receiver and the power available from the source. Next, the definitions of the voltage waves are used to express the power ratio in terms of voltage. This can then be related to the S_{21} as measured by a VNA. The power and voltage ratio of (27) assumes that the system as a whole has a 50Ω characteristic impedance. By substituting (27) into (25), and replacing the receive antenna with the cable tray, the following is obtained:

$$\frac{|S_{21measured}|^2}{(1 - |S_{11}|^2)(1 - |S_{22}|^2)} = \frac{G_{transmit\ antenna} G_{cabletray} \lambda^2}{(4\pi R_{cabletray-antenna})^2} \quad (28)$$

This is the fundamental equation used to calculate not only the gain function of the cable tray and enclosure, but also the gain functions of the various antennas used to illuminate the cable tray. The particular gain function which is being calculated, is defined in (28) in terms of the S-parameters measured directly for a calibrated system similar to the setup shown in Figure 5.3. From the above explanation it becomes clear that the gain function calculated in (28) is defined as a power ratio which is presented on a logarithmic scale using (29):

$$G = 10 \log_{10} \frac{P_2}{P_1} \text{ dBW} \quad (29)$$

5.3. Induced Voltage Calculation

Consider the measurement arrangement shown in Figure 5.3. To obtain the induced voltage on the victim conductor inside the cable tray, the S_{21} parameter measured by the VNA is needed. A simplified expression for S-parameters from the definitions given in Chapter 2 section 2.7 is given again:

$$S_{ij} = \left. \frac{V_i^-}{V_j^+} \right|_{V_k^+ = 0 \text{ for } k \neq j} \quad (30)$$

In (30) V_j^+ is the incident voltage applied by the VNA at port j , and V_i^- the transmitted voltage measured by the VNA at port i . If it is assumed that $V_j^+ = 1 \angle 0^\circ \text{ V}$ for all frequencies, the measured S-parameter $S_{ij \text{ measured}}$. $1 \angle 0^\circ = V_i^-$, effectively gives the voltage measured at port i by the VNA. However, $S_{ij \text{ measured}}$ has to be compensated for the reflection loss of the cable tray victim conductor to which port two of the VNA connects, in order to find the actual voltage on the conductor. The correction is done by making use of the power ratio concept used up to this point. Making use of (27), the incident voltage is replaced with the $1 \angle 0^\circ \text{ V}$ quantity defined above, which is also reflected in the power ratio.

$$\frac{P_{delv-in}}{1} = \frac{|b_2|^2}{1} = \frac{|V_2^-|^2}{1} = |S_{21 \text{ measured}}|^2 \quad (31)$$

The power delivered to the receiver in (31) is replace with the power available from the receiving device, which in this case is the cable tray, using (24).

$$\frac{(1 - |S_{22}|^2)P_{ava-in}}{1} = \frac{|V_2^-|^2}{1} = |S_{21measured}|^2 \quad (32)$$

Using (32) and incorporating the input reflection coefficient of the victim conductor S_{22} , the associated available voltage on the conductor is obtainable from the square root of the compensated S_{21} measurement.

$$\frac{P_{ava-in}}{1} = \frac{|V_2^-|^2}{(1 - |S_{22}|^2)} = \frac{|S_{21measured}|^2}{(1 - |S_{22}|^2)} \quad (33)$$

The adjustment of the measured S_{21} shown in (33) has to be made regardless of the receiving device used. Similar comparisons of induced voltages are described in [18]. The linear voltages, calculated from measurements and computed using CST MWS, are presented in dBV format and defined using (34) below.

$$V_{cabletray} := 20 \log_{10} \frac{|V_{cabletray}| \text{ in Volt}}{1 \text{ Volt}} \text{ dBV} \quad (34)$$

5.4. Antenna Calibration

From (28) it is clear that the gain function of the transmitting antenna is required for the frequency range being investigated. This meant that for initial experiments the gain function of a 2 to 18 GHz horn antenna had to be determined over a limited frequency band. The final experiments were conducted with a LPDA covering the entire band. Each antenna had to be calibrated and, in order to uniquely define its gain function, two additional antennas were required. This is the well-known three-antenna method. For the purpose of this calculation, three antennas namely *ant1*, *ant2* and *ant3* are defined. Using all three antennas (28) can be modified by defining a new variable which represents the compensated S_{21} measurement as shown in (35).

$$A_{ant1-ant2} := \frac{|S_{21ant1-ant2}|^2}{(1 - |S_{11}|^2)(1 - |S_{22}|^2)} \quad (35)$$

$$G_{ant1} = \frac{A_{ant1-ant2} (4\pi R_{ant1-ant2})^2}{\lambda^2 G_{ant2}} \quad (36)$$

$$G_{ant1} = \frac{A_{ant1-ant3} (4\pi R_{ant1-ant3})^2}{\lambda^2 G_{ant3}} \quad (37)$$

$$G_{ant2} = \frac{A_{ant2-ant3} (4\pi R_{ant2-ant3})^2}{\lambda^2 G_{ant3}} \quad (38)$$

Equation (36), (37) and (38) are obtained by combining (28) and (35) and re-writing the resulting equation to obtain the gain of a particular antenna. Next (36), (37) and (38), which provides three equations containing three unknowns, are combined by a method of substitution (refer to Appendix B) to obtain the following equation:

$$G_{ant3} = \sqrt{\frac{A_{ant2-ant3} A_{ant1-ant3} (4\pi R_{ant2-ant3} R_{ant1-ant3})^2}{A_{ant1-ant2} (\lambda R_{ant1-ant2})^2}} \quad (39)$$

The equation shown in (39) allows the unique calculation of the gain of *ant3*. To calculate the gains of *ant1* and *ant2*, (39) is substituted into (37) and (38) respectively. Through a similar method, except for replacing one antenna with the cable tray model, the gain of the cable tray can also be calculated using (41). A similar variable describing the compensated S_{21} measurements of the cable tray is defined in (40) and again substituted into (28).

$$A_{ant-cabletray} := \frac{|S_{21ant-cabletray}|^2}{(1 - |S_{11ant}|^2)(1 - |S_{22cabletray}|^2)} \quad (40)$$

$$G_{cabletray} = \frac{A_{ant-cabletray} (4\pi R_{ant-cabletray})^2}{\lambda^2 G_{ant}} \quad (41)$$

The cable tray model is treated as an unknown antenna. As shown in (40), the reflection coefficient of the cable tray, similar to that of the radiating antenna, is needed to account for the tray's reflection loss. This was measured separately.

When conducting radiated measurements, the DUT could be susceptible to ambient interference. Another possible source of interference is multi-path reflections from the environment. The impact that both the ambient interference and multi-path reflections have on the measured results is determined by the measurement environment. For this reason it is better to define this environment as precisely as possible. Two commonly used options for conducting radiated measurements of any kind are either an OATS or an anechoic chamber. Each have their advantages and disadvantages, and one will be more suited to certain measurements than the other. Results from measurements conducted using both will be presented later in the chapter.

5.5. Computational Equivalent Calculations

Two techniques were used in CST MWS to replicate the illumination measurements discussed in section 5.2. The first calculates the far field gain function of the cable tray model when the victim conductor inside the cable tray is excited. The second makes use of the plane wave excitation, available as part of the time-domain-based transient solver, to illuminate the model and induce a voltage on the victim conductor.

5.5.1. Far Field Gain

The first technique analyses the Model 1 cable tray and enclosure over the specified frequency range by making use of CST MWS's ability to calculate the far field gain of a radiating device. This is achieved by making use of a dedicated far field monitor defined for a particular frequency. As indicated in [21], this calculation can yield the far E-field transversal components, theta and phi (Figure 5.8). A visualisation of the far field calculation at a particular frequency for the computational model is shown in Figure 5.5.

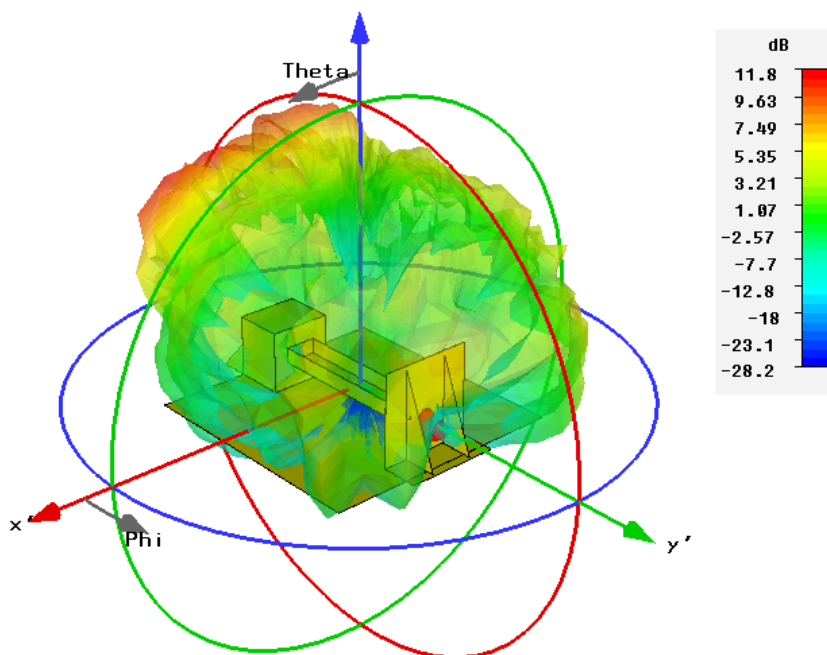


Figure 5.5: Cable tray far field gain calculated at 4005 MHz.

With the template-based post processing available in CST MWS it was possible to calculate the broadband gain for particular values of theta and phi. By specifying these coordinates the gain that corresponded to a particular angle of incidence was obtained. From Figure 5.5 it was

important to set the phase centre to correspond to the victim conductor inside the tray. The computed gain using the computational analysis is compared absolutely with the gain calculated from measured results using (41). This is presented later in the chapter.

5.5.2. Plane Wave Illumination

CST MWS can simulate an incident wave onto a DUT from a source located a long distance away. The user not only specifies the value of the E-field vector, but also its polarisation as discussed in [21]. The propagation normal is defined in terms of global xyz -coordinates and so allows any angle of incidence to be created. Figure 5.6 shows how this is implemented in the computational analysis for the simulation of Model 1, where a particular angle was defined.

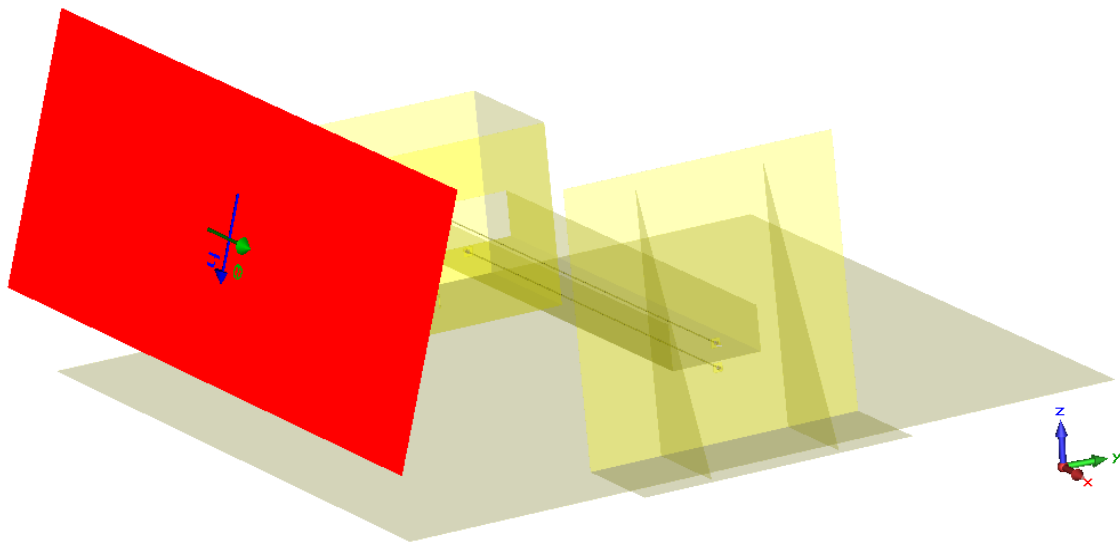


Figure 5.6: Computational environment showing the cable tray model and plane wave excitation.

Because the user specifies the excitation of E-field in V/m, S-parameters are undefined for this simulation. Instead, the induced voltage on the victim wire inside the cable tray is measured directly as shown in Figure 5.7. A voltage monitor is defined along a curve drawn between the centre and outer conductor of the Sub-Miniature version A (SMA) connector. In the simulation the victim conductor inside the cable tray is connected to the centre conductor of this SMA connector. The voltage monitor integrates the change in E-field along the defined curve to produce a voltage output as a function of frequency. The consequence is that a different voltage is produced as an output for each simulation in which the angle of incidence is changed.

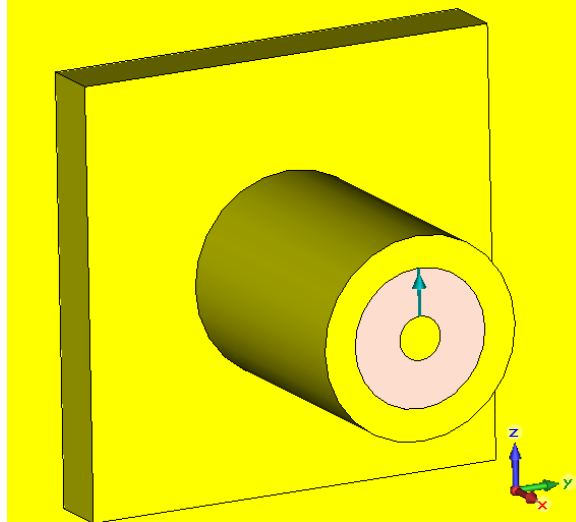


Figure 5.7: Close-up view of voltage monitor included at SMA port to measure the induced voltage with frequency.

Before the computed and calculated voltages induced on the victim conductor could be compared, a correction factor had to be calculated. This correction factor was applied to the computed results to accommodate the fact that the user-defined E-field vector in the computation remains constant for all frequencies. The E-field radiated by the transmitting antenna in the actual measurement varies with frequency. This means that the voltage on the victim conductor, calculated from the measured S_{21} , has the effect of the radiating antenna and free space loss already incorporated. This is not the case for the voltage in the computational analysis. The process involved comparing the actual E-field radiated by the antenna and the computational E-field specified in the simulation. The difference between them provided the correction factor which specifies a value at each frequency point with which the computed results have to be adjusted. This correction effectively standardises the radiated E-field from the antenna and plane wave, but does not remove influences caused by differences between the actual and computational models. It also does not remove possible reflections from the measurement environment. Correlation between the results is therefore still dependent on the accuracy of the computational model.

The propagating E-field from the transmitting antenna in Figure 5.3 has an associated H-field. For the transverse electromagnetic (TEM) wave this H-field, in the far field, is described in [46] as follows:

$$H_{\phi} = \frac{E_{\theta}}{\eta_0} \quad (42)$$

The propagation vector is indicated in Figure 5.8 and $\eta_0 = 377 \, \Omega$ is the free space wave impedance.

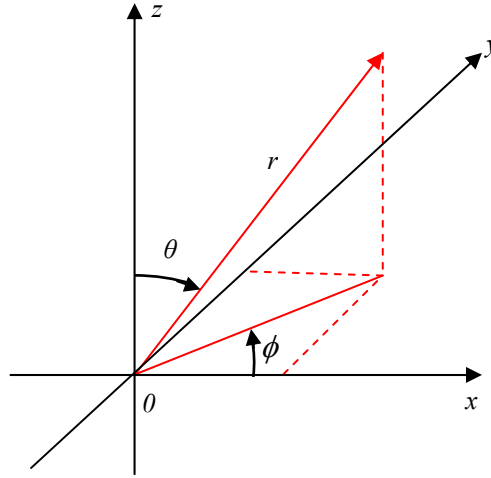


Figure 5.8: Spherical coordinate system.

The Poynting vector for electromagnetic fields, as given in [46], is the cross product of the electric and magnetic field vectors:

$$\vec{S} = \vec{E} \times \vec{H} \text{ W/m}^2 \quad (43)$$

(43) can be simplified by including (42), as shown in (44) when considering only the magnitude of the E and H-field vectors.

$$S = \frac{E^2}{\eta_0} \quad (44)$$

Next, a different form of the Friis transmission equation, also given in [46], is used. (45) describes the power density in W/m^2 , in the direction of the main beam, radiated by a single transmitting antenna with directivity greater than 0 dB, at a distance R .

$$S_{avg} = \frac{P_t G_t}{4\pi R^2} \text{ W/m}^2 \quad (45)$$

The definition in (45) is well known and reflects the fact that all the radiated power from an isotropic radiator must be recoverable by integrating over a sphere with a radius R that surrounds the radiator. The antenna that is used has directivity greater than 0 dB, and losses as indicated in (20) associated with its radiation efficiency. The power density above that of an isotropic radiator can be found by incorporating both of these factors. By combining (44) and (45), the radiated E-field of the transmitting antenna is given by the following:

$$E = \sqrt{\frac{G_t P_t}{4\pi R^2}} \eta_0 \text{ V/m} \quad (46)$$

The expression shown in (46) is confirmed in [49], and provides the magnitude of the radiated E-field at a distance R where the cable tray is positioned, as a function of frequency. This calculated E-field was compared to the constant 1 V/m E-field specified for the computational model and a correction factor was calculated. The computed voltage in CST MWS was divided by the calculated correction factor. This effectively incorporates the characteristics of the transmitting antenna, located a distance R away, into the computed voltage. Comparison of induced voltage from measurements and computation are presented in the following section.

5.6. Measurements of Cable Tray Model

An OATS was considered first for conducting the proposed radiated measurements on Model 1. The use of a VNA, as discussed up to this point, was not possible on the day of the measurement. As a consequence a Rohde & Schwarz SWM05 signal generator (SG) and Hewlett Packard 8562A spectrum analyser (SA), in maximum-hold mode, were used as the source and receiver respectively. The measurements were done over a reduced frequency range. Subsequent measurements of the cable tray model using a new LDPA were conducted inside an anechoic chamber at Stellenbosch University's Department of Electrical and Electronic Engineering, using a Hewlett Packard 8510 VNA over the full 300 MHz to 6000 MHz band. Results for both measurement environments are presented for horizontal and vertical polarisations. Reference will be made to results measured with the enclosure at the end of the cable tray either open as shown in Figure 5.9 (a), or closed using a cover as shown in Figure 5.9 (b).

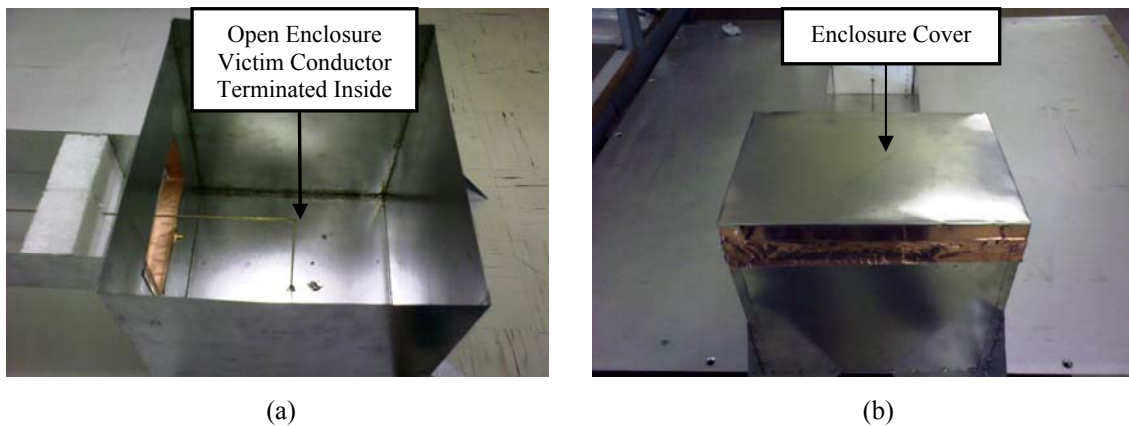


Figure 5.9: This photo taken from above the cable tray model shows a detailed view of the enclosure at end of the tray (a) without a cover and (b) with a cover. The termination of the victim conductor inside the enclosure can also be seen.

5.6.1. Using the OATS

5.6.1.1. Measurement Setup

CISPR 16-1-4 [50] and Williams [13] explain the requirements and guidelines for the construction of an OATS. Specifications regarding the size and surface roughness of the ground plane, free space around the site, and determination of the site attenuation are given. The basic description of an OATS is an obstruction free area with no significant scatterers of electromagnetic fields around or in the area. All the cables connecting to the DUT do so from underneath the ground plane through proper rotary connectors.

The OATS used for the cable tray measurements is shown in Figure 5.10. All the structures on the OATS visible in the photo are non-metallic, and the antenna positioner seen on the right operates using compressed air. All the measuring equipment (not shown) is located below the ground plane level. This ensures minimal interference from the measuring devices.

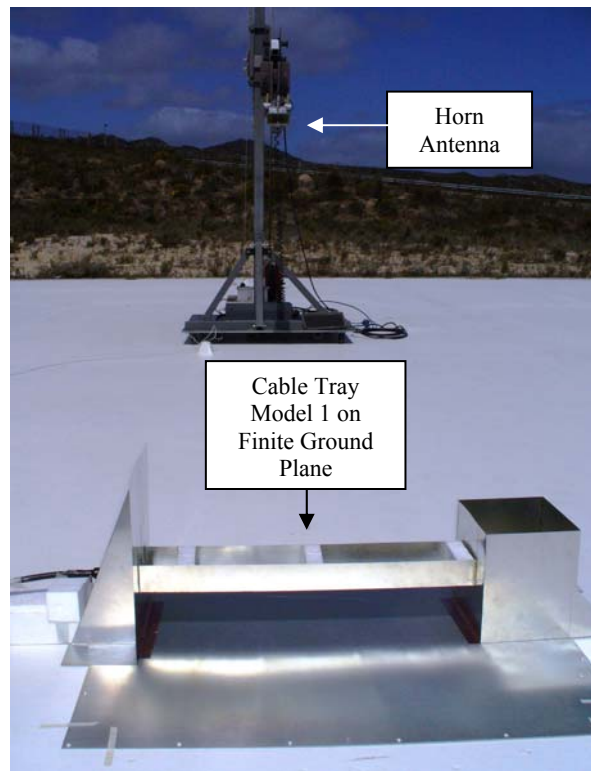


Figure 5.10: The OATS at ISSA (near Grabouw in the Western Cape) used for initial high frequency cable tray measurements.

With any radiated measurement performed on an OATS, multi-path interference will influence measured results. To characterise the multi-path effect the height of either the transmitting or receiving device is kept constant, while the height of the other device is scanned as discussed by Christopoulos and Argyri in [45] and Sevgi et al. in [51]. This provides a maximum response between the two devices (occurring when direct and indirect wave are in-phase). In the case of the cable tray measurement this was not possible. The cable tray and enclosure needs to be

mounted on a ground plane to facilitate the flow of common mode current induced on it, as discussed in Chapter 4 section 4.2.4. Moving the entire model mounted on a 1 m x 1 m ground plane up and down by a couple of meters was not practically possible. Furthermore, by moving either the cable tray or the transmitting antenna up or down, the angle of incidence of the incoming signal would vary. This variation could then be attributed to the multi-path interference associated with the OATS, as well as the variation in angle of incidence. This would have defeated the purpose of the experiment.

Consequently, the antenna was positioned at a constant 45° angle of incidence. The model and its finite ground plane were fixed directly onto the OATS ground plane, as shown in Figure 5.11 (a), rather than placing it on top of a table having a certain height above the ground plane. This attempted to limit, as much as possible, the difference in direct and reflected signal path lengths arriving at the model. The separation distance between the transmitting antenna and cable tray was minimised while still remaining in the antenna far field. A schematic representation of the measurement setup is shown in Figure 5.11 (b).



(a)

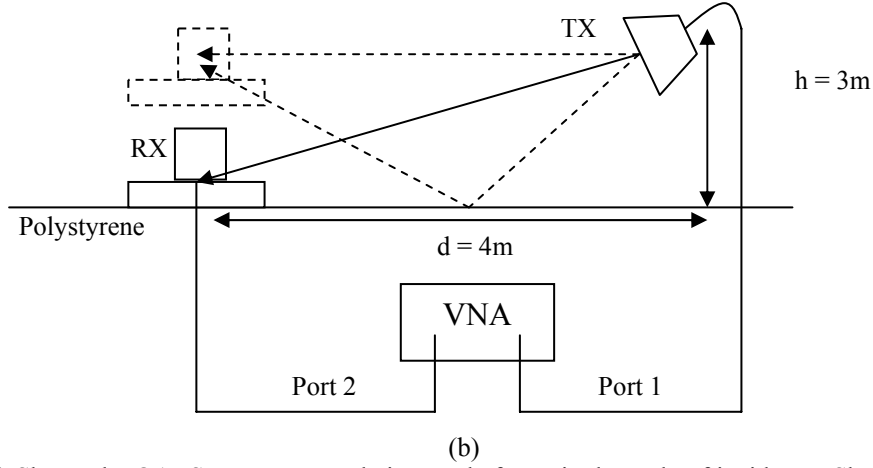


Figure 5.11: (a) Shows the OATS measurement being made for a single angle of incidence. Shown schematically in (b) is the attempt to minimise the multi-path interference by positioning the cable tray on the ground. The VNA indicated in the schematic was replaced by a separate SG and SA.

Having to use the SG and SA to excite and measure the response of the system was not ideal, with the biggest problem caused by the timing synchronisation of the two instruments. A delayed sweep time of 10 s was used on the SG with a faster sweep time specified on the SA. Despite the SA being set to sweep at 100 ms, it still took a period of time for the SA to complete the spectrum. The sweep time also directly influences the resolution bandwidth, which impacts on the ability of the band pass filter in the SA to sample the various peaks in the spectrum.

By contrast, the advantage of using a SG and SA was that power levels at each frequency point were known. Because the losses in the various cables are also known, it was possible to calculate P_{in} and P_{out} specified in (25), and use it to calculate the gain function of the cable tray. The relevant reflection coefficients required in (25) were measured separately.

Additionally, P_{in} was also used to calculate the voltage measured by the receiver as a function of frequency, using the power law shown in (47):

$$P_{in} = \frac{V_{measured}^2}{R} \text{ W} \quad (47)$$

Considering that the reflection loss associated with the victim conductor port has to be taken into account, $V_{measured}$ is not the actual voltage on the victim conductor. The correction process was explained in section 5.3 which subsequently gave $V_{cabletray}$. This was compared to the corrected computed voltage obtained from CST MWS. The voltage was corrected using the E-field-generated correction factor calculated using the method described in section 5.5.2. The finite ground plane, shown in Figure 5.6, was included in the simulation of the computational model.

5.6.1.2. Comparison: Measured and Computed Results

A comparison between the measured and computed results for the single angle of incidence is shown in Figure 5.12 (a) and (b) below. The frequency range was limited to between 1 and 3 GHz. The lower limit was determined by the 2 to 18 GHz operational bandwidth of the horn antenna. The upper limit was chosen so that a narrow frequency band was considered to help reduce the effects of multi-path interference on the results. The gain of the horn antenna, shown in Appendix B, was calculated using the three-antenna method described in section 5.4.

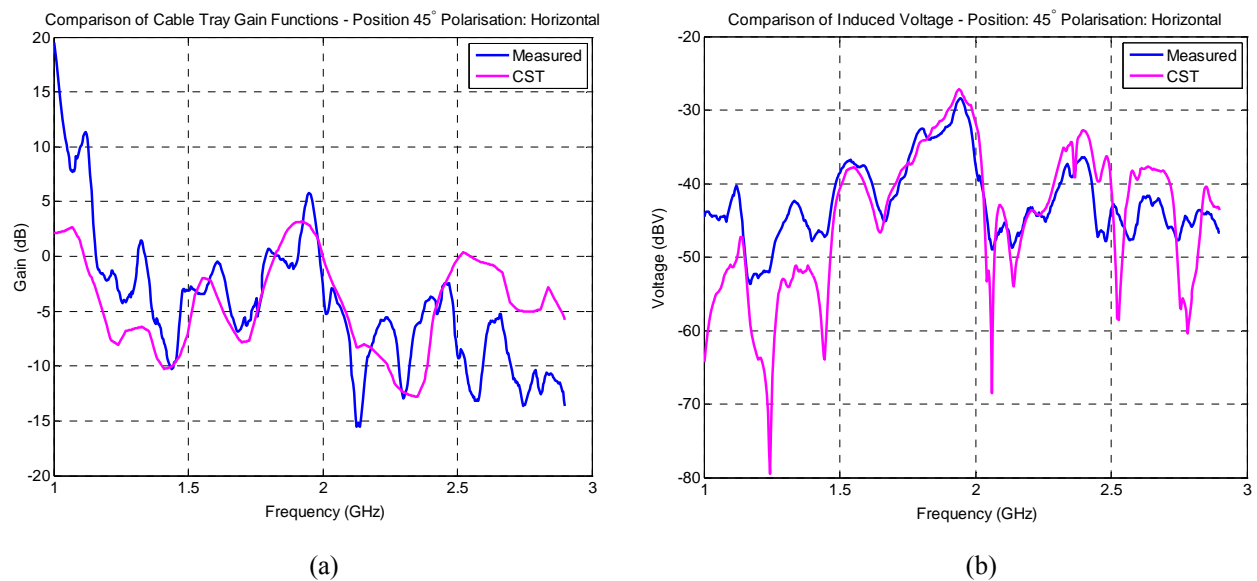


Figure 5.12: Comparison of (a) gain function and (b) induced voltage both calculated from measured results and computed using CST MWS for a 45° angle of incidence for the OATS measurement environment.

Model 1 was measured with a horizontally polarised E-field incident on the model (Figure 5.11 (a)), and the enclosure at the end of the cable tray having no cover (Figure 5.9 (a)). Agreement in levels between the calculated and computed gain functions, shown in Figure 5.12 (a), is seen for the mid-band frequencies. Differences are noticeable particularly at the higher and lower extremities of the band. This is also the case for the induced voltage shown in Figure 5.12 (b). This, to some extent, can be attributed to the multi-path interference which, despite including the ground plane in the simulation, is not as accurately replicated in the computational analysis. Constructive and destructive interference occurs differently in the computational analysis than in the actual measurement. Surface roughness and finite conductivity associated with any OATS are also not defined in the computational model.

Despite the disagreement between the calculated and computed results in certain parts of the band, the agreement in the central part establishes the accuracy of the computational analysis.

This applies to both the computed values of the far field gain function and plane wave induced voltage. It also confirms that the computed voltage from CST MWS can be successfully corrected to effectively incorporate free space loss and the antenna gain function for any radiated measurement setup. This will be reinforced by results from measurements made in the anechoic chamber, and discussed in the following section. Other factors influencing the agreement of the results were the fact that the measuring cables was unintentionally exposed to the radiating field and could have influence the results on the SA which was not shielded in any way. The impedance mismatch of the SA was not compensated for and a constant 50 Ω impedance was assumed. This is not a very accurate assumption when using a SA as receiver.

By replacing the SG and SA used for this measurement with a VNA, the synchronisation problems with using two separate instruments are solved, resulting in a more accurately sampled received signal. Using the VNA the system can be calibrated. This implies that the measured S_{21} can be more accurately compensated for the relevant cable loss, and the input impedance mismatch is significantly reduced. The consequence is better agreement between the compared data shown in Figure 5.12 (a) and (b).

5.6.2. Using an Anechoic Chamber

5.6.2.1. Measurement Setup

It was decided to use the fully anechoic chamber, which incorporates absorbing material on the floor as well, and a VNA to do a second set of measurements. In addition to the change in the measurement setup, a new LPDA operating over the entire specified band was used. An anechoic chamber is becoming a preferred alternative to an OATS for general EMC testing. Much less space is required and measurement schedules are not dependent on weather conditions. With the increase in ambient radio noise, if the chamber can be both screened and anechoic, it becomes an even more attractive option. The chamber at Stellenbosch University is only anechoic.

Before measurements of the cable tray could be done, the gain function of the new LPDA had to be determined. Two additional versions of the new antenna were produced which, together with an older version of a similar bandwidth LPDA, were used in the three-antenna method described in section 5.4. The gain function for the LPDA is given in Appendix B. The cable tray measurement setup inside the anechoic chamber is shown in Figure 5.13 with a schematic representation shown in Figure 5.14. Included in the setup is a permanently-installed amplifier

driving into port two of the VNA. The amplifier supplies a gain of approximately 38 dB between 500 MHz to 20 GHz. The use of the amplifier in the setup allows more sensitive measurements to be conducted by improving the system's dynamic range. It also counteracts the significant loss in signal strength associated with the long cables used inside the chamber.

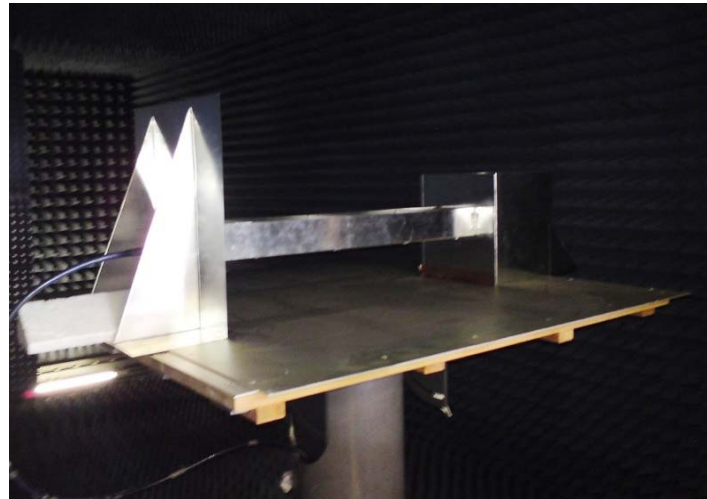


Figure 5.13: Cable tray measurement setup inside anechoic chamber at the Stellenbosch University.

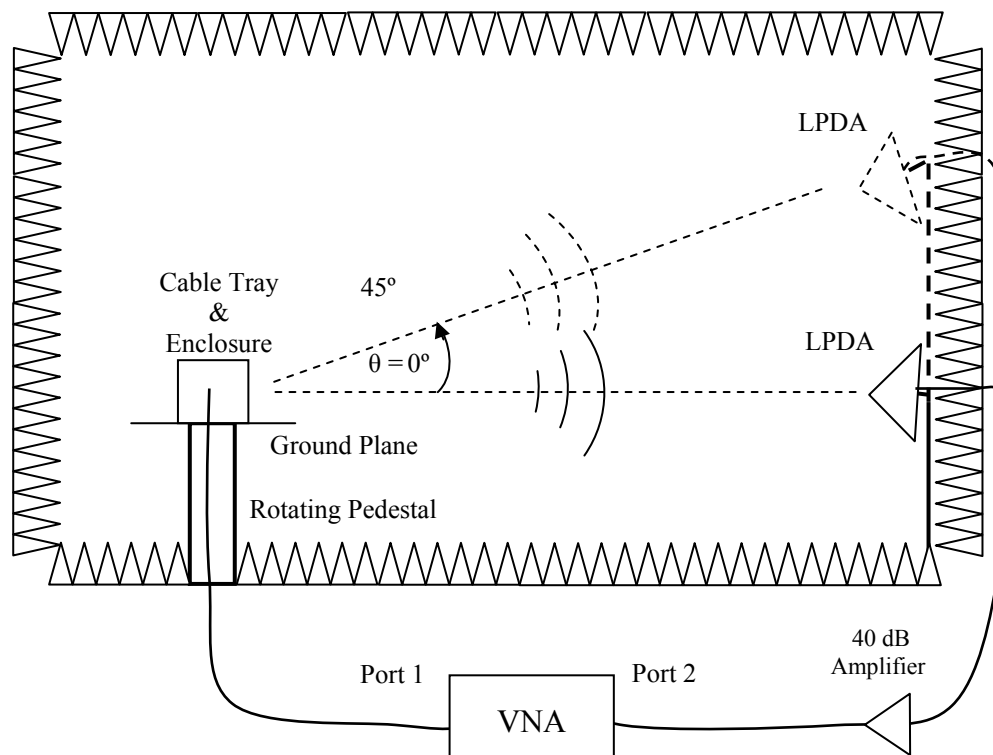


Figure 5.14: Schematic showing the setup for the cable tray measurements inside anechoic chamber.

The schematic also shows the connection of the cable tray to port one and the antenna to port two of the VNA. The reason for analysing the reciprocal problem to the one defined in Figure

5.3 was because of the layout of the equipment inside the chamber. A rotating pedestal is located at port one, which facilitated the positioning of the cable tray and ground plane as shown in Figure 5.13. At port two, an antenna positioner was available, which made moving the antenna up or down to generate the various angles of incidence possible. With the amplifier driving into port two it was unsafe for the instrument to excite the system in reverse (S_{12} measurements). As a consequence, reciprocity as stated in [49] was applied, and S_{21} measurements were made.

5.6.2.2. Reciprocity of the System

The reciprocity law can be described in several forms but will be discussed in terms of voltage and current inputs to a two-port system. A two port system (Figure 5.15) can be described by the general impedance representation given by [49].

$$\begin{aligned} V_1 &= Z_{11}I_1 + Z_{12}I_2 \\ V_2 &= Z_{21}I_1 + Z_{22}I_2 \end{aligned} \quad (48)$$

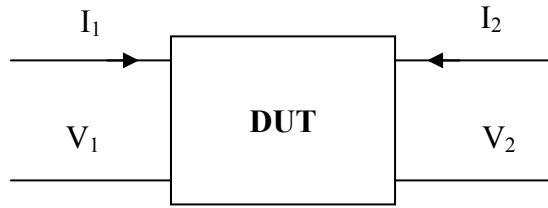


Figure 5.15: Two-port system.

The statement of reciprocity is that $Z_{12} = Z_{21}$ [49]. To apply this to our radiation problem, the DUT in Figure 5.15 is replaced with the schematic representation in Figure 5.14. The current I_1 and voltage V_1 are applied at port one with I_2 and V_2 applied at port two. The derivation used in [49] for a similar radiation setup is used to validate the law's applicability to this problem.

If it is assumed that only port one in Figure 5.14 is excited with current I_1 , i.e. $I_2 = 0$, the voltage at port two, which is the output of the antenna, is given by (48) as $V_2 = Z_{21}I_1$. V_2 is therefore dependent on the radiation from the cable tray described by Z_{21} . If the antenna at port two is moved up or down along the edge of a circle (not indicated) around the cable tray, V_2 changes according to the relative change in θ as the antenna is moved. Because the antenna is always pointing at the cable tray as it moves, the change caused by Z_{21} must be an indication of the cable tray's radiation pattern. Similarly, if only port two is excited with current I_2 , i.e. $I_1 = 0$, the voltage at port one induced by the radiation of the antenna would be $V_1 = Z_{12}I_2$. If the angular orientation θ of the cable tray were again changed by essentially rotating the tray with respect to

the antenna, V_1 would change according to the receiving pattern of the cable tray. This receiving pattern of the cable tray is then described by Z_{12} . By setting the currents $I_1 = I_2$ in (48), the reciprocity statement that $Z_{12} = Z_{21}$ means that the radiation and receiving patterns are the same, and that V_1 and V_2 are the same function of the angle of incidence θ shown in Figure 5.14.

5.6.2.3. Comparison: Calculated and Computed Gain Functions

The gain of the cable tray as a function of frequency for different angles of incidence was calculated from the measured S_{21} parameters using the method described in section 5.2. Equally, the gain was obtained from the computational analysis using the method described in section 5.5.1. Comparison of the calculated and computed gain functions for the three angles of incidence, 0° , 45° , and 90° , are shown in Figure 5.16.

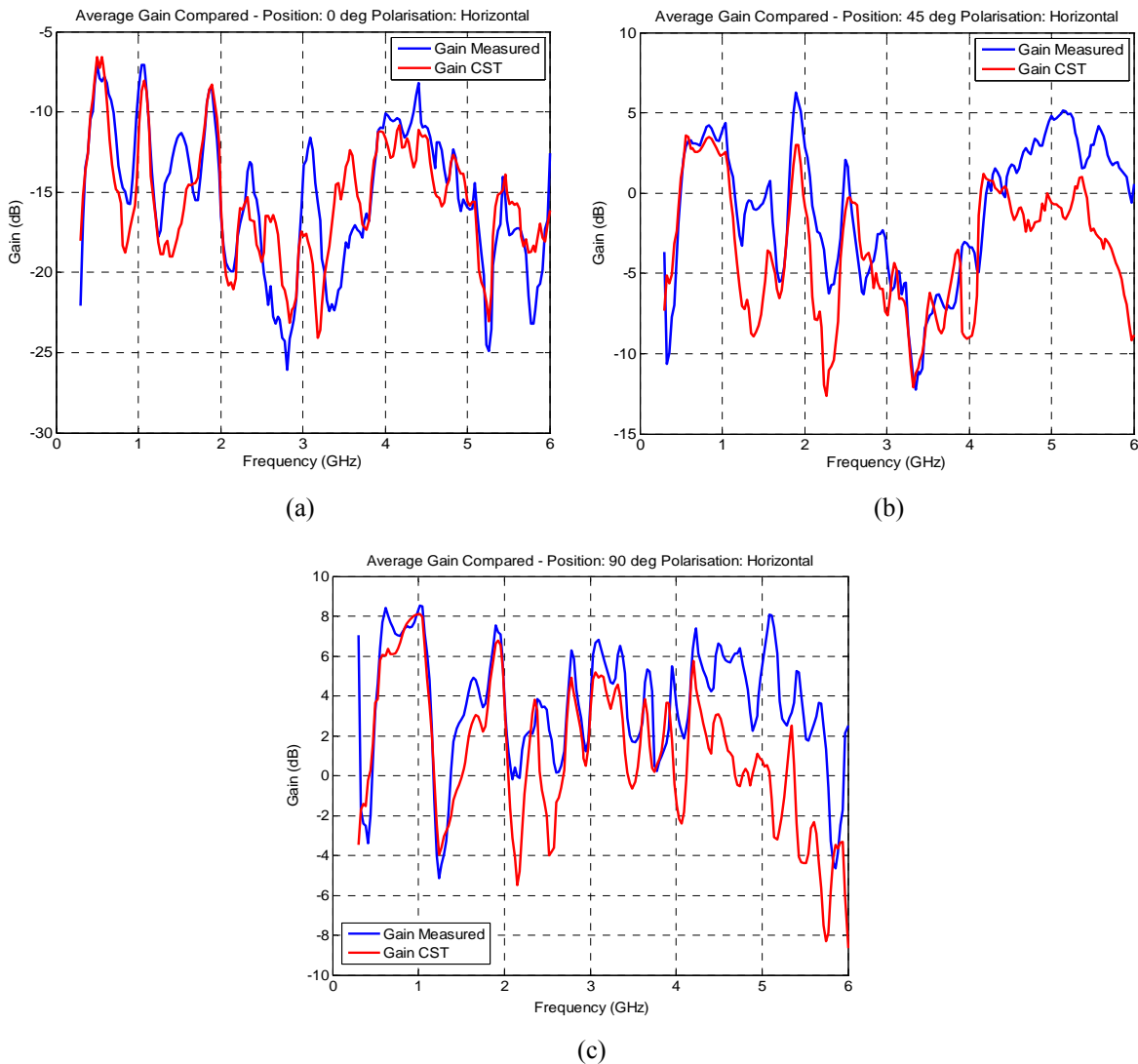


Figure 5.16: Comparison of calculated and computed cable tray gain functions for horizontal polarisation of the E-field for three different angles of incidence; (a) 0° , (b) 45° , and (c) 90° . Note that these results are for an open enclosure at the end of the cable tray.

An averaging function has been applied to both the calculated and computed results shown in Figure 5.16 to present a better visual comparison. These results are for an open enclosure at the end of the cable tray (Figure 5.9 (a)). Good agreement between the calculated and computed gain functions for each angle is seen in Figure 5.16. However, similar as with the OATS experiment the measurement cable connected to the cable tray was to some extent exposed to the radiated field. Despite using low transfer impedance cables this, along with the fact that the anechoic chamber is not shielded could influence the results measured by the VNA. This again confirms the accuracy of the computational analysis. In Figure 5.17 the individual gains from Figure 5.16 are combined to show the increase in gain for the three angles using only the calculated measurements.

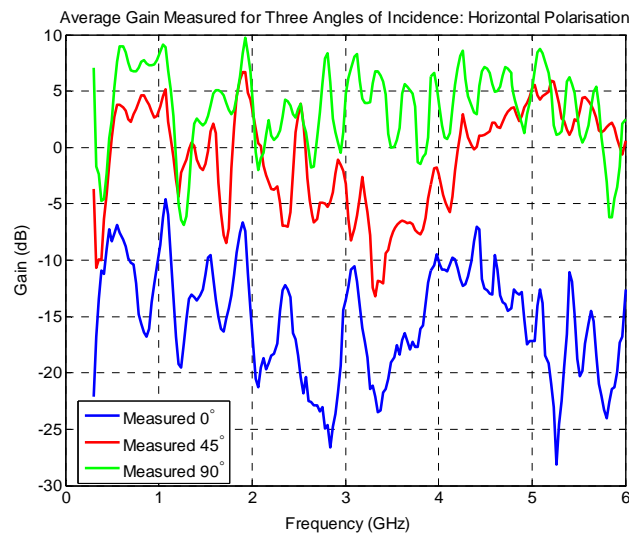


Figure 5.17: Comparison of the gain functions calculated from measurements of the cable tray for horizontal polarisation of the E-field with the receiving antenna positioned at three different angles of incidence.

Figure 5.17 shows that for a 90° angle of incidence, the cable tray increases the incident power by an average value of 3 dB, which is the worst scenario. That average value decreases to -1 dB when the angle of incidence is 45° and to -15.34 dB when it is 0°. These results should be considered while remembering that the victim conductor is positioned in the middle of the cable tray at a height of 25 mm above the tray floor. With the cable tray having a total side-wall height of 62.5 mm and a height-to-width ratio of 1:2, the victim conductor is by no means in the optimal position in terms of shielding the tray can provide. The results shown in Figure 5.17 will change as the position of the victim conductor inside the cable tray changes.

The gain functions of the cable tray calculated from measurements for vertical polarisation of the receive antenna are considered next. Only a 45° and 90° angle of incidence were considered.

These results, shown in Figure 5.18 below, are again for an open enclosure at the end of the cable tray.

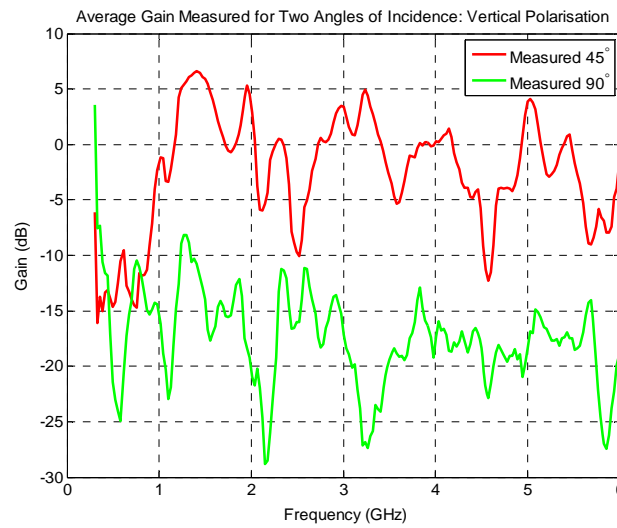


Figure 5.18: Comparison of the gain functions calculated from measurements of the cable tray, with the antenna positioned to receive vertically polarised E-field, is considered for two angles of incidence.

The above results show that for a 90° angle of incidence, the gain of the cable tray is significantly lower than for 45°. This low level is as expected because, for the vertical polarisation of the antenna, very little of the predominantly horizontal E-field from the victim conductor inside cable tray will couple with the antenna. Considering the reciprocal scenario where a plane wave is incident on the cable tray, with a vertical polarisation of the E-field, the associated B-field is horizontally polarised. This horizontal polarisation is parallel to the conductive loop inside the cable tray created by the victim conductor, and as a result the B-field does not induce a significant amount of CM current in the loop.

For the 45° angle of incidence, similar gain levels are seen when comparing Figure 5.17 and Figure 5.18. This could be attributed to the influence of the open enclosure at the end of the cable tray. To evaluate this, the results for the 45° angle of incidence for both polarisations are considered with and without an enclosure cover (Figure 5.9 (a) and (b)). The results are shown in Figure 5.19 (a) and (b).

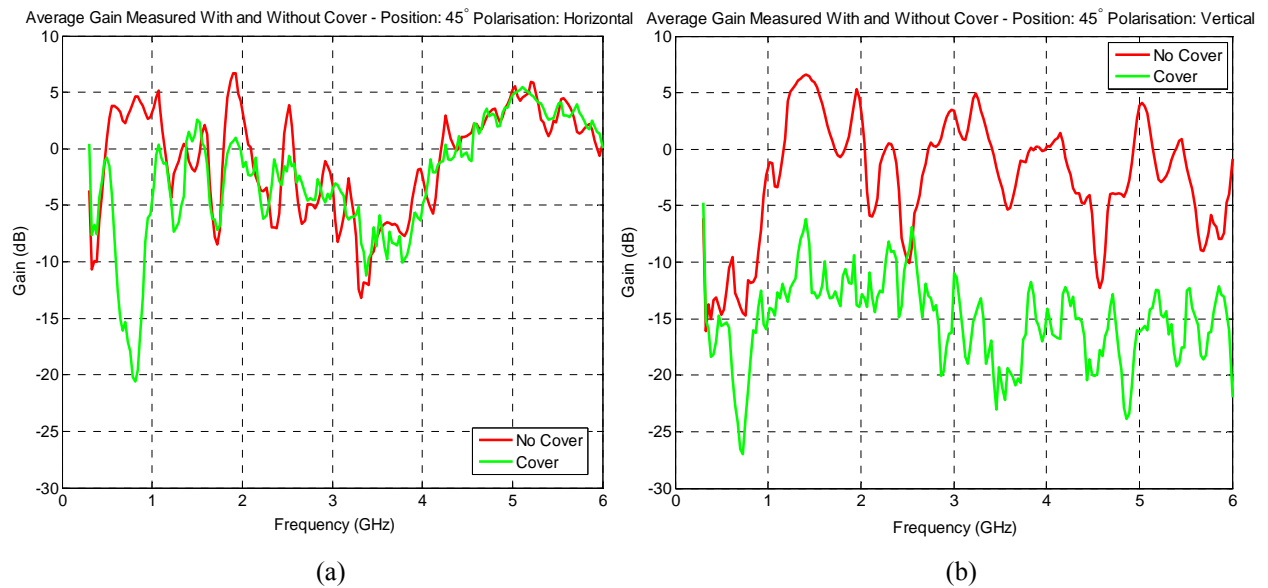


Figure 5.19: Comparison of the change in calculated gain functions of the cable tray using measured results, for a 45° angle of incidence, are shown. Results for the horizontal polarisation of the antenna, with and without an enclosure cover are shown in (a), and for vertical polarisation with and without an enclosure cover shown in (b).

From Figure 5.19 (a) it becomes clear that for horizontal polarisation, only a small change is seen in the gain of the cable tray when the enclosure cover is included. Most of the horizontally radiated E-field measured by the antenna, originates from the victim conductor inside the tray. Only a small amount is generated by the conductor inside the enclosure. In Figure 5.19 (b) a bigger difference is seen when considering vertical polarisation. In this case the vertical orientation of the victim conductor inside the enclosure (Figure 5.9 (a)) is producing the only E-field measured by the similarly orientated antenna.

Adding the cover to the enclosure prevents the conductor inside from radiating energy out, and an overall lower gain function is obtained. In this case the shielding ability of the enclosure was more important than that of the cable tray. The results, therefore, show that the environment in which the tray is used should be considered in its entirety. The amount of coupling to conductors in a system through radiated interference will not always be highest when they are exposed in open cable trays.

5.6.2.4. Comparison: Measured and Computed Voltages

After evaluating the gain of the cable tray for the various angles of incidence, the voltage induced on the victim conductor inside the cable tray, for the same three angles, is considered. The voltage obtained from the computational analysis for each angle was corrected with the correction factor calculated using the method described in section 5.5.2. Obtaining a similarly

induced voltage for each angle from the measured S_{21} parameters, required using the technique described in section 5.3.

Having proven the accuracy of the computational analysis, comparative results for calculated and computed voltages are shown for only the 45° angle of incidence. Comparisons for the remaining angles are shown in Appendix B. The results, shown in Figure 5.20 (a), are considered for an open enclosure and horizontal polarisation. The same averaging function that was used for the gain calculations, were also applied to the voltages to again improve their visual comparison.

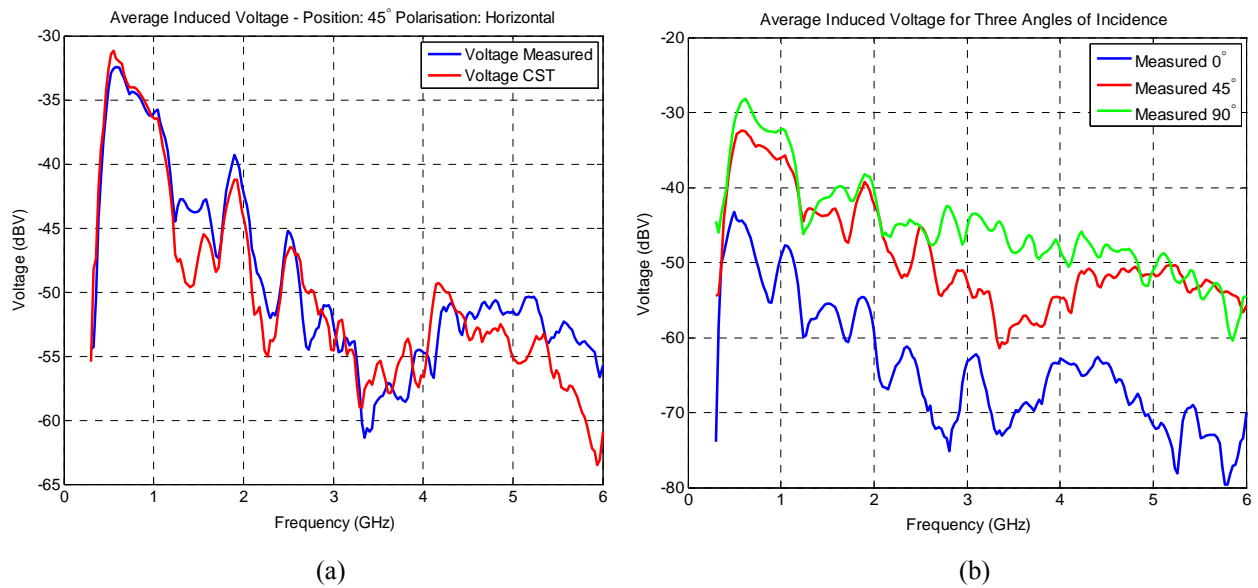


Figure 5.20: Comparison of calculated and computed induced voltages on the victim conductor inside the cable tray for a horizontally polarised antenna, are shown in (a) for a 45° angle of incidence. The comparison between the calculated voltages for all three angles is shown in (b).

Adequate agreement between the measured and computed results again confirms the accuracy of the computational analysis across the band. Some of the differences between the calculated and computed voltages in Figure 5.20 (a) can be attributed to the assumption made in section 5.3 regarding the incident voltage at port one being $V_j^+ = 1 \angle 0^\circ$ V. The applied voltage from the VNA varies both in terms of magnitude and phase and this is not corrected for. This variation should be small and would account for the small offsets visible in Figure 5.20 (a). Using these results the change in induced voltage for the three angles of incidence are shown in Figure 5.20 (b). As expected the voltage is the lowest when the angle of incidence is 0° and increases as the angle of incidence increases.

A noticeable difference for both the gain function and the induced voltage is seen when the angle of incidence changes from 0° to 45° . This is shown in Figure 5.17 and Figure 5.20 (b). A less significant change is evident when the incidence angle is changed from 45° to 90° , also shown in Figure 5.17 and Figure 5.20 (b). This is related to the position of the victim conductor inside the tray by considering Figure 5.21 which is an end-view of the cable tray.

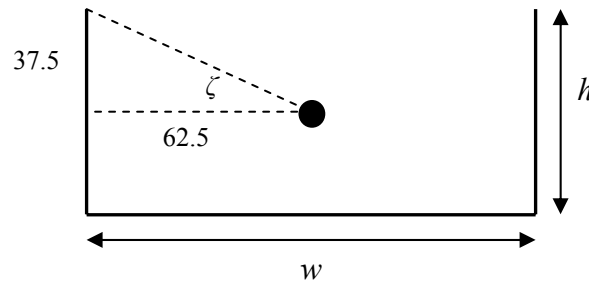


Figure 5.21: End-view schematic of the cable tray and victim conductor.

The width of the cable tray is $w = 125$ mm and the height $h = 62.5$ mm. With the victim conductor kept at a constant height of 25 mm as previously mentioned, the angle ζ between the conductor and the top edge of the cable tray side is 31° . Considering only the horizontal polarisation, when the antenna was moved from 0° to 45° , it crossed this threshold angle ζ , and the victim conductor inside the cable tray became ‘visible’ to the antenna. This caused a clearly noticeable change in the measured results. When the antenna was moved from 45° to 90° , no such threshold was crossed and as a result a smaller increase in both the gain function and induced voltage was seen.

By keeping the receiving antenna at a constant angle of incidence, and increasing the angle ζ by moving the conductor inside the cable tray down and towards the side of the tray, will result in a decreased gain function and induced voltage calculated from the measurement. This is confirmed by the investigations in [18]. With the horizontal E-field polarisation the associated B-field circulates perpendicularly around the cable tray, and intersects the conductive loop created by the victim conductor inside the tray. The U-shape inherently inhibits this B-field coupling by preventing the field from bending down into the tray. The result is less coupling to the victim conductor when it is positioned lower down and closer to the corner of the tray.

The comparison of the induced voltages for incidence angles of 45° and 90° with vertical polarisation of the antenna is shown in Figure 5.22.

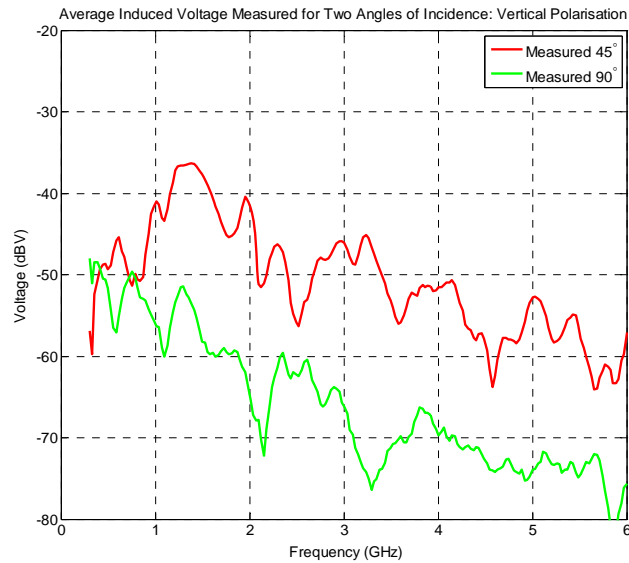


Figure 5.22: Comparison of induced voltage on the victim conductor inside the cable tray calculated from measurements for a vertically polarised antenna, is shown for two different angles of incidence.

Similar to the results shown in Figure 5.18 is the fact that for a 90° angle of incidence the voltage is lower than for 45°. With the excitation of the victim conductor inside the cable tray producing horizontally polarised E-field, this is to be expected. The influence of the enclosure cover on the induced voltage is also considered and it is again only done for a 45° angle of incidence. The influence of the cover with horizontal polarisation is seen in Figure 5.23 (a) and for vertical polarisation in Figure 5.23 (b).

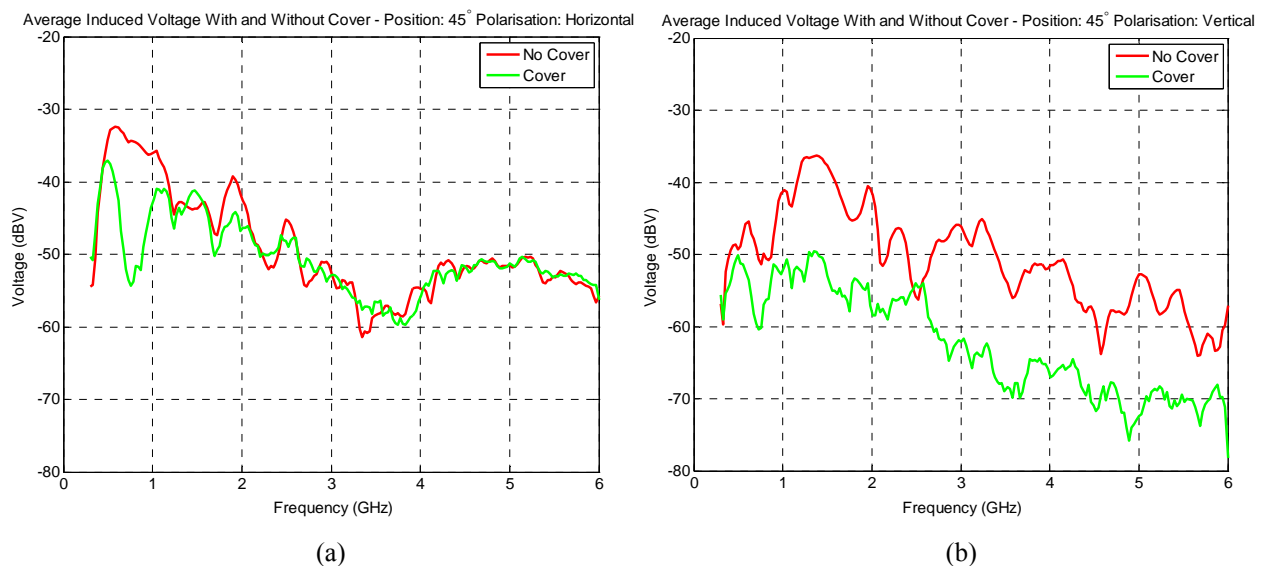


Figure 5.23: Comparison of the change in induced voltage calculated using measured results for a 45° angle of incidence is shown. The results for horizontal polarisation with and without enclosure cover are shown in (a), and for vertical polarisation with and without cover shown in (b).

Little difference in the induced voltage for the horizontal polarisation is seen when the cover is added to the enclosure (Figure 5.9 (b)). A larger difference is once again seen for the vertical polarisation. Radiation from the conductor inside the enclosure, which is vertically positioned, dominates. The induced voltages follow the same trend as the gain functions. It again shows that the level of shielding provided by a cable tray is influenced by the shielding ability of the relevant enclosure or cabinet at which the cable tray is terminated.

5.7. Conclusion

This chapter evaluated the shielding ability of a cable tray with an added enclosure, at frequencies where the wavelength of the disturbance field is similar, or even smaller, than the width of the tray. This was done by illuminating the Model 1 cable tray model of Chapter 4 using a known-gain antenna. The antenna was moved around the cable tray to produce three distinct angles of incidence. The S_{21} parameter that was measured for each angle was used to calculate the tray's gain function using the Friis transmission equation, as well as the induced voltage on the victim conductor inside the tray. Both of these results were compared with similarly computed results from an equivalent computational model which was analysed in CST MWS.

Good agreement was obtained for measured and computed results. The calculated cable tray gain using the Friis transmission equation was proven by comparing results computed using a dedicated far field monitor. The characteristics of a transmitting antenna and free space loss were incorporated into computed voltages from the simulation. By comparing the E-field radiated by the actual antenna to the E-field specified in CST MWS, a correction factor was calculated with which the computed voltage was adjusted. The agreement of results produced an accurate computational model which can be used to study the high frequency shielding ability of cable trays further.

An OATS and an anechoic chamber were both used during this investigation. The inherent multi-path interference associated with the OATS showed that it is not suitable to evaluate the shielding ability of cable trays for varying angles of incidence. The anechoic chamber provided the ideal environment, but reciprocity had to be applied in order to make S_{21} measurements using a VNA and amplifier. The valid application of reciprocity was confirmed for the measurement setup that was used.

It was stated that the findings from this investigation should be considered in addition to Kapora's results obtained in [18]. By considering only a 90° angle of incidence as the study in [18] does, the highest possible induced voltage and current on the various conductors inside the tray were predicted. This gives the worst case results. However, the angle of incidence of the disturbance field might also vary, and for this reason the results shown in this chapter should be considered simultaneously with the results presented in [18].

Finally, by including an enclosure which was either open or closed using a cover, it was shown that the shielding ability of the enclosure was more important in certain instances than that of the cable tray. In a practical installation, inadequate shielding of a cabinet represented by the open enclosure would be the main contributor to induced interference, and not the open cable tray. What this shows is that, if at all possible, the environment in which a cable tray will be used should also be considered in terms of overall shielding.

The results show that even at these short wavelengths cable trays could be used in environments where they would be exposed to higher frequency interference. Although the cable trays that are considered in this dissertation are specialised installations and would have relatively high installation cost, this might be offset by limiting their installations to specialised cases over short distances. Possible installations for the KAT-7 and possibly MeerKAT may be areas such as the antenna services chamber or main correlator room. However, readily available meshed or wire trays which are cheaper are a more viable option. Therefore as part of future work, the shielding ability of meshed cable trays could be determined as a more cost-efficient solution.

Chapter 6

RF Current Audit for KAT-7 Telescope

6.1. Introduction

This chapter continues the theme of investigating common mode (CM) currents as a source of radio frequency interference (RFI). The basis for the investigation is a radio frequency (RF) current audit that was done on the existing Karoo Array Telescope (KAT-7) radio telescopes. Each telescope (Figure 6.1) makes use of shielded cabinets which house all the control and feed electronics. Attempts have been made to screen each cable connecting the electronics inside the telescope pedestal, with the motor drives and antenna feed, using over-braiding. This was done with varying degrees of success. However, because of the sensitivity of the instrument, conventional methods of RFI mitigation are not sufficient.

Attempts were made to shield the lower pedestal section (Figure 6.1) against electromagnetic interference (EMI), by installing metallic interface barriers (floor and ceiling). This created unique mechanical engineering difficulties associated with the manufacturing and installation of these barriers. The result was that at the time this reported audit was conducted, not all of the possible recommendations for shielding had been implemented. One KAT-7 telescope did have additional measures incorporated, and this will be referred to as a hardened telescope; the one without additional shielding will be referred to as the non-hardened telescope. The objective of the audit was to evaluate the additional shielding by comparing the distribution of CM current on the outside of both a hardened and non-hardened telescope. This particular evaluation method is described in section 6.6.

The measured results from the audit are presented in three parts. The findings from the various sections are intended to present a developing picture of the telescope's shielding characteristics. These shielding characteristics are finally evaluated more accurately, using computational analysis presented in the fourth and final part of the chapter.

Part 1: The development of accurate 1/20th scale models, both physical and computational are discussed. The comparison and agreement of results measured using these models, with actual measured data from the current audit, are shown. The validity of the computational analysis is proven for further use in investigating specific aspects of the actual dish. In the chapter reference will be made to the KAT-7 telescope which refers to the actual instrument shown in Figure 6.1. The two scale models will be referred to as either the physical or computational model.

Part 2: A self-evaluation of the measurement setups used in the RF audit is presented. Attention falls on comparing the change in distribution, measured around the outside of the telescope, for directly injected and induced CM currents. The purpose is to determine if the method of direct injection is causing any mis-interpretation in the understanding of telescope shielding properties.

Part 3: The change in the distribution of CM current is compared specifically for a hardened and non-hardened telescope in different scenarios. The difference between the preferred hardening and what was actually implemented, is also discussed. Comment it made on how diversion of CM current on the outside of the telescope pedestal, could lessen the stringent shielding requirements that is required on the inside.

Part 4: A more appropriate method to determine the level of shielding provided by the suggested interfaces is discussed. This method appears to predict more conservative values compared to the commonly used definition of shielding effectiveness. The level of shielding provided by the top interface in particular is investigated. This analysis was done using only Computer Simulation Technology's Microwave Studio CST MWS [21].

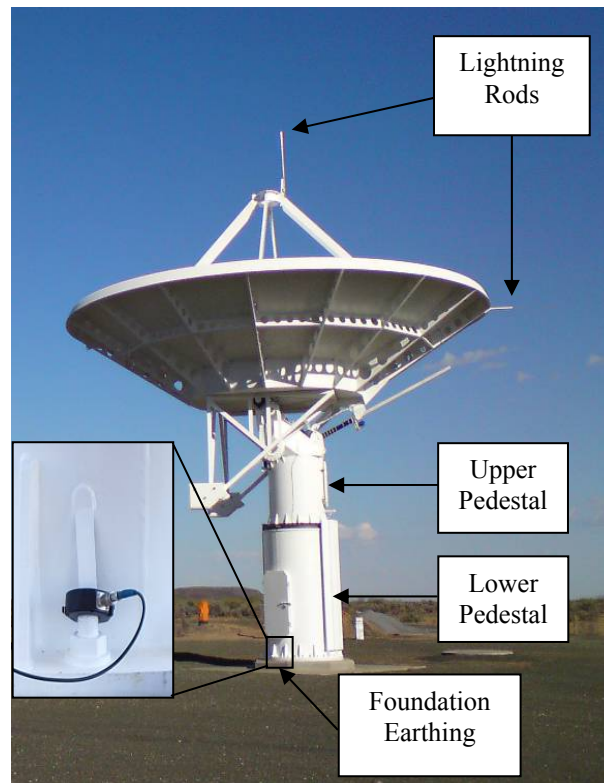


Figure 6.1: One of the KAT-7 dishes built in the Northern Cape as part of the South African demonstrator project. A CM current probe was used during the audit to measure the current around the telescope is shown in the insert.

Part 1 – Physical and Computational Model Development

6.2. KAT-7 RF Audit Measurement Description

The audit consisted of measuring the distribution of CM current between four earthing connections at the bottom of the telescope pedestal, for different scenarios. Each scenario represents the dish in a different position. The CM current was either directly injected onto the LDC or induced through E and B-field coupling. The earthing connections (see insert Figure 6.1), are part of a lightning down conductor (LDC) system installed on each telescope, and are equally spaced around the telescope foundation. They have been welded to the pedestal and foundation bolts which are connected to the re-enforcing within the concrete foundation. This provides the real-earth connection. The measurements of current on these connections were made using a CM current probe connected to a receiver. Four copper shoes fixed to the lower

pedestal provide galvanic contact with a rotation ring which is fixed to the upper pedestal. The ring allows for the dish rotation, and the installation is shown in Figure 6.2 (a) and (b). The shoes, along with the four earthing connections and two LDCs on the upper pedestal, make up the entire LDC system designed as analysed by Wiid [5].



Figure 6.2: View of the galvanic connection between the upper and lower pedestal where the copper shoe and LDC connection to the rotation plate are (a) aligned and (b) misaligned. Note that the four copper shoes on each telescope (only one shown in both (a) and (b)) are fixed to the lower pedestal.

The distribution using direct current injection, on both the KAT-7 telescope and the physical model, were measured using a vector network analyser (VNA). A two-port setup was used with port one exciting the system and port two measuring the response. The distribution of induced CM current measured during illumination measurements was only made on the KAT-7 telescope. An antenna driven by a signal generator and positioned in the antenna's far field was used to illuminate the structure. A handheld battery-driven Rohde and Schwarz FSH 8 spectrum analyser (FSH 8 SA) served as the receiver, measuring the currents with the CM current probe.

In all cases the system under investigation was excited with a spectrum of frequencies. These frequencies, similar to the dimensions of the telescope, were linearly scaled. A chosen range of 0 to 2 GHz for the scale models is equivalent to 0 to 100 MHz on the KAT-7 telescope. The wavelength at 100 MHz is 3 m and the total pedestal height is approximately 6 m. This produced standing waves on the structure at the upper limit of the band, replicating higher frequency RFI.

The telescope was analysed with the dish in four positions. Of the four, two were with the dish in the stow position (Figure 6.3 (a)) and will be referred to as scenario one. The other two were

with the dish positioned vertically, and will be referred to as scenario two (Figure 6.3 (b)). For each of the two scenarios the dish was rotated. The reason for rotating the dish was firstly, to disrupt the current path between the upper and lower pedestal. This path is created through the alignment of the LDC on the upper pedestal, and the copper shoe on the lower pedestal. An aligned scenario is one where the connection of the LDC onto the rotation plate is directly above a copper shoe as shown in Figure 6.2 (a). A misaligned scenario is when they are separated by 45° as shown in Figure 6.2 (b). The second reason for rotating the dish was to change the alignment between the direct injection point, and the position of the four earthing connections. By rotating the dish the fixed injection points that were chosen, also rotated. A depiction of the direct current injection is seen in Figure 6.3. The change in alignment is used to comment on the possible influence the direct feeding technique has on the measured results. For scenario one, the current is injected onto LDC located on the side of the dish (Figure 6.3 (a)), and for scenario two onto the LDC located on the feed struts (Figure 6.3 (b)). For the rest of the chapter, reference is made to scenario one aligned or misaligned and scenario two aligned or misaligned.

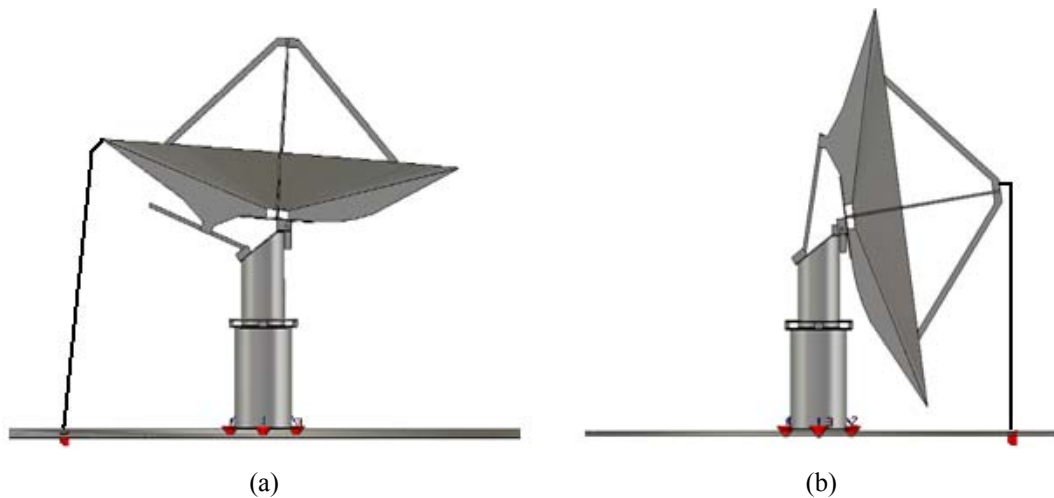


Figure 6.3: Computational representation of (a) scenario one and (b) scenario two. The feed conductors used in the direct injection analysis together with the excitation and termination ports are all shown.

6.3. Model Definitions

6.3.1. Physical Scale Model

The scale model (Figure 6.4) was created and used in [5] as part of the LDC evaluation. It was adapted since then according to subsequent changes and installations made on the actual telescope. The changes, which include the four earthing connections, were due to unforeseen production issues which affected the functioning of the LDC. As the current measurements were

made on the earthing connections, they had to be included in the physical model. Their implementation as well as the inclusion of the shoes between the upper and lower pedestal, are shown in Figure 6.4. The intricate LDC on the upper pedestal was not included in the physical model. To facilitate the disruption of the current path between the upper and lower pedestal in the model, the shoes, indicated in Figure 6.4, were rotated along with the dish and upper pedestal. Consequently, for an aligned scenario, the shoes are aligned with the earthing connections (see insert Figure 6.4), and for a misaligned scenario they are rotated by 45° and do not line up with bottom connections.

The 12 m diameter of the dish scales to a 600 mm diameter model with a pedestal height of 310 mm from the foundation to the elevation shaft. It is mounted on an 820x960 mm ground plane. The latter not only creates a physical barrier between the model and the cables connecting to it, but also defines the calibration plane. The four earthing connections are continued on from the foundation-ring of the model through the ground plane (see insert Figure 6.4). They terminate in Sub-Miniature version A (SMA) connectors mounted underneath the ground plane which are used for measurement purposes. Equally, the feed cable also connects to an SMA connector mounted the same way.

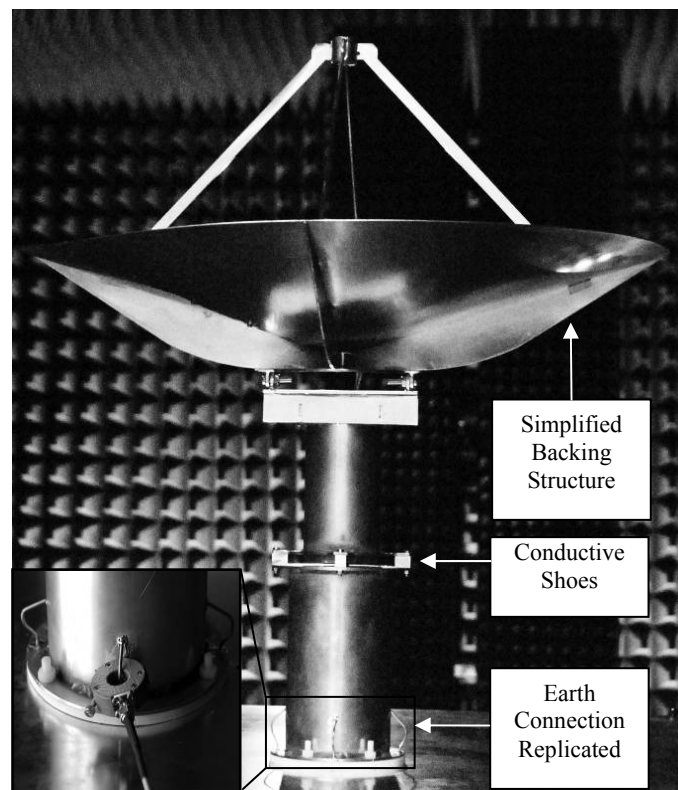


Figure 6.4: Physical scale model of the KAT-7 radio telescope in a stow position being measured inside an anechoic chamber.

This feed is simply an exposed centre conductor extended from the SMA port. Apart from injecting the current onto the model, the feed also creates magnetic field around it. This couples to various conductive loops assisting in inducing CM current on the structure. Because all cables involved in the measurement connect to the model from below the ground plane, the amount of potential CM current on them is minimised.

6.3.2. Computational Scale Model

A computational representation of the physical model was also created as part of [5]. It was, however, defined in a MoM based code, which discretised the model using triangular surface meshing. After importing the model into CST MWS using their advanced CAD rendering tools, all the relevant structural changes and port definitions were added. This included the earthing connections according to the actual telescope installations. Similarly to the physical scale model, the LDCs on the upper pedestal were not included in the simulation. The model was adapted in some areas to improve the spatial discretisation used by CST MWS's transient solver. A simplification applied to both physical and computational models, was the electrical connection between the dish and the backing structure. This and other computational model simplifications were described in more detail in Chapter 4 section 3.2.2. Dimensionally the computational scale model is identical to the physical model which includes the ground plane.

The trade-offs between having an efficient simulation while still ensuring an accurate mesh density were also discussed more thoroughly in Chapter 3 section 3.2.1. This section explained how the discretisation of the computational domain is done automatically to a certain level of accuracy. Apart from certain meshing criteria which the user can manually change, CST MWS also provides different types of meshing algorithms. The Fast Perfect Boundary Approximation (FPBA) is one such algorithm which allows the fast and robust discretisation of imported or arbitrary shapes [21]. FPBA is especially useful when analysing structures with big variation in geometry dimensions. This is the case with the telescope model. The meshing has to simultaneously resolve large objects such as the dish, along with a small spacing between the foundation and ground plane.

Used in conjunction with this is a multi-level subgridding technique available as part of the time-domain-based transient solver. The subgridding algorithm increases the mesh density in areas where there are significant changes in currents and/or fields, and reduces it elsewhere. This

means a reduction in the number of mesh cells used in the simulation. This technique of multi-scaled meshing was discussed in Chapter 2 section 2.8.2 and recommended by Christopoulos in [28]. The effect is seen in Figure 6.5 when looking at a sectioned mesh view of the top half of the telescope model. The increased mesh density is visible in most areas of the telescope, but reduced in areas of free space. At positions where particularly high concentrations of E and B-fields are calculated, the meshing is increased further. This is seen in the insert in Figure 6.5. Here the feed conductor connects to the side of the dish. The localised staircase meshing associated with the hexahedral discretisation is clearly visible.

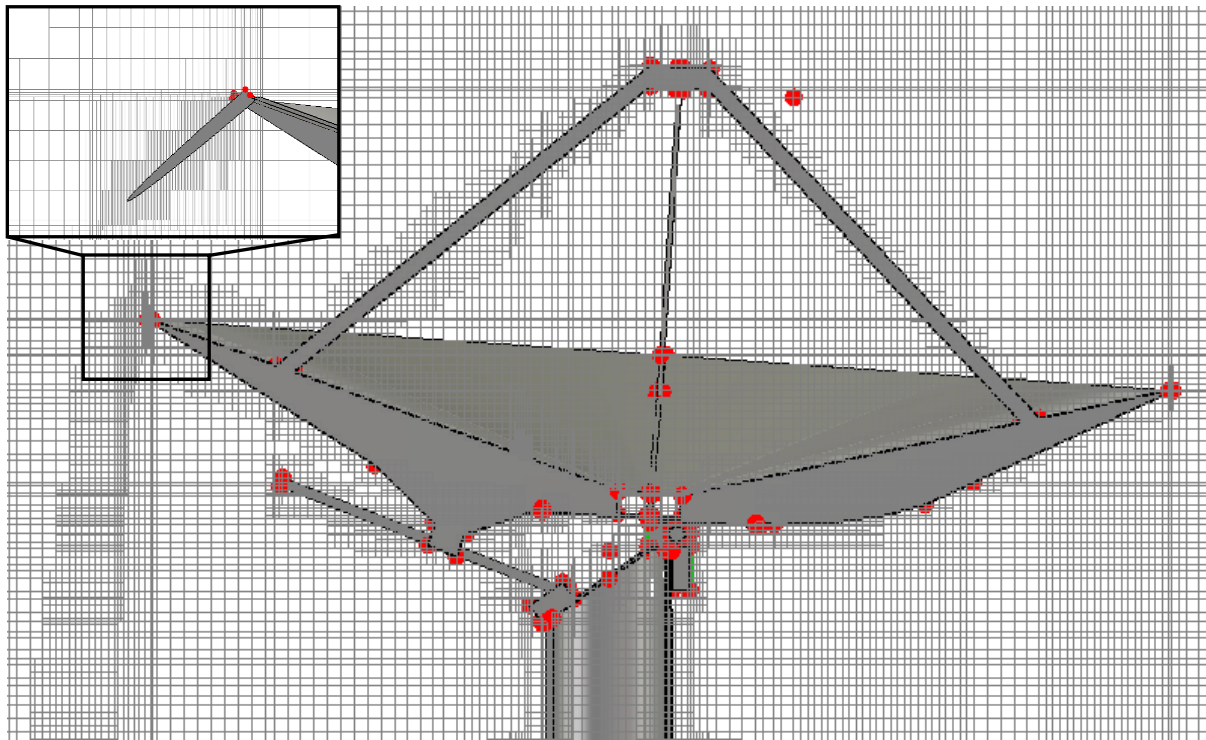


Figure 6.5: Cross-sectional view of the upper half of the scale model implemented in CST MWS. In the mesh view, the change in mesh density as applied by the subgridding algorithm is clearly visible. Note the staircase meshing visible in the insert.

The use of subgridding is, however, only effective in problems where the number of mesh cells can be reduced by at least a factor of four. Otherwise, the associated numerical overhead is substantial enough to potentially increase the simulation time.

6.4. Verification of Measurement and Computation

Initially our focus was on establishing the accuracy of our scale model analysis. Two types of measurements were made on both the physical and computational models when using direct

current injection. Firstly, S-parameters describing the model's input reflection and insertion loss were measured. The comparison of the measured and numerically computed S-parameters for each scenario was used to validate the accuracy of the computational model. Secondly, once agreement of the S-parameters was found, the current flowing on the four earthing connections was determined, again for each scenario. The FSH 8 SA and CM current probe were used to measure the current on the physical model, and Ampère's Integral Law defined around a closed contour was used to compute it in the computational analysis. The measured and computed CM current distributions from both models are compared to the distribution measured on the KAT-7 telescope.

6.4.1. S-parameter Measurements: Scale Models

For the physical model all the measurements were conducted inside the same anechoic chamber described in Chapter 5 section 5.6.2.1. Using a VNA to measure the response of the device provided a closed and calibrated environment. A full two-port calibration was performed.

A schematic of the setup is shown in Figure 6.6. Port one of the VNA is connected to the feed conductor and used to measure S_{11} . Port two of the VNA was moved between each earthing connection terminated in the four SMA connectors described in section 6.3.1. S_{21} therefore, describes the transmission of energy injected by the feed as it moves over the model and through each earthing connection. When measuring on one of the four ports, the remaining three were terminated using 50 Ω loads.

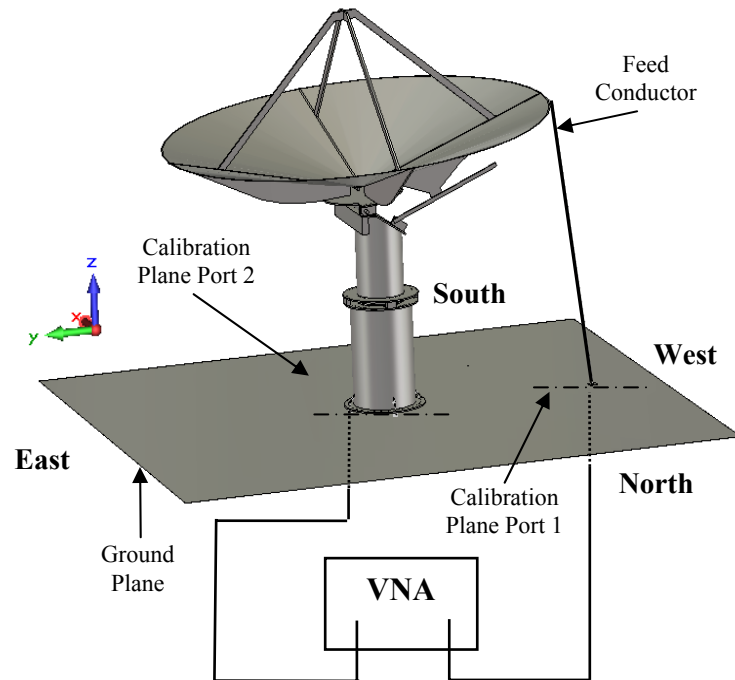


Figure 6.6: Computational model of the KAT-7 radio telescope scenario one aligned, with the measurement setup indicated.

Each earthing connection will be referred to as north, east, south or west-facing depending on their location. The naming according to their placement on the actual dish coincides with the geographical North, East, South and West. It was decided to always position the feed conductor in a westerly direction for aligned scenarios, and in a south-westerly direction for misaligned scenarios on the KAT-7 telescope. This convention was replicated on the scale models with the orientation and position of the feed indicated in Figure 6.6.

Using discrete ports (discussed Chapter 3 section 3.2.3) with the computational model enabled the calculation of S-parameters. Satisfactory computational results were obtained using only discrete ports as terminations, which meant the four SMA connectors present around the foundation of the physical model were omitted. This simplification is indicated in Figure 6.7.

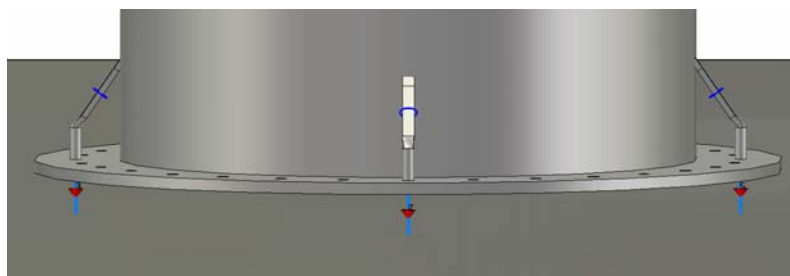


Figure 6.7: No modelled SMA connectors were used for the termination of the four earthing connections. Discrete ports were sufficient.

A comparison of measured and computed S-parameters for the dish positioned in scenario one aligned is shown in Figure 6.8 and Figure 6.9. S_{11} for the feed conductor is shown in Figure 6.8 and S_{21} for all four earthing connections shown in Figure 6.9. Agreement of the results for both models to within 10 dB can be seen, except at certain resonances in some of the S_{21} results.

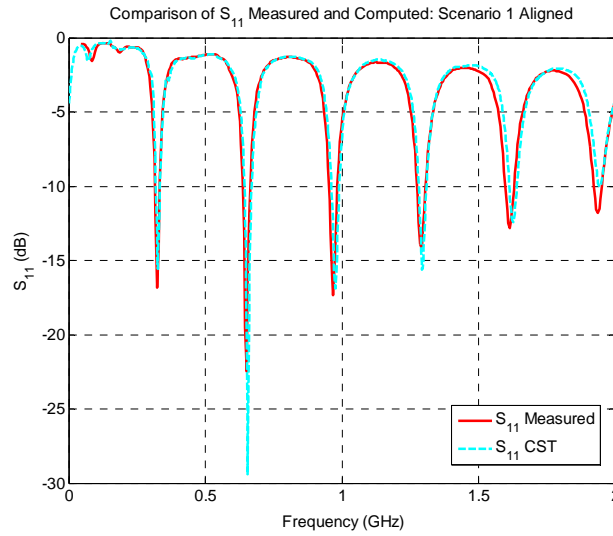
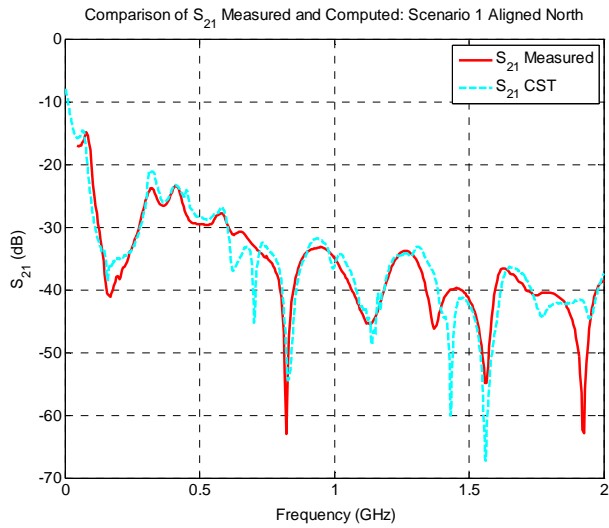
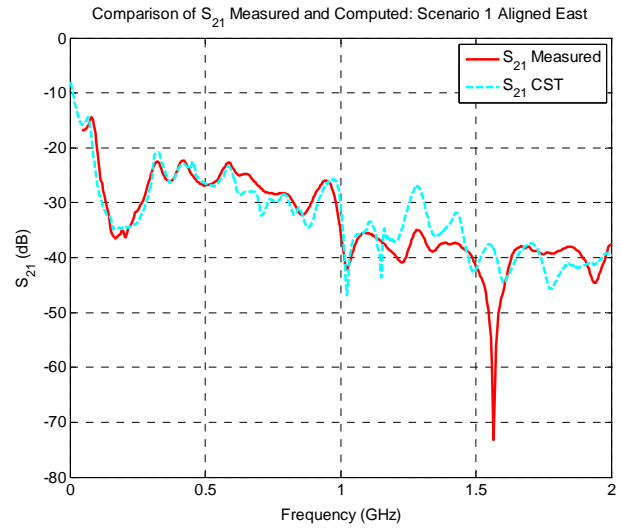


Figure 6.8: Comparison of measured and computed S_{11} for both models in scenario one aligned state.



(a)



(b)

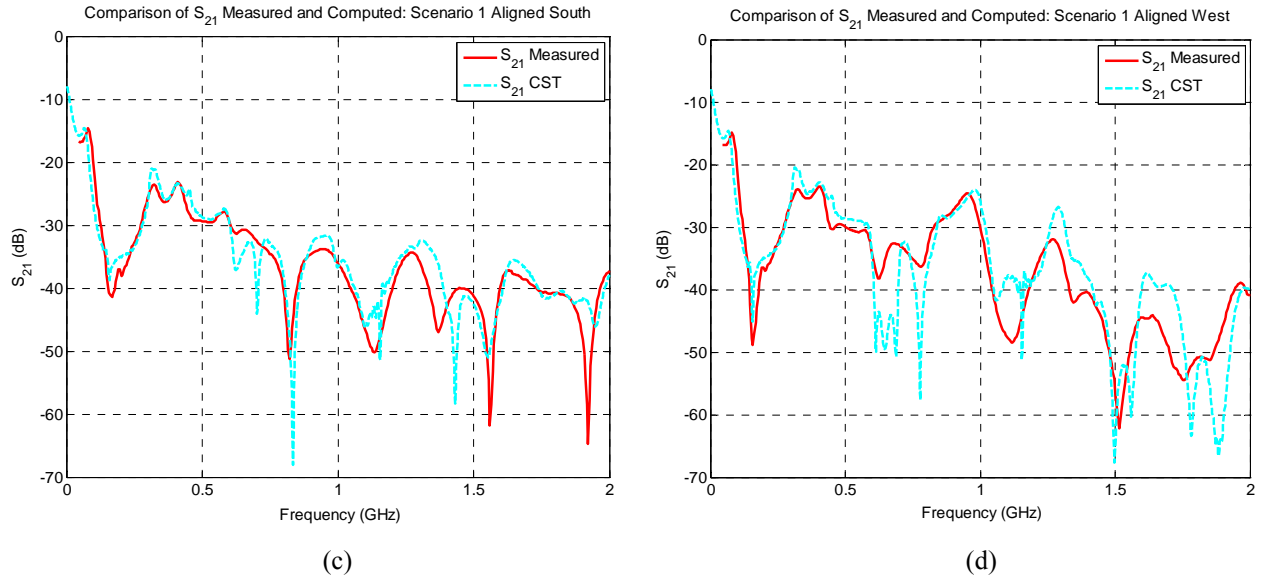


Figure 6.9: Comparison of measured and computed S-parameters for both models in scenario one aligned state. All four earthing connections are shown with (a) north-facing, (b) east-facing, (c) south-facing and (d) west-facing.

Relatively good alignment of resonant frequencies is also evident especially for S_{11} . Small changes in the length and angle of the feed conductor showed significant changes in the results particularly for S_{11} . Slight changes in the elevation angle of the dish proved to change the frequency of certain resonances measured in S_{21} . S_{21} for the north-facing connection for scenario two aligned is shown in Figure 6.10. The alignment of the S-parameter data provided confidence to continue using both scale models in the rest of the investigation.

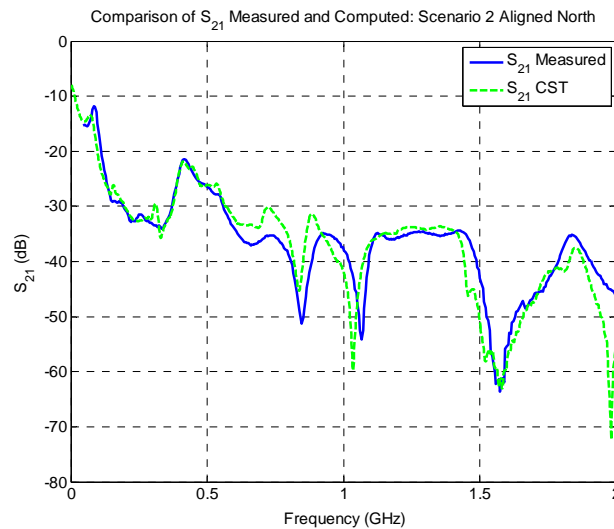


Figure 6.10: Comparison of S_{21} measured and computed using the physical and computational scale models. The north-facing earthing connection for scenario two aligned is shown.

Similarly good agreement is indicated for this scenario between the measured and computed S-parameter. The remaining results for each scenario are shown in Appendix C.

6.4.2. Current Measurements: Scale Models

6.4.2.1. Physical Model

Agreement of the S-parameters provided confidence in the accuracy of both the computation and measurement. This made it possible to characterise the CM current distribution between the four earthing connections. These measurements were made by connecting a CM current probe (see insert Figure 6.4) to port two of the VNA. The detachable probe was connected around each earthing connection on the model. The device's compact design with an inner diameter of 13 mm, limits the size of cable it can measure. Its advantage lies in the 10 MHz to 3 GHz operating bandwidth. The probe's transfer impedance ($Z_{t\ probe}$) is especially flat at close to 22 dB Ω from 400 MHz to 3 GHz. The current flowing on the relevant earthing connection is measured and converted to a voltage through this transfer impedance. This voltage is contained in the S_{21} parameter, which is measured by the VNA. It is, however, required to compensate the measured S_{21} for the input reflection loss associated with the current probe. This compensation technique was described in Chapter 5 section 5.3, but is discussed again for this particular implementation.

The definition of S-parameters is defined in Pozar [46] and given in (49).

$$S_{ij} = \left. \frac{V_i^-}{V_j^+} \right|_{V_k^+ = 0 \text{ for } k \neq j} \quad (50)$$

In (50) V_j^+ is the incident voltage at port j and V_i^- the transmitted voltage measured at any one of the four terminating ports represent as i . Assuming that $V_j^+ = 1 \angle 0^\circ$ V for all frequencies, the measured S-parameter in (50), $S_{ij\ measured} \cdot 1 \angle 0^\circ = V_i^-$ effectively gives the measured voltage at port i . For this investigation, $S_{ij\ measured}$ has to be compensated for the reflection loss of the CM current probe. The definition of the voltage waves as given in Chapter 5 section 5.3 in (26) is again used to show the compensation. The same representation of the S-parameter as a power ratio given by (31) is used in (51). The excitation voltage defined above is also included.

$$\frac{P_{delv-in}}{1} = \frac{|b_i|^2}{1} = \frac{|V_i^-|^2}{1} = |S_{ij\ measured}|^2 \quad (51)$$

In this case the available power is from the current probe used to measure the CM current. The same conversion as used in (32), is implemented to obtain the delivered power from the current probe. This can be related to the delivered voltage from the current probe as follows:

$$\frac{P_{ava-in}}{1} = \frac{|V_i^-|^2}{(1-|S_{ii}|^2)} = \frac{|S_{ijmeasured}|^2}{(1-|S_{ii}|^2)} \quad (52)$$

The current probe is placed around the connection. Incorporating the influence of the probe, the output voltage $V_{i\ probe}^-$ can be converted to obtain a correct indication of the current on the connection (see insert Figure 6.4). The resulting current is finally calculated from the voltage by using the transfer impedance ($Z_{t\ probe}$), of the probe show in (53).

$$\frac{V_{i\ probe}^-}{Z_{t\ probe}} = I_{connection} \quad A \quad (53)$$

As a method of verification, the measurement was repeated for all connections and all scenarios. Instead of using the VNA as receiver, the current probe was connected to the FSH 8 SA. Using the FSH 8 SA means no power cable could be involved in possible ground loops. The VNA still excited the system at port one over a reduced 51 discrete frequency points. The SA was swept across the same band in a maximum-hold mode. To obtain the compensated probe voltage $V_{i\ probe}^-$, the reflection loss of the probe as well as the transmission loss of the cable used to connect the probe to the FSH 8 SA, had to be added to $V_{i\ probe}^-$. Once this was done the current could again be calculated by including the probe $Z_{t\ probe}$ as shown in (53). Comparisons between results obtained using the VNA and SA to measure the currents on the same north-facing connection for scenario one aligned and misaligned are shown in Figure 6.11 (a) and (b).

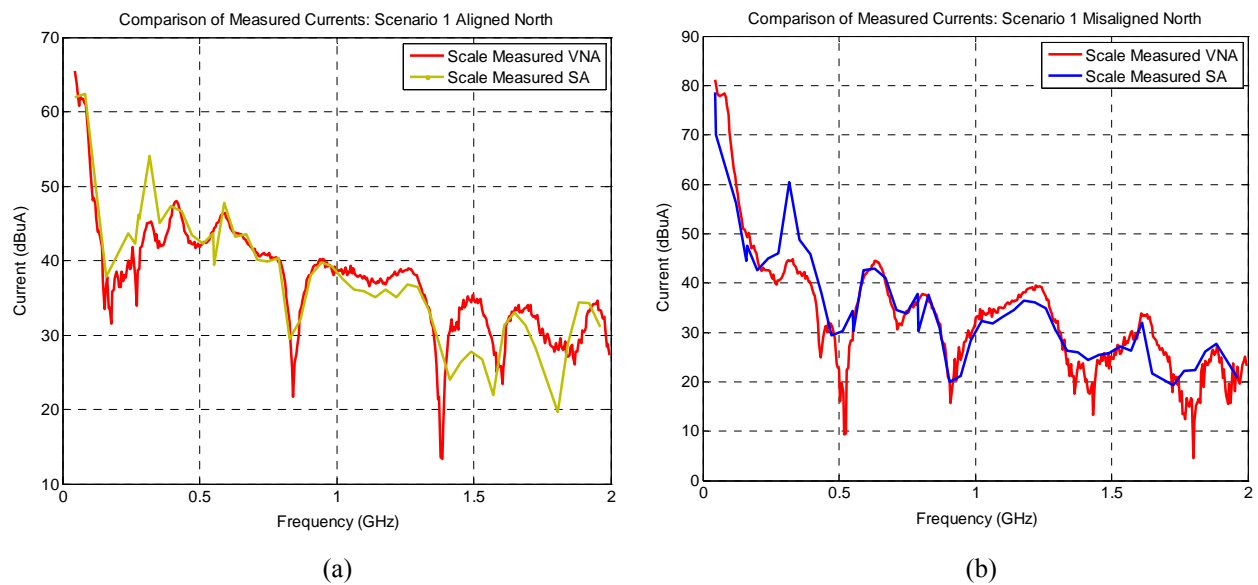


Figure 6.11: Comparison of measured current using the VNA and SA as receiver. The currents were measured on the north-facing earthing connection for (a) scenario one aligned and (b) scenario one misaligned.

Small differences between the results using the two techniques can be seen. This can be attributed to the fact that the SA measurements are not calibrated. The assumption that $V_j^+ = 1 \angle 0^\circ$ V for all frequencies is not valid anymore. The source voltage from the VNA is used in its raw format which will vary with frequency both in terms of magnitude and phase. The SA, contrary to the VNA, measures the response of the system according to this raw voltage. Additionally, sweep time and resolution bandwidth settings on the FSH 8 SA will also determine how accurately resonant features are sampled. The results for all the remaining scenarios are shown in Appendix C.

6.4.2.2. Computational model

Determining the currents on the connections in the computational analysis required the use of Ampère's Integral Law as given by (54) Haus et al. [52]. This relates the magnetic field intensity around a closed contour to its source, the current density.

$$\oint_C H \cdot ds = \int_S J \cdot da + \frac{d}{dt} \int_S \epsilon_0 E \cdot da \quad (54)$$

The setup in CST MWS used for this calculation is shown in Figure 6.12 with the contours defined around each earthing connection indicated.

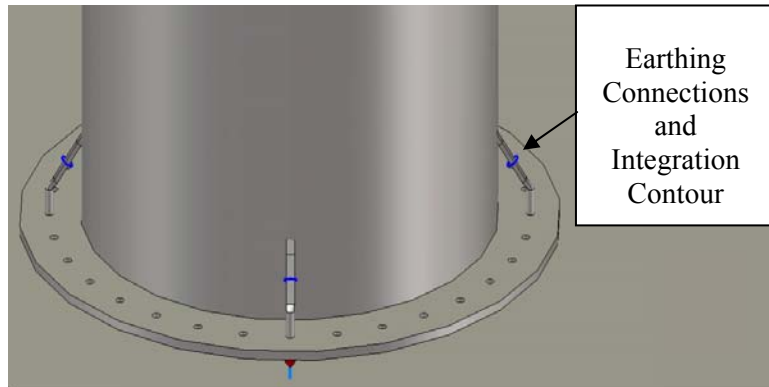


Figure 6.12: Computational representation of the earthing connections. The closed contours around which the magnetic fields are integrated are also shown.

The current density is calculated by integrating the known magnetic field intensity around each contour denoted by C . It is considered to be a quasi-static problem which assumes that the displacement flux density $\epsilon_0 E$ is zero. This then provides the current through an area enclosed by the contour C . Assuming this to be a line current on an infinitely thin wire, (55) as given by [52] provides the current in Amperes.

$$i = \lim_{\substack{|J| \rightarrow \infty \\ A \rightarrow 0}} \int_A J \cdot da \quad \text{A} \quad (55)$$

The comparison of the current calculated in CST MWS using (54) and (55) for the north-facing earthing connection of scenario one aligned is indicated in Figure 6.13. Computational intensity led to the selection of only 11 frequency points used to verify the trend in the distribution. Results for the remaining scenarios are also shown in Appendix C.

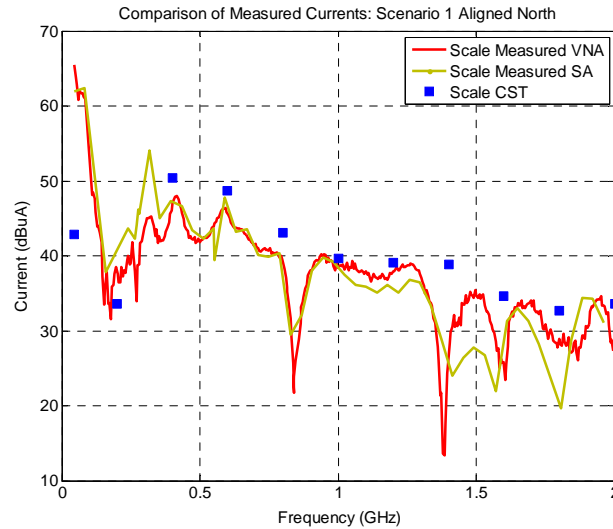


Figure 6.13: Comparison between measured results using a VNA and SA as receiver, and computed results using CST MWS.

The prediction of current using the computational analysis is, on average, within 5 dB of the measured values. The differences between the measured and computed results in this case, are attributed to the variation in the excitation of the VNA compared to the discrete S-parameter port used in CST MWS. As explained in [21], the discrete S-parameter port in the computation realises an input power of 1 W for all frequencies. Despite S-parameters traditionally being defined in terms of a voltage ratio, according to [23], S-parameters can be defined as a power wave ratio. However, the power applied to port one of the DUT by the VNA, is by no means constant. In the middle of the operational band of the VNA's directional coupler, it can be approximated as constant. Variations in power are accounted for and corrected through the calibration of the VNA. CST MWS cannot be calibrated, but it does not have to be. It applies the constant power to the relevant discrete S-parameter port. Because it knows what the corresponding outgoing voltage time signal is, it can normalise the incoming voltage time signal accordingly to create the required S-parameter in terms of voltage. The slight offset in the results is therefore attributed to the fact that the excitation of the physical model at port one by the

VNA, is not constant as is the case in CST MWS. The fact that the variations in Figure 6.13 are so small is a tribute to the accuracy of the VNA.

6.4.3. Current Measurements: KAT-7 Telescope

On-site measurements of a non-hardened KAT-7 telescope were made using the FSH 8 SA with VNA-mode capability. The measurement setup is shown in Figure 6.14. Both calibrated and uncalibrated measurements were made on the telescope. When measuring in an uncalibrated state the FSH 8 is still calibrated up to its two measurement ports [53]. Calibration of the device therefore only removes effects added outside of the instrument. For the current measurements, that effectively removed the influence of the cable connected to the CM current probe. However, due to the low-loss of the cable little difference between results measured in a calibrated or uncalibrated state was seen. The feed cable used for the direct current injection seen in Figure 6.14, was included in both scale models and so does not need to be removed from the data.

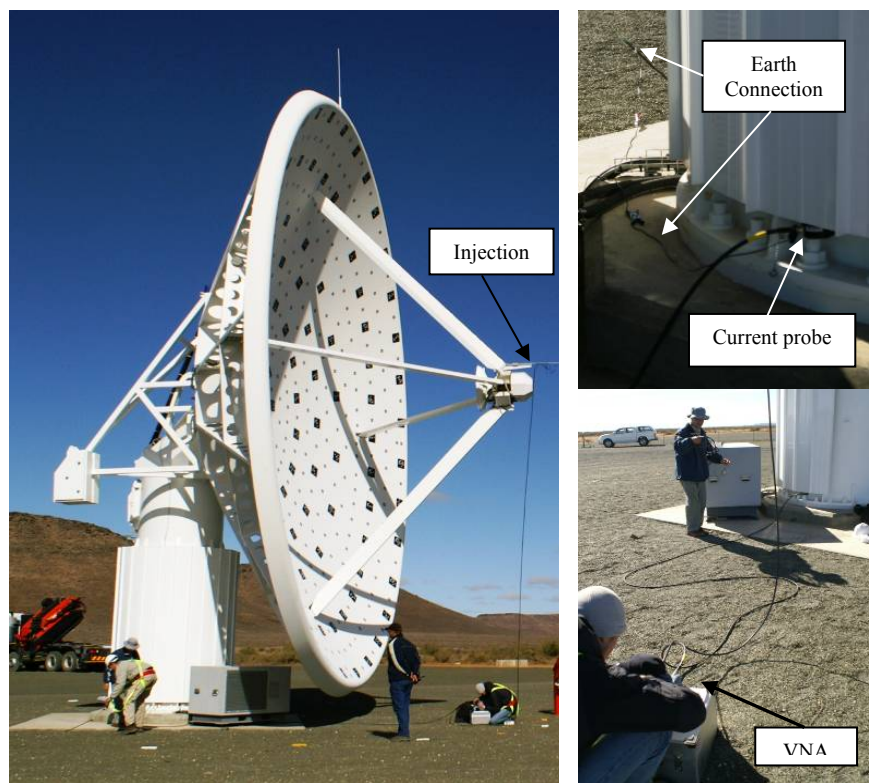


Figure 6.14: Setup illustrated for making current measurements on KAT-7 telescope using FSH 8 SA in VNA mode.

The two port setup, similar to that discussed in section 6.4.1, is seen in Figure 6.14 where port one connects to the LDC on the feed of the antenna. Port two is connected to the current probe measuring the CM current on each connection. An additional earth return path, which is

modelled differently, had to be created to provide a closed conductive path for the injected current to flow in. This was done using a physical wire as shown in Figure 6.14.

For the measurements on the KAT-7 telescope the frequencies under investigation were 100 kHz to 100 MHz. This relates to a range of 2 MHz to 2 GHz for the scale models. The linear scaling factor means it is possible to directly compare measured results of the two scale models with results from and KAT-7 telescope. This comparison for the current measured on the north-facing earthing connection for all four scenarios is shown in Figure 6.15. Here the comparison is for measured results of the physical scale model using the VNA and FSH 8 SA, computed results using the computational scale model, and KAT-7 telescope measurements.

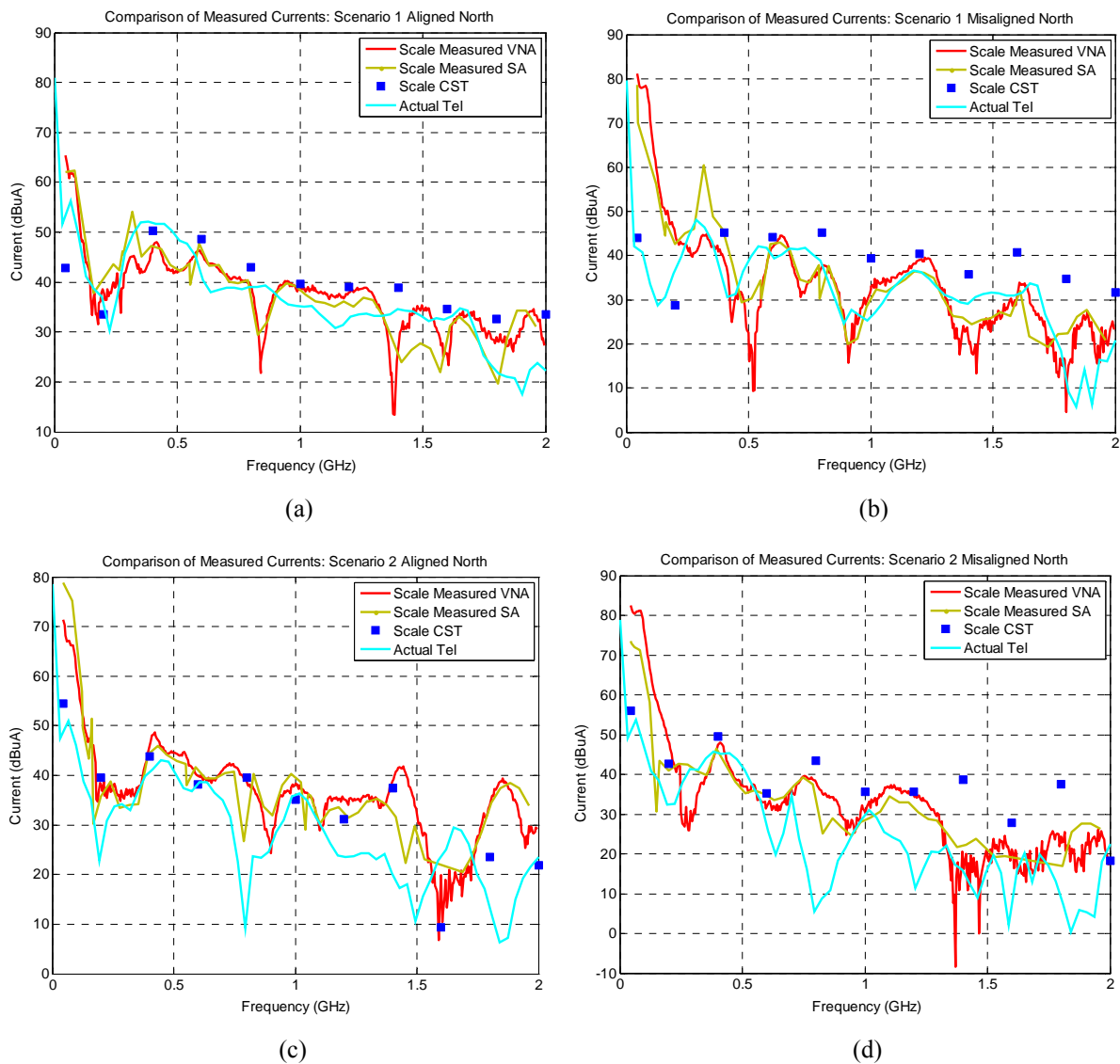


Figure 6.15: Comparison of currents flowing on the north-facing earth connection. These include measured results for the physical model using the VNA and SA, computed results for the computational model, and measurements on the KAT-7 telescope. Results are shown for (a) scenario one aligned, (b) scenario one misaligned, (c) scenario two aligned and (d) scenario two misaligned.

Overall level agreement is achieved for the results in Figure 6.15. However, certain resonant features for the KAT-7 telescope measurements are less accurately represented by both scale model results. The results have to be considered while keeping in mind the differences in how the models and the KAT-7 telescope are earthed. In the models, current is injected at port one onto the structure with the feed conductor, and returns to port one via the ‘perfectly conducting’ ground plane. The earthing connections connect the telescope to the ground plane through $50\ \Omega$ loads. With the KAT-7 telescope there is no perfect ground plane, just real earth. The earth return path, mentioned earlier, created by connecting the outer conductor of one of the VNA ports to the telescope earth (Figure 6.14), is not ideal. It did provide a closed path for the current injected at port one, and changes in the S_{21} results were noticed when it was not connected. Inductive and capacitive differences between these two paths will contribute significantly to the absence of some resonant features in Figure 6.15. Results for the remaining connections are shown in Appendix C.

6.4.4. Discussion

For the first part of this chapter, the focus was on establishing reliable physical and computational scale models, which can be used to provide accurate results for further analysis. The two scale models were initially compared with each other through measured and computed S-parameter data (Figure 6.9 and Figure 6.10). Once agreement was obtained, the next step was to measure the distribution of CM current on four earthing connections which forms part of an LDC system installed on the telescope. The CM current was directly injected onto the structure. Different measurement techniques were compared where a CM current probe was connected either to a VNA or an FSH 8 SA. The measurement of current for the same connections in the computational analysis was made. Good results for the current were again found when comparing the two models (Figure 6.13).

The ultimate goal was to replicate results, as part of a site audit, from a non-hardened KAT-7 telescope. A similar measurement procedure which injects CM current directly onto the structure was used. The measurements (Figure 6.15) are in relatively good agreement with computation. The agreement is good enough to trust either of the scale models for further analysis. Differences between the measurement environments could explain some of misalignments seen in the results. The influence of the physical differences between each version of the telescope is noticeable.

Part 2 – Measurement Setup Evaluation

6.5. Current Distribution on KAT-7 Telescope

This part of the chapter examines the possible influence the direct injection method used to establish the CM current on the telescope, might have on the measured distribution. Initial comparisons are for distributions measured using a direct current injection method, explained in section 6.3.1, with different alignments of the feed conductor. This is compared to the distributions measured when inducing the CM currents by antenna illumination. Results from a non-hardened KAT-7 telescope, as well as measurements using the physical model, are considered in determining how the distribution might be affected.

6.5.1. Influence of Direct Injection

As indicated, the feed conductor was positioned west for the aligned case, and south-west for the misaligned case. The distribution measured on the four earthing connections on the KAT-7 telescope for scenario one aligned is shown in Figure 6.16 (a); the misaligned scenario is shown in Figure 6.16 (b). From Figure 6.16 (a) it is clear that for the aligned case the most current was measured on the west-facing connection for almost all of the frequencies investigated. Note that the unscaled frequencies of 100 kHz to 100 MHz are used.

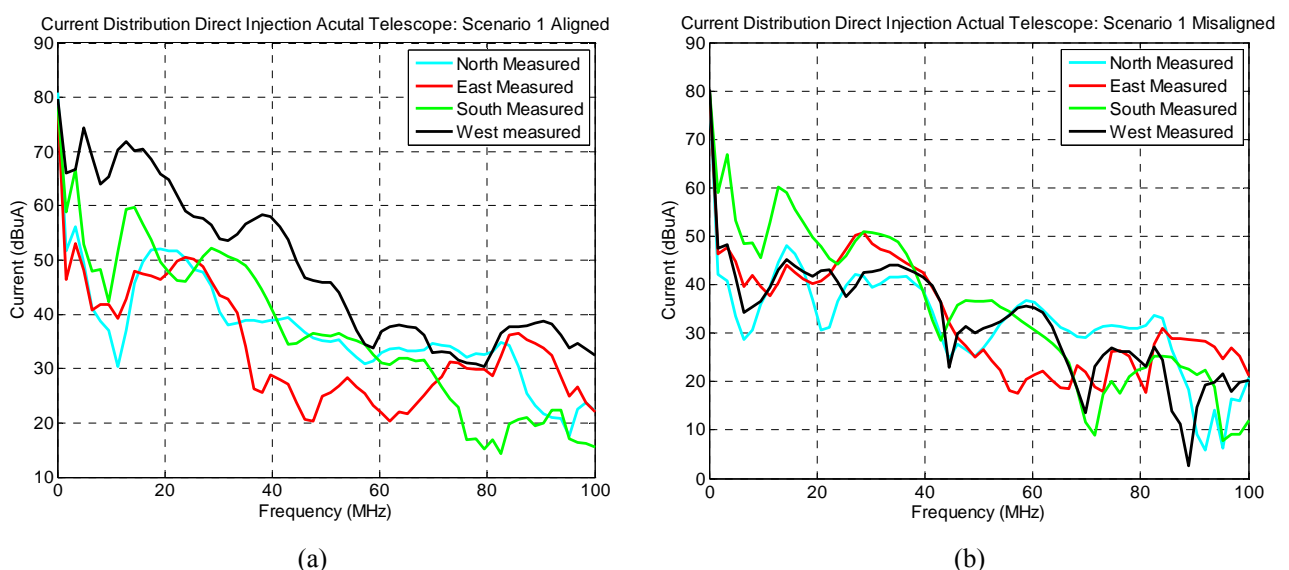


Figure 6.16: Comparison of injected currents measured on the four earthing connections for the KAT-7 telescope. Scenario one aligned is shown in (a) and misaligned shown in (b).

A more even distribution is seen for the misaligned case shown in Figure 6.16 (b). Here current on the west-facing connection has decreased, while remaining relatively constant on the other three connections. Whether the misalignment of the feed is the only reason that a more even distribution was measured, is not entirely clear. The reason being that for the misaligned scenarios, the current path between the upper and lower pedestal, explained in section 6.2, is interrupted and could also contribute to the change in distribution measured.

A further investigation made use of the physical scale model in a third scenario. The dish was kept in the stow position with only the feed conductor still misaligned. The dish, and therefore the upper pedestal, was rotated back to again align the copper shoes with the earthing connections. The additional scenario was an attempt to isolate which of either the shoes, or the feed conductor, had the bigger influence. The results are shown in Figure 6.17.

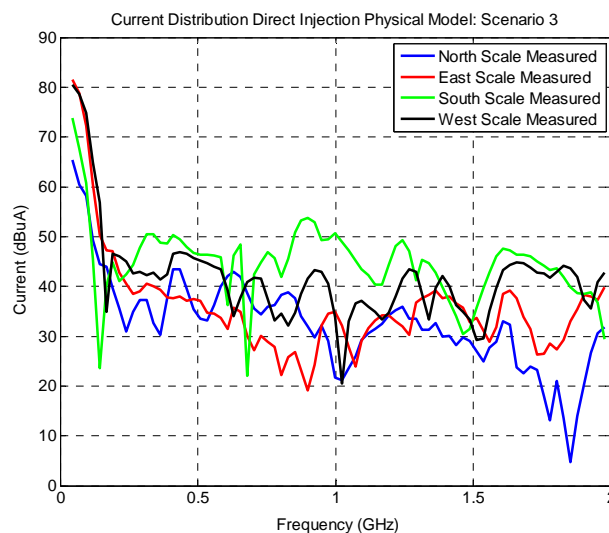


Figure 6.17: Comparison of injected currents measured on the four earthing connections for the physical scale model for scenario three.

From Figure 6.17 it is clear that the west-facing connection did not regain the level of current seen in Figure 6.16 (a) when the copper shoes and earthing connections were brought back into alignment. Continuing the investigation, a fourth scenario was created with the dish remaining in the stow position. Here the feed conductor was again aligned, but the dish and upper pedestal were rotated to misalign the copper shoes and earthing connections. The results are shown in Figure 6.18 which indicates a similar distribution to scenario three.

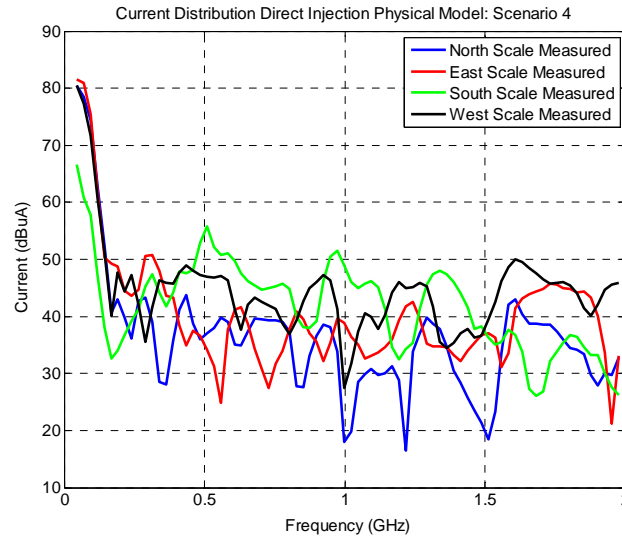


Figure 6.18: Comparison of injected currents measured on the four earthing connections for the physical scale model for scenario four.

From Figure 6.17 and Figure 6.18, it is fair to conclude that neither the alignment between the feed conductor and the earthing connections, nor the copper shoes and the earthing connections is the dominant influence. The CM current distribution around the lower pedestal is influenced by a combination of the two. To better understand the implications of changing the alignment of various objects, the average current for each scenario investigated was determined. The averages are shown in Table 6:1. Although not presented elsewhere, the results for scenario two aligned and misaligned were also measured and are represented in Table 6:1. A similar change in distribution to scenario one is seen when changing scenario two aligned to misaligned. Plots of the currents for each of these two scenarios are available in Appendix C.

Table 6:1: Comparison of average injected currents measured on the four earthing connections.

| | Scenario 1 Aligned (dB μ V) | Scenario 1 Misaligned (dB μ V) | Scenario 2 Aligned (dB μ V) | Scenario 2 Misaligned (dB μ V) | Scenario 3 (dB μ V) | Scenario 4 (dB μ V) |
|--------------|---------------------------------------|--|---------------------------------------|--|----------------------------|----------------------------|
| North | 36.87 | 32.24 | 28.43 | 24.59 | 34.75 | 31.31 |
| East | 34 | 32.87 | 24.86 | 26.04 | 38.57 | 34.27 |
| South | 36.69 | 35.40 | 25.17 | 29.47 | 40.35 | 43.26 |
| West | 48.31 | 32.32 | 42.75 | 28 | 42.92 | 40.16 |

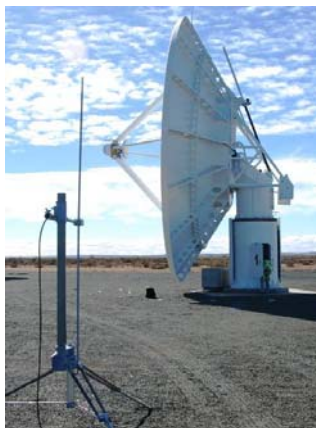
Comparing the averages with a complete alignment in scenarios one and two, the closest connection to the feed carries the most current. The field coupling associated with the feed conductor, mentioned in Section 6.3.1, enhances the current flowing down the structure along a defined path. When the feed conductor is moved and the current path between the upper and lower pedestal interrupted (scenarios one and two misaligned) a more even distribution is

obtained. Field coupling still takes place but now the rotation ring in the middle of the pedestal, to which the copper shoes make contact, distributes the current more evenly.

For scenario three, the feed conductor was misaligned but the shoes were kept in alignment. Despite the shoes and earthing connections creating a direct path for the injected current down to ground, the field coupling is concentrating the induced current between two connections. This sees the south and west-facing connections carrying more current than the north and east-facing. For scenario four the highest average current is on the south and west-facing connection. Ultimately, the distribution around the four connections is influenced by a combination of factors which include the position of the feed conductor. Depending on the type of experiment of interest, the direct injection technique still provides a reliable method of system excitation. The comparative distributions for induced currents through field coupling only, are considered in the following investigation.

6.5.2. Induced Current Distribution

With this technique, antennas were used to illuminate the telescope inducing CM current on the structure through E and B-field coupling. The process involved two antennas covering most of the 100 kHz to 100 MHz band. A sweeping signal generator was used as the source, and an FSH 8 SA and current probe were used to measure the CM current distribution. Measurements were only made for scenario one and two aligned, with a vertically polarised E-field. For each scenario, the dipole (Figure 6.19 (a)) was used from 25-80 MHz, and the LDPA (Figure 6.19 (b)) from 80-100 MHz.



(a)



(b)

Figure 6.19: Illumination measurement done on one of the KAT-7 telescopes for (a) scenario two aligned and (b) scenario one aligned.

For both cases the radiating antenna was positioned due-south, illuminating the structure side-on. Various closed conductive loops are formed by different components on the structure. The most noticeable two are firstly the elevation drive and backing structure, and secondly the feed struts in front of the dish. With the vertically polarised E-field, horizontally polarised B-fields will intersect these loops, increasing the amount of coupling to the telescope. Also, for scenario two, the amount of energy reflected by the dish surface is minimised when radiating it from the side. The result for the distribution for scenario one aligned is shown in Figure 6.20 (a) and for scenario two aligned shown in Figure 6.20 (b).

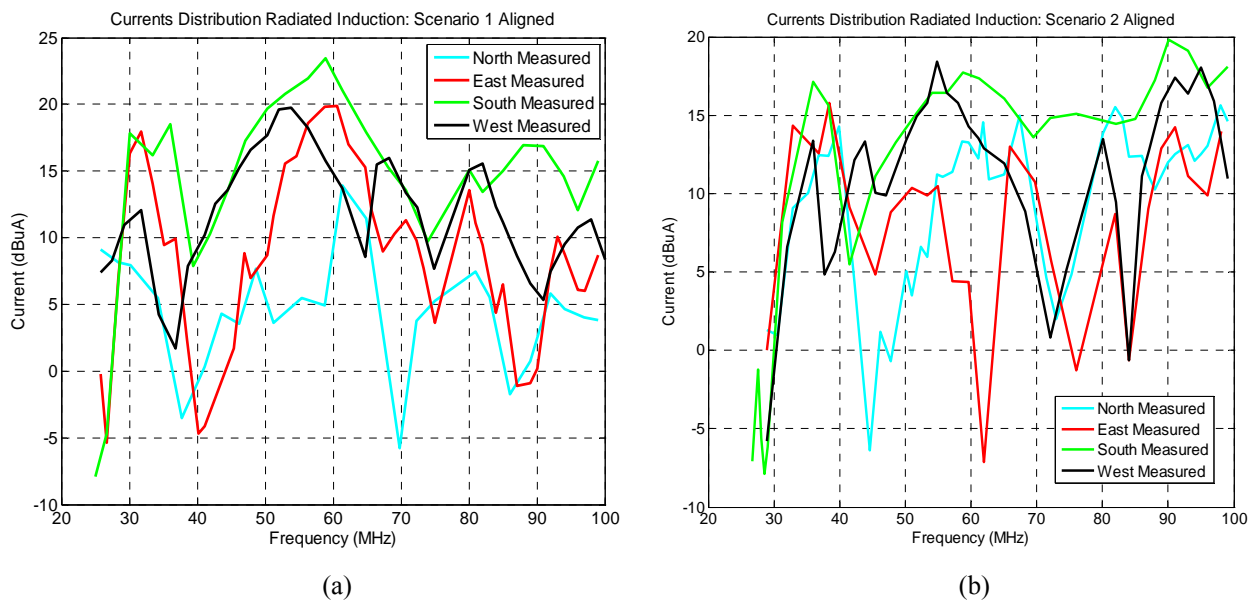


Figure 6.20: Comparison of induced currents on the four earthing connections of the KAT-7 telescope with scenario one aligned shown in (a) and scenario two aligned shown in (b).

The south-facing connection measured slightly higher levels for most of the band, with the east and west-facing connections showing similar levels. This is not unsurprising as most of the current will be induced on the south-facing surface of the pedestal. This was also observed for scenario two aligned (Figure 6.19 (a)) for which the results are shown in Figure 6.20 (b).

Variations of 10-20 dB between the minimum and maximum currents measured are seen for both scenarios. This is because the telescope is a more efficient receiver at certain frequencies than at others. The variation of the transmitting antenna's gain will also influence the results; for this investigation these are not removed from the data. The purpose of the experiment is to do a relative comparison of CM current measured on each of the four earthing connections. Because of the variation in the measured levels seen in Figure 6.20 (a) and (b), an average is again calculated for the above two scenarios for each connection. The results are shown in Table 6:2.

As part of a follow-up measurement audit, CM current distribution measurements will be made for the misaligned scenarios when making use of the illumination method of excitation.

Table 6:2: Comparison of average induced currents measured on the four earthing connections.

| | Scenario 1 Aligned (dBμV) | Scenario 2 Aligned (dBμV) |
|--------------|---|---|
| North | 4.53 | 9.76 |
| East | 8.53 | 8.84 |
| South | 14.59 | 11.9 |
| West | 11.44 | 11.2 |

6.5.3. Discussion

A similar direct current injection method, discussed in Chapter 2 section 2.9, is used actively by the aviation industry to do High-Intensity Radiated Field (HIRF) testing on aircraft. It has been gaining favour over illumination measurements. One of the reasons, as discussed in [30], is because direct injection produces significantly higher levels of surface current density than what can be achieved using illumination methods. In the study of avionic system susceptibility inside the aircraft fuselage, similar results have been obtained when using direct injection compared to free-field illumination. However, the type of return conductor used, also discussed in Chapter 2 sections 2.9.1 and 2.9.2, does influence the distribution of surface current observed on the DUT [31].

The results shown in Table 6:1 seem to agree with the observation in [31] and what has been found in aircraft testing, but it is also dependent on the alignment of the current path established on the outside of the telescope. When using the direct injection, the aligned scenarios show an average difference of more than 10 dB between the highest and lowest measured current. It is assumed that the alignment of the LDCs on the upper pedestal with the copper shoes and earthing connections provides a direct current path to ground. This, coupled with an asymmetrical injection position, leads to a non-uniform current distribution. Comparatively, the average results in Table 6:2 show a smaller difference between the highest and lowest current that was measured for the illumination measurements. More current is still present on the side of the telescope facing the illuminating antenna, but the difference is smaller.

Concluding this part of the chapter it is stated that both methods of system excitation are valid. The EMC testing that is performed for a particular device, should determine which method of excitation (direct injection or illumination) is more appropriate. The results ultimately confirm that the illumination method is less intrusive in establishing CM current on the telescope than the direct injection method. This would continue to be true if the frequencies under investigation were increased. However, to accurately determine the effectiveness of the shielding measures installed on a hardened telescope, higher levels of CM current on the telescope structure and the relevant equipment cables are required. The reason for this is to ensure enough dynamic range to be able to measure the full extent of the shielding provided by the interfaces. If the CM current measured outside the shielded environment is too low, the attenuated signal inside would be in the noise floor and therefore immeasurable. Comparing Table 6:1 and Table 6:2 high enough levels of CM current can only be achieved with the direct injection method.

Part 3 – Evaluation of Shielding Measures

6.6. Comparison: Hardened vs. Non-hardened Telescope

The inherent operational sensitivity of the KAT-7 radio telescope requires EMI mitigation measures surpassing that of most commercial applications. The objective of hardening a telescope was to create a shielded lower pedestal that minimises RFI entering or exiting this volume. This required installing continuous metallic interface barriers to serve as the floor and ceiling of the pedestal. All braided cables entering the pedestal would do so through individual 360° connectors with the braiding correctly terminated. Compressible RF gasketting would be used on the access door to ensure a galvanic seal once it is closed. EMC cabinets would house the dish control and antenna feed electronics. Collectively all these shielding measures would combine creating a pedestal hardened against RFI.

The shielding measures described, with exception of the EMC cabinets, were post-build additions. This made their ideal implementation difficult. The interface barriers had to be multi-sectioned (Figure 6.21 (a)) to enable installation. The various sections were joined at seams, each of which required gasketting for reasonable galvanic connection. However, each join was a possible weak point in the shielding interface. Also, as seen from Figure 6.21 (b), tabs provided the connection between the interface and the cable braiding for the cables entering through the

barrier. Such an interface had to be used because removing and reconnecting the cables was not possible. The asymmetrical connection between the tab and the cable braiding is reasonable but less effective than a 360° connection. The cable braiding, in some instances, did not extend to connect to the EMC cabinets, and was not properly terminated in the upper pedestal.

Despite the hardening measures not being implemented ideally, it was the best first-effort. Improving the shielding in a developing project such as this is an interactive process, which requires feedback to justify expenditure of both time and money. This section presents the findings of the investigation made on the initial hardening attempt. This was accomplished by investigating the differences in the exterior current levels measured between a hardened and non-hardened telescope. The added shielding influenced the amount of CM current entering the pedestal and this reflected in the current flowing on the outside of the structure.

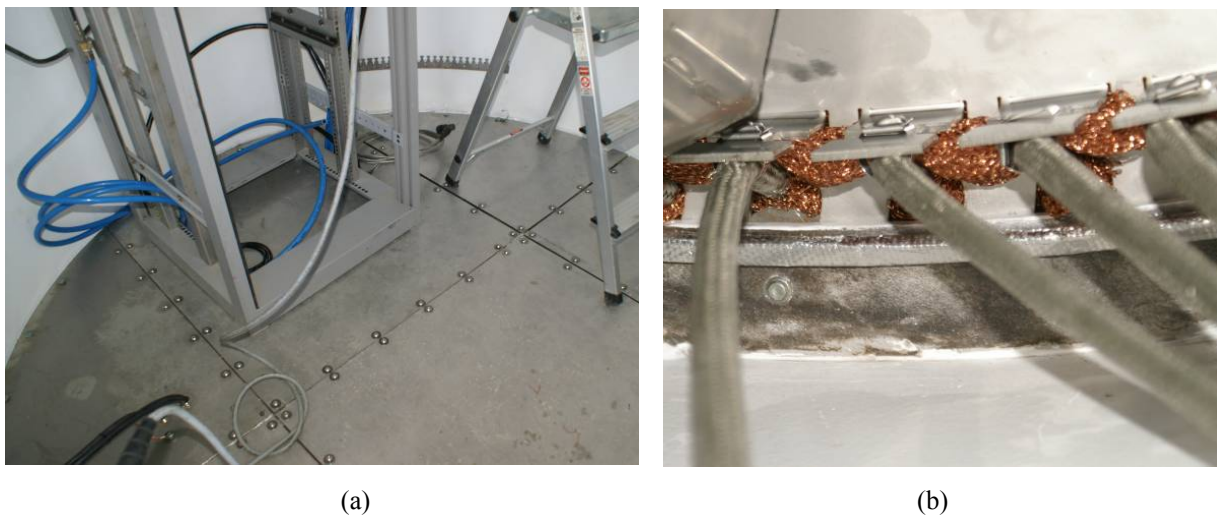


Figure 6.21: The hardening policies used in one of the KAT-7 telescopes include (a) a multi-sectioned metallic interface plate and (b) gasketing added to interface for braided cables.

6.6.1. Hardened vs. Non-hardened for Direct Injection

Comparison between a hardened and non-hardened telescope is firstly made for the direct current injection method. The increase in measured CM current as a result of the shielding measures is clearly noticeable when comparing aligned and misaligned results for a particular connection. The results shown in Figure 6.22 are for the west-facing connection for scenario one.

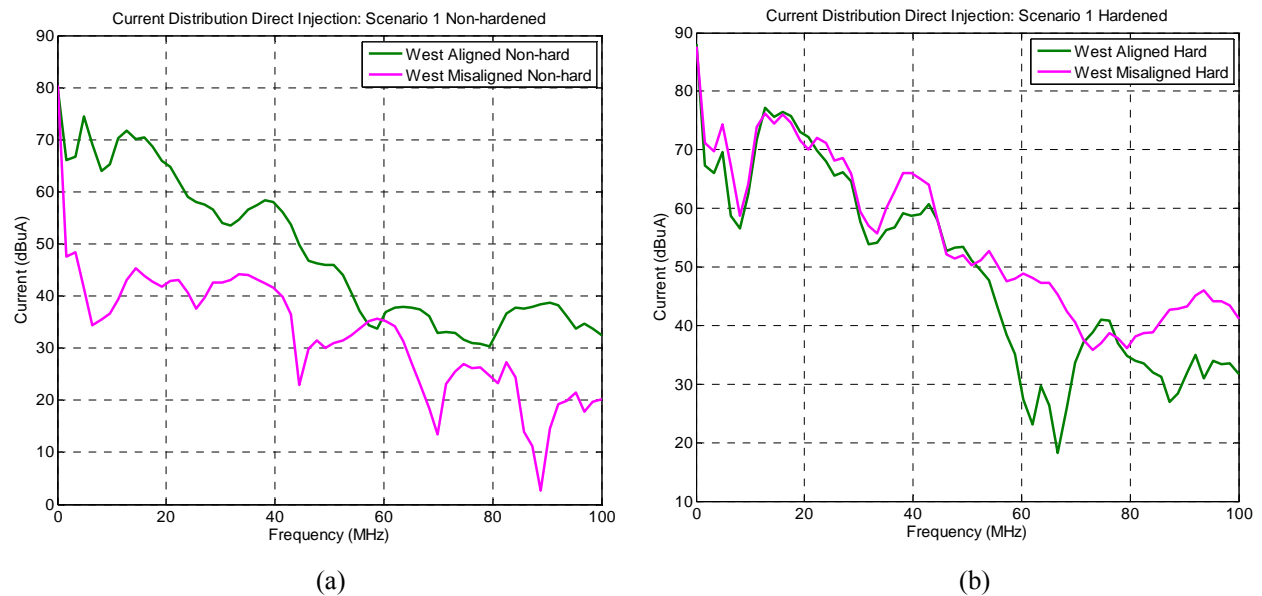


Figure 6.22: Current measured on the west-facing connection for scenario one aligned and misaligned compared for (a) a non-hardened telescope and (b) a hardened telescope.

It is assumed that for the aligned case the LDCs on the upper pedestal, along with the copper shoes and earthing connections on the lower pedestal, form a direct current path to ground. CM current flowing down the pedestal to ground does so either on the outside or the inside of the pedestal. If the assumption of a more direct path for the aligned scenario is correct, less current will flow on the inside of the pedestal. As a consequence the current measured on the earthing connections for the non-hardened telescope should be higher when the dish is aligned, than when it is misaligned. The misalignment interrupts this direct current path. This leads to more current flowing on the inside of the pedestal attempting to find an alternative path to ground. The results shown in Figure 6.22 (a) do in fact verify this point and confirm a change in CM current.

The hardened telescope, on the contrary, shows only a small difference when comparing the aligned and misaligned results (Figure 6.22 (b)). It is only a small difference because the bulk of the current is already flowing on the outside of the pedestal as a consequence of the hardening policies that were added. The hardening policies, despite being incomplete, are therefore providing a certain level of shielding. The aligned scenarios do not indicate this point very clearly. The misaligned scenarios which creates a less defined path, increases the amount of current wanting to enter the inside of the pedestal. As a result, a more substantial difference between a hardened and non-hardened telescope is seen for these scenarios. This result is consistent for the remaining connections which are shown in Appendix C.

6.6.2. Hardened vs. Non-hardened for Induced CM Current

A comparison is made for the induced currents from the radiated measurements presented in section 6.5.2. Results for the west-facing connection are shown with comparison between a hardened and a non-hardened case. As before, for the illumination measurements, only scenario one and two aligned were measured. The comparison for scenario one aligned is shown in Figure 6.23.

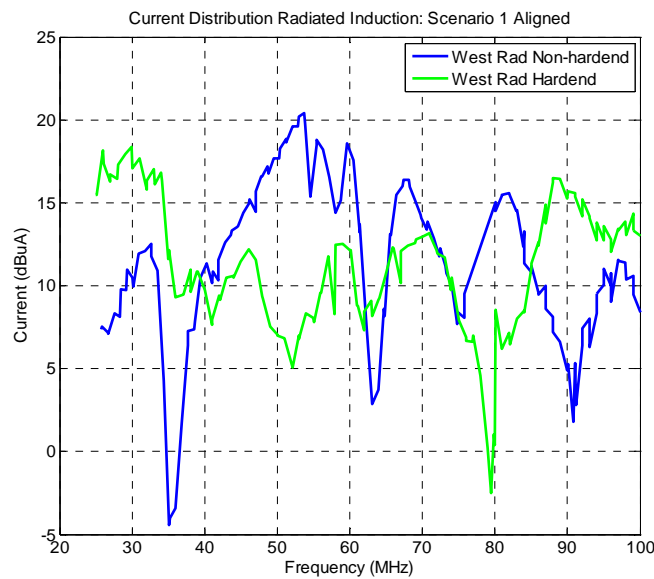


Figure 6.23: Current compared for a hardened and non-hardened telescope for scenario one aligned.

From the results shown in Figure 6.23 neither of the two cases shows a definitively higher current level. The average measured level for the non-hardened telescope was 11.4 dB and for the hardened telescope 11.2 dB. This is as expected with an aligned scenario, because most of the current seems to be already flowing on the outside of the pedestal due the clearly defined current path. Similar results can be seen for scenario two aligned which is shown in Figure 6.24. The hardened case is only higher for certain parts of the investigated band. Here average levels of 11.2 dB and 15.3 dB were measured for the non-hardened and hardened telescopes respectively.

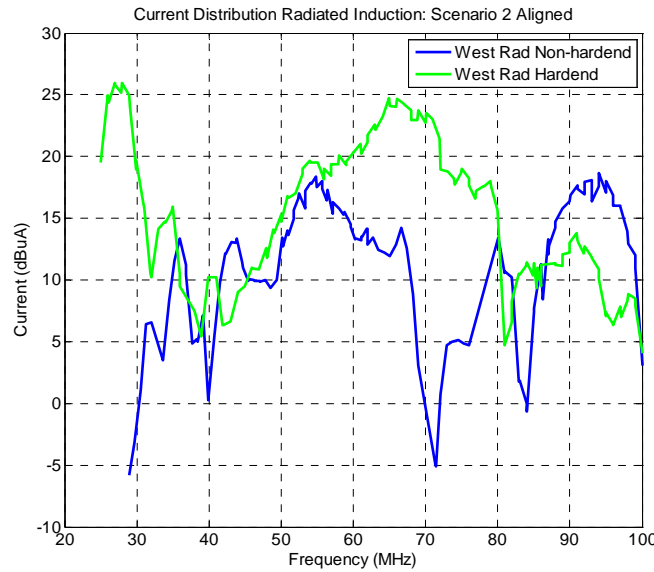


Figure 6.24: Current compared for a hardened and non-hardened telescope for scenario two aligned.

6.6.3. Discussion

This part of the chapter shows that the shielding measures, despite not being completely refined, do provide some level of additional shielding. A convincing indication of this is seen in the comparison of results for a hardened and non-hardened telescope in a misaligned position. Results were compared for the direct current injection and illumination methods. Findings indicate that if a more defined current path can be provided on the outside of the telescope, non-ideal shielding measures could be considered more acceptable. The fact that the cables do not enter through 360° connectors, or that the interfaces have seams providing possible points of entry, will not cause such a dramatic increase in CM current levels inside the pedestal.

Presently, the current path between the upper and lower pedestal is established by the two LDCs mounted on the upper pedestal and the four copper shoes mounted on the lower pedestal as discussed in section 6.2. The four earthing connections around the circumference of the foundation are always in alignment with the copper shoes. Therefore, by increasing the number of positions the LDC on the upper pedestal connects to the rotation ring, an aligned connection between the upper and lower pedestal will be established more often as the dish rotates. This will create defined paths to ground for the CM current to follow more frequently. This is confirmed by the finding in [5] Chapter 6 section 6.4.5. Additional verification will be done using measurements on the physical scale model as part of future investigations.

Part 4 – Evaluate Pedestal Shielding

6.7. Level of Interface Shielding

6.7.1. Defining a Computational Model

Measuring the change in CM current on the outside of the pedestal for a hardened and non-hardened telescope seems to provide some indication of whether the shielding interfaces influences the amount of CM current inside the pedestal. However, this technique is not ideal and the proposal of this part of the chapter is to conduct measurements inside the pedestal as a better method of defining the level of shielding. To determine the level of shielding offered by the top interface barrier only, a simplified computational model (Figure 6.25) of the one presented in section 6.3.2 is discussed. The purpose is to compare predictions from common shielding effectiveness formulations and calculations of CM current either side of the top interface barrier. The model therefore has to incorporate a conductor entering the lower pedestal through its top interface.

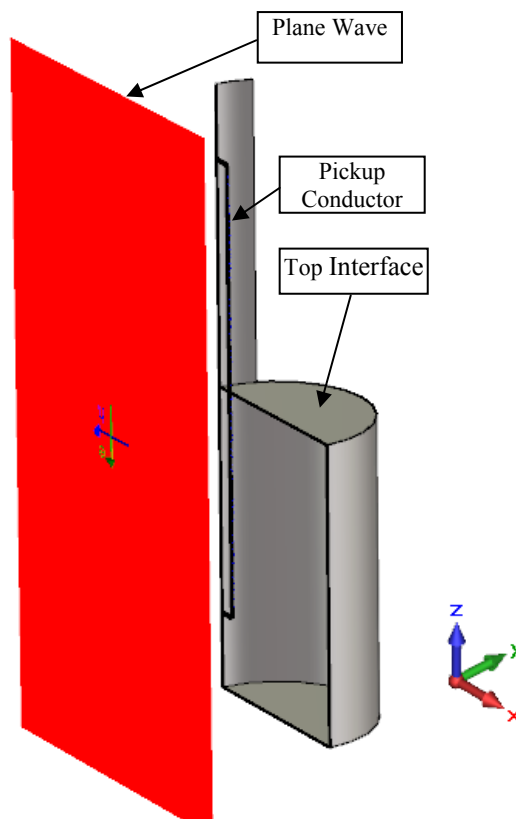


Figure 6.25: Pedestal in sectioned view with conductor and interface plates added. The plane wave used to excite the system is also shown.

The decision to rely on CST MWS for this investigation is justified by the accuracy of the computational analysis proven in Part 1 of the chapter. Also, because the presently-implemented pedestal hardening is incomplete, actual measurements cannot correctly test the shielding potential of the top interface barrier. The access door and seams in each interface are not included in the analysis.

Contrary to the previous model, this model is unscaled with a total height of approximately 6 m. The conductor is slightly shorter with a length of 4.6 m. The curved surface, on top of the lower pedestal (Figure 6.25), connecting to the conductor, provides a return path for current induced in a closed loop created by their combination. The conductor is terminated at the bottom inside wall of the lower pedestal. The connection between the conductor and top interface barrier is shown in Figure 6.26. This is replicating the actual connection seen in Figure 6.21 (b).

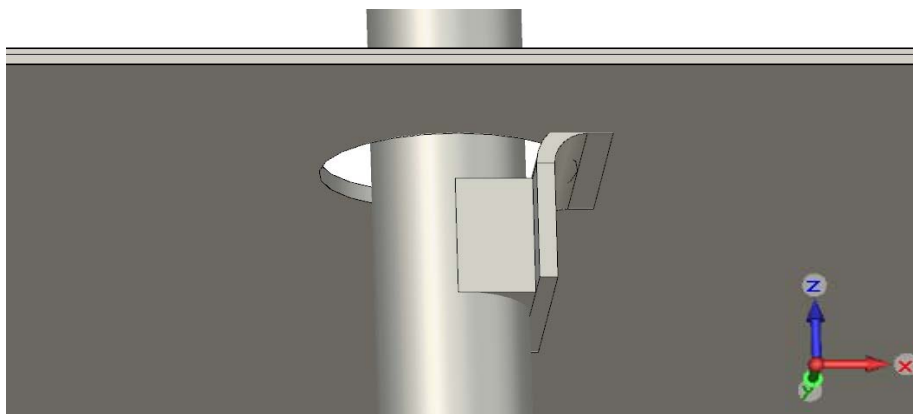


Figure 6.26: The connection between the cable and interface replicated in CST MWS.

A plane wave is used as excitation because of its relative ease of implementation in CST MWS. It is defined to have vertical E-field polarisation illuminating the structure from 0-200 MHz similar to the radiative measurements discussed in section 6.5.2. The upper limit of the band was chosen to ensure that standing waves with a number of wave repetitions are induced on the conductor. The position of the interface connection and shield, relative to the peaks and nulls of the induced standing wave, would directly influence the interface's level of shielding.

6.7.2. Definition of Shielding Effectiveness

The common definition of electric shielding effectiveness at an arbitrary point q within a shielded volume as indicated in [34]-[38] is:

$$SE_e|_q = 20 \log_{10} \frac{|\vec{E}^{unshield}|_q}{|\vec{E}^{shield}|_q} \text{ dB} \quad (56)$$

The definition in (56) compares the magnitude of the E-field measured with the shield, \vec{E}^{shield} , to the magnitude of the field measured without the shield, $\vec{E}^{unshield}$ at the same point q inside the volume. This formulation is mostly used for analysing the effect of apertures in a shielded enclosure as part of radiating problems. It furthermore assumes that the dimensions of the shield are smaller than the shortest wavelength investigated. For the computational model in Figure 6.25, with a perfectly connected bottom interface, the shield that is added or removed to generate \vec{E}^{shield} and $\vec{E}^{unshield}$ respectively, is the top interface and cable connection shown in Figure 6.26. The assumption in (56) regarding the dimension of the shield becomes less accurate at frequencies exceeding 150 MHz due to the 2 m diameter of interface. According to Klinkenbusch [34], at frequencies where the dimension of the shield is comparable or larger to the wavelength, the attenuation of electromagnetic field (rather than E and H-fields alone) has to be considered. The alteration of (56) given by [34] is as follows:

$$SE_{em}|_q = 10 \log_{10} \frac{2}{\frac{|\vec{E}^{shield}|_q^2}{|\vec{E}^{unshield}|_q^2} + \frac{|\vec{H}^{shield}|_q^2}{|\vec{H}^{unshield}|_q^2}} \text{ dB} \quad (57)$$

As a consequence (56) will be used at frequencies below 100 MHz and (57) will be used at frequencies above 100 MHz.

For wavelengths shorter than the length of the conductor, resonant effects associated with the dimensions of the enclosure, mean that the position q where the E-field is measured, will influence the shielding effectiveness that is calculated. When q is positioned at a minimum in the field distribution with the shield present, a more optimistic factor will be calculated. When q is positioned at a maximum, the opposite is true. Ideally q needs to be positioned at the maximum of the E-field when using (56), but the location of this maximum changes with frequency. Considering (57), it becomes clear that q cannot be moved to the maximum of both the E and H-field distributions inside the enclosure simultaneously. As a consequence in [34], the position of q is kept constant in the geometric centre of the volume for all frequencies. The position inside the enclosure is not the only factor influencing the calculation of shielding effectiveness for a

particular shield. As pointed out by Khan et al. [35], additional factors such as the angle of incidence of the disturbance field, size and position of the shield, all indicate that a proper statistical analysis is required to formulate an accurate prediction when using the traditional definition of shielding effectiveness.

Because the conductor is introducing interference into the pedestal, the problem is a conductive rather than radiative one, and different to the purpose of (56) and (57). The next section will show an approach in calculating the level of shielding which is more appropriate for our conductive problem. This is done by determining the reduction in the average CM current on the conductor either side of the interface.

6.7.3. Adaptation of Shielding Effectiveness

To determine the level of shielding calculated from the reduction in the average CM current either side of the interface, the definition in (56) is considered. In (56) \vec{E}^{shield} and $\vec{E}^{unshield}$ are replaced with I^{inside} and $I^{outside}$ giving (58):

$$SE_i = 20 \log_{10} \frac{|I^{unshield}|}{|I^{shield}|} \text{ dB} \quad (58)$$

Here I^{inside} and $I^{outside}$ represent an average calculated by integrating the current over the length of the conductor inside and outside the lower pedestal. Similarly the calculation in terms of current with and without the shield can also be made by defining $I^{inside \ shielded}$ and $I^{inside \ unshielded}$. Here the average is calculated by integrating the current in both cases over the length of the conductor inside the pedestal. Results for both methods are provided. The calculation of current on a conductor in CST MWS requires the use of Ampère's integral law as discussed in section 6.4.2.

6.7.4. Effects of Standing Waves

Wavelength effects require the current to be sampled at multiple positions along the conductor. In practical measurements, discrete frequencies over the band of interest will be chosen to evaluate the level of shielding. The sampled current on the conductor at four discrete frequencies, without the top interface barrier present, is shown in Figure 6.27. The current is displayed as a function of the number of points where it was measured. 61 sampling points

spaced 76 mm apart were used along the 4.6 m conductor to evaluate the current. For higher frequencies, more sampling positions have to be defined. The conductor has equal lengths either side of the interface.

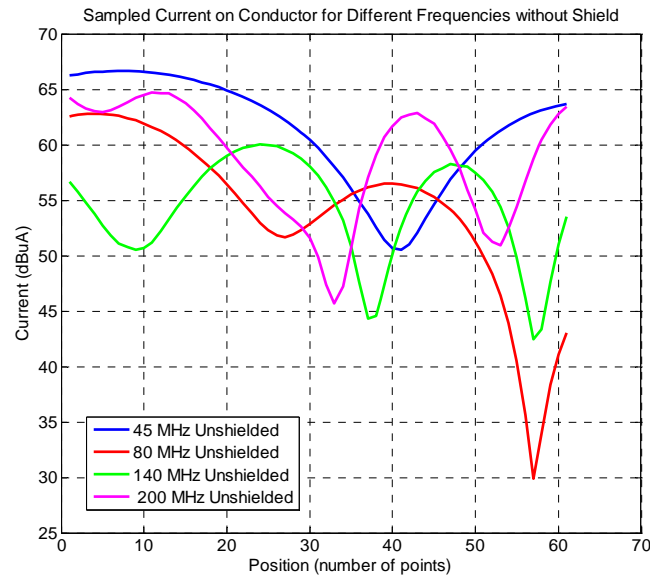


Figure 6.27: Current sampled along the length of the conductor at four discrete frequencies without the top interface present.

The effect on the sampled current, when adding the top interface barrier to the computational model, can be seen in Figure 6.28. Notice the re-organisation of the induced current according to the new interface that was added.

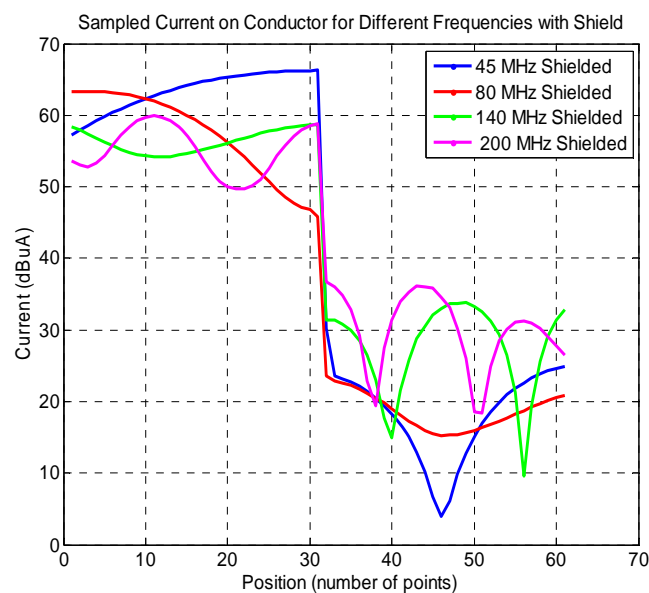


Figure 6.28: Current sampled along the length of the conductor at four discrete frequencies with the top interface present.

The change in current amplitudes along the length of the conductor at the various frequencies can be seen Figure 6.27 and Figure 6.28. This variation is the reason for calculating the average of currents I^{inside} and $I^{outside}$, providing a more realistic representation of the level of shielding. Furthermore, it now becomes clear why the level of shielding varies with frequency. If, at a particular frequency, a standing wave is induced on the conductor with the peak of the wave positioned at the top interface, the change in current observed either side of this interface would be high. This is because the peak current is terminated by the interface connection. For frequencies where the wave is going through a minimum, a smaller change in the current is calculated because the current is zero at the top interface. This means that at certain frequencies the top interface would be less effective than at others. Measures to reduce the amount of CM current on the conductor over a broad frequency range would be to increase the length of the connection between the conductor and the top interface. While this is not very practical, a different alternative is to connect the conductor to the side of the pedestal at multiple positions before the interface barrier. Such connections will help shed some of the CM current present on the conductor, and also break up the standing wave patterns shown in Figure 6.27 and Figure 6.28

6.7.5. Comparative Shielding Effectiveness Results: Radiative vs. Conductive

The purpose of this investigation is to compare the level of shielding for the top interface barrier predicted by (56) and (57) when calculating the change in E-field, to that predicted by (58) when calculating the change in the average CM current. Such a comparison is done at a number of discrete frequencies, which had to be identified. Because the results from (56) and (57) are dependent on the position of q inside the pedestal, the magnitude of the E-field was determined for q at the geometric centre of the pedestal in the computational model for the entire frequency range. The E-field was determined with the top interface present. Using this magnitude, a number of discrete frequencies were identified where the field was both a maximum and minimum. The chosen frequencies are highlighted in the plot of \vec{E}^{shield} in Figure 6.29. The corresponding frequencies are tabulated in Table 6:3. It includes a low 1 MHz investigation point.

Table 6:3: Marker frequencies

| M1 | M2 | M3 | M4 | M5 | M6 | M7 | M8 |
|-------|--------|--------|--------|---------|---------|---------|---------|
| 1 MHz | 45 MHz | 64 MHz | 80 MHz | 124 MHz | 140 MHz | 185 MHz | 200 MHz |

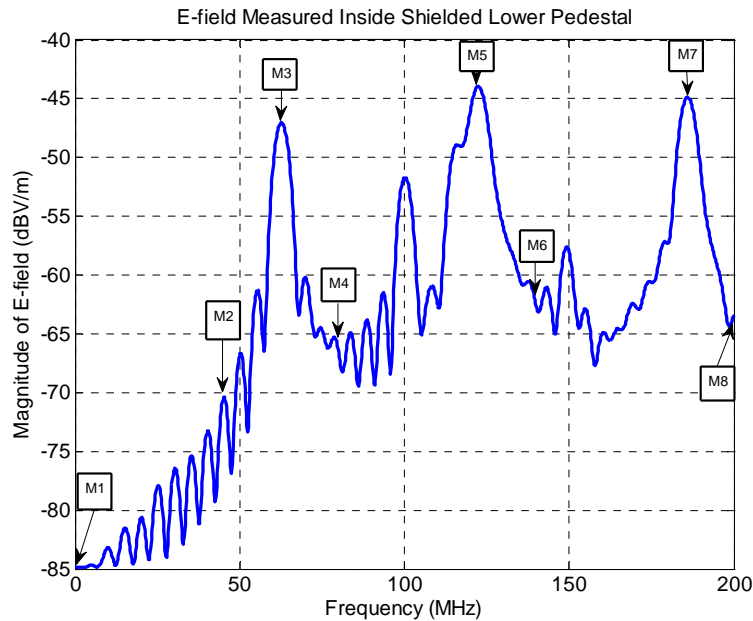


Figure 6.29: Calculated E-field on the inside of the pedestal with the shielding interface in place

The frequencies tabulated in Table 6:3 were firstly used to calculate the level of shielding provided by the top interface using (56) and (57). As mentioned in section 6.7.2, (56) was used for the chosen frequencies below 100 MHz and (57) used for the frequencies above 100 MHz. The results are shown in the first row in Table 6:4. Secondly, the level of shielding for the top interface was calculated at the same frequencies using (58). These results are shown in the second row in Table 6:4. The third row in the table shows the results again using (58) but compares the average CM currents inside the pedestal with and without the shield as described in section 6.7.3. A more conservative value for the level of shielding provided by the top interface was calculated for every sampled frequency, by comparing the average CM currents either side of the interface.

Table 6:4: Comparison of shielding values calculated for E-field and current measurements.

| | M1 | M2 | M3 | M4 | M5 | M6 | M7 | M8 |
|---------------------------------------|-------|-------|-------|-------|-------|-------|-------|-------|
| Shielding E-field (dB) | 56.42 | 46.1 | 32.71 | 56.15 | 30 | 51.15 | 38.19 | 46.87 |
| Shielding Current inside (dB) | 48.35 | 44.28 | 27.02 | 40.37 | 21.96 | 27.59 | 20.99 | 24.84 |
| Shielding Current inside/outside (dB) | 43.05 | 38.6 | 19.71 | 33.51 | 21.8 | 24.34 | 20.24 | 27.12 |

6.7.6. Discussion

In this final part of the chapter, a computational model was created to evaluate a method to determine the level of shielding provided by an interface barrier. This barrier is part of additional shielding measures installed on a hardened KAT-7 telescope pedestal, and all the cables entering the pedestal do so through this barrier. The method determines the attenuation in CM current on a conductor entering the pedestal, by evaluating it at a number of positions either side of the barrier. The process is repeated for each frequency point under consideration. The results from this method are compared to results for the level of shielding predicted by the common definition of shielding effectiveness.

A more conservative estimate for the level of shielding the interface provides at each frequency is predicted when using this new method. This shows that, regardless of whether the E-field inside the pedestal is resonant or not, the definition for shielding effectiveness in this case predicts higher levels of shielding than what is actually provided. This can be attributed to the definition of shielding effectiveness which assumes that the excitation of fields inside the shielded volume takes place via field coupling. With the cable entering the lower pedestal this is no longer the case.

6.8. Conclusion

The work presented in this chapter was divided into four parts. The first three examine the distribution of CM current on two of the seven KAT-7 radio telescopes. The investigation was conducted on the basis of an RF current audit carried out on site. Of the two telescopes measured, the hardened telescope had shielding measures which included interface barriers at the roof and floor of the lower pedestal section. These measures were installed after the telescope was built so ideal installation was not possible. The fourth and final part evaluates a new method to determine the level of shielding the hardened telescope's interface barrier provides.

Part 1 investigated the use of both a physical and computational scale model to confirm measurements made on the KAT-7 telescope. Once the accuracy of the models was proven, they could be used for further investigations. The models make it possible to conduct measurements in a local controlled environment without having to travel to the actual site which has time and financial implications. From section 6.4.4, and the results presented in Figure 6.15, comparisons

between the scale model results and KAT-7 telescope measurements, proved the accuracy of the two scale models that were created. Also, the ability to accurately measure current on the physical model using two different measurement techniques was shown. An advantage of using the computational model is the visual representation of fields and CM current distributions on the telescope structure.

In Part 2, CM currents and their distribution between the four earthing connections around the foundation of the telescope pedestal became the focus. During the current audit, CM current was either directly injected or induced onto the telescope structure. It was important in terms of the validity of the measured data, to determine whether the direct current injection method was influencing the results. Distributions due to direct injection and illumination were investigated using results from the RF audit and physical scale model measurements. The findings show that with the illumination measurement, on average, a more even distribution between the four earthing connections was measured as compared to the direct injection. The illumination measurement is therefore less intrusive. The direct injection of CM current, for the purpose of investigating the shielding ability of the pedestal interfaces is a more appropriate method to use. With the higher dynamic range this method provides, a more conclusive indication of what the shielding ability of the interface is. Future measurements will include illuminating scenario one and two misaligned to confirm that an even distribution remains regardless of the LDC alignment.

In Part 3 the CM current on the earthing connections was compared for a hardened and non-hardened telescope. The purpose was to determine if the additional shielding measures were affecting the flow of CM current on the telescope. The measured results in Figure 6.22 show that in fact it does. It is especially noticeable when comparing a hardened and non-hardened telescope where the LDCs and copper shoes are misaligned. Similar amounts of current are measured on the outside of the pedestal for the aligned scenarios regardless of the level of pedestal hardening. For the misaligned non-hardened case, the appreciable decrease in measured current on the outside is a result of the current re-directing to flow on the inside of the pedestal. However, by increasing the number of connections between the LDCs on the upper pedestal and the rotation ring, aligned scenarios will be created more often as the dish is rotated. Therefore, the effect of the pedestal hardening that is implemented is less significant and CM currents are diverted to ground more effectively.

Now that current has been studied on the outside of the pedestal, future investigations will focus on measuring current inside the pedestal. For this, the physical scale model will be modified to incorporate a conductor on the inside of the pedestal on which the change in current for different LDC connections can be measured.

Concluding the chapter with Part 4, an alternative method to the common definition of shielding effectiveness was discussed using only computational analysis. This method succeeded in determining what levels of shielding the interface barrier that is installed inside the pedestal provides, when measuring the CM currents either side of the barrier. Compared to measuring of the E-field as commonly defined by shielding effectiveness, more conservative levels were calculated for each frequency point. This is true even for frequencies where the lower pedestal is resonant in terms of E-field distribution. In practice this method is more time consuming because each frequency has to be sampled at a number of positions on the cable, but the accuracy of the results warrants the effort.

Chapter 7

Conclusion, Recommendations and Future Work

The dissertation has evaluated methods to reduce a conductive system's susceptibility to electromagnetic interference (EMI). The conductive system in this case consists of more than just a source, return conductors, and a load. It could also include other physical objects such as enclosures, cable trays, interface barriers, and even the entire lower pedestal of the KAT-7 telescope. Any conductive system is a differential mode (DM) system by design. However, as discussed in Chapter 2, such a system has connections to the outside world surrounding it. This can be a deliberate connection in the form of an earth return conductor, or a non-deliberate connection in the form of parasitic capacitances. Regardless of how the galvanic connections are made, an additional common mode (CM) circuit is always created. This will induce disturbance voltages in the DM circuit through the transfer impedance (Z_t) mechanism. The disturbances cannot be characterised accurately until the implementation of the DM circuit.

A review of literature that explains the major concepts used in the different investigations was provided. Z_t was discussed using an example of a simple conductive system. This illustrated the relationship between the two circuits. The Z_t between a DM and CM circuit can be reduced by using cable trays as earthed parallel conductors (EPC). Cable trays in general provide a lower resistive connection to earth. They also shield the DM circuit inside from magnetic field coupling. The ability of a cable tray to perform these two functions is reflected in its Z_t . An overview of existing research on cable tray Z_t was presented. From this overview no one definitive investigation regarding different types of cable tray mid-span and end-connections was available. Recommendations are mostly provided for the best connections to use, but no technical information explaining the recommendations are given. An investigation of a cable tray's shielding ability against high frequency interference was then considered. This is relevant because cable trays will not only be exposed to low frequency interference. The final introductory work on cable trays discussed their two-port network representation. For

measurement purposes a two-port network can be entirely described by scattering parameters measured using a vector network analyser (VNA).

Further concepts used in the dissertation, which needed to be reviewed, included the use of physical and computational unscaled and scaled models. Their suitability to represent actual systems accurately was studied. Other disciplines in which they are used successfully were considered. Computational issues unique to electromagnetic compatibility (EMC) investigations were highlighted. The direct current injection (DCI) method as means of excitation for EMC investigations was introduced. This was compared to the plane wave illumination method in order to consider the advantages and disadvantages of both. Finally, the concept of shielding effectiveness used in the analysis of the KAT-7 pedestal shielding was discussed. This was by no means a complete overview of shielding effectiveness, but it merely served to introduce the definitions used later.

Computational analysis using Microwave Studio from Computer Simulation Technology (CST MWS) was used extensively throughout. In all the material presented, CST MWS validated the accuracy of measured results. In some instances, such as the study of shielding effectiveness, only computational analysis was used. The flexibility of the computational software is especially useful for electromagnetic (EM) simulations as part of EMC investigations. With a more detailed knowledge of CST MWS's functionality, more accurate computational models could be created without substantially increasing simulation time. Identifying the use of volumetric hexahedral meshing associated with the time domain analysis, meant that models could be simplified to suit the meshing. Correct mesh cell alignment is determined mainly by the mesh line ratio limit. The mesh line ratio limit is therefore the main determining factor of the accuracy of the computed results. It also is the main determining factor of the number of mesh cells used in the simulation. This, along with the smallest mesh step width, determines the total simulation time. To this end some techniques used to simplify the various computational models were discussed.

With an intimate knowledge of the computational analysis, cable tray connections were investigated using physical and computational models. Described in Chapter 2 is how cable trays (as EPCs) are used to lower a conductive system's Z_t . The reason for this investigation is because EMI shielding provided by a cable tray extends further than the tray itself. Proper terminating connections to an enclosure or cabinet are required to ensure the continued shielding of the victim conductors inside the tray. This is equally relevant for connections joining two cable tray

sections together. The analysis was based on replicating actual cable tray installations using two models with different CM current distributions. An enclosure added to both models, enabled the analysis of end-connections. The purpose was to provide a definitive analysis of the most widely used mid-span and end-connections. This identified the better option for a particular cable tray installation and why. The use of CST MWS was again invaluable in finding agreement between measured and computed results. With the computational analysis, both field and current arguments were examined for each model and of each connection. The computation also highlighted the interaction between the model and the measurement environment. Changes to the computational volume brought about the agreement between measured and computed results.

The operational bandwidth of the KAT-7 demonstrator is 1.6 GHz to 1.8 GHz and the electronic stages thereafter could be susceptible to interference down to intermediate frequency bands and below. It was necessary to determine if the cable trays being investigated provided any level of protection against interference at these frequencies. To test the upper range, considered measurements from 300 MHz to 6 GHz were introduced. A reliable analysis of cable tray shielding in this band, required the use of plane wave illumination with a known-gain antenna. For this work, multiple angles of incidence of the disturbance field were considered. Because of the illumination method, the shielding ability of the cable tray could no longer be represented in terms of Z_r . Instead the shielding, for the various angles of incidence, was expressed through both the induced voltage on the victim conductor inside the tray, as well as its far field gain function. Scattering parameters described the characteristics of the antenna-and-cable tray measurement setup. Through the Friis transmission equation, the measured S-parameters were used to calculate the induced voltage as well as the gain function. An enclosure at the end of the cable tray was included. This provided a model which was representative of an actual cable tray installation. Measurements were conducted on an open area test site (OATS) as well as inside an anechoic chamber. It was deduced that an OATS is not suitable to measure cable tray shielding for varying angles of incidence. Computational analysis was once again used to confirm the measured results. The characteristics of the radiating antenna and free space loss of the measurement were incorporated successfully into computed voltage. Measured and computed results indicated that cable trays, even at wavelengths much shorter than the width of the tray, do provide protection to enclosed conductors.

In a complex system such as the KAT-7 interferometer, the reduction of both conducted and radiated radio frequency interference (RFI) is particularly valuable. Solid cable tray could be

used in specialised applications. As they would only be needed for specific installations over short distances, they would not be used in large volumes, so cost would also be low. As part of future work it is recommended that meshed and wire cable trays be investigated more thoroughly. It would be advantageous to determine their shielding ability both at low and higher frequencies. The solid cable trays in this dissertation were specialised installations making them expensive. Their widespread use in a large project such as the MeerKAT is unlikely to be a viable option. If meshed or wire trays are shown to provide some level of shielding against RFI, the simple fact that they would also help to order cable runs makes them an attractive option. An overview of cable tray usage at lower frequencies was given in Chapter 2. By combining the study of cable tray connections up to 100 MHz (Chapter 4), as well as the investigation of cable tray shielding from 300 MHz to 6 GHz, a coherent picture of cable trays analysis over a wide frequency range is presented.

The final investigation presented, arose from an RF current audit which was made on two of the seven KAT-7 radio telescopes. The findings from the audit were presented in four connected parts. The first three focussed on the distribution of CM current on the two telescopes for various scenarios. One telescope had additional EM shielding measures installed, which included interface barriers at the roof and floor of the lower pedestal section. The second telescope had no additional shielding measures installed. Part 1 established agreement between measurement and computation using a physical and computational scale model. Once accuracy between the two was proven, findings from the KAT-7 site audit were compared with modelled results. The outcome provided an accurate physical and computational model which was used for additional investigations. For Part 2 attention shifted to the distribution of CM current on the outside of the pedestal. Comparative results from measurements using DCI and plane wave illumination were evaluated. The purpose of the evaluation was to determine the integrity of each method of excitation. Distributions when using DCI showed higher levels of current closest to the feed conductor which injected the current onto the telescope. On the contrary, the plane wave illumination showed a more even distribution with fewer variations in the measured levels around the pedestal. However, for the purpose of determining the level of shielding provided by the interface barrier, the DCI is more appropriate than plane wave illumination.

Part 3 again investigated the distribution of CM current around the pedestal, but this time with a comparison between the hardened and non-hardened telescope. Preliminary results showed that the role of the conductive path on the outside of the pedestal is under-estimated. This path, which

is established by a lightning down conductor (LDC), influences how CM current is diverted to ground. If the path is well defined, similar levels of current were measured on the outside of the pedestal for a hardened and non-hardened scenario. If the path is not well defined, the hardening measures become much more relevant. The results showed noticeable differences between measured CM currents for a hardened and non-hardened scenario, when the current path was interrupted. In this case current starts to flow on the inside of the pedestal, potentially increasing interference. A recommendation would then be that the number of LDC connections on the outside of the pedestal be increased. This would provide more defined CM current paths regardless of how the dish is moved. Consequently, less stringent demands would be placed on the additional shielding measured installed on the pedestal. This has both cost and time implications. Correct installation of the hardening measures are much more time consuming than the addition of LDCs to the outside of the pedestal. The cost involved for the additional LDC connections should be lower than for the extra shielding measures. It must be emphasised that these are preliminary findings from the first current audit of its kind conducted on the KAT-7 telescopes. Further investigations are required regarding the influences of the shielding measures. It is recommended that measurements should be made both on the outside and inside of the pedestal. This will confirm a reduction of the inside current when the outside current path is well defined. The physical and computational scale models should also be used to analyse the effect of more LDC connections on current levels inside the pedestal.

The final investigation of this dissertation, described in Part 4 of Chapter 6, proposed a different method to determine the level of shielding that the interface barrier inside the lower pedestal provides. The method measured CM current on a conductor which enters the pedestal at multiple positions either side of the barrier. By evaluating the reduction in CM current rather than E and H-fields, more conservative values for the level of shielding were calculated by the current measuring method. The investigation was performed using computational analysis alone. At the time of completing this dissertation, measurements similar to the computation had not yet been made. As part of future investigations, it would be valuable to verify these computed results experimentally².

² One month after completing this dissertation a subsequent current audit was conducted on a fully hardened KAT-7 telescope. Initial results indicate that current measurements can be used to predict the level of shielding provided by the interface barriers. By adding additional LDC connections a more even distribution of CM currents were measured around the circumference of the pedestal. These findings will be published in 2011.

Bibliography

- [1] A. van Ardenne, J. D. Bregman, W. A. van Cappellen, G. W. Kant, J. G. B. de Vaate, "Extending the Field of View With Phased Array Techniques: Results of European SKA Research," *Proceedings of the IEEE*, vol. 97, no. 8, pp. 1531-1542, August 2009.
- [2] South African SKA (Square Kilometre Array), www.ska.ac.za.
- [3] R. T. Lord, "RFI and Radio Astronomy – Why the Fuss?," technical report, SKA SA, K0000-2001V1-009 TR, Revision 1, 8 July 2009.
- [4] J. L. Jonas, "MeerKAT-The South African Array With Composite Dishes and Wide-Band Single Pixel Feeds," *Proceedings of the IEEE*, vol. 97, no. 8, pp. 1522-1530, August 2009.
- [5] P. G. Wiid, "Lightning Protection and Radio Frequency Interference Mitigation for the Karoo Array Telescope," Ph.D. dissertation, University of Stellenbosch, Stellenbosch, South Africa, 2009.
- [6] D. L. Decker, "Conduit or Cable tray: the Choice is Yours," *Conference Record of 1994 Annual Pulp and Paper Industry Technical Conference*, pp. 171-179, June 1994.
- [7] C. L. Kalupa, "Guide for Design of Electrical Cable Tray Systems," *IEEE Transactions on Industry Applications*, vol. IA-13, no. 6, pp. 533-538, November/December 1977.
- [8] A. P. J. van Deursen, "Electromagnetic Compatibility. Part 5, Installation and Mitigation Guidelines. Section 3, Cabling and Wiring," EUT Report 93-E-275, Eindhoven University of Technology Research Reports, July 1993, ISBN 90-6144-275-3.
- [9] M. J. A. M. van Helvoort, "Grounding Structures for the EMC-Protection of Cabling and Wiring," Ph.D. dissertation, Technical University of Eindhoven, Eindhoven, The Netherlands, 1995 ISBN: 90-386-0037-2.
- [10] E. Pettus, "An Examination of the Shielding Provided by the Use of Cable Trays," *IEEE Transactions on Nuclear Science*, vol. 29, no. 6, pp. 1924-1929, December. 1982.
- [11] A. P. J. van Deursen, F. B. M. van Horck, M. J. A. M. van Helvoort, P. C. T. van der Laan, "Transfer Impedance of Nonmagnetic Conduits of Various Shapes," *IEEE Transactions on Electromagnetic Compatibility*, vol. 43, no. 1, pp. 18-28, February 2001.
- [12] N. W. Ebertsohn, "Cable Trays and EMC: Modelling and Measurement," MSc thesis, University of Stellenbosch, Stellenbosch, South Africa, 2005.
- [13] T. Williams, "Systems EMC," in *EMC for Product Designers*, 4th Edition, Oxford, UK: Elsevier Ltd, 2007, pp 403-423.
- [14] IEC Electromagnetic Compatibility (EMC) – Part 5: Installation and mitigation guidelines Section 2, IEC 61005-2, 1997.

BIBLIOGRAPHY

- [15] IEC Amendment 2, Electrical Installations of Buildings – Part 4-44: Protection for Safety – Protection Against Voltage Disturbances and Electromagnetic Disturbances, IEC 60364-4-44, 2006-08.
- [16] *NEMA Cable Tray Installation Guidelines*, Standards Publication, VE 2-2006, 2006.
- [17] *National Electrical Code, 2005 Cable Tray Manual*, Based on the 2005 National Electrical Code
- [18] S. Kapora, “Protection by Open Systems: an EMC Study,” Ph.D. dissertation, Technical University of Eindhoven, Eindhoven, The Netherlands, 2005 ISBN: 90-386-1743-7.
- [19] S. Kapora, E. Laermans, A. P. J. van Deursen, “Protection of Cables by Open-Metal Conduits.” *IEEE Transactions on Electromagnetic Compatibility*, accepted for publication.
- [20] FEKO®, User Manual, www.feko.info/
- [21] CST MICROWAVE STUDIO®, User Manual Version 2009, Sep. 2008, CST AG. Darmstadt, Germany, www.cst.com.
- [22] K. L. Kaiser, “Electromagnetic Compatibility Handbook,” CRC Press, 2005.
- [23] K. Kurokawa, “Power Waves and the Scattering Matrix,” *IEEE Transactions on Microwave Theory and Techniques*, vol. 13, no. 2, pp. 194-202, March 1965.
- [24] A. R. Ruddle, “Electromagnetic Modelling for EMC.” *Preprint of invited paper for 7th International Conference on Computation in Electromagnetics*, Brighton, UK, April 2008.
- [25] Q. Zhang, W. Wu, C. Fang, F. Xing, “Application of Scale Brass Model in EMC Design for Naval Ship,” *8th International Symposium on Antennas, Propagation and EM Theory*, pp. 1001-1004, 2008,
- [26] H. C. Reader, R. H. Geschke, P. G. Wiid, P. S. van der Merwe, R. G. Urban, D. J. Rossouw, “Issues in EMC Metrology and Modelling for Square Kilometre Array Demonstrator,” *2008 URSI General Assembly, Commissions A and E: EMC Measurements*, Chicago, USA, August 2008.
- [27] C. Christopoulos, “Multi-Scale Modelling in Time-Domain Electromagnetics,” *AEU International Journal of Electronics and Communications*, no. 2, pp. 100-110, January 2003.
- [28] C. Christopoulos, “The Challenges of Numerical Modelling in EMC Studies (Invited),” *2101 Asia-Pacific International Symposium on Electromagnetic Compatibility*, Beijing, China, April 2010.
- [29] Z. Bingwei, J. Uanxing, “Research Progress of Direct Current Injection Technique in Aircraft EMC Test,” *3rd IEEE International Symposium on Microwave, Antenna, Propagation and EMC Technologies for Wireless Communications*, pp. 843-849, 2009.

BIBLIOGRAPHY

- [30] D. McQuilton, J. M. Oakley, C. Budd, "A Computational Assessment of Direct and Indirect Current Injection Techniques for Missile EMC Testing," *Ninth International Conference on Electromagnetic Compatibility*, 1994, no. 396.
- [31] G. A. Rasek, S. E. Loos, "Correlation of Direct Current Injection (DCI) and Free-Field Illumination for HIRF Certification," *IEEE Transactions on Electromagnetic Compatibility*, vol. 50, no. 3, pp. 499-503, August 2008.
- [32] A. Rautio, M. Uusimäki, "A Simple Direct Injection Method for Determination of Immunity Performance of Battery Operated Device," *IEEE International Symposium on Electromagnetic Compatibility*, 2004, vol. 1, pp. 81-84, August 2004.
- [33] M. Rothenhäusler, A. Ruhfass, T. Leibl, "Broadband DCI as a Multi Usable EMC-test Method," *IEEE International Symposium on Electromagnetic Compatibility*, 2008, pp. 1-5, August 2008.
- [34] L. Klinkenbusch, "On the Shielding Effectiveness of Enclosures," *IEEE Transactions on Electromagnetic Compatibility*, vol. 47, no. 3, pp. 589-601, August 2005.
- [35] Z. A. Khan, C. F. Bunting, M. D. Deshpande, "Shielding Effectiveness of Metallic Enclosures at Oblique and Arbitrary Polarizations," *IEEE Transactions on Electromagnetic Compatibility*, vol. 47, no. 1, February 2005.
- [36] X. Nenghong, Y. Xueqin, S. Wenwu, "Shielding Effectiveness and Coupling Characteristics of Metallic Enclosures with Apertures under EMP," in *Power and Energy Engineering Conference APPEEC Asia-Pacific*, 2009, 1-4.
- [37] L. Golestani-Rad, J. Rashed-Mohassel, "The Effects of Apertures' Shape and Configuration on the Shielding Effectiveness of Metallic Enclosures," in *Asia-Pacific Conference Proceedings, Microwave Conference Proceedings*, 2005, vol. 5, pp. 4.
- [38] M. P. Robinson, T. M. Benson, C. C. Christopoulos, J. F. Dawson, M. D. Ganley, A. C. Marvin, S. J. Porter, D. W. P. Thomas, "Analytical Formulation of the Shielding Effectiveness of Enclosures with Apertures," *IEEE Transactions on Electromagnetic Compatibility*, vol. 40, no. 3, August 1998, pp. 240-248.
- [39] J. Bernauer, R. Weis, A. J. Schwab, "Shielding Effectiveness Measurement of a 19" – Case through Direct Current Injection (DCI)," *International Symposium on Electromagnetic Compatibility 1997*, pp. 567-572, August 1997.
- [40] L. Sevgi, "Electromagnetic Screening and Shielding-Effectiveness (SE) Modeling," *IEEE Antennas and Propagation Magazine*, vol. 51, no. 1, February 2009.
- [41] D. B. Davidson, "Computational Electromagnetics for RF and Microwave Engineering," Cambridge University Press, 2005.
- [42] E. Bachelier, F. Issac, S. Bertuol, J.P. Parmantier, J. C. Alliot, "Numerical EM Simulations for the Definition of the Lightning Protection Systems of the Future VEGA and SOYUZ Launching Pads," *ESA Workshop on Aerospace EMC, Florence, Italy*, 30 March – 1 April.

BIBLIOGRAPHY

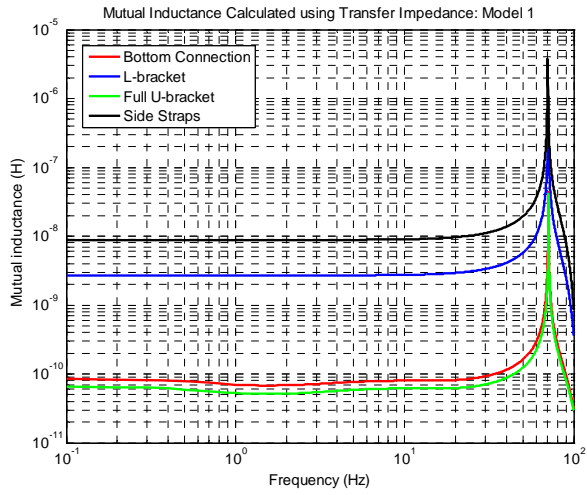
- [43] H. C. Reader, T. E. W. Stuart, M. Bemmelmans, "Metrology in Electromagnetics: Simple Problems," Millennium Conference on Antennas and Propagation, Davos, April 2000, ESA (European Space Agency), SP-444 Proceedings, Session 3P7, paper 0527.
- [44] T. V. Chow Ting Chan, H. C. Reader, "Field Studies in Multimode Cavities," in *Understanding Microwave Heating Cavities*, Artech House, Inc, 2000, pp 83-88.
- [45] C. Christopoulos, I. Argyri, "Measurement Uncertainties in Screened Rooms and in Open Area Test Sites – A Tutorial Introduction," *IEE Colloquium on The Correlation Between Measurements in Screened Rooms and in Open Area Test Sites*, pp. 1/1-1/5, August 2002.
- [46] D. M. Pozar, "The Scattering Matrix," in *Microwave Engineering*, 3rd Edition, John Wiley & Sons, Inc, 2005, pp 174-182.
- [47] D. J. Rossouw, "EMC Investigation of Cable Trays," Final year project, University of Stellenbosch, Stellenbosch, South Africa.
- [48] S. J. Haigh, C. J. Hardwick, "The Determination of Induced Voltage due to Lightning with the aid of Computer Modelling," *IEEE Colloquium on Lightning and EMC*, pp. 4/1-4/7, January 1996.
- [49] R. L. Coren, "Reciprocity in EMI-EMC," in *Symposium Record of the IEEE 1991 International Symposium on Electromagnetic Compatibility*, 1991, 184-188.
- [50] *CISPR 16: Specification for radio disturbance and immunity measuring apparatus and Methods*. CISPR Standard, Publication 16-1-4, 2007-02.
- [51] L. Sevgi, S. Çakir, G. Çakir, "Antenna Calibration for EMC Test and Measurements," *IEEE Antennas and Propagation Magazine*, vol. 50, no. 3, pp. 215-224, June 2008.
- [52] H. A. Haus, J. R. Melcher, "Ampère's Integral Law," in *Electromagnetic Fields and Energy*, Volume 1, Prentice Hall, 1989.
- [53] Rohde & Schwarz®, FSH User Manual, 2010, Rohde & Schwarz GmbH & Co. KG, Munich, Germany.

Appendix A.

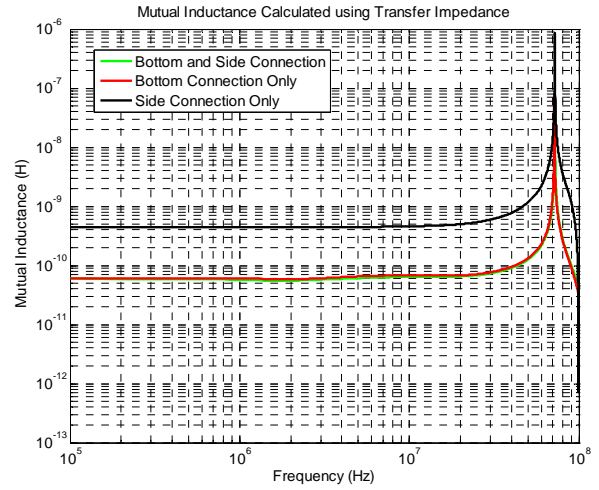
Modelling of Cable Tray Connection

A.1. Model 1 Mid-span Connections

The mutual inductance calculated for Model 1 mid-span connections is shown in Figure A.1 (a) and for the end-connections shown in Figure A.1 (b).



(a)



(b)

Figure A.1: Comparison of mutual inductance calculated from transfer impedance using Model 1 for (a) the four mid-span connections and (b) the three end-connections are shown.

Appendix B.

Antenna and Cable Tray High Frequency Analysis

B.1 Antenna Gain Calculations

The method of substitution can be used to uniquely calculate the gain of each antenna, by making use of the Friis transmission formula and defining three antenna gains $ant1$, $ant2$ and $ant3$. By already compensating for the reflection loss in the measured S-parameter data (Chapter 5 section 5.4), the following three equations can be defined:

$$G_{ant1} = \frac{A_{ant1ant2} (4\pi R_{ant1-ant2})^2}{\lambda^2 G_{ant2}} \quad (59)$$

$$G_{ant1} = \frac{A_{ant1ant3} (4\pi R_{ant1-ant3})^2}{\lambda^2 G_{ant3}} \quad (60)$$

$$G_{ant2} = \frac{A_{ant2ant3} (4\pi R_{ant2-ant3})^2}{\lambda^2 G_{ant3}} \quad (61)$$

By setting equal (59) and (60) and simplifying:

$$\frac{A_{ant1ant2} (R_{ant1-ant2})^2}{G_{ant2}} = \frac{A_{ant1ant3} (R_{ant1-ant3})^2}{G_{ant3}} \quad (62)$$

$$G_{ant2} = \frac{A_{ant1ant2} (R_{ant1-ant2})^2 G_{ant3}}{A_{ant1ant3} (R_{ant1-ant3})^2} \quad (63)$$

Substituting (61) into (63) and simplifying gives the equation used to calculate the gain of $ant3$. Using the calculated gain for $ant3$, the gain of the remaining two antennas can also be calculated.

$$\frac{A_{ant1ant2} (R_{ant1-ant2})^2 G_{ant3}}{A_{ant1ant3} (R_{ant1-ant3})^2} = \frac{A_{ant2ant3} (4\pi R_{ant2-ant3})^2}{\lambda^2 G_{ant3}} \quad (64)$$

$$G_{ant3} = \sqrt{\frac{A_{ant2ant3} A_{ant1ant3} (4\pi R_{ant2-ant3} R_{ant1-ant3})^2}{A_{ant1ant2} (\lambda R_{ant1-ant2})^2}} \quad (65)$$

B.2. Antenna Gain Functions

The gain functions of the antennas that were used to illuminate the cable tray model with were calculated using a three-antenna method described in Chapter 5. The first antenna that was used was a 2 to 18 GHz horn antenna of which the gain function is shown in Figure B.1.

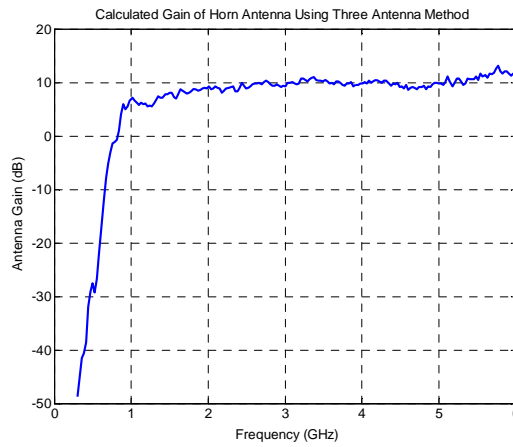


Figure B.1: Gain function of horn antenna calculated using the three-antenna method.

A wideband LPDA which was designed to function between 300 MHz to 10 GHz was designed at Stellenbosch University's Department of Electric and Electronic Engineering. The gain function for this antenna was also calculated using the three-antenna method and the result is shown in Figure B.2. It was only used to the 6 GHz upper frequency limit specified in Chapter 5.

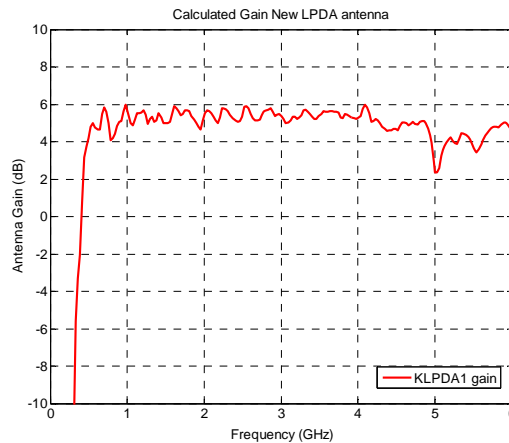


Figure B.2: Gain function of new LPDA antenna which was used for cable tray gain measurements. The gain was calculated using the three-antenna method described in Chapter 5.

B.3. Comparison of Cable Tray Gain Functions

The results shown below are comparisons between the cable tray gain functions calculated using measured data, and computed using CST MWS. In Figure B.3 the comparison is shown for a 45° angle of incidence for horizontal polarisation with a cover added to the enclosure.

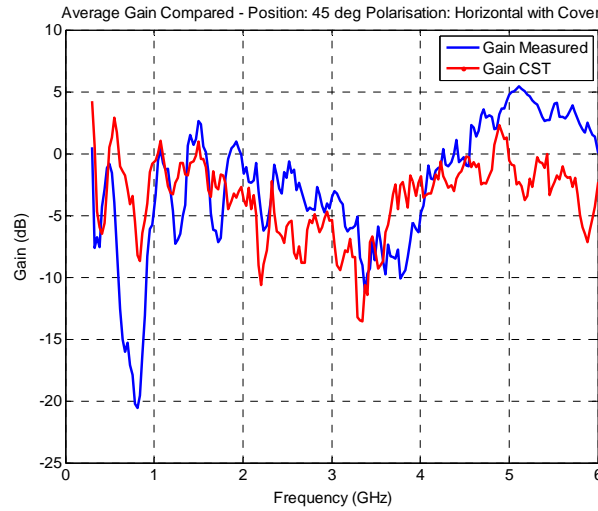
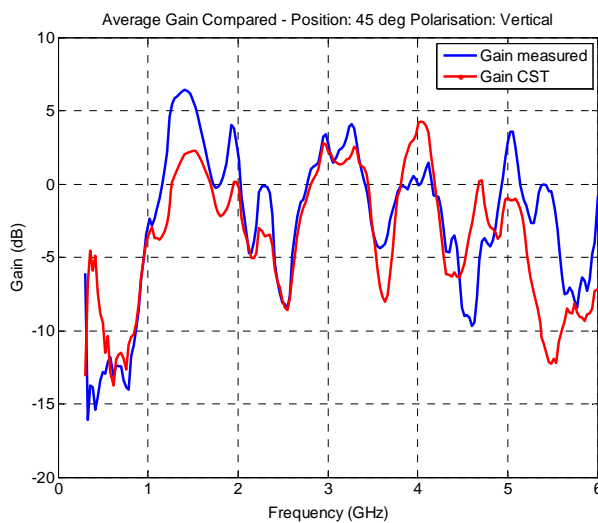
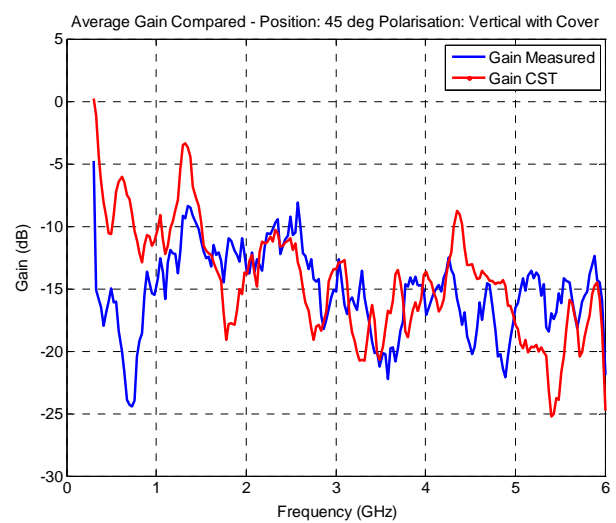


Figure B.3: Comparison of gain function calculated using measured results and computed using computational analysis for a 45° angle of incidence. Horizontal polarisation with the enclosure cover included was considered.

In Figure B.4 (a) the comparison is shown for a 45° angle of incidence for vertical polarisation with the enclosure at the end of the cable tray having no cover. The results in Figure B.4 (b) are also for a 45° angle of incidence for vertical polarisation but the enclosure cover is included.



(a)



(b)

Figure B.4: Comparison of gain functions calculated using measured results and computed using computational analysis. The results shown in (a) are for a 45° angle of incidence for vertical polarisation without the enclosure cover. In (b) the enclosure cover was included.

B.4. Comparison of Induced Voltages

The following results show the comparison of the induced voltage on the victim conductor inside the cable tray between calculated and computed data. S_{21} illumination measurements of the cable tray were used to calculate the relevant voltages for different angles of incidence on the tray. The computed results were obtained from CST MWS in which a plane wave illuminated the cable tray at the same angles of incidence. The results in Figure B.5 (a) and Figure B.5 (b) are for horizontal polarisation with an open enclosure at the end of the cable tray.

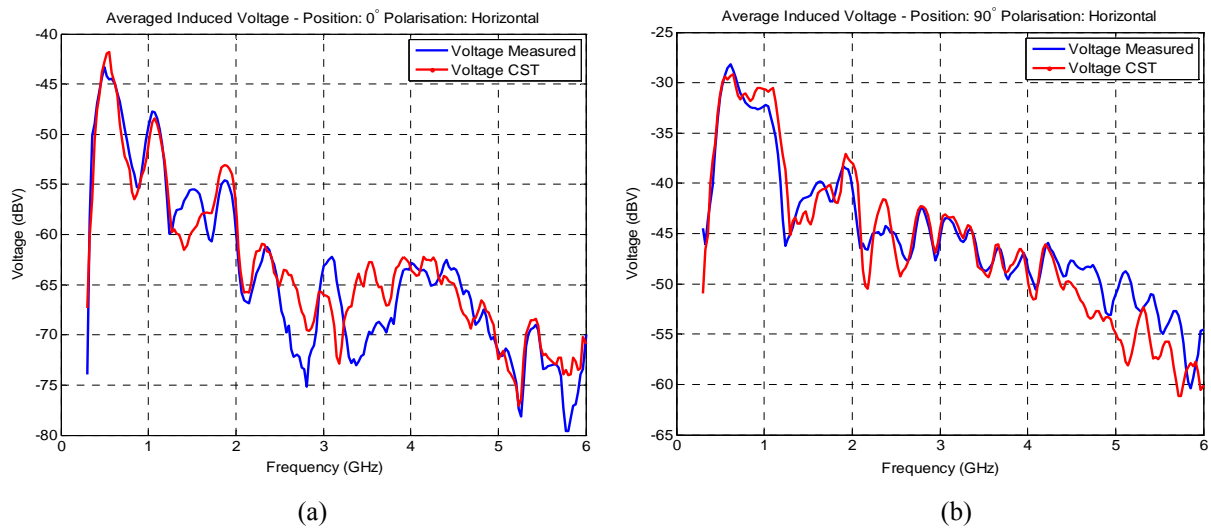


Figure B.5: Comparison of calculated and computed induced voltage on the victim conductor inside the cable tray. The results for horizontal polarisation for (a) 0° and (b) 90° angle of incidence are shown.

The results shown in Figure B.6 are a comparison of induced voltage for a 45° angle of incidence for horizontal polarisation with an enclosure cover added.

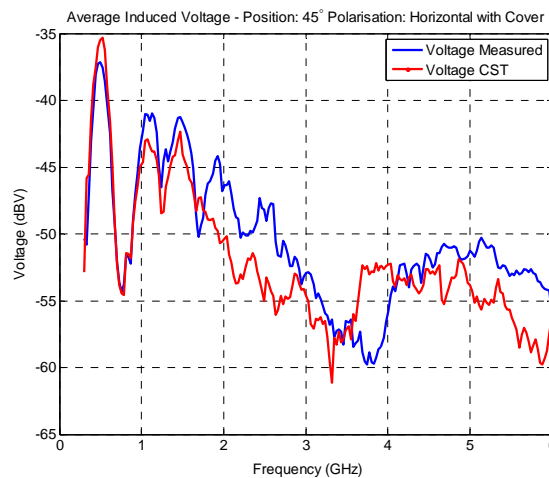


Figure B.6: Comparison of calculated and computed induced voltages for a 45° angle of incidence with horizontal polarisation. A cover was added to the enclosure.

The comparison of induced voltages for a 45° angle of incidence for vertical polarisation is seen in the following two plots. In Figure B.7 (a) the results can be seen without an enclosure cover and Figure B.7 (b) with one.

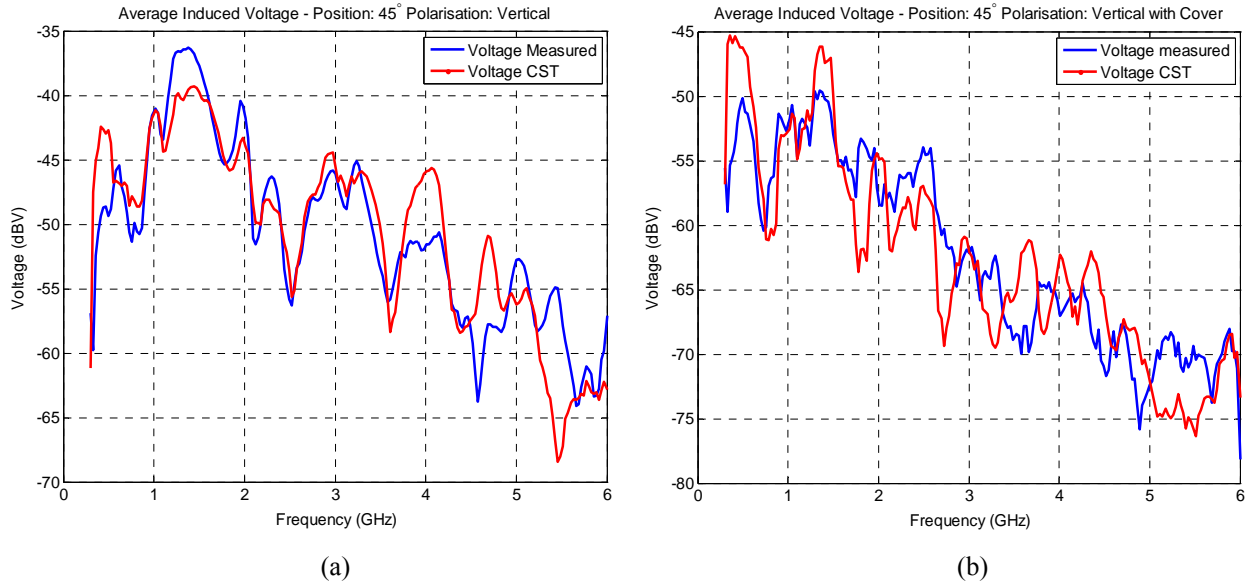


Figure B.7: Comparison of calculated and computed induced voltages for a 45° angle of incidence with vertical polarisation. Shown in (a) is the comparison without the enclosure cover and in (b) the comparison with the cover.

Appendix C.

KAT-7 RF Current Audit Results

C.1. Comparison of Scale Model S-parameter: Measured and Computed

The measured and computed S_{11} results for scenario one misaligned are shown in Figure C.1, with the measured and computed S_{21} results shown in Figure C.2 below.

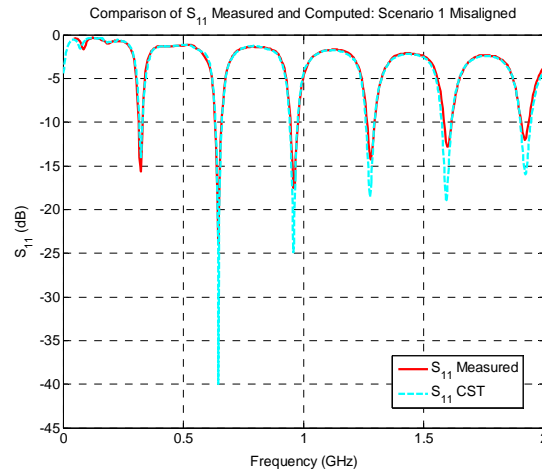
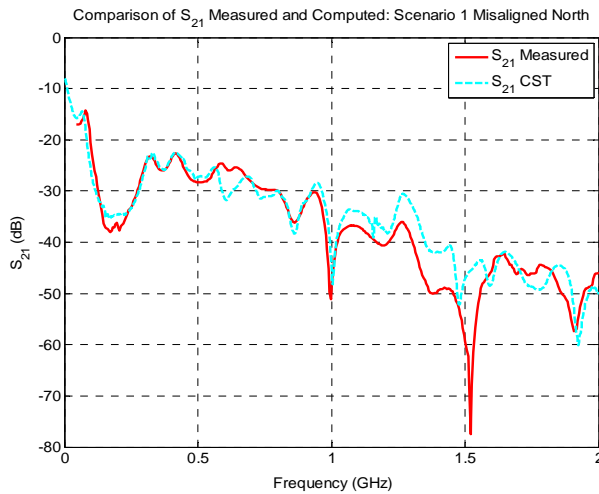
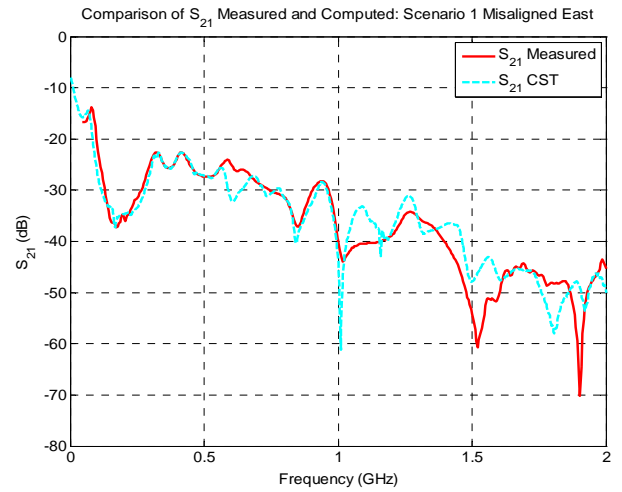


Figure C.1: Comparison of measured and computed S_{11} for both models in scenario one misaligned state.



(a)



(b)

APPENDIX C – KAT-7 RF CURRENT AUDIT RESULTS

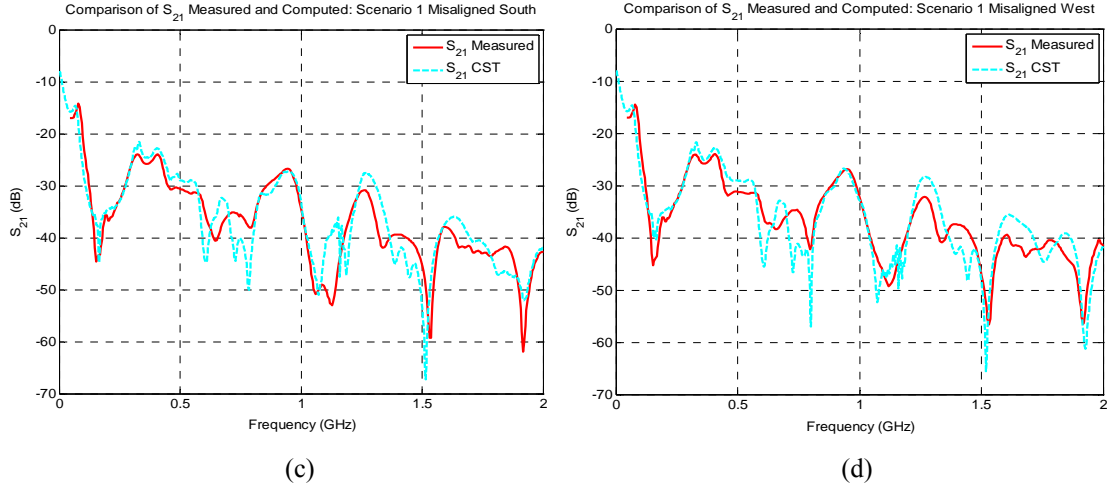


Figure C.2: Comparison of measured and computed S-parameters for both models in scenario one misaligned state. All four earthing connections are shown with (a) north-facing, (b) east-facing, (c) south-facing and (d) west-facing.

Comparison of measured and computed S_{11} results for scenario two aligned is shown in Figure C.3 with the S_{21} results for each connection shown in C.4.

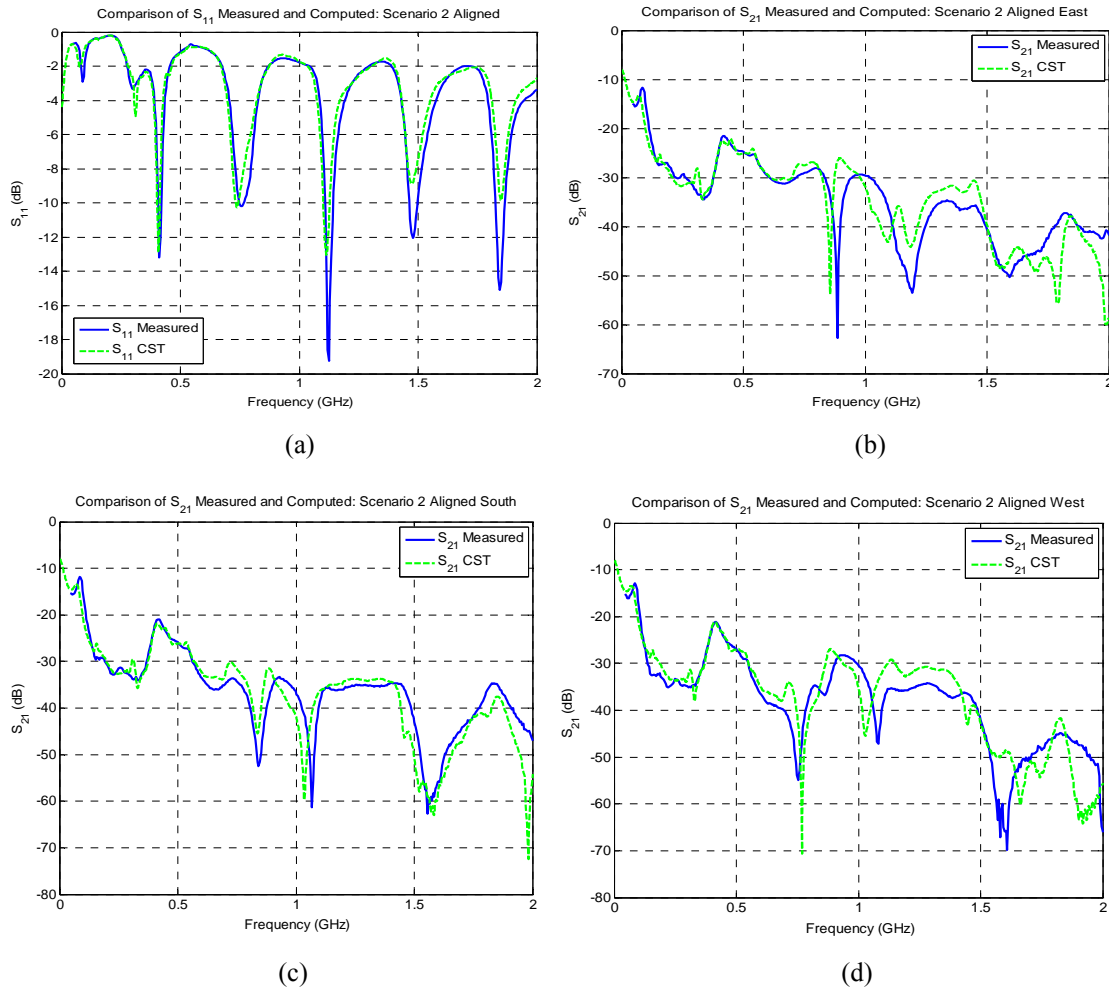


Figure C.4: Comparison of measured and computed S-parameters for both models in scenario two aligned state. S_{11} are shown in (a) with the remaining three of the four earthing connections shown as follows: (b) east-facing and (c) south-facing and (d) west-facing. The result for the north-facing connection is shown in Chapter 6.

APPENDIX C – KAT-7 RF CURRENT AUDIT RESULTS

Comparison of measured and computed S_{11} results for scenario two misaligned is shown in Figure C.5 with the measured and computed S_{21} for each connection shown in C.6.

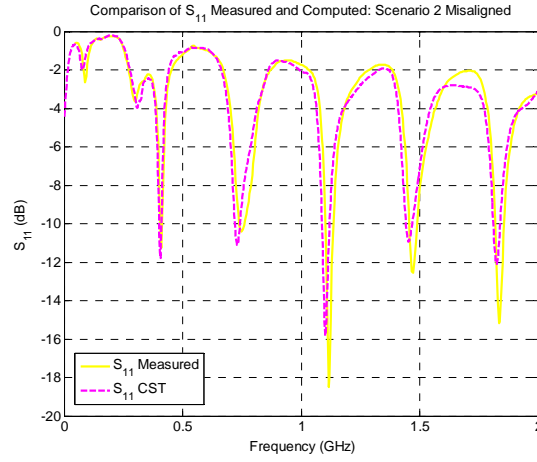


Figure C.5: Comparison of measured and computed S_{11} for both models in scenario two misaligned state.

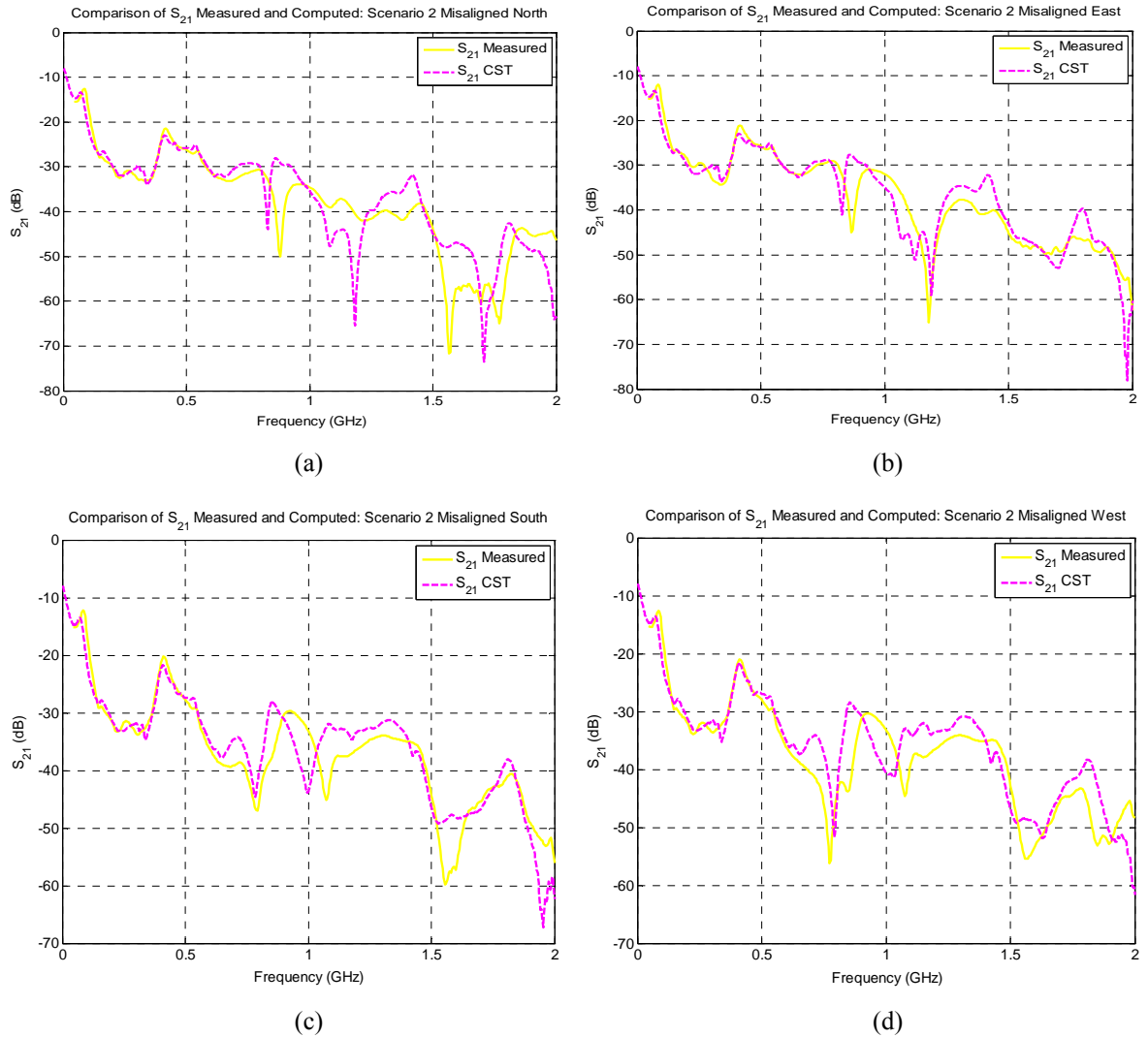


Figure C.6: Comparison of measured and computed S-parameters for both models in scenario two aligned state. All four earthing connections are shown with (a) north-facing, (b) east-facing, (c) south-facing and (d) west-facing.

C.2. Comparison of Current Distributions: Measured and Computed

Comparison of CM current flowing each of the four earthing connections for all four scenarios are shown. The comparisons include measured results for the physical scale models using the VNA and SA, computed results from the computational model and KAT-7 telescope measurements. The results for scenario one aligned are shown in C.7.

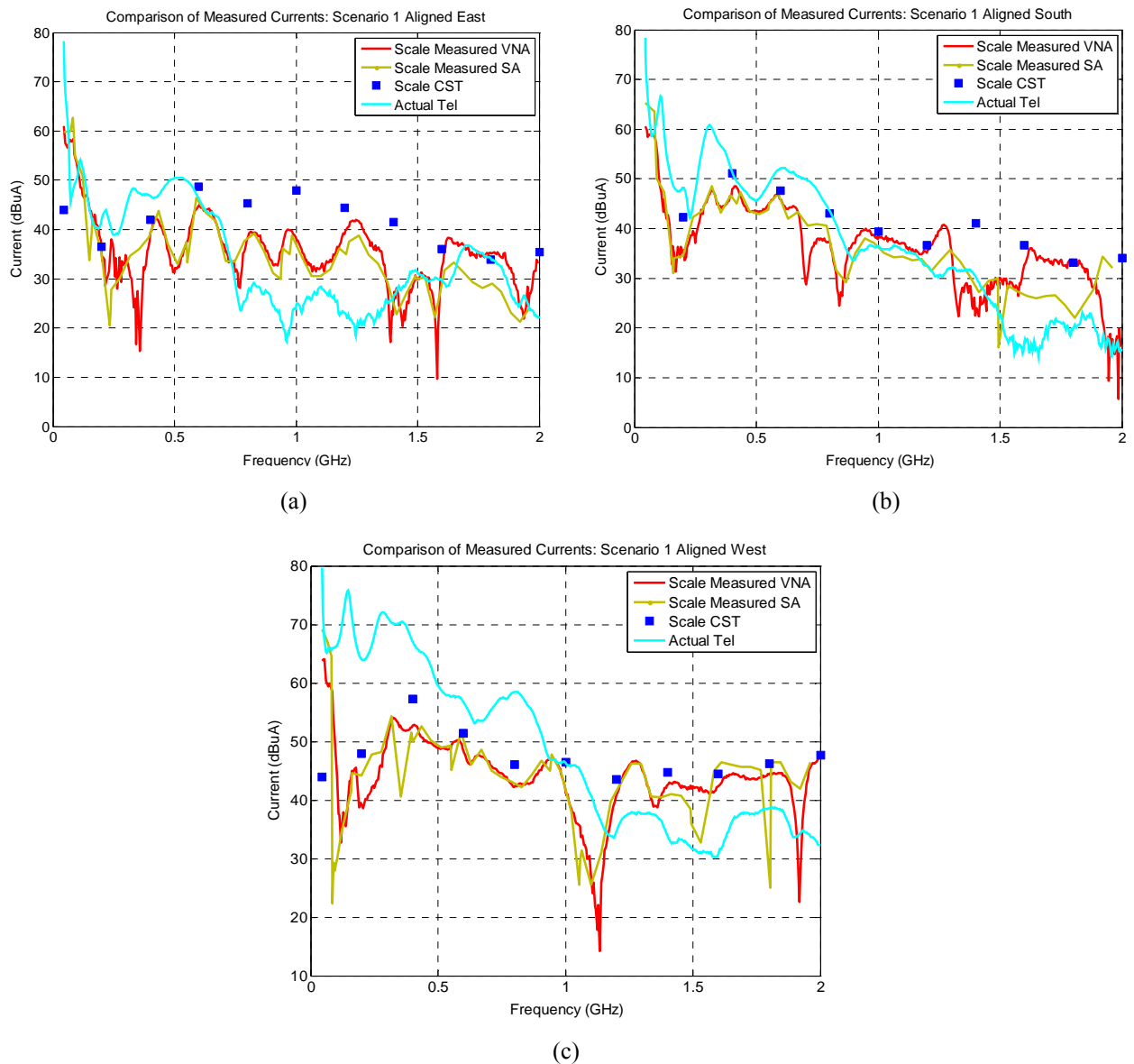


Figure C.7: Comparison of currents flowing on three of the four earth connections. These include measured results for the physical model using the VNA and SA, computed results for the computational model, and measurements on the KAT-7 telescope. Results for scenario one aligned are shown for (a) east-facing, (b) south-facing, (c) west-facing.

The results for scenario one misaligned are shown in Figure C.8.

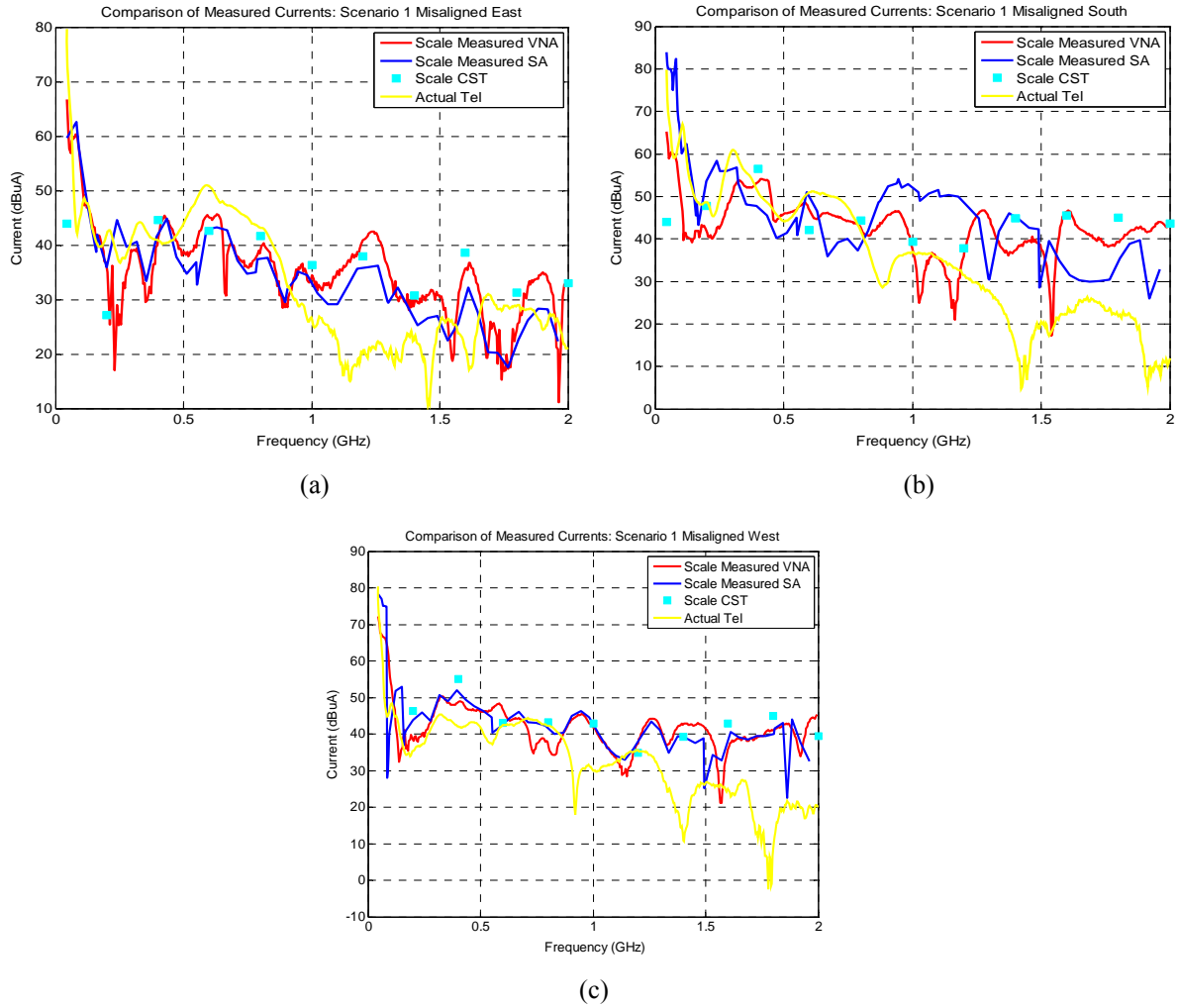
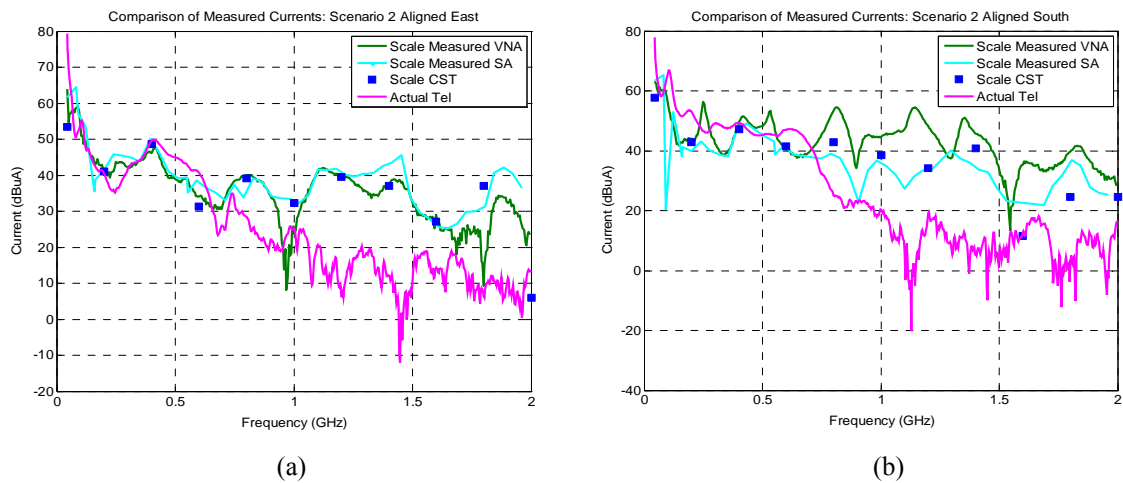
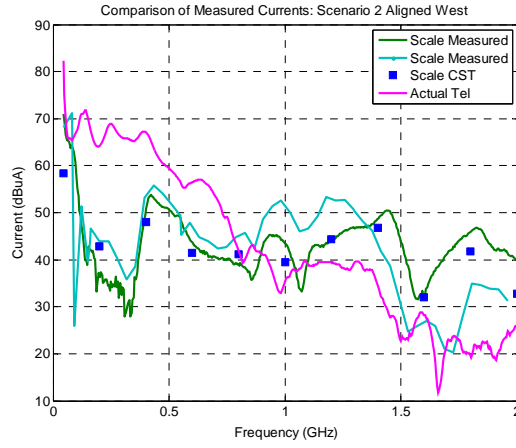


Figure C.8: Comparison of currents on three of the four earth connections. These include measured results for the physical model using the VNA and SA, computed results for the computational model, and measurements on the KAT-7 telescope. Results for scenario one misaligned shown for (a) east-facing, (b) south-facing, (c) west-facing.

The results for scenario two aligned are shown in Figure C.9.



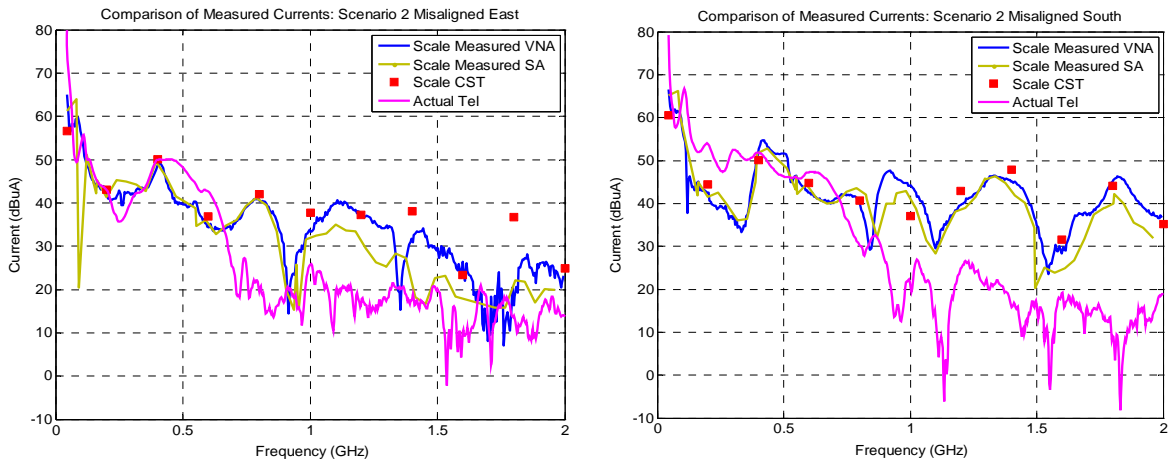
APPENDIX C – KAT-7 RF CURRENT AUDIT RESULTS



(c)

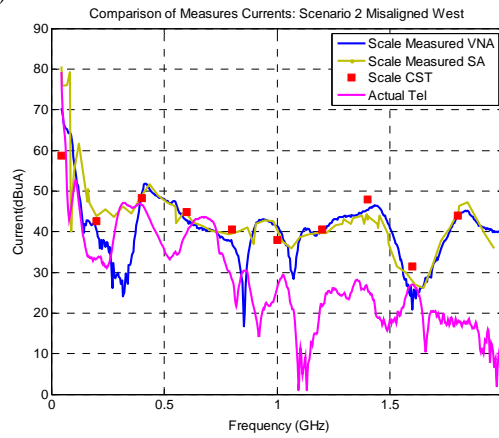
Figure C.9: Comparison of currents on three of the four earth connections. These include measured results for the physical model using the VNA and SA, computed results for the computational model, and measurements on the KAT-7 telescope. Results for scenario two aligned are shown for (a) east-facing, (b) south-facing, (c) west-facing.

The results for scenario two misaligned are shown in Figure C.10.



(a)

(b)



(c)

Figure C.10: Comparison of currents on three of the four earth connections. These include measured results for the physical model using the VNA and SA, computed results for the computational model, and measurements on the KAT-7 telescope. Results for scenario two misaligned are shown for (a) east-facing, (b) south-facing, (c) west-facing.

C.2. Current Distribution: Direct Injection

The distribution of CM current on the four earthing connections for a direct injection method for scenario two aligned is presented. Shown in Figure C.11 is a comparison of the measured currents between the four connections.

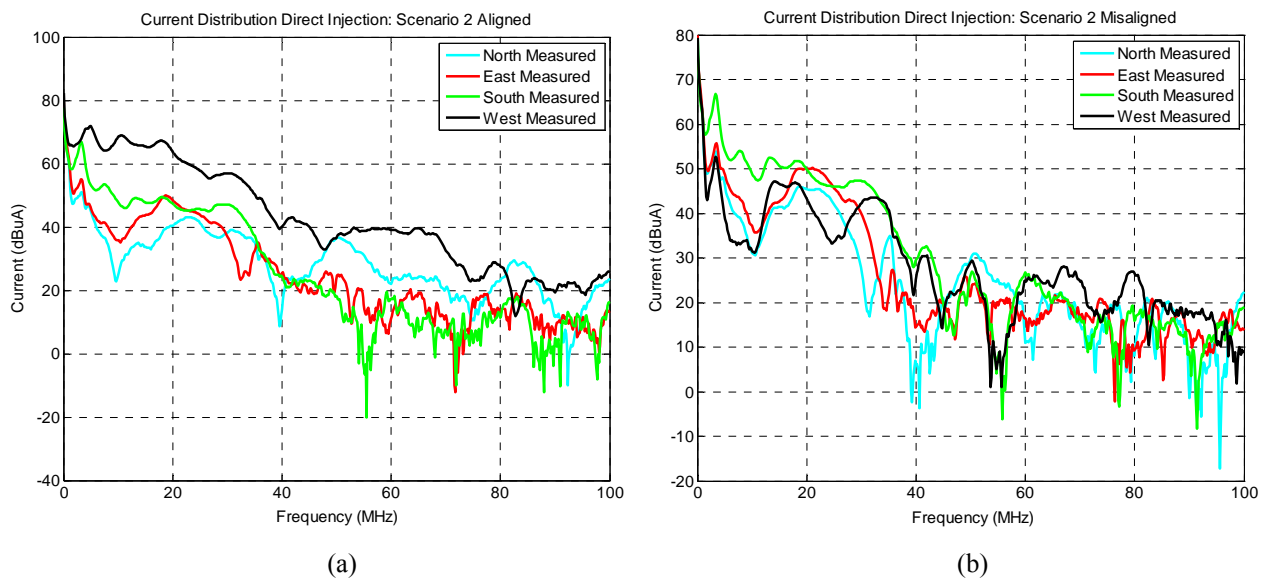


Figure C.11: Comparison of injected currents measured on the four earthing connections for the KAT-7 telescope. Scenario two aligned is shown in (a) and misaligned shown in (b).

C.3. Current Comparisons: Hardened vs. Non-hardened Direct Injection

The comparative results between a hardened and non-hardened telescope are presented in this section. The comparison is made by investigating the change in CM current on each of the four earthing connections when both the hardened and non-hardened telescopes are aligned and misaligned. With the LDC on the outside of the telescope aligned, more current will flow on the outside of the pedestal.

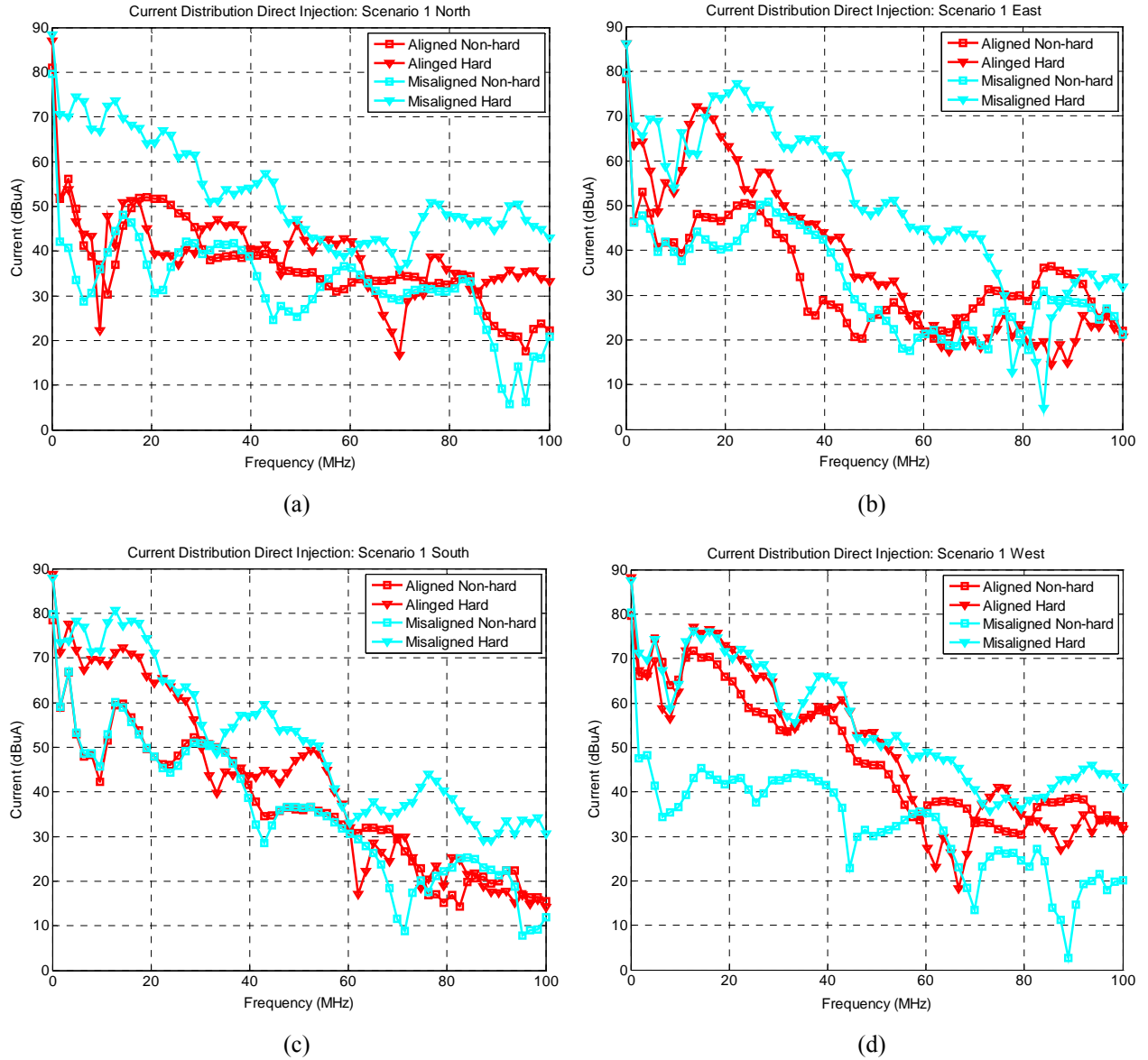


Figure C.12: Comparison of CM currents measured on the four earthing connections for a hardened and non-hardened telescope. Results are also compared when both the hardened and non-hardened telescopes are aligned and misaligned. The currents are calculated for each of the four connections starting with (a) north-facing, (b) east-facing, (c) south-facing and (d) west-facing.

The results for scenario two are compared in the same manner. Results are once again compared for the aligned and misaligned scenarios for both a hardened and non-hardened telescope.

APPENDIX C – KAT-7 RF CURRENT AUDIT RESULTS

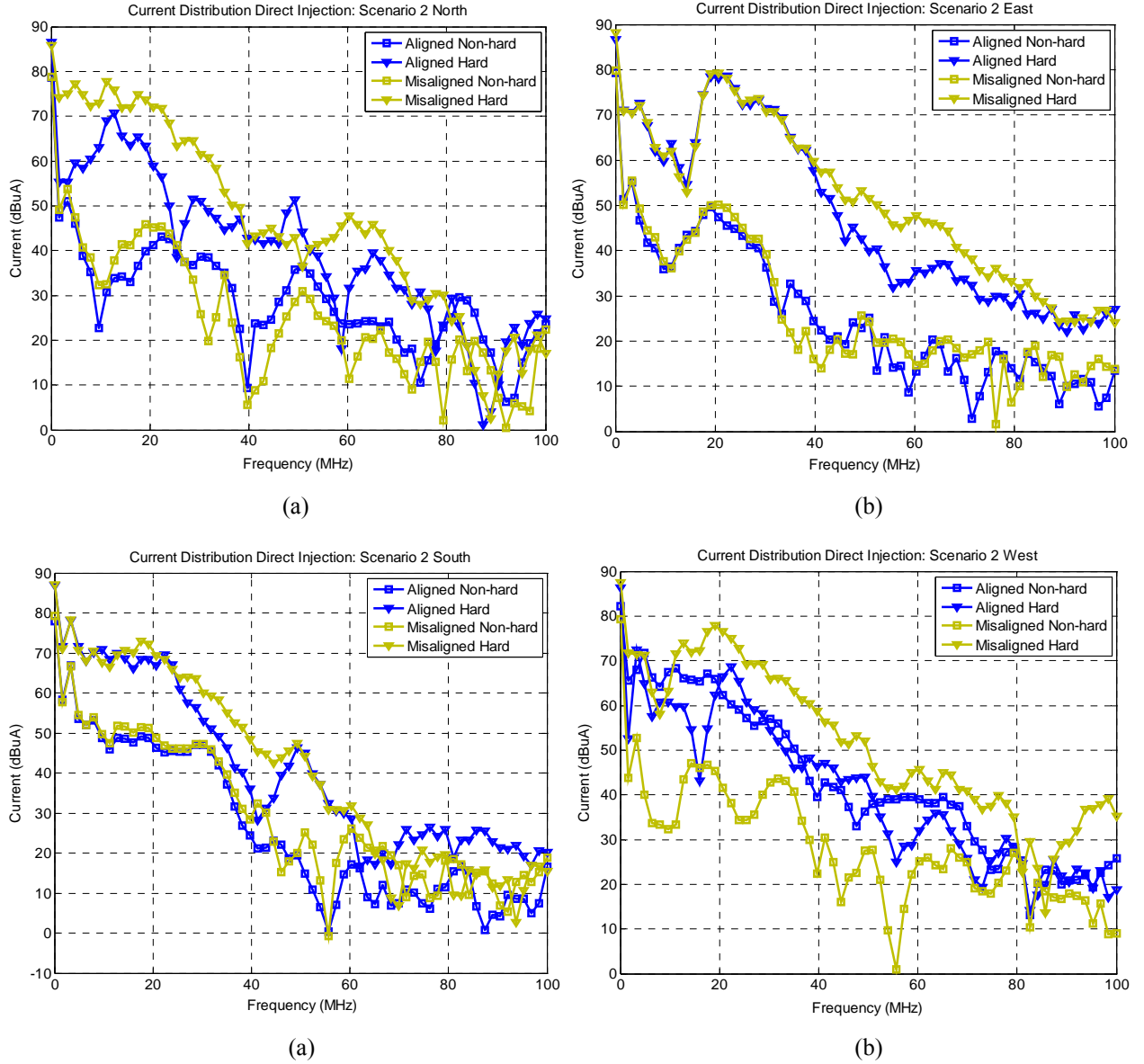


Figure C.13: Comparison of CM currents measured on the four earthing connections for a hardened and non-hardened telescope. Results are also compared when both the hardened and non-hardened telescopes are aligned and misaligned. The currents are calculated for each of the four connections starting with (a) north-facing, (b) east-facing, (c) south-facing and (d) west-facing.